

INFORMATION TO USERS

This manuscript has been reproduced from the microfilm master. UMI films the text directly from the original or copy submitted. Thus, some thesis and dissertation copies are in typewriter face, while others may be from any type of computer printer.

The quality of this reproduction is dependent upon the quality of the copy submitted. Broken or indistinct print, colored or poor quality illustrations and photographs, print bleedthrough, substandard margins, and improper alignment can adversely affect reproduction.

In the unlikely event that the author did not send UMI a complete manuscript and there are missing pages, these will be noted. Also, if unauthorized copyright material had to be removed, a note will indicate the deletion.

Oversize materials (e.g., maps, drawings, charts) are reproduced by sectioning the original, beginning at the upper left-hand corner and continuing from left to right in equal sections with small overlaps.

Photographs included in the original manuscript have been reproduced xerographically in this copy. Higher quality 6" x 9" black and white photographic prints are available for any photographs or illustrations appearing in this copy for an additional charge. Contact UMI directly to order.

**ProQuest Information and Learning
300 North Zeeb Road, Ann Arbor, MI 48106-1346 USA
800-521-0600**

UMI[®]

University of Alberta

**Metal-Directed Self-Assembly Synthesis:
Supramolecular Chemistry Using
Axial Coordination and Metal Chelation**

by

Kelly Chichak



A thesis submitted to the Faculty of Graduate Studies and Research in partial fulfillment
of the requirements for the degree of
Doctor of Philosophy

Department of Chemistry

Edmonton, Alberta

Spring 2002



**National Library
of Canada**

**Acquisitions and
Bibliographic Services**

**395 Wellington Street
Ottawa ON K1A 0N4
Canada**

**Bibliothèque nationale
du Canada**

**Acquisitions et
services bibliographiques**

**395, rue Wellington
Ottawa ON K1A 0N4
Canada**

Your file Votre référence

Our file Notre référence

The author has granted a non-exclusive licence allowing the National Library of Canada to reproduce, loan, distribute or sell copies of this thesis in microform, paper or electronic formats.

The author retains ownership of the copyright in this thesis. Neither the thesis nor substantial extracts from it may be printed or otherwise reproduced without the author's permission.

L'auteur a accordé une licence non exclusive permettant à la Bibliothèque nationale du Canada de reproduire, prêter, distribuer ou vendre des copies de cette thèse sous la forme de microfiche/film, de reproduction sur papier ou sur format électronique.

L'auteur conserve la propriété du droit d'auteur qui protège cette thèse. Ni la thèse ni des extraits substantiels de celle-ci ne doivent être imprimés ou autrement reproduits sans son autorisation.

0-612-68543-8

Canada

University of Alberta

Library Release Form

Name of Author: Kelly Chichak

Title of Thesis: Metal-Directed Self-Assembly Synthesis:
Supramolecular Chemistry Using Axial Coordination and Metal Chelation

Degree: Doctorate of Philosophy

Year this Degree Granted: 2002

Permission is hereby granted to the University of Alberta Library to reproduce single copies of this thesis and to lend or sell such copies for private, scholarly or scientific research purposes only.

The author reserves all other publication and other rights in association with the copyright in the thesis, and excepts as herein before provided, neither the thesis nor any substantial portion thereof may be printed or otherwise reproduced in any material form whatever without the author's prior written permission



172 Highland Way
Sherwood Park, AB
T8A 5R2

December 12, 2001


University of Alberta

Faculty of Graduate Studies and Research

The undersigned certify that they have read, and recommend to the Faculty of Graduate Studies and Research for acceptance, a thesis entitled **Metal-Directed Self-Assembly Synthesis: Supramolecular Chemistry Using Axial Coordination and Metal Chelation** submitted by Kelly Chichak in partial fulfillment of the requirements for the degree of Doctor of Philosophy.



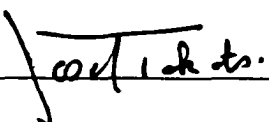
Associate Professor Neil R. Branda



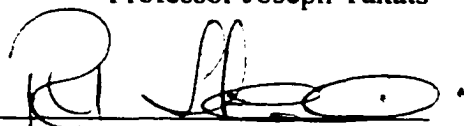
Professor Ole Hindsgaul




Professor Linda Reha-Krantz



Professor Joseph Takats



Assistant Professor Rik Tykwinski



Professor Stephen Loeb

December 12, 2001

Abstract

A series of heteroaromatic ligands were synthesized and their metal binding properties were probed using metal-directed self-assembly synthesis to construct *supramolecular* architectures. Through self-assembly processes, the binding information stored in both the metal and ligand building blocks was translated into the geometries of the products formed.

The transition metal-based template synthesis of a porphyrin cube was studied employing axial coordination as a binding motif. In order to emulate the octahedral geometry of a cube, a template was designed around an octahedral transition metal containing three (4,4'-di(4''-pyridyl)-2,2'-bipyridine) tetrapyridyl ligands. In this environment, six porphyrin walls were assembled around the central template that produced a false cube.

The viability of axial coordination in *supramolecular* chemistry was studied and exploited to construct a series of neutral and charged arrays with controlled topology. The spatial arrangements of the molecular components can be modified and controlled by the central template building block. The central templates were used to position ruthenium(II) carbonyl porphyrins in linear, tetrahedral, and octahedral spatial arrangements.

Coordination to the axial position of a metalloporphyrin effectively end-capped the 1,2-bis(4,4'-dipyridinium)ethane dication•dibenzo[24]crown-8 [2]pseudo-rotaxane to generate the stable porphyrinic [2]rotaxane. ¹H NMR spectroscopy was used to highlight the dynamic properties of the [2]rotaxane and it provided a convenient method for tracking the progress of the self-assembly process.

Mononuclear and Binuclear ruthenium(II) carbonyl complexes with Schiff base ligands were prepared and their axial coordination properties were probed. The mononuclear ruthenium(II) carbonyl complex was shown to spontaneously form linear and three-dimensional assemblies through axial coordination to pyridyl Lewis bases. The binuclear ruthenium(II) carbonyl complexes offered two accessible axial metal binding sites separated by different intermetal distances. By taking advantage of axial coordination, molecular prisms and rectangles were constructed using these bimetallic carbonyl complexes.

Table of Contents

1	Preamble	1
1.1	Supramolecular Chemistry and Self-Assembly Synthesis	2
1.2	Self-Assembly Synthesis Using Coordination Chemistry	5
1.3	Self-Assembly Synthesis of Closed-Shelled Molecules	17
1.4	The Template Synthesis of a Porphyrin Cube	19
1.5	The Photosynthetic Reaction Center	25
	1.5.1 Excited-State Properties of Porphyrins	26
	1.5.2 Positioning Chromophores in Space Using Metal Coordination	29
1.6	References	35
2	Axial Coordination and Multi-Component Porphyrinic Arrays	39
2.1	Characterizing Supramolecular Architectures	39
2.2	Spectroscopic Properties of the Building Blocks	40
	2.2.1 Pyridyl Adducts of Ru(II) Carbonyl Metalloporphyrins	41
	2.2.1.1 ¹ H NMR Spectroscopy	42
	2.2.1.2 UV/Vis and IR Spectroscopy	43
	2.2.2 Characterizing Polypyridyl Transition Metal Complexes	45
	2.2.2.1 ¹ H NMR Spectroscopy	45
	2.2.2.2 UV/Vis Spectroscopy	46
	2.2.2.3 Electrospray Ionization Mass Spectrometry	46
2.3	Solvent Effects on Axial Coordination	47
2.4	General Remarks	49

2.5	Linear Axially Coordinated Metalloporphyrin Arrays	51
2.5.1	Transition Metal Complex Design for Linear Templates	52
2.5.2	Results and Discussion	53
2.5.2.1	Metalloporphyrin Synthesis	53
2.5.2.2	Core Complex Ligand Synthesis	56
2.5.2.3	The Synthesis of the Transition Metal Core Complexes	57
2.5.2.4	Self-Assembly Synthesis of the Linear Porphyrin Arrays	60
2.5.2.5	Characterizations Using ¹ H NMR Spectroscopy	62
2.5.2.6	Characterizations Using ESI Mass Spectrometry	64
2.5.2.7	Characterizations Using IR Spectroscopy	64
2.5.2.8	Photophysical Properties of the Ru(II) and Os(II) Triads	65
2.6	Tetrahedral Axially Coordinated Metalloporphyrin Arrays	69
2.6.1	Transition Metal Complex Design for Tetrahedral Templates	69
2.6.2	Results and Discussion	71
2.6.2.1	Self-Assembly Synthesis of a Tetrahedral Porphyrin Array	71
2.6.2.2	Stabilized Bipyridine Complexes of Copper(I)	73
2.6.2.3	Characterization Using ESI Mass Spectrometry	84
2.6.2.4	Characterization Using IR Spectroscopy	85
2.6.2.5	Characterization Using UV/Vis Spectroscopy	85
2.7	Octahedral Axially Coordinated Metalloporphyrin Arrays	87
2.7.1	Transition Metal Complex Design for Octahedral Templates	88
2.7.2	Results and Discussion	89
2.7.2.1	Synthesis of the Transition Metal Core Complexes	89

2.7.2.2	Synthesis of Another Metalloporphyrin	91
2.7.2.3	Synthesis of the Ruthenium(II) Octahedral Arrays	93
2.7.2.4	Self-Assembly Synthesis of the Iron(II) Octahedral Arrays	99
2.7.2.5	Characterizations Using IR Spectroscopy	100
2.7.2.6	Characterizations Using ESI Mass Spectrometry	101
2.7.2.7	Photophysical Properties of the Ru(II) Octahedral Arrays	102
2.8	Experimental	109
2.9	References	140
3	Axially Coordinated Metalloporphyrin Stoppers for Rotaxanes	144
3.1	Introduction	144
3.1.1	Methods in Rotaxane Synthesis	146
3.2	Metalloporphyrin Stoppered Rotaxanes	150
3.3	Results and Discussion	151
3.3.1	[2]Pseudo-Rotaxane Design	151
3.3.2	Spontaneous Pseudo-Rotaxane Formation	152
3.3.3	Metalloporphyrin Capping for [2]Rotaxane Formation	155
3.3.4	[2]Rotaxane X-Ray Crystal Structure	157
3.3.5	[2]Rotaxane Solution Dynamics	159
3.3.6	[2]Rotaxane Synthesis Using an Axially Coordinated Axle	162
3.3.7	Characterization Using ESI Mass Spectrometry	165
3.3.8	Characterizations Using IR Spectroscopy	166
3.3.9	Characterization Using UV/Vis Spectroscopy	166

3.4	Experimental	168
3.5	References	173
4	Ruthenium(II)salophen Assemblies Using Axial Coordination	176
4.1	Introduction	177
4.1.1	Metallosalens and Metallosalophens in Supramolecular Chemistry	178
4.2	Results and Discussion	179
4.2.1	Synthesis of the Ru(II) Carbonyl Salophen Building Block	179
4.2.2	¹ H NMR Solution Studies of the Ru(II) Carbonyl Salophen	183
4.2.3	¹ H NMR Variable-Temperature Studies	184
4.2.4	Two-Dimensional ¹ H NMR COSY and NOESY Studies	189
4.2.5	X-Ray Crystallographic Analysis of the Ru(II) Carbonyl Salophen	192
4.2.6	Synthesis of the Ru(II) Carbonyl Salophen Pyridyl Adduct	195
4.2.7	Construction of Neutral Assemblies	197
4.2.8	Construction of Charged Assemblies	199
4.3	Synthesis of the Bis(salophens) and Bis(metallosalophens)	203
4.4	UV/Vis Spectroscopic Analysis	209
4.5	Electrochemistry of the Metallosalophens	211
4.6	Self-Assembly Studies of Bimetallic Salophens and Porphyrins	212
4.6.1	The Construction of Two Dimensional Rectangles	213
4.6.2	The Construction of Three Dimensional Prisms	220
4.7	Experimental	224
4.8	References	247

5	Conclusions	251
5.1	Metalloporphyrins and Metallosalophens in Supramolecular Chemistry	252
5.2	Future Studies	253
	5.2.1 Characterization of the Supramolecular Properties	253
	5.2.2 The Templated Synthesis of the Porphyrin Cube	255
5.3	Future Extensions	257
	5.3.1 Photoelectromchemical Devices Using Axial Coordination	257
5.4	References	261

List of Equations

Chapter 1

Equation 1	Equation of Supramolecular Chemistry	2
Equation 2	Thermodynamic Expression of Formation Constants	8

Chapter 2

Equation 1	Synthesis of the Iron(II) Pyridylterpyridine Complex	58
Equation 2	Self-Assembly Synthesis of the Iron(II) Linear Porphyrin Array	61
Equation 3	Synthesis of the Bipyridine Ligand for the Tetrahedral Complex	71
Equation 4	Synthesis of the Tetraphenylbipyridine	76
Equation 5	The Bond Rotation of Bipyridine Ligands for Chelation	82
Equation 6	Synthesis of the Tris(bipyridyl)iron(II) Core Complex	90

Chapter 3

Equation 1	[2]Pseudo-rotaxane Formation	151
Equation 2	Metalloporphyrin Capping of the [2]Pseudo-rotaxane	155
Equation 3	Schematic Representation of Solution Equilibria	160
Equation 4	Synthesis of the Axially Coordinated Axle	163

Chapter 4

Equation 1	Formation of the Metallosalophen Tetrameric Complex	192
Equation 2	Synthesis of the Metallosalophen Pyridine Adduct	195
Equation 3	Synthesis of the Metallosalophen Bipyridine Assembly	197

Equation 4	The Self-Assembly Pathway of the Bis(porphyrin) Rectangle	214
Equation 5	The Self-Assembly Pathway of the Bis(porphyrin) Rectangle	218
Equation 6	Schematic Representation of the Bis(metalloporphyrin) Prism	220
Equation 7	Schematic Representation of the Bis(metallosalophen) Prism	221

List of Figures

Chapter 1

Figure 1	Examples of Metal Coordination in Supramolecular Chemistry	6
Figure 2	Examples of Dative Bonds	7
Figure 3	Position and Electrostatic Relationships of a Metal Ion's Orbitals	9
Figure 4	Strong and Weak Ligand Field Splitting Effects	10
Figure 5	Crystal Field Stabilization Energies for the Irving–Williams Series	12
Figure 6	The Jahn–Teller Tetragonal Distortion	12
Figure 7	The Removal of Orbital Degeneracy <i>via</i> the Jahn–Teller Distortion	12
Figure 8	Orbital Energy Level Diagrams for Transition Metal Complexes	13
Figure 9	Metal Binding Motifs of Some Common Ligands	14
Figure 10	Examples of Closed-shelled Tetrahedrons	17
Figure 11	The Platonic Hexahedron	19
Figure 12	Chemical Equivalents of a Square and an Octahedral Template	21
Figure 13	Example of Molecular Templating	22
Figure 14	Molecular Templating Approach to Synthesize a Porphyrin Cube	23
Figure 15	The Octahedral Porphyrin Array	24
Figure 16	Bacterial Photoreaction Center of <i>Rhodobacter sphaeroides</i>	25
Figure 17	Photoexcitation of Porphyrins	26
Figure 18	Dexter Mechanism for Energy Transfer	28
Figure 19	Oxidative and Reductive Electron Transfer of Porphyrins	29
Figure 20	An Artificial Photoreaction Center Mimic	30
Figure 21	Examples of Polymeric and Dendritic Porphyrin Arrays	31

Figure 22	Examples of Cyclic and Non-cyclic Porphyrin Arrays	32
Figure 23	Examples of Ambidentate Ligands	33
Figure 24	Molecular Models of the Templating Transition Metal Complexes	33
Chapter 2		
Figure 1	Key Spectroscopic Changes Upon Pyridine Coordination	41
Figure 2	The Bonding Modes of Carbon Monoxide to Metal <i>d</i> Orbitals	44
Figure 3	The Conformational Change of 2,2'-Bipyridine for Chelation	45
Figure 4	Molecular Model of the Linear Porphyrin Array	51
Figure 5	Design Layout of the Linear Template	53
Figure 6	The Reduced Porphyrin Macrocycle of Chlorin	55
Figure 7	Upfield Shifts of Pyridine Resonances in ¹ H NMR Spectroscopy	62
Figure 8	¹ H NMR Studies of the Ru(II) Linear Porphyrin Array	63
Figure 9	Absorption Spectra of the Os(II) Linear Array and Components	65
Figure 10	Emission Spectra of the Os(II) Linear Array and Components	66
Figure 11	Emission Spectra of the Ru(II) Linear Array and Components	67
Figure 12	Design Layout of the Tetrahedral Template	70
Figure 13	Solvent Assisted Oxidation of Copper(I) to Copper(II)	73
Figure 14	Preventing the Solvent Assisted Oxidation of Copper(I)	74
Figure 15	Crystal Structure of a Stabilized Copper(I) Complex	77
Figure 16	Selected Bonds Angles of a Pseudotetrahedral Cu(I) Complex	77
Figure 17	¹ H NMR Spectra of Proper Bipyridine Copper(I) Chelation	79
Figure 18	¹ H NMR Self-Assembly Studies of the Stable Tetrahedral Array	81

Figure 19	Molecular Model of the Tetrahedral Porphyrin Array	82
Figure 20	ESI Mass Spectrum of the Tetrahedral Porphyrin Array	85
Figure 21	Absorption Spectrum of the Tetrahedral Porphyrin Array	86
Figure 22	Design Layout of the Octahedral Template	88
Figure 23	Characteristic Upfield Shifts of Axially Coordinated Pyridines	95
Figure 24	¹ H NMR Studies of the Ru(II) Octahedral Porphyrin Arrays	96
Figure 25	Molecular Models of the Octahedral Arrays and Components	98
Figure 26	ESI Mass Spectrum of a Ru(II) Octahedral Porphyrin Array	101
Figure 27	Absorption Spectra of a Ru(II) Octahedral Array and Components	102
Figure 28	Absorption Spectra of a Ru(II) Octahedral Array and Components	103
Figure 29	Emission Spectra of an Octahedral Array and Components	105
Figure 29	Emission Spectra of an Octahedral Array and Components	107
 Chapter 3		
Figure 1	[2]Rotaxane Formation	144
Figure 2	A Molecular Shuttle	145
Figure 3	Three Common Strategies Used for Rotaxane Synthesis	146
Figure 4	Imine Stoppering Method	147
Figure 5	Metal Directed Stoppering	148
Figure 6	Alternative Methods Used to Assemble Wheels and Axles	148
Figure 7	¹ H NMR Self-Assembly Study of [2]Pseudo-rotaxane Formation	153
Figure 8	Important Interactions Involved in the Threading Process	153
Figure 9	¹ H NMR Self-Assembly Study of Metalloporphyrin End-Capping	156

Figure 10	X-ray Crystal Structure of [2]Rotaxane	158
Figure 11	¹ H NMR Spectra of the Solution Behaviour of the [2]Rotaxane	159
Figure 12	¹ H NMR Spectra of Metalloporphyrin End-Cap Removal	162
Figure 13	¹ H NMR Self-Assembly Study Using the Capped Axle	164
Figure 14	Absorption Spectrum of the [2]Rotaxane	167
 Chapter 4		
Figure 1	Structures of Metallosalen and Metallosalophen Complexes	178
Figure 2	Molecular Structures of an Iron(II) Salen Dimer	180
Figure 3	Molecular Structure of an Aluminum(III) Salen Dimer	182
Figure 4	¹ H NMR Solution Dynamics of the Ru(II) Salophen Monomer	184
Figure 5	Spectra of the Variable-Temperature ¹ H NMR Experiment	185
Figure 6	Spectra of the Variable-Temperature ¹ H NMR Experiment	186
Figure 7	The Enantiomeric Pair of Trigonal Bipyramidal Complexes	187
Figure 8	The Enantiomeric Pair of Distorted Square Pyramidal Complexes	188
Figure 9	The Oxygen-Bridged Dimer Equilibrium	189
Figure 10	COSY Map of the Ru(II) Salophen Monomer at -20°C	190
Figure 11	NOESY Spectrum of the Ru(II) Salophen Monomer at -20°C	191
Figure 12	X-Ray Crystal Structure of the Ruthenium Salophen Tetramer	193
Figure 13	¹ H NMR Study of the Bipyridine Assembly	198
Figure 14	X-Ray Crystal Structure of the Small Nickel(II) Bis(salophen)	206
Figure 15	X-Ray Crystal Structure of the Large Nickel(II) Bis(salophen)	207
Figure 16	Crossley's Ruthenium(II) Carbonyl Bis(porphyrin) Complex	208

Figure 17	UV/Vis Spectra of the Mono- and Bis(metallosalophens)	210
Figure 18	Cyclic Voltammograms of the Mono- and Bis(metallosalophens)	212
Figure 19	Schematic Representations of Bimetallic Panels and Linkers	213
Figure 20	¹H NMR Self-Assembly Study of the Bis(porphyrin) Rectangle	216
Figure 21	¹H NMR Self-Assembly Study of the Triangular Prism	222
Figure 22	Molecular Models of the Water Accessible Surfaces of the Prism	223

Chapter 5

Figure 1	Examples of Suitable Control Complexes	254
Figure 2	Molecular Models of Octahedral Templates	256
Figure 3	An Example of a Photoelectrochemical Device	258
Figure 4	A Photoelectrochemical Device Using Axial Coordination	259
Figure 5	A Larger Photoelectrochemical Device Using Axial Coordination	260

List of Schemes

Chapter 1

Scheme 1	Preorganization of Hydrogen Bonding Surfaces Using Metal Ions	3
Scheme 2	Retrosynthetic Approach to a Molecular Cube	20

Chapter 2

Scheme 1	Synthesis of Ruthenium(II) Carbonyl Tetratolylporphyrin Complex	54
Scheme 2	Synthesis of the Pyridylterpyridine Ligand	56
Scheme 3	Synthesis of the Phenylterpyridine Ligand	57
Scheme 4	Synthesis of the Bis(terpyridyl)ruthenium(II) Complexes	58
Scheme 5	Synthesis of the Bis(terpyridyl)osmium(II) Complexes	59
Scheme 6	Synthesis of the Fe(II), Ru(II), and Os(II) Linear Porphyrin Arrays	60
Scheme 7	Synthesis of a Bis(bipyridyl)copper(I) Porphyrin Array	71
Scheme 8	Synthesis of the Stabilized Ligand for Copper(I) Chelation	75
Scheme 9	Synthesis of a Protected Ligand for Copper(I) Chelation	78
Scheme 10	Self-Assembly Synthesis of the Tetrahedral Porphyrin Array	80
Scheme 11	The Unproductive Binding Algorithm of the Bipyridine Ligand	83
Scheme 12	The Unproductive Binding Algorithm of the Bipyridine Ligand	84
Scheme 13	Synthesis of the Tris(bipyridyl)ruthenium(II) Core Complex	90
Scheme 14	Synthesis of Ru(II) Carbonyl Octaethylporphyrin Complex	92
Scheme 15	Synthesis of Ruthenium(II) Octahedral Porphyrin Arrays	94
Scheme 16	Self-Assembly Synthesis of Iron(II) Octahedral Porphyrin Arrays	99

Chapter 3

Scheme 1	Synthesis of the Dicationic Axle Component	152
-----------------	---	------------

Chapter 4

Scheme 1	Synthesis of the Salophen and Ru(II)salophen Carbonyl Complex	181
Scheme 2	Synthesis of the Charged Linear Assemblies	200
Scheme 3	Synthesis of the Charge Octahedral Assemblies	202
Scheme 4	Synthesis of the Small Bis(metallosalophen)	203
Scheme 5	Synthesis of the Large Bis(metallosalophen)	204

List of Tables

Chapter 1

Table 1	Examples of Metal-Ligand Complexes	16
---------	------------------------------------	----

Chapter 2

Table 1	Spectrometric Methods and Applicable Conditions	40
Table 2	Crystallographic Data of [Cu(16) ₂]PF ₆	139

Chapter 3

Table 1	Selected ¹ H NMR data of the [2]Rotaxane	157
Table 2	Crystallographic Data of the [2]Rotaxane	172

Chapter 4

Table 1	¹ H NMR Data of the Pyridyl Adduct	196
Table 2	¹ H NMR Data of the Bipyridyl Adduct	199
Table 3	¹ H NMR Data of the Charged Assemblies	201
Table 4	Selected UV/Vis Absorption Data of the Assemblies	209
Table 5	Crystallographic Data of the Bimetallic Nickel(II) Analogs	246

List of Abbreviations

Ac	acetyl
APT	attached proton test
bpy	2,2'-bipyridine
BSP	<i>N,N'</i> -bis(3,5-di- <i>tert</i> -butylsalicylidene)-1,2-phenylenediamine
BS2P	<i>N,N'',N''',N''''</i> -tetra-(3,5-di- <i>tert</i> -butylsalicylidene)-1,2,4,5-phenylenetetra-amine
BS2DP	<i>N,N'',N''',N''''</i> -tetra-(3,5-di- <i>tert</i> -butyl-salicylidene)-2,3,7,8-dibenzo[1,4]dioxin-tetraamine
br	broad
calcd	calculated
CO	carbon monoxide
COSY	correlated Spectroscopy
δ	chemical shift in parts per million downfield from TMS
d	doublet
decomp	decomposition
DB24C8	dibenzo-24-crown-8
DN	donor number
DNA	deoxyribonucleic acid
DMF	dimethylformamide
DMSO	dimethylsulfoxide
dpybpy	4,4'-di(4''-pyridyl)-2,2'-bipyridine
dpyphbpy	4,4':6,6'-(4'',4''')-dipyridyl)-2,2'-bipyridine

EI	electron impact
ESI	electrospray ionization
Et	ethyl
Et₂O	diethyl ether
g	gram
IR	infrared
<i>J</i>	coupling constant
<i>K_a</i>	association constant
<i>K_f</i>	formation constant
<i>K_n</i>	equilibrium constant (where n equals an integer)
<i>k_{off}</i>	decomplexation rate
<i>k_{on}</i>	complexation rate
m	multiplet
MHz	megahertz
min	minute
M.p.	melting point
MS	mass spectrometry
<i>m/z</i>	mass to charge ratio
NOESY	nuclear Overhauser and exchange spectroscopy
NMR	nuclear magnetic resonance
OEP	2,3,7,8,12,13,17,18-octaethylpophyrinato dianion
Ph	phenyl
phtpy	4'-phenyl-2,2':6',2''-terpyridine

ppm	parts per million
PPh₃	triphenylphosphine
py	pyridine
pytpy	4'-(4'''-pyridyl)-2,2':6',2''-terpyridine
R	rest of molecule
RT	room temperature
s	singlet
t	triplet
<i>t</i>-Bu	<i>tert</i>-butyl
THF	tetrahydrofuran
TMS	trimethylsilane
TPP	5,10,15,20-tetraphenylporphyrinato dianion
TTP	5,10,15,20-tetratolylporphyrinato dianion
UV	ultraviolet light
Vis	visible light

Metal-Directed Self-Assembly Synthesis: Supramolecular Chemistry Using Axial Coordination and Metal Chelation

by

Kelly Chichak

Chapter 1 – Preamble

An atom is comprised of a nucleus containing neutrons and protons that is surrounded by electrons. Because atoms are mostly empty space it is amazing that chemists are capable of manipulating them to form molecules. The logic of chemistry stems from its theoretical and physical roots which provide the understanding of the fundamental events that are related to atomic structure and chemical bonding. In the field of synthetic chemistry, the construction of molecules is carried out through a series of manipulations based on an understanding of chemical reactivity. The development of new synthetic methods assists in providing efficient routes to prepare small molecules. Several questions remain: How can we take chemistry further? Is the traditional synthetic approach the best suited to prepare nanoscale molecular architectures? How can a 90° bond be created using only carbon atoms (*p*-block elements) when the theory of hybridization does not accommodate this geometry? To address these questions, a lesson should be taken from Nature. Nature uses dynamic events to create macroscopic assemblies from small building blocks with maximum efficiency *via* self-assembly. In

this process, the building blocks aggregate with a high degree of specificity and structural integrity guided by the structural information provided by strategically placed labile intermolecular bonding motifs. The use of these small building blocks provides Nature with an extremely large pool of molecules that can be used for aggregate formation. As a consequence, the aggregation of small building blocks, whose preparation requires significantly fewer synthetic steps than the final assembly, has allowed Nature to go “beyond the molecule”. The concept of taking chemistry “beyond the molecule” is the underlying principle behind *Supramolecular* chemistry.¹

1.1 – Supramolecular Chemistry and Self-Assembly Synthesis

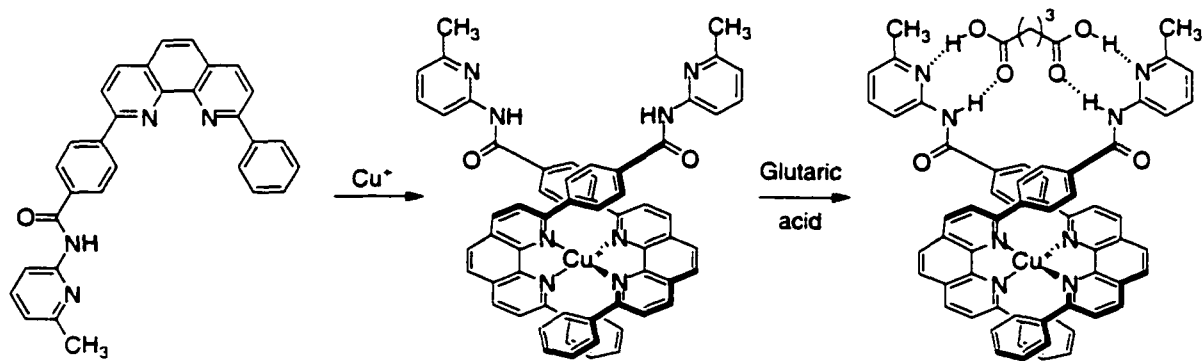
Supramolecular chemistry relies on the manipulation of kinetically labile bonds (intermolecular associations) and is concerned with the structure/function relationships of the assemblies formed by the directed association of two or more monomeric species (Equation 1). The results are similar to those found in polymer chemistry, where the properties of the assemblies are not the same as those of the monomers. The discovery of assemblies whose properties outweigh the sum of the properties of the monomers is a paramount feature in *Supramolecular* chemistry (Equation 1).

$$P_{assembly} \neq P_{monomers}$$

$$P_{assembly} \gg \sum P_{monomers}$$

Equation 1.

The key to the success of *supramolecular* chemistry is the design of molecules that contain *molecular recognition elements* as the means to control the aggregation process and construct the desired architecture. The *molecular recognition elements* can be thought of as different types of supramolecular glue, which is a generic term used to describe the kinetically labile bonding interactions that force molecules to associate with each other. Common types of glue include: ion pairing, the hydrophobic effect, hydrogen bonding, π - π stacking, and van der Waals interactions.¹ Another common supramolecular glue is the coordination motif, which uses transition metals, multidentate ligands and dative bonding to drive and direct aggregate formation. The different types of supramolecular glue can also be used in combination. For example, metal ions can be used to preorganize hydrogen bonding surfaces under strict geometric control (Scheme 1).²



Scheme 1.

Unlike the supramolecular approach, the use of traditional synthesis to prepare large aggregates through kinetically non-labile attachments can be plagued with problems that are usually manifested by the formation of unwanted side products or undefined

polymers. Problems can also surface in the form of geometric constraints because building-up from only sp , sp^2 , and sp^3 carbon atoms, or other light p -block elements, restricts the variation of how small molecules project in space. For example, it is extremely laborious to create a 90° angle between two points of attachment when relying on basic organic carbon, oxygen, and nitrogen covalent bonds that provide bond angles ranging from 180° to 109° . One way to get around these synthetic challenges is to drive molecular associations in a directed fashion using a combination of coordination chemistry and self-assembly synthesis as will be highlighted within this thesis.

In order to take full advantage of the supramolecular approach when designing supramolecular systems, one needs to have a good appreciation for the molecular recognition elements in terms of their electronic and steric restrictions. The advent of computer programs devoted to molecular modeling assist in answering the question of whether or not the supramolecular components will be structurally compatible with each other. Ideally, the construction of a properly designed supramolecular system requires only the mixing of the component compounds that then assemble into the desired aggregate. Using this "self-assembly" approach, extensive synthetic steps are minimized because the pathway to the formation of the assemblies is guided by the binding information of the recognition surfaces programmed into the components. This provides access to high yields under thermodynamic control because the kinetically labile bonds holding the species together are able to reversibly form, eventually producing the thermodynamically favoured product. The reversible formation of the favoured assembly at the expense of unfavourable ones defines the concept of "error filtering" and is what makes self-assembly chemistry so powerful. Any intermediates formed along the self-

assembly pathway whose electronic and steric requirements are destabilizing as compared to those of the desired assembly are eliminated. In a different sense, this “error filtering” behaviour may be amplified through the use of “cooperativity”. Cooperativity results from inter-component communication and reorganization that enhances the strengths of the interactions used. For example, once a process is initiated, the subsequent steps will be more effective if the initial interaction causes a structural change that prepares the compound for the next recognition process. The “zipping up” of a DNA double helix is a good example of a cooperative self-assembly process. In this case, the process is nucleated by the interaction of two complementary hydrogen bonding surfaces located on the nucleic acid partners. As a result of this nucleation, a larger aromatic surface is created (the nucleic acid dimer). This surface can then attract incoming aromatic surfaces through secondary π - π stacking interactions. Although π - π stacking is generally a weak interaction, it guides subsequent nucleotides into place, and when it is combined with hydrogen bonding, this positive attractive force is propagated cooperatively throughout the helix providing stability.

1.2 – Self-Assembly Synthesis Using Coordination Chemistry

The proper function of well-ordered supramolecular assemblies requires strict control over the relative positioning of the building blocks within the final assembly. In light of this, self-assembly synthesis has been combined with the concepts of coordination chemistry³ to produce a variety of elegant structures including helicates,⁴

squares,⁵ closed-shell capsules,⁶ linear ribbons, 2-dimensional nets and 3-dimensional weaves (Figure 1).⁷

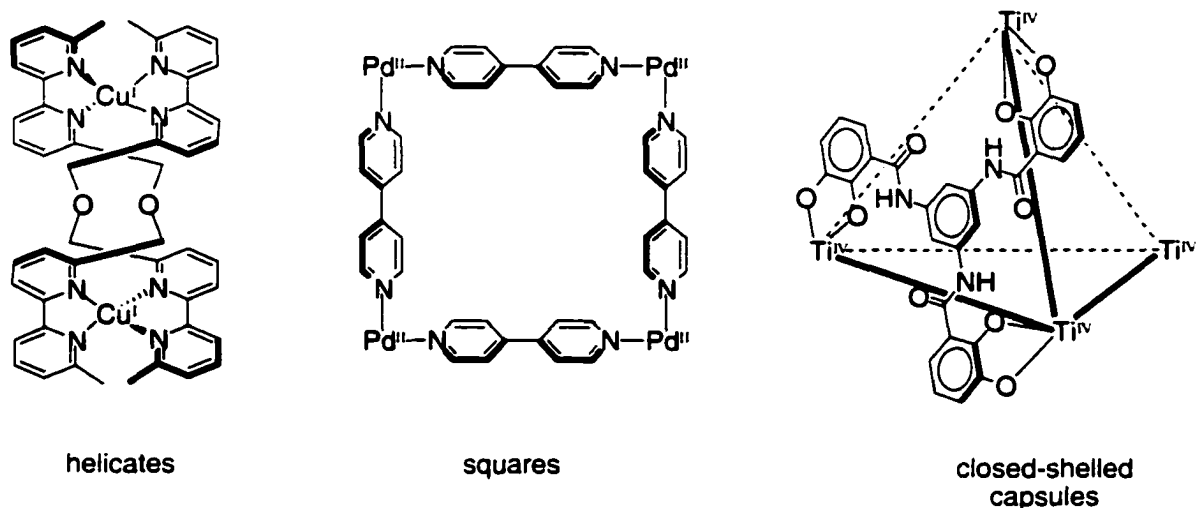


Figure 1. Examples of metal-coordination in supramolecular chemistry.

The metal coordination motif has proven to be a reliable tool to construct large assemblies because the final morphology can be controlled by the strict choice of the metal and ligand. As constituent parts of the design and construction phases for metal-based supramolecular architectures, it is important to consider structural elements of topology and symmetry. In order to gain control over these elements, it is critical to carefully select the coordination states and geometries of transition metals (*d*-metals) as well as the shapes and geometries of the multidentate ligands.

The literature acceptance of the utility of metal-ligand coordination motifs as the supramolecular glue is based on an understanding of four important features. First, metal-ligand coordination motifs have varying degrees of binding strengths. The types of dative

bonds formed range from pure σ -bonds and/or π -bonds as well as bonds that possess combinations of σ - and π -character (Figure 2).

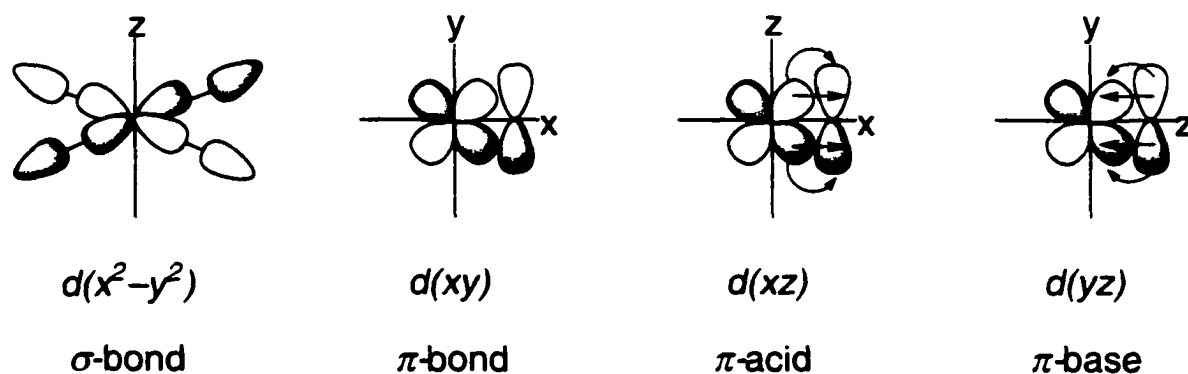
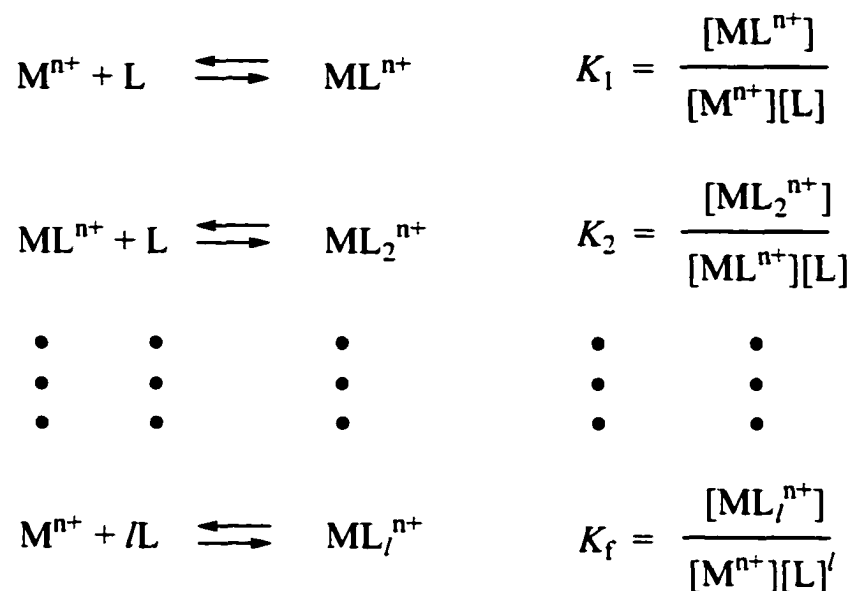


Figure 2. Types of dative bonds.

In general, the binding strengths for metal ions increase as their effective nuclear charge increases and ionic radius decreases. In addition, a dative bond increases in its strength when moving to higher atomic numbers within the same group or moving to higher oxidation numbers and is attributed to additional electrostatic attractions due to an increase in nuclear charge of the metal ion.⁸

Instead of rationalizing bond strength trends of transition metal complexes based on their electronegativities and ionic radii, the stability of the complex can be expressed thermodynamically (ΔG) and reveal the strengths (ΔH) of the interactions holding the complex together and of any binding induced solvent reorganization effects (ΔS) (Equation 2).



$$\Delta G^\theta = -RT \ln K_f$$

$$\Delta G^\theta = \Delta H^\theta - T\Delta S^\theta$$

Equation 2.

For example, the Irving–Williams series that states: for any given ligand the stability order for complexes with M^{2+} ions of the first row transition metals follows: $\text{Mn}^{2+} < \text{Fe}^{2+} < \text{Co}^{2+} < \text{Ni}^{2+} < \text{Cu}^{2+} > \text{Zn}^{2+}$ (d^5 to d^{10} complexes). These observations contradict bond strength trends that are based solely on the electronegativities and ionic radii of the metal ions. Alternatively, crystal field theory can be used to explain the gradual increase and decrease in stability (changes in the magnitude of the formation constant K_f) and is expressed by changes in the crystal field stabilization parameter (Δ).⁹

Crystal field theory explains the outcome of electrostatic interactions between electrons located in the metal d orbitals and in the surrounding ligand orbitals in octahedral, tetragonal, square planar, and tetrahedral environments. For example, consider the case where a spherical d metal ion is placed in an octahedral environment

with six ligands regarded as negative point charges directed toward the metal (top of Figure 3). In the absence of ligands, the five metal d orbitals: $d(z^2)$, $d(x^2-y^2)$, $d(xy)$, $d(yz)$, and $d(xz)$ are equivalent and have the same energy. These orbitals are degenerate. However, when the metal ion is placed in an octahedral ligand field, the metal d orbitals are effected differently by the negative charges on the ligands and are split into two orbital sets (bottom of Figure 3).

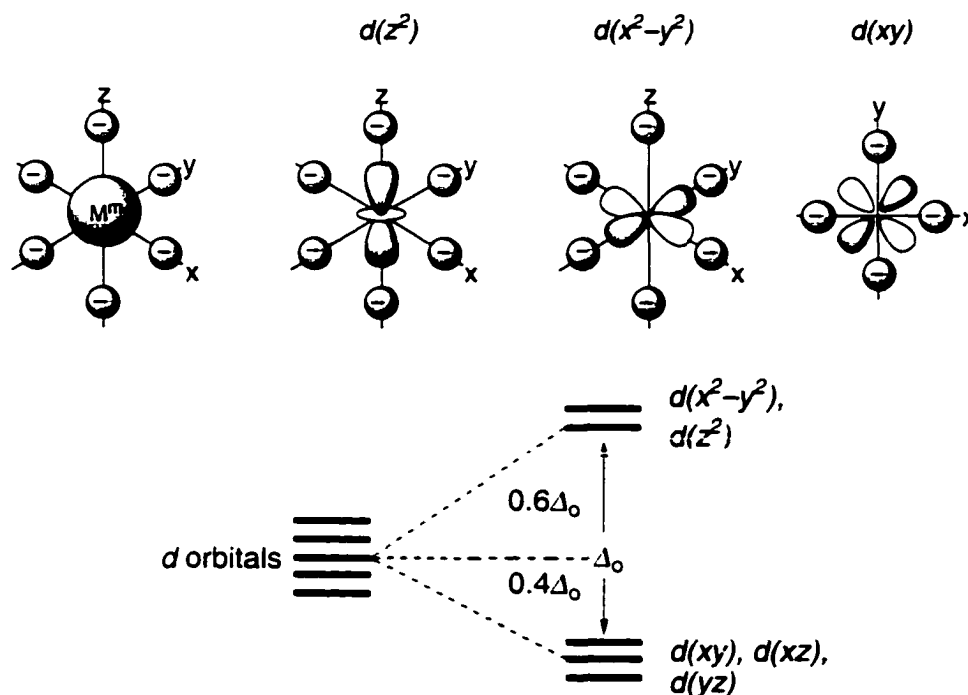


Figure 3. Schematic representation of position and electrostatic relationships between a metal ion's d orbitals and six point charges in an octahedral environment (top). The ligand field splitting effects of a metal's d orbitals in an octahedral environment (bottom). The symbol Δ_o represents the octahedral crystal field stabilization parameter.

The orbital splitting results from whether or not the d orbitals are positioned along the axes connecting the metal and ligands or in the directions bisecting the axes (top of Figure 3). In this hypothetical case, the $d(z^2)$ and $d(x^2-y^2)$ orbitals are destabilized because they experience a greater electrostatic repulsion than the $d(xy)$, $d(xz)$, and $d(yz)$

orbitals (top of Figure 3). The energy difference between the two sets of orbitals in an octahedral ligand field is assigned the symbol Δ_o (crystal field stabilization parameter) (bottom of Figure 3). The values $0.6\Delta_o$ and $0.4\Delta_o$ in the figure result from maintaining the average energy of the ten electrons in the d metal orbitals when changing from five degenerate d metal orbitals to two degenerate sets. For example, if these five metal d orbitals contained ten electrons with their spins paired the crystal field stabilization energy will equal zero ($\Delta_o = (4 \times 0.6\Delta_o) - (6 \times 0.4\Delta_o) = 0$). Deviations in this energy occur when placing more than three electrons into these orbitals. For example, consider the case of the $d^5 \text{Mn}^{2+}$ ion. The first three electrons can be placed into the low energy orbitals with parallel spins (left of Figure 4).

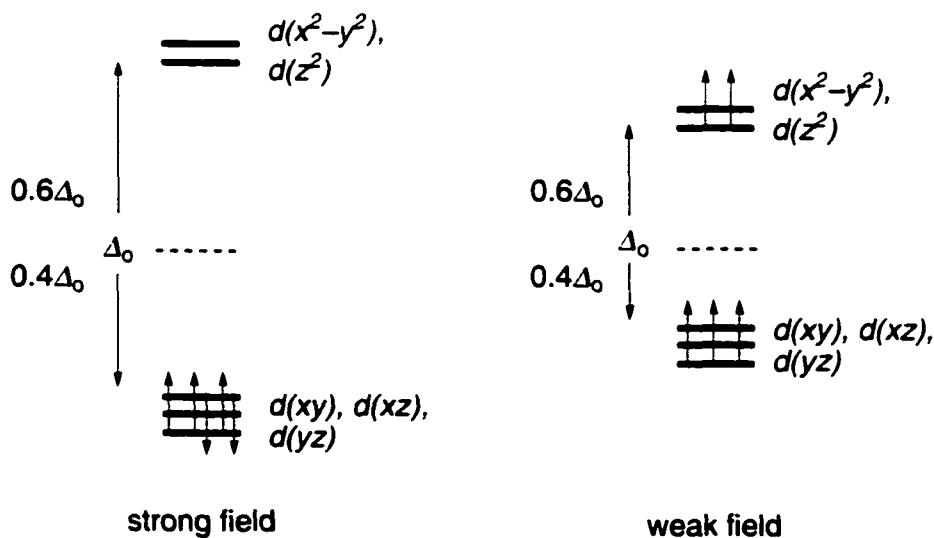


Figure 4. The strong ligand field splitting effects of a $d^5 \text{Mn}^{2+}$ ion in an octahedral environment (left). The weak ligand field splitting effects of a $d^5 \text{Mn}^{2+}$ ion in an octahedral environment (right). The symbol Δ_o represents the octahedral crystal field stabilization parameter.

The next two electrons can pair with two of the electrons in the half-filled lower energy d orbitals. If this occurs, these electrons are penalized by a pairing energy (P) due to strong coulombic repulsions ($\Delta_o = (0 \times 0.6\Delta_o) - (5 \times 0.4\Delta_o) + P = -2.0\Delta_o + P$). Instead

of pairing up, the two electrons may enter the higher energy orbitals avoiding the pairing penalty, but with a cost in the amount of $2\Delta_o$ because the crystal field stabilization energy now equals zero ($\Delta_o = (2 \times 0.6\Delta_o) - (3 \times 0.4\Delta_o) = 0$) (right of Figure 4). The two outcomes are governed by the relative sizes of the values of Δ_o and P , and the final placement of electrons depends on which outcome provides the greater stabilization energy. In this case, the choice is $-2.0\Delta_o + P$ or zero. These two possible outcomes are referred as the strong and weak ligand field effects (Figure 4).

These strong and weak field effects are determined by the ligand. The size of Δ_o increases through the ligand spectrochemical series for any fixed metal ion. More specifically, the size of Δ_o is controlled by how the metal d orbitals overlap with the ligand orbitals which effects their relative energy values. The size of Δ_o is also controlled electrostatically by the nature of the metal ion, it's charge, and the distance separating the metal and ligands.

Using this theory, the crystal field stabilization energies can be calculated and the values can be compared for the Irving–Williams series of dicationic metal ions placed in a weak octahedral ligand field environment ($\text{Mn}^{2+} < \text{Fe}^{2+} < \text{Co}^{2+} < \text{Ni}^{2+} < \text{Cu}^{2+} > \text{Zn}^{2+}$) (Figure 5). The trends in stability for this series reflect a balance between gradual increases in Δ_o and P up to Ni^{2+} , all of which stabilize the complexes. But these trends do not explain how $d^9 \text{Cu}^{2+}$, which has a lower Δ_o value and pays a larger pairing energy penalty, is more stable than $d^8 \text{Ni}^{2+}$. This anomaly is a result of a Jahn–Teller distortion of an octahedral to a tetragonal complex (Figure 6). A distortion of this type lengthens the two axial bonds along the z-axis and compresses the four equatorial bonds along the x- and y-axes. As a consequence, this distortion for $d^9 \text{Cu}^{2+}$ removes the degeneracy of the

$d(z^2)$ and $d(x^2-y^2)$ orbitals by lowering the energy of the $d(z^2)$ orbital and raising the energy of the $d(x^2-y^2)$ orbital (Figure 7).

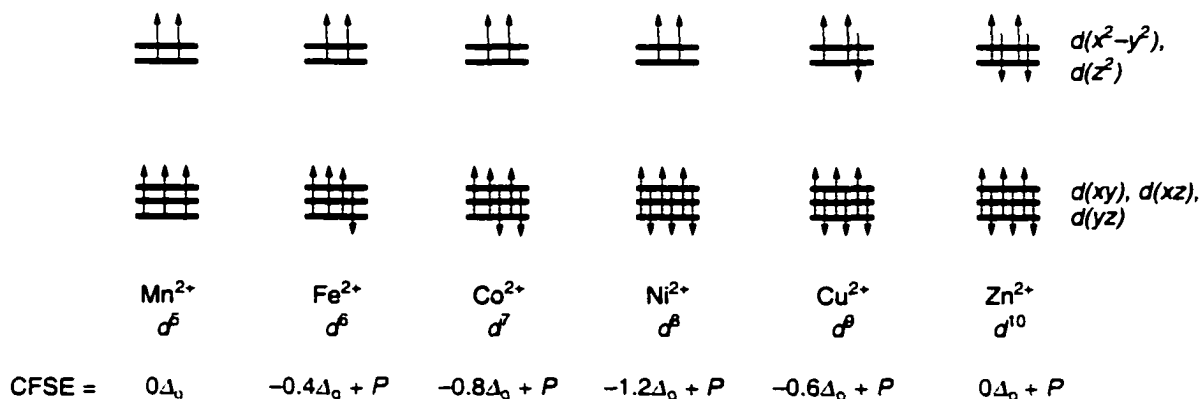


Figure 5. The calculated crystal field stabilization energies (CFSE) for the Irving-Williams series of dicationic metal ions in a weak field octahedral environment ($\text{Mn}^{2+} < \text{Fe}^{2+} < \text{Co}^{2+} < \text{Ni}^{2+} < \text{Cu}^{2+} > \text{Zn}^{2+}$). The symbol Δ_o represents the octahedral crystal field stabilization parameter.

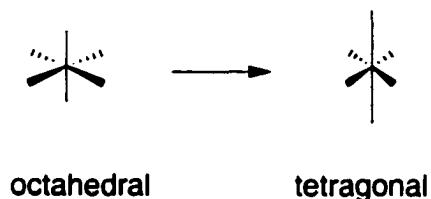


Figure 6. The Jahn-Teller tetragonal distortion of an octahedral complex.

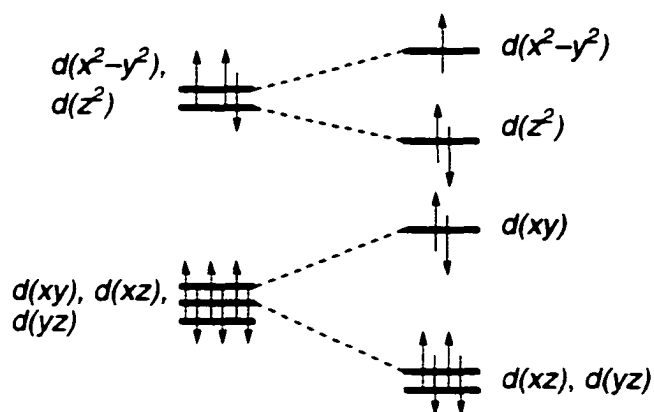


Figure 7. The Jahn-Teller distortion of an octahedral d^9 Cu^{2+} ion resulting in the removal of orbital degeneracy and stabilization of the complex.

The two electrons that occupy the $d(z^2)$ orbital are stabilized while the single electron that occupies the $d(x^2-y^2)$ orbital is destabilized. The departure from octahedral to tetragonal symmetry results in a gain in the crystal field stabilization energy and in the process generates two labile axial ligands. If $d^8 \text{Ni}^{2+}$ proceeds through the same tetragonal distortion, the orbital degeneracy is removed but there is no gain in stabilization energy because the amount that the electron in the $d(z^2)$ orbital is stabilized is equaled by the amount that the electron in the $d(x^2-y^2)$ orbital is destabilized. This also applies to the lower stability observed for of $d^{10} \text{Zn}^{2+}$ complexes because they cannot gain stabilization energy by proceeding through a tetragonal distortion, nor do they initially gain any crystal field stabilization energy (recalling that for $d^{10} \text{Zn}^{2+}$ $\Delta_o = (4 \times 0.6\Delta_o) - (6 \times 0.4\Delta_o) = 0$). If the tetragonal distortion continues with the eventual loss of both axial ligands, the tetracoordinate square planar or tetrahedral complex is formed. This is a very simple theory that can be used to quickly visualize the effects of ligands on the metal's d orbitals and justify the stability of a complex in different ligand field environments (Figure 8).

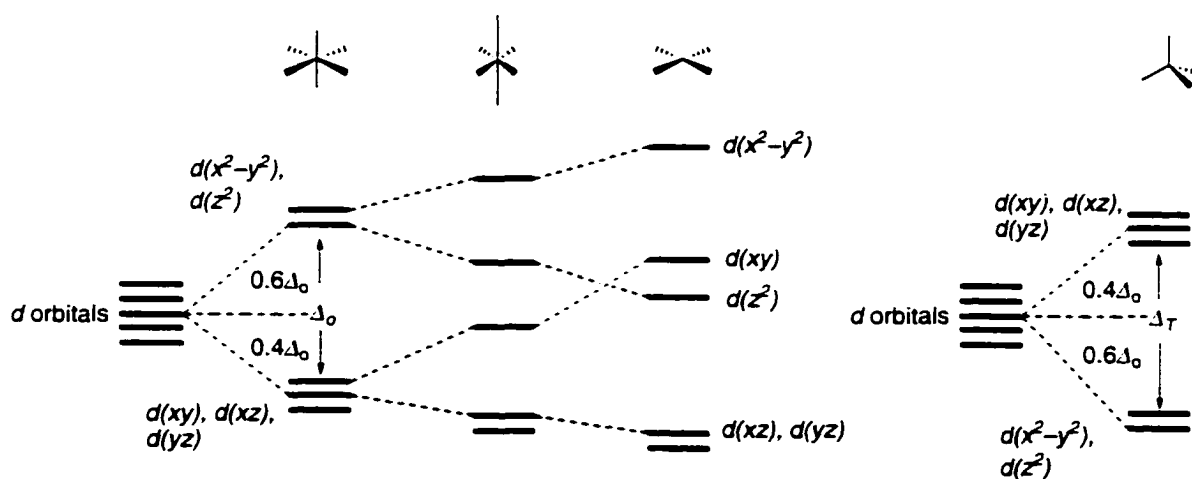


Figure 8. The changes in orbital energy levels of octahedral, tetragonal, square planar and tetrahedral d metal complexes. The symbol Δ_o represents the octahedral crystal field stabilization parameter. The symbol Δ_T represents the tetrahedral crystal field stabilization parameter.

The second feature that must be taken into consideration when using coordination chemistry to construct supramolecular assemblies is that the strengths of the bonds and the stability of the complex can be controlled through the number of attachment points that the ligand uses to coordinate to the metal ion. The known metal binding motifs include: monodentate (one attachment point), bidentate (two attachment points), tridentate (three attachment points), tetradentate (four attachment points), macrocyclic tetradentate, and polydentate. Some common examples of ligands that utilize these different binding motifs include: pyridines, polypyridines, Schiff bases, and porphyrins respectively (Figure 9).

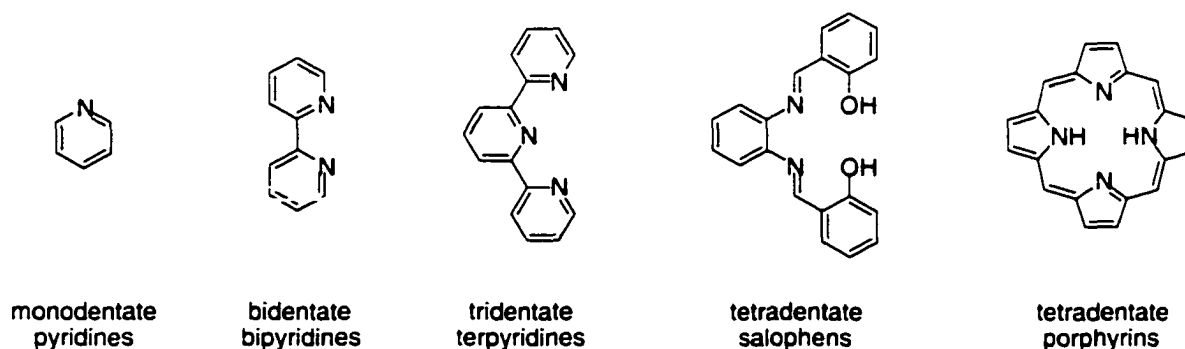


Figure 9. Metal binding motifs of some common ligands.


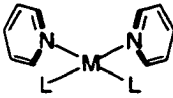

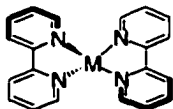

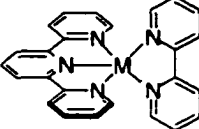

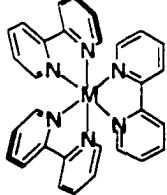
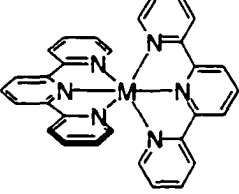
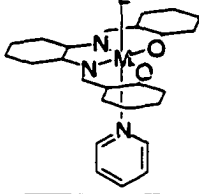
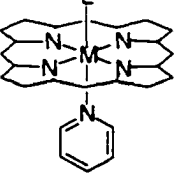
The latter four ligands in Figure 9 are chelating and form complexes of higher stability. This is due to a more positive change in entropy by increasing the number solvent molecules released into solution after coordination. These ligands are easily modified and have well-established synthetic procedures. This allows other molecular recognition elements to be installed onto the backbone of the ligand. It is this ability to

introduce other molecular recognition elements onto the ligand that allows for the formation of larger polymolecular aggregates.

The third consideration is that transition metals provide well-defined coordination sites that position, with precision, ligands in space. This is more commonly referred to as *metal-directed templating*.¹⁰ The number and placement of coordinating ligands can be rapidly altered by a simple change of the metal. As a result of having controlled geometries, the position of any molecular recognition elements installed onto the ligand will also be subjected to changes in the geometry of the metal. Thus, a properly chosen ligand and metal pair can be used to position the tethered molecular recognition vectors in square planar, tetrahedral, square pyramidal or octahedral environments, for example. Examples of metal-ligand complexes that provide different geometries are given in Table 1.

The last consideration is that transition metal complexes of the types listed in Table 1 have well behaved electrochemical and photochemical properties and numerous efforts have been initiated to incorporate such complexes into highly organized multicomponent assemblies where these interesting properties can be harnessed.

Table 1. Metal-Ligand Complexes

Geometry	Examples	Common Metals	Properties
<p>Square Planar</p> 		Rh(I), Pd(II), Pt(II)	Redox-active
<p>Tetrahedral</p> 		Cu(I), Ag(I), Zn(II), Ni(II)	Photo- and redox-active
<p>Square Pyramidal</p> 		Cu(II)	Photo- and redox-active
<p>Octahedral</p> 		Fe(II), Ru(II), Co(II), Ni(II), Co(III), Cr(III)	Photo- and redox-active
		Fe(II), Ru(II), Os(II), Ni(II), Cu(II)	Photo- and redox-active
		Fe(II/III), Ru(II), Co(III), Zn(II)	Photo- and redox-active
		Fe(II/III), Ru(II), Os(II), Rh(III), Zn(II)	Photo- and redox-active

1.3 – Self-Assembly Synthesis of Closed-Shelled Molecules

Pioneering self-assembly and metal-coordination studies helped to conceptualize the development of a *metal-directed template* synthesis of closed-shelled molecules. A closed-shelled molecule is one that possesses discrete walls that enclose some three-dimensional space. Because they enclose space, they are capable of encapsulating guest molecules. With this in mind, literature examples describe the design and synthesis of encapsulating molecules and their important ties to applications concerning transport,¹¹ isolation,¹² and catalysis.¹³ The smallest closed-shelled molecule that can be made from walls of exactly the same shape is a tetrahedron (Figure 10).

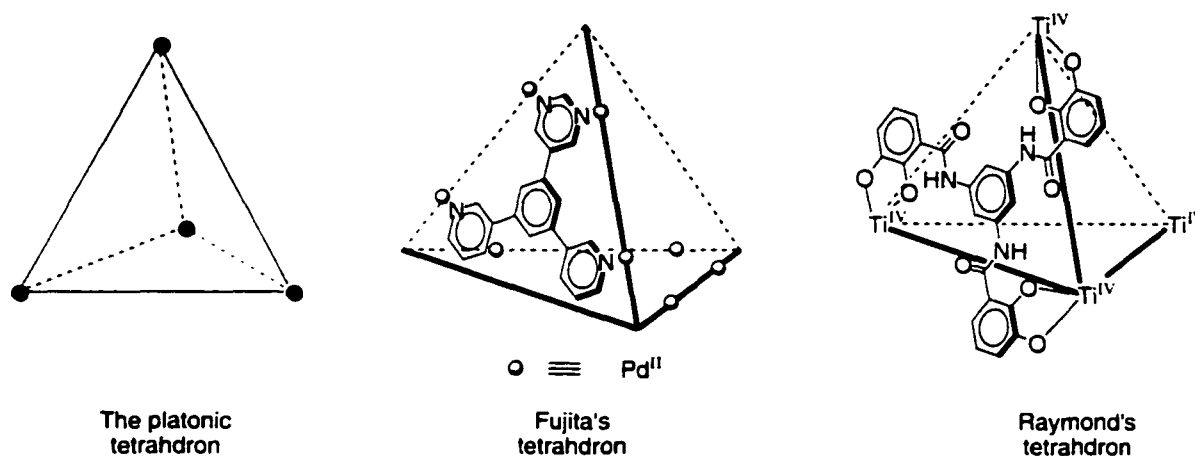


Figure 10. Closed-shelled tetrahedrons.

The groups of Fujita and Raymond have already shown that self-assembly synthesis can afford this type of architecture using the metal-coordination strategy and triangular-shaped walls.⁶

The example of Fujita's tetrahedron and other encapsulating molecules that he has designed and synthesized uses labile Pd(II) hinges that hold the organic panels in place.^{6a} Encapsulation occurs readily with small molecules that have similar dimensions to the apertures of the closed-shelled structure which allows their passage.^{6a} In order to encapsulate molecules that have larger dimensions than the apertures, the hinged assembly must be heated to disassemble it and then encapsulation occurs during the reassemble process. The term "labile" is relative and can be amplified by raising the temperature of the environment. The labile nature of the hinges may interfere when the size of an encapsulated guest molecule is large enough to destabilize the closed-shelled structure and prevent encapsulation. Thus, it will be difficult to permanently trap large guest molecules inside containers of this type.

The incorporation of transition metals into closed-shelled molecules can result in new properties for these potential host molecules. More specifically, important properties including magnetism, redox activity, Lewis acidity or luminescence can be introduced into closed-shelled molecules that incorporate transition metals. The two tetrahedrons in Figure 10 contain transition metals that are tied-up in connecting the organic ligands together and the ligands themselves do not confer interesting properties to the final assembly. The appeal lies in the creation of a molecular-scale chamber that can encapsulate guest species and place them inside a reactor that contains interesting catalytic/photochemical/electrochemical walls. The construction of closed-shelled capsules using transition metal complexes of the types listed in Table 1 may lead to encapsulating molecules with novel properties.

The next largest closed-shelled molecular chamber has six walls of the same shape and is a hexahedron (Figure 11).^{6a} The triangular-walled version^{6b} has already been synthesized but the square-walled version, namely the cube, has not been made and this is the starting point of this thesis.

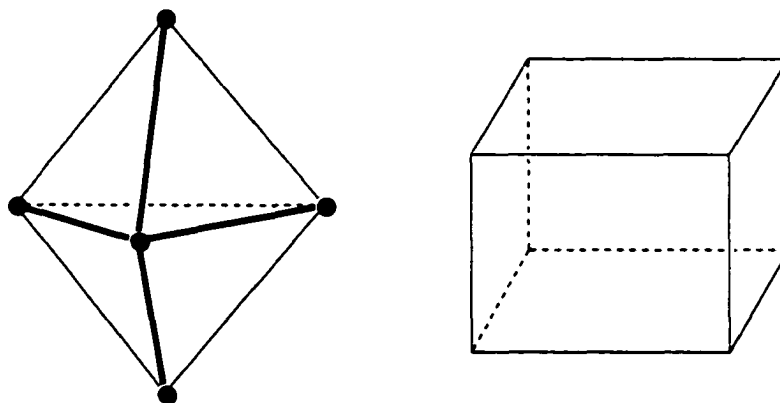
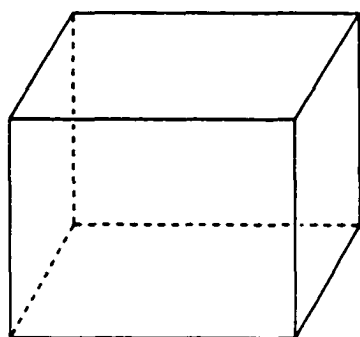


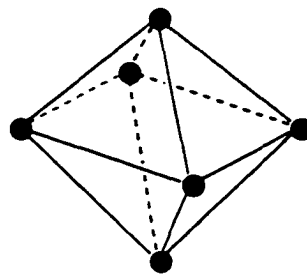
Figure 11. The platonic hexahedrons.

1.4 – The Template Synthesis of a Porphyrin Cube

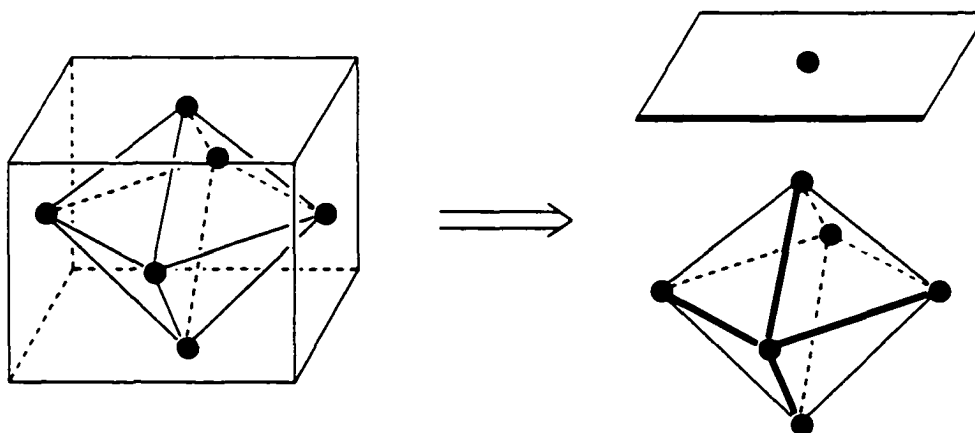
If the synthesis of a molecular cube is the goal, then six square walls must be brought into close proximity long enough to be covalently fused together. This seemingly impossible task can be readily accomplished using the strategies of self-assembly and molecular templating. The symmetry of the cube allows a regular octahedron to be placed inside, such that each vertex of the octahedron points to the center of each wall. The synthesis of a cube can be realized and designed from a retrosynthetic templated point of view; six square walls need to be assembled around an octahedral template and then fastened together (Scheme 2).



cube



**regular
octahedron**



Scheme 2. The retrosynthetic approach to a molecular cube.

The chemical-equivalent of a square wall with a central molecular recognition site that can be positioned 90° to the template is a metalloporphyrin. The chemical-equivalent of an octahedron that emulates this environment is a tris(bipyridyl) transition metal complex and these two building blocks are shown in Figure 12. A wide variety of substituents can be introduced onto the *meso*-position of porphyrins and this is the position that must be modified appropriately to facilitate future wall connection. Insertion of the appropriate metal into a porphyrin brandishes a vacant axial coordination site that

can be accessed by Lewis bases such as pyridines and, thus, axial coordination can be used to hold the porphyrins around the template.

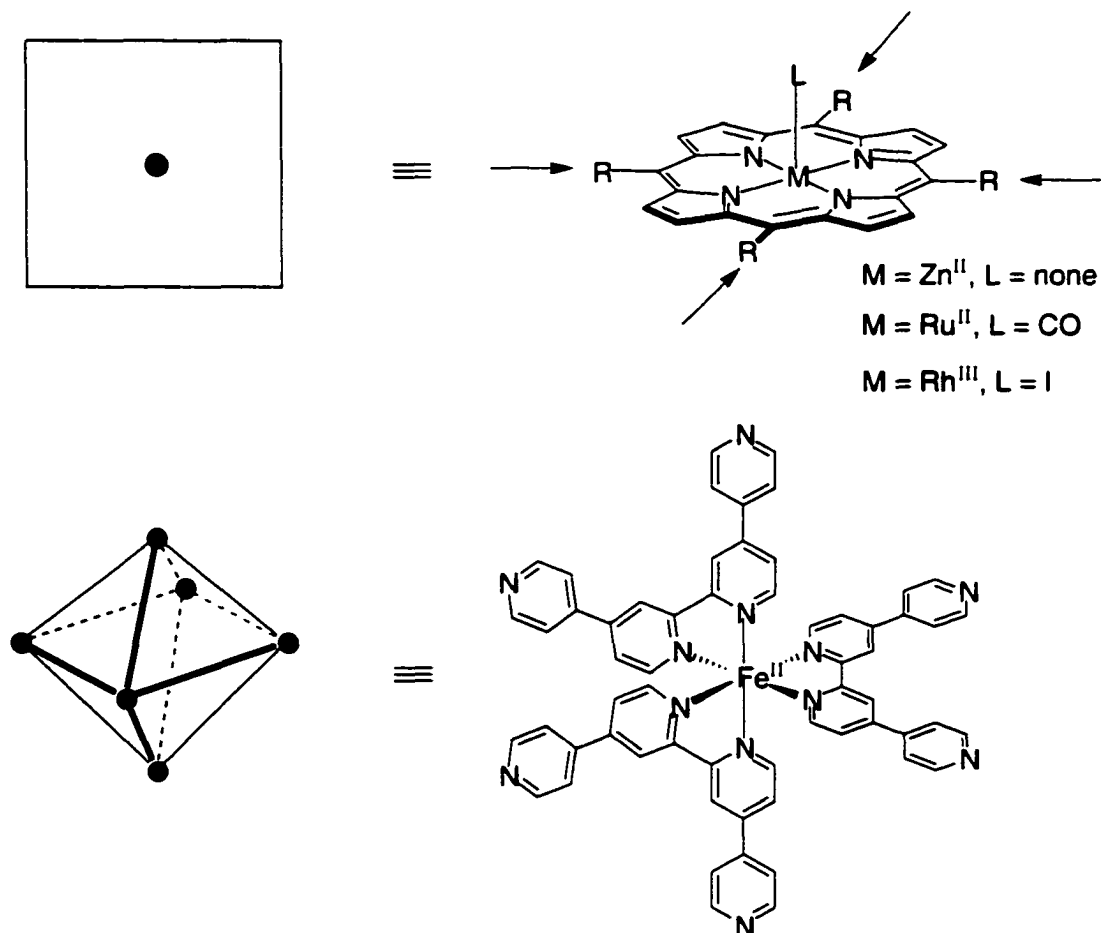


Figure 12. Chemical equivalents of a square and an octahedral template. The arrows highlight the *meso*-substituents of the porphyrin where covalent bonds can be formed to hold the cube together.

Sanders and coworkers have taken advantage of axial coordination to zinc(II), ruthenium(II), and rhodium(III) porphyrins in combination with template synthesis to construct macrocyclic polyporphyrinic assemblies.¹⁴ This example is useful to outline the steps involved in the molecular templating strategy.^{14b} It is a two step procedure. The first step is an assembly step while the second step is a coupling step (Figure 13). The first

step involves the pre-organization of building blocks that strategically places them in space and directs their connection sites around the template, a triangle in the case of Sanders and coworkers. In the second step, the strategically placed connection sites are fused together. Since this coupling reaction occurs more rapidly while the synthons are wrapped around the template, the triangular macrocycle is exclusively formed over dimeric, tetrameric, and oligomeric products.

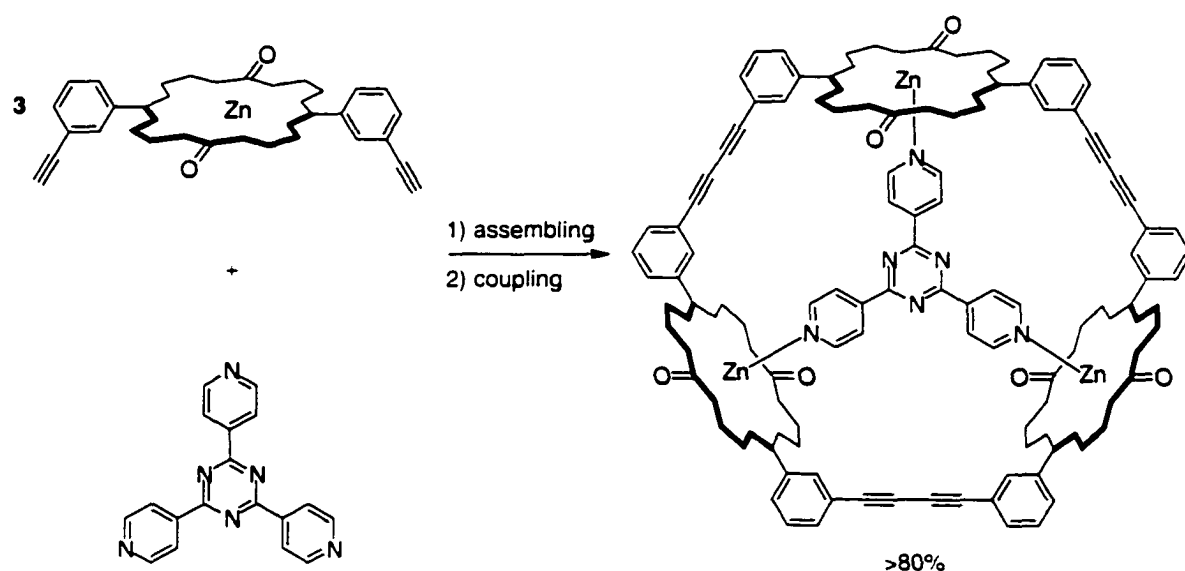


Figure 13. An example of molecular templating a triangular macrocycle that highlights the required steps of assembling and coupling.

In order to synthesize a porphyrinic cube following a templated synthetic protocol, the six porphyrins must be pre-assembled around the octahedral template and then a total of twelve wall-connecting reactions must follow (Figure 14). The reaction conditions of the coupling step should be compatible with axial coordination, such that displacement of the porphyrins off the template does not occur. Another important aspect regarding the twelve coupling reactions is that they must be high yielding in order to

synthesize the cube in sufficient quantities. For example, if a coupling reaction used results in an 80% to 90% yield for a single reaction then the expected maximum yield for the cube, which requires twelve reactions, is only between 7% to 28% yield.

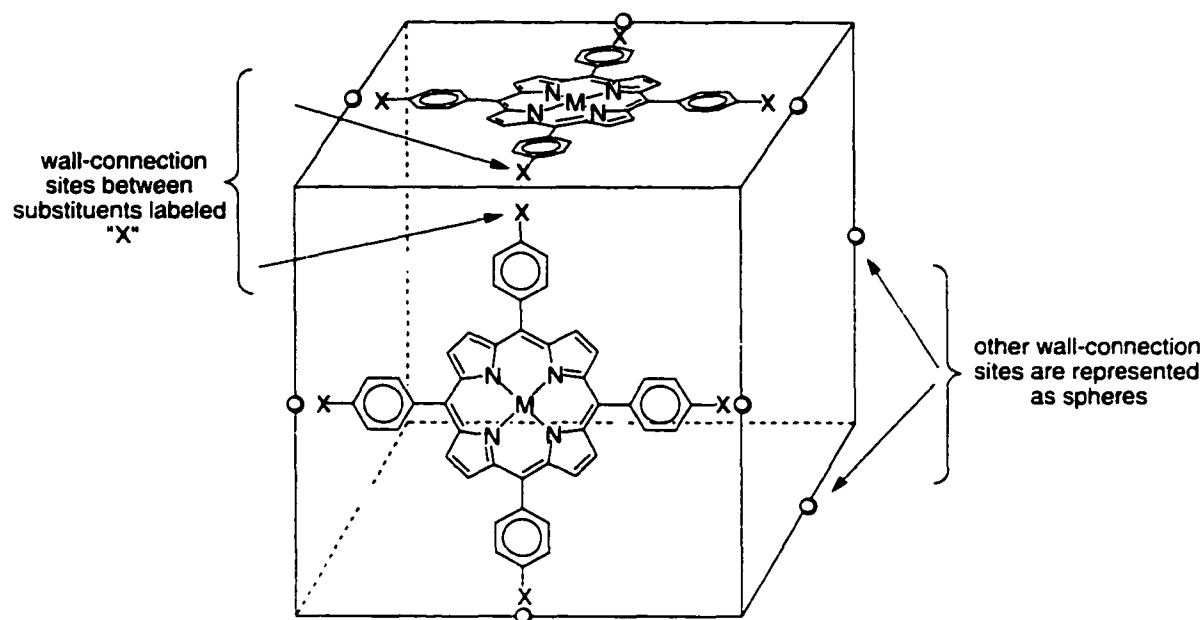


Figure 14. The positions of the twelve wall-connection sites.

Unlike the two tetrahedrons of Fujita and Raymond, which are made from walls that do not confer additional properties to final assembly previously mentioned in this introduction, the proposed cube's walls will be photo- and redox-active. They will also contain a central metal that in combination can provide the cube with photochemical, electrochemical, and multi-point binding properties. The ability to form the octahedral porphyrin array was first tested using the known ruthenium(II) carbonyl tetratolylporphyrin¹⁵ and the known iron(II) octahedral template¹⁶ (Figure 15).

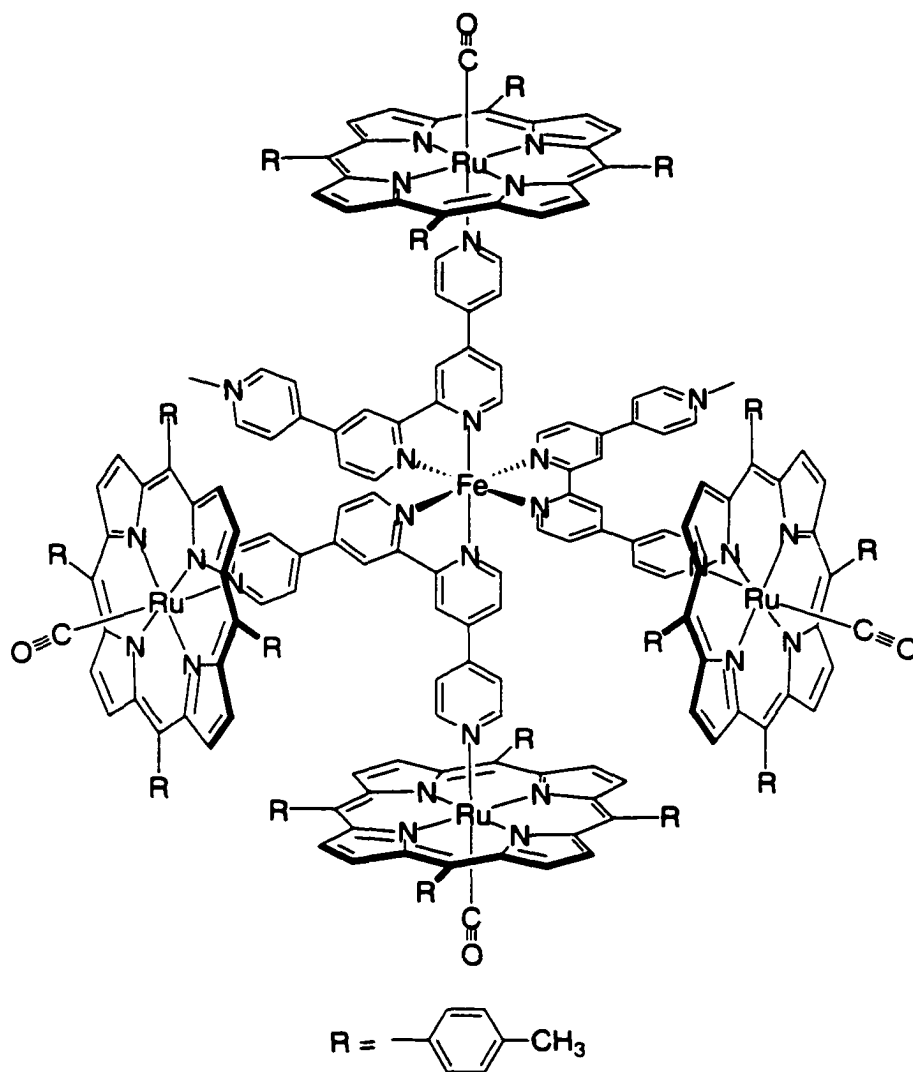


Figure 15. The octahedral porphyrin array.

The covalent fusing of the walls together was not pursued in this thesis work, not because it was deemed impossible, but rather because of the need to investigate the formation and spectral properties of other porphyrinic arrays using axial coordination. This synthetic strategy can provide an alternative method to construct, control, and alter the position of porphyrins (chromophores) around transition metal complexes and provide suitable model systems for studying the photo-induced energy and electron transfer reactions that occur during photosynthesis.

1.5 – The Photosynthetic Reaction Center

One of the primary concerns when designing photosynthetic reaction center mimics is to control how the chromophoric building blocks project in space, as their relative positioning will influence the resulting energy or electron transfer processes. For example, in Nature, the bacterial photosynthetic reaction center consists of ten important components that are held and positioned in the thylakoid membrane by three protein subunits (Figure 16).¹⁷

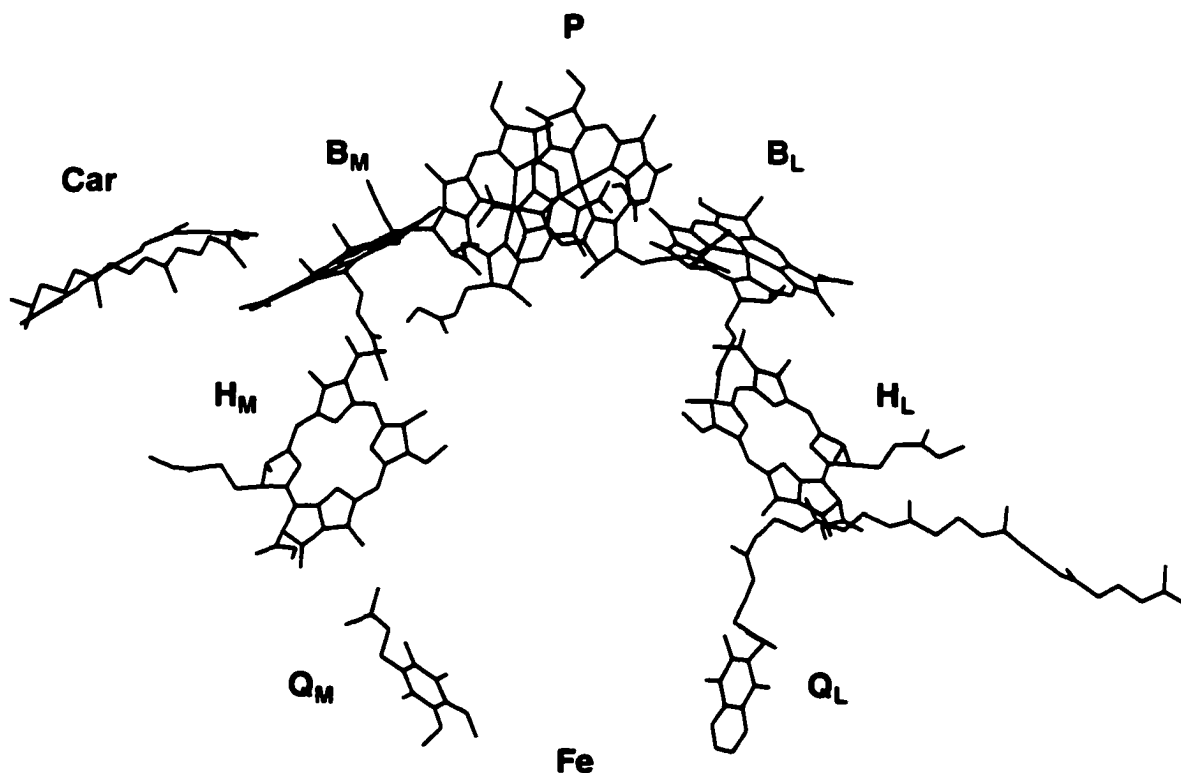


Figure 16. Crystal structure of the bacterial photosynthetic reaction center of *Rhodospirillum rubrum*.¹⁷ P is the special pair; B is the monomeric bacteriochlorophyll-*a* molecule; H is the monomeric bacteriopheophytin molecule; Q is the ubiquinone molecule; Car is the carotenoid molecule and Fe is the non-heme iron. The subscripts M and L denote the protein/component relationship.^{17b}

The ten components responsible for efficient energy and electron transfer are two closely positioned bacteriochlorophyll-*a* molecules (P) that make up the “special pair”

electron donor, two monomeric bacteriochlorophyll-*a* molecules (B_M and B_L), two bacteriopheophytins (H_M and H_L), two ubiquinones (Q_M and Q_L), a carotenoid (Car), and a non-heme iron as shown in Figure 16. Excitation of the special pair is achieved by rapid and efficient energy transfer from either the monomeric bacteriopheophytins (H_M and H_L) and bacteriochlorophylls (B_M and B_L). After the light energy is transferred to the special pair (P), an electron is transferred to an electron acceptor (H_L) which traps the excitation energy as a charge-separated species.¹⁸ In order to afford efficient energy and electron transfer rates ($k \approx 3 \times 10^{11} \text{ s}^{-1}$) Nature positions the active porphyrinic species with a center-to-center separation of *ca.* 17 Å (10 Å for H/B and 10 Å for B/P) (Figure 16).^{18d} The controlled center-to-center separation between chromophores maximizes the electronic interactions of the distance dependent energy transfer processes.

1.5.1 – Excited-State Properties of Porphyrins

Porphyrin chromophores are attractive supramolecular building blocks as they have rich photo- and redox-properties in their ground and excited states. Depending on the type of porphyrin, either free-base or metallo-, photo-excitation produces a singlet or triplet excited state (Figure 17).

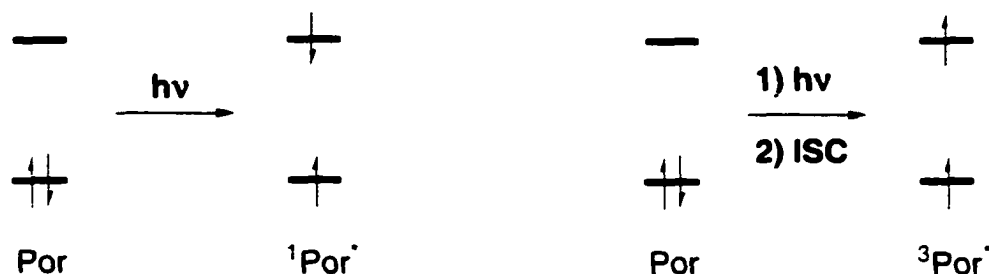


Figure 17. Photoexcitation of a porphyrin producing either a singlet (left) or triplet (right) excited state. The abbreviation ISC stands for intersystem crossing.

The triplet excited state is produced from the singlet state *via* an intersystem crossing (ISC) process in which the spin of the electron is inverted. Intersystem crossings are promoted by heavy-atom effects which increase the overlap between vibrational states and increase the spin/orbital interactions. Excited porphyrins will fluoresce from their singlet state or phosphoresce from their triplet state when relaxing down to their ground state (Figure 17).¹⁹

When porphyrins are excited in the presence of excitation energy acceptors, as in the photosynthetic reaction center, two types of energy transfer processes can occur and are defined by electronic interactions. The first type is the Coulombic interaction affected by through-space dipole–dipole moment coupling and is identified as the Förster energy transfer mechanism. The Förster mechanism is operative at large interchromophore distances and the rate of this energy transfer depends on the distance separating the energy donor and energy acceptor.²⁰ In order for a Förster mechanism to occur for a given donor-acceptor pair, there must be significant spectral overlap between the fluorescence and absorption spectra of the donor and the acceptor. Spectral overlap is important for the Förster mechanism because the energy is transferred in the form of a photon (fluorescence) and therefore the energy acceptor must be able to absorb that particular wavelength of light.

The second type of energy transfer process is the electron exchange interaction and is governed by orbital overlap of the excited state electron donor and the electron acceptor. This electron exchange interaction is identified as the Dexter mechanism and is effective at much smaller interchromophore distances because orbital overlap is only maximized at shorter distances.²¹ For a Dexter energy transfer process, a double electron

transfer occurs which transfers a portion of the initial energy absorbed to an excited state quencher; the donor/acceptor species (Figure 18).

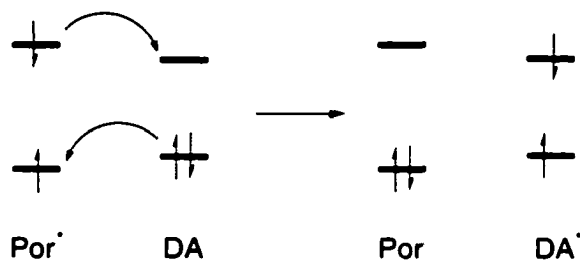


Figure 18. The Dexter mechanism for energy transfer between a porphyrin and a donor/acceptor species.

This type of a double electron transfer results in no net charge transfer, requires less solvent reorganization energy and is preferred over the Förster mechanism when there is significant orbital overlap between the active components. The overall product of the two energy transfer processes is the production of the quencher's excited state and the porphyrin's (chromophores) ground state or *visa-versa*.

The cascade of light driven events for the photosynthetic reaction center results in a final electron transfer reaction that traps the energy by forming a charge separated species. In general, the driving force for electron transfer processes relies on the relative differences in redox potentials of the electron donor and electron acceptor. The reasoning follows that the promotion of an electron from a filled low energy orbital to an empty high energy orbital results in the creation of an excited state that is either a stronger oxidizing or reducing agent than it was in the ground state (Figure 19). The promoted electron can transfer to an electron poor quencher and act as a reducing agent (left of Figure 19). On the other hand, the half-filled orbital that is created after excitation can

accept an electron from an electron-rich quencher and act as an oxidizing agent (right of Figure 19). A single electron transfer produces a net charge and requires higher solvent reorganization by forming a charge-separated species.

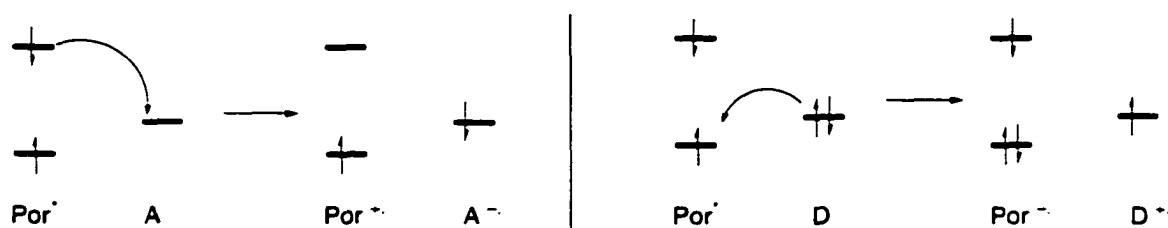


Figure 19. Oxidative (left) and reductive (right) electron transfer processes involving porphyrins.

1.5.2 – Positioning Chromophores in Space Using Metal Coordination

To date, numerous polymolecular assemblies held together by covalent or labile bonding interactions have been used to model solar energy capture and transfer in naturally occurring photosystems as well as to create artificial molecular photonic wires, optoelectronic gates, and light-harvesting funnels.²² Some significant challenges for developing models of energy capture and transfer reactions lies in the synthesis of the active components and connecting them together, with special attention paid towards their relative spatial arrangements.

For example, Sauvage's triad (Figure 20) acts as a model for the electron transfer steps in bacterial photosynthesis, but it is synthesized in seven steps in 0.05% yield.^{23a} Even though the yield is extremely low; it's functions are extraordinary. The central transition metal complex plays three important roles: 1) it controls the spatial arrangement of the two different porphyrins, 2) it mediates component communication,

and 3) it regulates the important electron transfer steps from the free base porphyrin to the Au^{III} porphyrin.

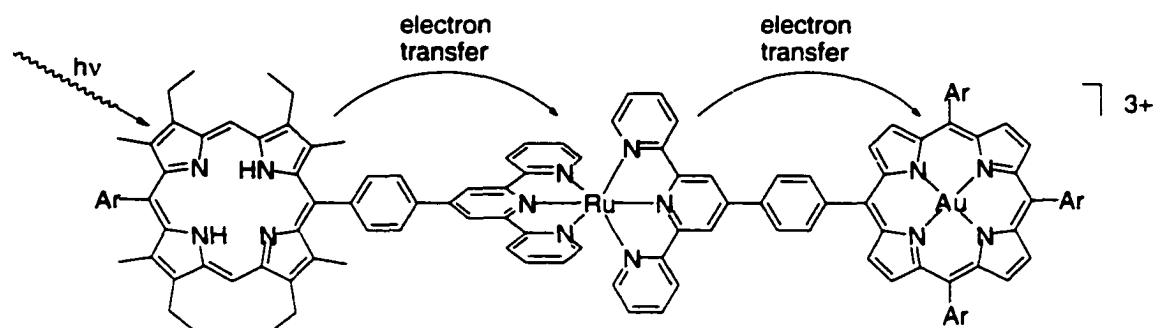


Figure 20. Artificial photosynthetic reaction center mimic.

The properties of this linearly arranged porphyrin array can be altered either by inserting a Zn^{II} metal ion into the free base porphyrin, changing the porphyrins, or by changing the metal located in the central terpyridine fragment from Ru^{II} to Ir^{III}.^{23b,23c} These alterations tune the excited state oxidizing and reducing properties of the active component compounds, which alters the system's electron transfer rates or changes its behaviour to cause energy transfer processes to occur. The major drawback of this system presents itself when major variants or modifications of the components are desired. This will require new syntheses starting from the rather difficult formation of dissymmetric porphyrins. Also, this system is limited in providing only linear arranged components because of the central transition metal complex's design. Again, if changing the spatial arrangement of the porphyrins is desired, then additional synthetic steps are required. An alternative to this is to use a much more modular approach to control the final topology by designing and synthesizing small component compounds and taking advantage of metal-ligand coordination. For example, there are several literature examples that use

axial coordination to metalloporphyrins to construct polymeric, dendritic, cyclic and noncyclic porphyrin arrays (Figure 21 and 22).^{24,25}

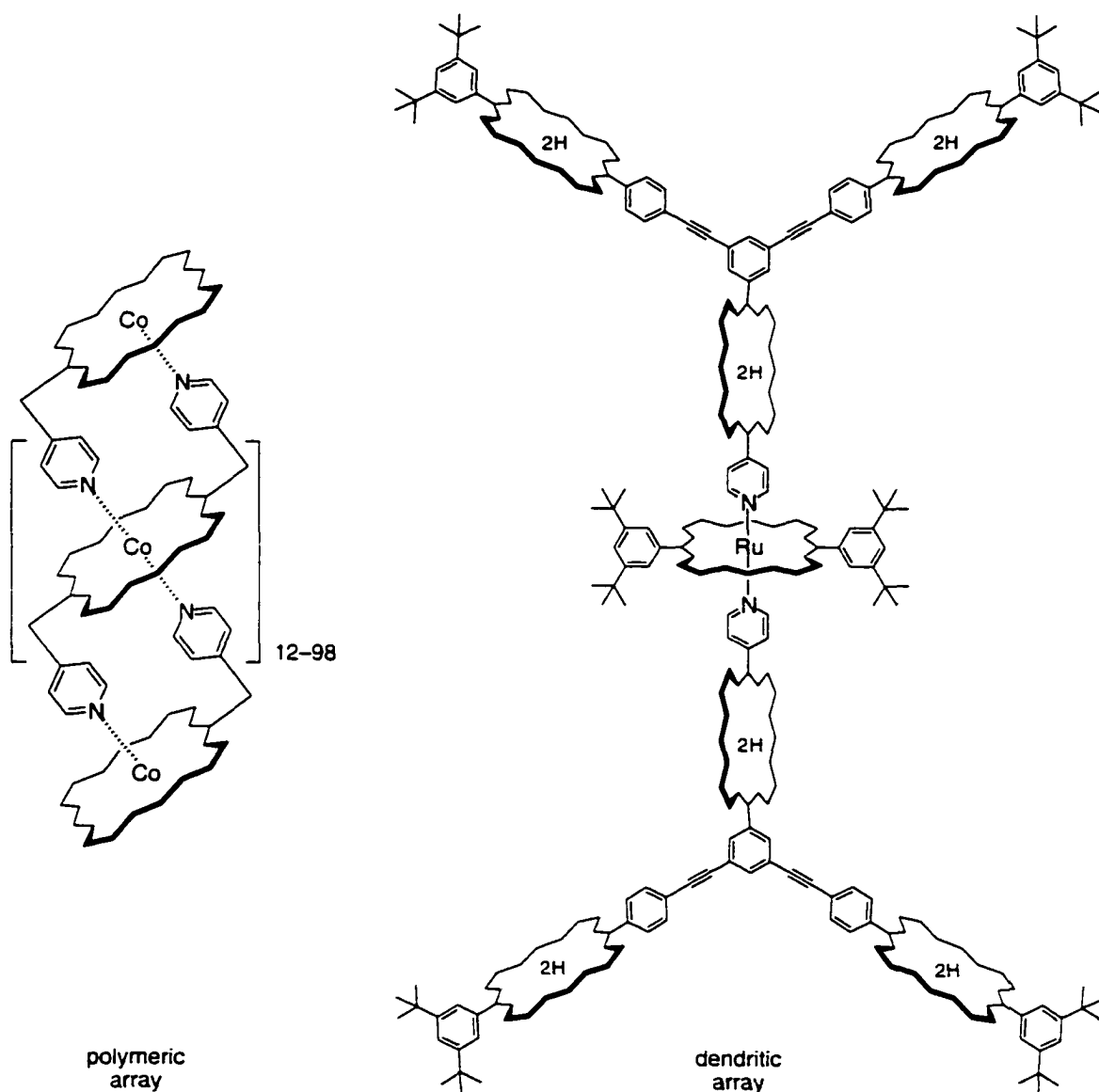


Figure 21. Examples of polymeric^{24a} and dendritic^{24c} porphyrin arrays.

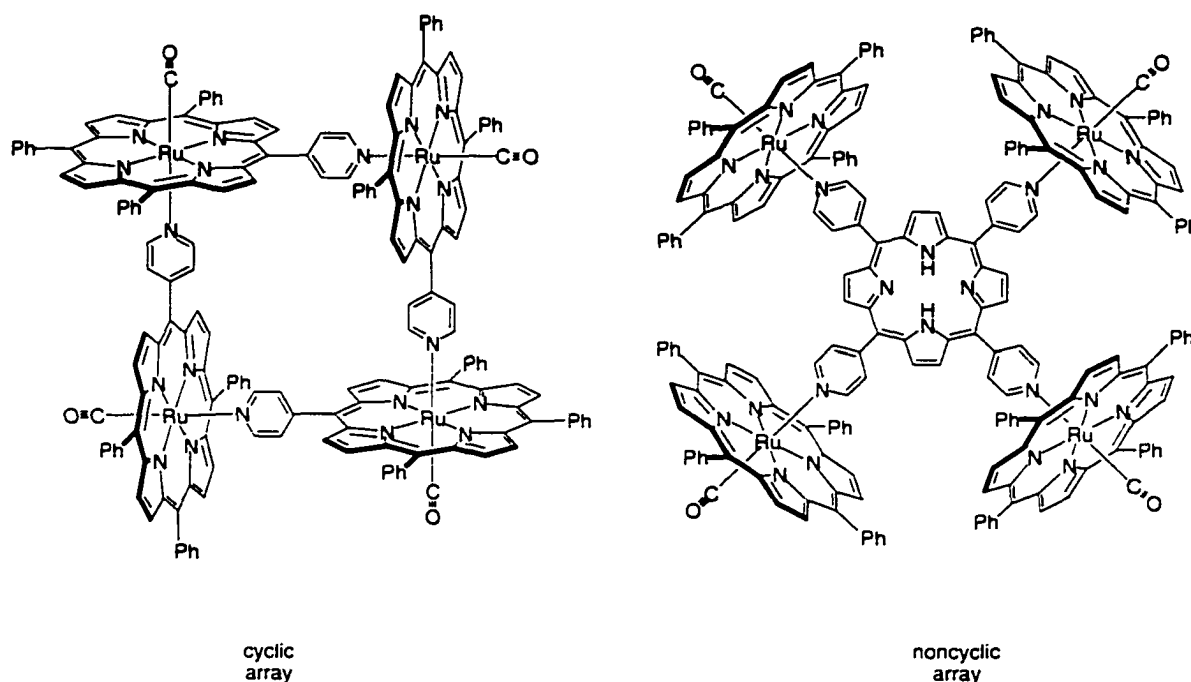


Figure 22. Examples of cyclic^{25a} and noncyclic^{25b} porphyrin arrays.

These axially coordinated arrays are rapidly generated from their component compounds and have been used to study the relationship between structure and function. Sauvage's linear multicomponent array highlights how transition metal complexes can be used to control the porphyrins' positions as well as how they participate in electron and energy transfer processes. By using a more convergent synthetic protocol (self-assembly for example), and incorporating axial coordination motifs into molecular architectures such as that of Sauvage's, small building blocks can be programmed to assemble into the final porphyrinic array in fewer synthetic steps. This thesis will describe how transition metals can be used in combination with ambidentate ligands to template the positioning of divergent pyridyl Lewis bases that, in turn, axially coordinate

to ruthenium-based metalloporphyrins and metallosalophens controlling their position in space (Figure 23 and Figure 24).²⁶

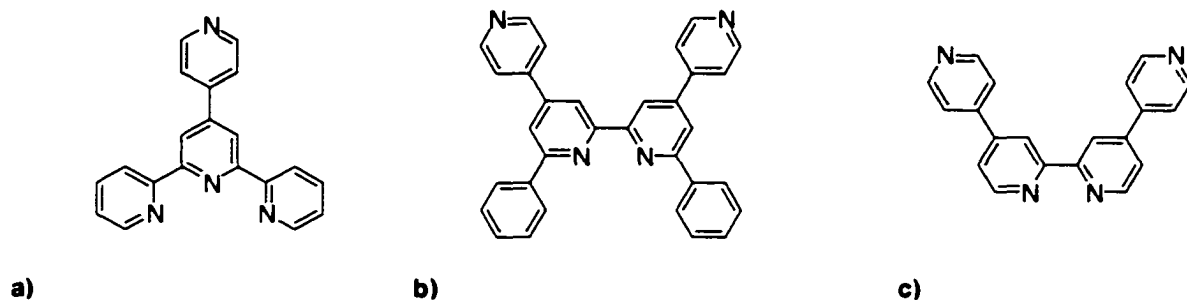


Figure 23. Ambidentate ligands that are used to form a) linear, b) tetrahedral, and c) octahedral porphyrin and salophen arrays.

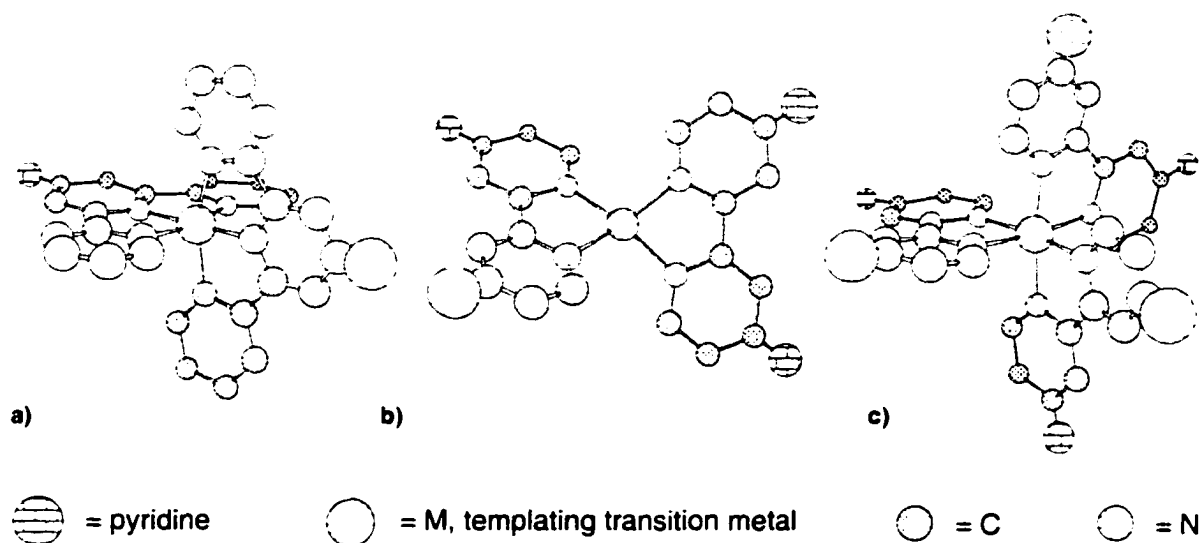


Figure 24. Computer generated molecular models that highlight the desired position to attach peripheral Lewis basic sites that can effectively extend the geometry around the central metal to form a) linear, b) tetrahedral, and c) octahedral arrays. The brick-walled balls on the periphery of the ligands denote the important positions where divergent pyridines will be appended to selectively extend the central metals' geometry. Refer to the legend for other atom types.

This thesis will focus on the synthetic utility of using axial coordination of small component compounds to chromophores to construct supramolecular aggregates and how such systems can be characterized and studied. Where possible, the focus has been placed

on highlighting the important self-assembly pathways that are responsible for aggregate formation. Chapter 2 introduces the features of axial coordination to ruthenium(II) carbonyl metalloporphyrins and describes how their spectroscopic features change upon pyridine coordination and how these changes can be probed to verify aggregate formation. The remaining three sections of Chapter 2 describe the metal-directed synthesis of hybrid porphyrin arrays based on transition metal complexes using the ambidentate ligands shown in Figure 23 and 24. Chapter 3 explores the utility of axial coordination to metalloporphyrins as new stoppering methods for rotaxane synthesis. Chapter 4 introduces metallosalophens as an alternative source of axial coordinating chromophores to construct a variety of hybrid salophen arrays. Chapter 5 summarizes the thesis, highlights the important future studies, and provides examples of future extensions using axial coordination to chromophores.

1.6 – References

1. (a) J.-M. Lehn, *Supramolecular Chemistry - Concepts and Perspectives*; VCH: Weinheim, 1995; (b) *Molecular Self-Assembly – Organic versus Inorganic Approaches*, Ed. M. Fujita, Springer-Verlag Berlin Heidelberg, New York, 2000; (c) P. D. Beer, P. A. Gale, D. K. Smith, *Supramolecular Chemistry*, Oxford University Press Inc., New York, 1999; (d) F. Vögtle, *Supramolecular Chemistry*, John Wiley and Sons, New York, 1991.
2. M. S. Goodman, A. D. Hamilton and J. Weiss, *J. Am. Chem. Soc.*, **1995**, *117*, 8447.
3. G. F. Swiegers and T. J. Malefetse, *Chem. Rev.*, **2000**, *100*, 3483.
4. M. Albrecht, *Chem. Soc. Rev.*, **1998**, *27*, 281 and references cited therein.
5. (a) M. Fujita, *Chem. Soc. Rev.*, **1998**, *27*, 417; (b) P. J. Stang, *Chem. Eur. J.*, **1998**, *4*, 19.
6. (a) M. Fujita, K. Umemoto, M. Yoshizawa, N. Fujita, T. Kusukawa and K. Biradha, *Chem. Commun.*, **2001**, 509; (b) N. Takeda, K. Umemoto, K. Yamaguchi and M. Fujita, *Nature*, **1999**, *398*, 794; (c) D. L. Caulder and K. N. Raymond, *J. Chem. Soc. Dalton Trans.*, **1999**, 1185 and references cited therein.
7. S. R. Batten and R. Robson, *Angew. Chem. Int. Ed.*, **1998**, *37*, 1460 and references cited therein.
8. (a) M. Bochmann, *Organometallics 1: Complexes with Transition Metal-Carbon σ -Bonds*, Oxford University Press Inc., New York, 1994; (b) R. L. Dekock and H. B. Gray, *Chemical structure and bonding*, University Science Books, Mill Valley, 1989.

9. B. N. Figgis, *Introduction to ligand fields*, R. E. Krieger Publishing Co., Malbar, 1986.
10. J. L. Atwood, J. E. D. Davies, D. D. MacNicol and F. Vögtle, *Comprehensive Supramolecular Chemistry*; Pergamon Oxford, 1996, vol. 9.
11. T. Kusukawa and M. Fujita, *Angew. Chem. Int. Ed.*, **1998**, *37*, 3142.
12. (a) D. J. Cram and J. M. Cram, *Container Molecules and Their Guests*, Royal Society of Chemistry, Cambridge, UK, 1995; (b) D. J. Cram, *Nature*, **1992**, *356*, 29; D. J. Cram, M. E. Tanner and R. Thomas, *Angew. Chem. Int. Ed.*, **1991**, *30*, 1024; (c) M. Yoshizawa, T. Kususkawa, M. Fujita and K. Yamaguchi, *J. Am. Chem. Soc.*, **2000**, *122*, 6311; (d) R. Warmuth and M. A. Marvel, *Angew. Chem. Int. Ed.*, **2000**, *39*, 1117.
13. (a) H. Ito. T. Kusukawa and M. Fujita, *Chem. Lett.*, **2000**, 598; (b) J. Kang, J. Santameria, G. Hilmersson, and J. Rebek, Jr., *J. Am. Chem. Soc.*, **1998**, *120*, 7389.
14. (a) H.-J. Kim, J. E. Redman, M. Nakash, N. Feeder, S. J. Teat and J. K. M. Sanders, *Inorg. Chem.*, **1999**, *38*, 5178 and references cited therein; (b) D. W. J. McCallien and J. K. M. Sanders, *J. Am. Chem. Soc.*, **1995**, *117*, 6611; (c) F. Diederich and P. J. Stang, *Templated Organic Synthesis*; Wiley-VCH: Weinheim, 2000.
15. S. S. Eaton and G. R. Eaton, *Inorg. Chem.*, **1977**, *16*, 72.
16. R. J. Morgan and A. D. Baker, *J. Org. Chem.*, **1990**, *55*, 1986.
17. (a) U. Ermler. G. Fritzsche, S. K. Buchanan, H. Michel, *Structure*, **1994**, *2*, 925; (b) C. H. Chang, O. Elkabbani, D. Tiede, J. Norris and M. Schiffer, *Biochemistry*, **1991**, *30*, 5352.

18. (a) B. A. King, T. B. McAnaney, A. deWinter and S. G. Boxer, *J. Phys. Chem. B*, **2000**, *104*, 8895; (b) B. A. King, A. de Winter, T. B. McAnaney and S. G. Boxer, *J. Phys. Chem. B*, **2001**, *105*, 1856; (c) X. J. Jordanides, G. D. Scholes and G. R. Fleming, *J. Phys. Chem. B*, **2001**, *105*, 1652; (d) G. D. Scholes, X. J. Jordanides and G. R. Fleming, *J. Phys. Chem. B*, **2001**, *105*, 1640.
19. M. D. Ward, *Chem. Soc. Rev.*, **1997**, *26*, 365.
20. (a) T. Förster, *Discuss. Faraday Soc.*, **1959**, *27*, 7; (b) T. Förster, In *Modern Quantum Chemistry, Part III*, Academic Press, New York, 1965; p 93.
21. D. L. Dexter, *J. Chem. Phys.*, **1953**, *21*, 836.
22. (a) A. Osuka, M. Ikeda, H. Shiratori, Y. Nishimura and I. Yamazaki, *J. Chem. Soc. Perkin Trans. II*, **1999**, 1019; (b) R. W. Wagner, J. Seth, S. I. Yang, D. Kim, D. F. Bocian, D. Holten and J. S. Lindsey, *J. Org. Chem.*, **1998**, *63*, 5042; (c) R. K. Lammi, A. Ambroise, T. Balasubramanian, R. W. Wagner, D. F. Bocian, D. Holten and J. S. Lindsey, *J. Am. Chem. Soc.*, **2000**, *122*, 7579; (d) L. Flamigni, F. Barigelletti, N. Armaroli, J.-P. Collin, J.-P. Sauvage and J. A. G. Williams, *Chem. Eur. J.*, **1998**, *4*, 1744; (e) J. L. Sessler, C. T. Brown, D. O'Connor, S. L. Springs, R. Wang, M. Sathiosatham and T. Hirose, *J. Org. Chem.*, **1998**, *63*, 7370; (f) C. C. Mak, N. Bampos and J. K. M. Sanders. *Angew. Chem. Int. Ed.*, **1998**, *37*, 3020; (g) T. Arimura, C. T. Brown, S. L. Springs and J. L. Sessler, *Chem. Commun.*, **1996**, 2293; (h) C. M. Drain, K. C. Russell and J.-M. Lehn, *Chem. Commun.*, **1996**, 337; (i) C. A. Hunter and R. J. Shannon, *Chem. Commun.*, **1996**, 1361; (j) R. K. Kumar, S. Balasubramanian and I. Goldberg, *Chem. Commun.*, **1998**, 1435.

23. (a) A. Harriman, F. Odobel and J.-P. Sauvage, *J. Am. Chem. Soc.*, **1995**, *117*, 9461; (b) L. Flamigni, F. Barigelletti, N. Armaroli, J.-P. Collin, J.-P. Sauvage and J. A. G. Williams, *Chem. Eur. J.*, **1998**, *4*, 1744; (c) I. M. Dixon, J.-P. Collin, J.-P. Sauvage, F. Barigelletti and L. Flamigni, *Angew. Chem. Int. Ed.*, **2000**, *39*, 1292.
24. For examples of other porphyrin arrays assembled through axial coordination, see: (a) T. Imamura and K. Fukushima, *Coord. Chem. Rev.*, **2000**, *198*, 133; (b) U. Michelsen and C. A. Hunter, *Angew. Chem. Int. Ed.*, **2000**, *39*, 764; (c) M. Gardner, A. J. Guerin, C. A. Hunter, U. Michelsen and C. Rotger, *New J. Chem.*, **1999**, 309; (d) J. E. Redman, N. Feeder, S. J. Teat and J. K. M. Sanders, *Inorg. Chem.*, **2001**, advance article; (e) S. L. Darling, C. C. Mak, N. Bampos, N. Feeder, S. J. Teat and J. K. M. Sanders, *New J. Chem.*, **1999**, *23*, 359.
25. For representative examples of ruthenium(II) porphyrin arrays assembled through axial coordination, see: (a) K. Funatsu, T. Imamura, A. Ichimura and Y. Sasaki, *Inorg. Chem.*, **1998**, *37*, 4986; (b) A. Prodi, M. T. Indelli, C. J. Kleverlaan, F. Scandola, E. Alessio, T. Gianferrara and L. G. Marzilli, *Chem. Eur. J.*, **1999**, *5*, 2668; (c) M. Ikonen, D. Guez, V. Marvaud and D. Markovitsi, *Chem. Phys. Lett.*, **1994**, *231*, 93 and references therein.
26. (a) K. Chichak and N. R. Branda, *Chem. Commun.*, **1999**, 523; K. Chichak and N. R. Branda, *Chem. Commun.*, **2000**, 1211.

Chapter 2 – Axial Coordination and Multi-Component Porphyrinic Arrays

2.1 – Characterizing Supramolecular Architectures

In general, as the structural complexity of a supramolecular architecture increases, the characterization of the final assembly increases in difficulty as well. The structure and stability of the architecture is of great importance, and relies on the choice of intermolecular interactions used. Whether the supramolecular assemblies are to be utilized in the solid, solution, or gaseous states will also dictate the characterization method. Characterization of solids is simple if high quality crystals can be isolated and, X-ray crystallographic analysis will accurately provide atom connectivity, atom positions, and molecular composition. Unfortunately, obtaining X-ray quality crystals is not a simple task because the isolated crystals can be plagued by two factors: improper crystal packing and crystal desolvation. These factors are magnified as the structural complexity increases and, as a consequence, effects the accuracy of the crystallographic data obtained. Independent methods to solid state characterizations are those performed in solution. Studies performed on solutions provide important kinetic, thermodynamic, and as well as structural information. The solution characterization methods and conditions chosen will rely heavily on the building blocks inherent associative properties. For instance, the lability of the molecular recognition elements and the stability of the architecture will vary when the solution's bulk properties are changed (pH, ionic strength and polarity, for example). Solvents can strongly compete with the molecular recognition elements and favour disassociation or decomplexation with the ultimate misleading of

any structural conclusions made. Fortunately, we are the beneficiaries of a wide variety of spectrometric methods that are used to characterize compounds under solid, solution, and gaseous conditions. In this aspect, we can be more intelligent in our design of the supramolecular building blocks and can choose methods that will provide facile structural characterizations. The common spectrometric methods that are used in characterizing supramolecular architectures, the information they provide and their applicable conditions are listed in Table 1.

Table 1. Summary of the spectrometric methods and applicable conditions

Spectrometric Method	Information	Conditions
Nuclear Magnetic Resonance (NMR)	kinetic, structural, and thermodynamic	solution or solid
X-ray Crystallography (X-ray)	structural	crystalline solid
Mass Spectrometry (MS)	structural composition	solution, solid, or gaseous
Infrared Spectroscopy (IR)	functional and structural	solution, solid, or gaseous
Ultraviolet–Visible spectroscopy (UV/Vis)		solution or solid

2.2 – Spectroscopic Properties of the Building Blocks

As mentioned in the final section of Chapter 1, the spectroscopic methods will be discussed in the context of characterizing axially coordinated arrays. First the discussion

will focus on the important spectroscopic properties specific to ruthenium(II) carbonyl metalloporphyrins. The focus will then shift to mention of the important spectroscopic properties used to characterize the polypyridyl transition metal complexes that make up the core units of the arrays. Finally, some general remarks regarding the methods and conditions used to characterize the axially coordinated arrays in this thesis will be highlighted.

2.2.1 – Pyridyl Adducts of Ruthenium(II) Carbonyl Metalloporphyrins

The binding of pyridines to ruthenium(II) carbonyl metalloporphyrins is strong and the large aromatic ring produces characteristic NMR,¹ IR,² and UV/Vis³ absorption spectroscopic properties (Figure 1). The most diagnostic and easily probed consequences of the binding of pyridines are highlighted separately for the known ruthenium(II) carbonyl tetraphenylporphyrin (Ru(TPP)(CO)) in Figure 1 and will serve to illustrate how ruthenium(II) metalloporphyrins are characterized.

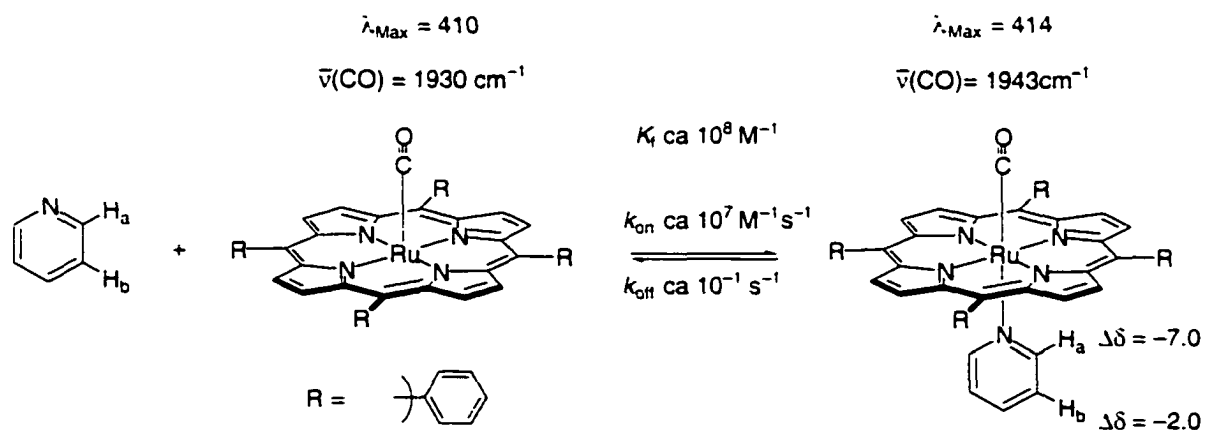


Figure 1. The key spectroscopic changes upon pyridine coordination to Ru(TPP)(CO). (1) a red-shift in the porphyrin's UV/Vis Soret absorption,³ (2) an increase in the C≡O stretching frequency,² (3) upfield shifts ($\Delta\delta$ in ppm) of the pyridine's resonances in its ¹H NMR spectrum.¹ Also shown are the rapid complexation rates ($k_{\text{on}} \text{ ca } 10^7 \text{ M}^{-1} \text{ s}^{-1}$) and slow decomplexation rates ($k_{\text{off}} \text{ ca } 10^{-1} \text{ s}^{-1}$) which are correlated to the formation constant ($K_f \text{ ca } 10^8 \text{ M}^{-1}$).⁴

The characterization of axially coordinated compounds of Ru(TPP)(CO) follows a standard approach by comparing spectra of the starting materials to those of the products. Each building block has a unique set of spectral data, which are different from those in the assembly and based on this, the appearance, disappearance, or the shifting of signals can be compared, evaluated and concluded upon.

2.2.1.1 – ¹H NMR Spectroscopy

¹H NMR spectroscopy is a very diagnostic technique for studying assembly processes involving axial coordination to ruthenium(II) carbonyl metalloporphyrins.¹ This technique is highly diagnostic because it conveniently provides component stoichiometry and the structure of axially coordinated metalloporphyrins. Not only does this technique provide important structural information, it also provides important kinetic and thermodynamic information about the self-assembly pathway. For example, consider Ru(TPP)(CO). As a consequence of the porphyrin's anisotropic ring current, the addition of pyridine results in the immediate appearance of new, sharp, and unchanging signals that correspond to the coordinated pyridyl adduct. These new signals do not shift from their relative positions when additional pyridine is added nor do they shift over the time course of a typical experiment. Important information can be extracted from these observations and each will be highlighted. First, from a structural point of view, the pyridine has an axial arrangement with the porphyrin plane with a bond angle of *ca.* 90°. Secondly, from a kinetic point of view, the immediate appearance of a new set of signals when less than one equivalent of pyridine is added means that the complexation rate (k_{on}) is fast and values have been calculated to be on the order of 10^6 – 10^7 M⁻¹s⁻¹.⁴ Lastly, since

the shapes of the signals are sharp and they do not shift when additional pyridine is added, this means, again from a kinetic point of view, that the decomplexation (k_{off}) is slow and values have been calculated to be on the order 10^{-1} s^{-1} .⁴ In other words, the coordinated pyridine is involved in a slow exchange process that can be monitored on the NMR time scale. The kinetic properties of axial coordination can be translated into thermodynamic terms, by taking the quotient of the on- and off-rates (k_{on}/k_{off}), an estimation of the formation constant can be calculated and it is large ($K_f \cong 10^8 \text{ M}^{-1}$).⁴ From these simple observations, we can conclude that the pyridine is tightly coordinated to the metalloporphyrin's axial site and it is positioned *ca.* 90° to the porphyrin plane, but it is not permanently bound because the dative bond is still kinetically labile.

2.2.1.2 – UV/Vis and IR Spectroscopy

The information obtained from ^1H NMR spectroscopy can be combined with other techniques such as UV/Vis and IR spectroscopy to support the event of pyridine coordination.^{2,3} For example, UV/Vis spectroscopy is useful for monitoring axial coordination to Ru(TPP)(CO) because a bathochromic shift (red shift from 410 to 414 nm) of the Soret band occurs when pyridine coordinates to the axial site.³ It must be remembered that UV/Vis spectroscopy is performed at lower concentrations (typically 10^{-5} M) than NMR spectroscopy and, thus, the competitive nature of the solvent for the axial site plays a larger role.

IR spectroscopy is another useful technique for probing axial coordination to Ru(TPP)(CO) by monitoring the changes in the stretching frequencies ($\Delta\nu_{\text{CO}}$ in cm^{-1}) of the axial carbon monoxide ligand.² The CO stretching band is located in an uncluttered

region of the IR spectrum and can be used to elucidate bonding properties of coordinating ligands to ruthenium(II) carbonyl metalloporphyrins. Historically, the monitoring of $\Delta\nu_{\text{CO}}$ has been common practice for examining changes in the electron density of metal carbonyl complexes after ligand coordination occurs. The coordination of CO to Ru(TPP) occurs through the formation of two bonds and is a useful example to illustrate the versatile bonding modes of metal d orbitals (Figure 2).

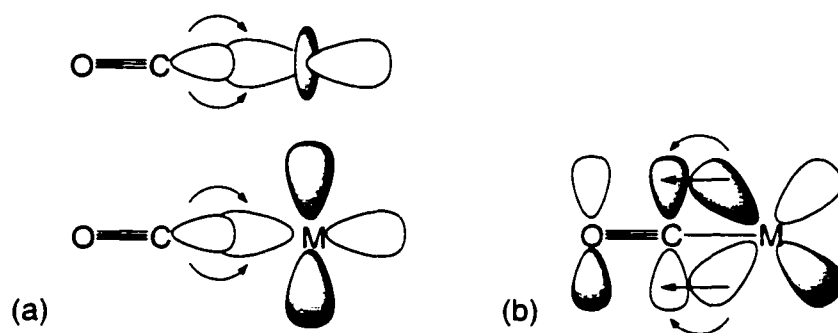


Figure 2. (a) The σ -bond of CO between metal $d(z^2)$ or $d(x^2-y^2)$ orbitals and (b) the π -bond of CO between metal $d(xy)$, $d(xz)$, or $d(yz)$ orbitals. The arrows represent the direction of electron delocalization.

First, CO forms a weak σ -bond, which donates electron density to the metal (Figure 2a). After this weak bond is formed, the electron density that is localized on the metal can be donated from filled metal d orbitals into the empty π^* orbitals on CO via π -back-bonding. Here the CO acts as a π -acid (Figure 2b). The amount of π -back-bonding alters the bond orders of both the carbon-oxygen triple bond and the metal-carbon bond. The greater the π -back-bonding, the greater the decrease in ν_{CO} and the greater the stability of the metal-carbon bond. Changes in ν_{CO} are amplified when an incoming ligand is *trans* to the CO because they compete for the same set of metal d orbitals. The magnitude of the change depends on whether the ligand is a strong or weak σ -donor, π -

donor, or π -acceptor. For example, the ν_{CO} of Ru(TPP)(CO) shifts from 1930 cm^{-1} to 1943 cm^{-1} when pyridine coordinates.² Since the ν_{CO} increases in frequency, this suggests that pyridine alters the amount of electron density back bonded to CO when it coordinates to the ruthenium(II) metal in Ru(TPP)(CO).

2.2.2 – Characterizing Polypyridyl Transition Metal Complexes.

In the absence of X-ray quality crystals, ^1H NMR, UV/Vis, and MS spectroscopy can be used to characterize the formation of polypyridine *d* metal complexes. The characterization is important to mention because these charged complexes make up the core units of the arrays. The approach is the same as already mentioned for characterizing pyridyl adducts of Ru(TPP)(CO), namely the comparison of the spectra of starting materials to those of the complexes.

2.2.2.1 – ^1H NMR Spectroscopy

^1H NMR spectroscopy can be used to monitor conformational changes in the ligand that occur after coordination and signals in a ligand's ^1H NMR spectrum will shift (Figure 3).

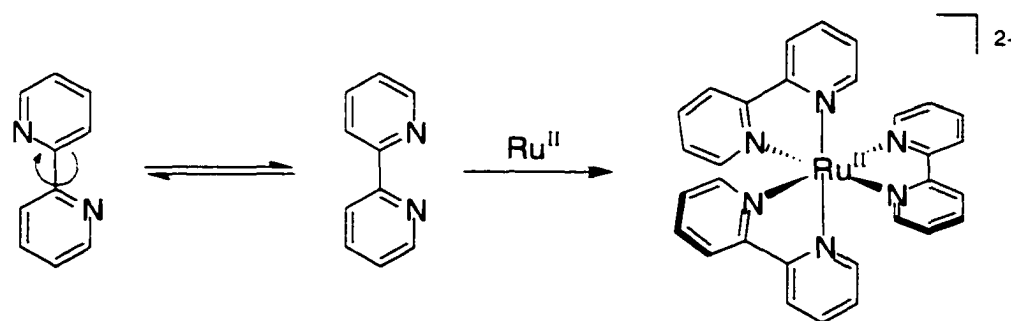


Figure 3. The conformational change of 2,2'-bipyridine required for chelation to occur.

Not only do the signals shift because of conformational changes, they will also shift from through-bond electron induction caused by the Lewis acidic transition metal that is held by the ligand(s).

2.2.2.2 – UV/Vis Spectroscopy

One other property of *d* metal complexes is the characteristic color change, in the visible spectral region, that occurs after coordination and the color change can be monitored using UV/Vis spectroscopy. Transition metal complexes that incorporate aromatic polypyridine ligands, for example tris(2,2'-bipyridyl)ruthenium(II) in Figure 3, have pronounced charge transfer bands.⁵ Charge transfer bands are responsible for the colors of transition metal complexes seen in solution and solid states. There are two types of charge transfer bands. The first type is called a ligand-to-metal charge transfer band (LMCT) and results from the promotion of an electron from a filled ligand orbital to an empty *d* metal orbital. The second type is called a metal-to-ligand charge transfer band (MLCT) and results from the promotion of an electron from a filled *d* metal orbital to an empty ligand π^* -orbital. Typically, ligand-to-metal charge transfer bands occur at shorter wavelengths while metal-to-ligand charge transfer bands occur at longer wavelengths. The excited state that arises from MLCT charge transfer bands is used to study photochemical redox properties of polypyridyl transition metal complexes.

2.2.2.3 – Electrospray Ionization Mass Spectrometry

Since the molecular composition of complex supramolecular architectures must be investigated, a technique that provides minimal loss of structural integrity is required.

Because mass spectrometry detects molecular ions, the most important aspect to mass spectrometry is the formation of molecular ions from a sample. Some MS methods require solid samples to be heated to high temperatures under vacuum or mixed with ion carrier matrices to transfer molecular species into the gas phase. The gas phase molecular species are then subsequently bombarded with electrons (EI), gases (FAB), or chemical species (CI) to produce molecular ions. Because of the sensitive nature of supramolecular complexes, these specific techniques are avoided because their conditions can promote fragmentation and jeopardize the architectures' structural integrity. A more mild technique to EI, FAB, and CI is electrospray ionization mass spectrometry (ESI-MS). This technique is gaining acceptance because of its ease to detect extremely large cations and anions in solution. Since most polypyridine *d* metal complexes bear charges, their molecular composition can be readily obtained using electrospray ionization mass spectrometry (Figure 3). The results from ESI-MS can not be used to make claims on solution equilibria because the solvent is stripped away and the strengths of supramolecular interactions are thus altered. But, these results can be used to verify the results obtained from solution characterizations using ¹H NMR, IR, and UV/Vis spectroscopy.

2.3 – Solvent Effects on Axial Coordination

Since the axially coordinated arrays in this thesis were characterized mainly using solution techniques, solvent selection plays an important role in producing reliable results. One important aspect when studying axial coordination in solution is a good

understanding of how the solvent properties effect the strength of the intermolecular bond (ie. the stability of the assemblies) formed between pyridine and the ruthenium metal center. Since axial coordination is a Lewis acid/Lewis base interaction, solvents that act as Lewis bases will alter the stability of the ruthenium-pyridine bond. One measure of the solvent's ability to interfere with Lewis acid/Lewis base associations is the solvent's donor number (DN) and these values have been provided by Gutmann.⁶ Gutmann has defined the donor number as the negative of the enthalpy of reaction of the solvent with the strong Lewis acid antimony(V) chloride. These numbers represent the ability of the solvent to donate electron density to electron deficient substances. In particular, these values can be used to estimate the ability of a solvent to act as a Lewis base and compete for the Lewis acidic metal of a metalloporphyrin. A solvent's donor number can be examined and the lower the number the greater the expected stability of the ruthenium-pyridine bond in that solvent. Kadish and Chang provide a better model, as their results directly represent solvent effects on axial coordination to Ru(TPP)(CO) than would the reference to just donor number values.^{3b} In their study, the magnitude of the formation constant was calculated for a variety of Lewis basic solvents, in CH₂Cl₂-0.1M TBAP, by monitoring changes in the UV/Vis spectrum of the five coordinate Ru(TPP)(CO) when forming the six coordinate Ru(TPP)(CO)(solvent) species. From these studies acetone and nitromethane ranked as the least stable adducts ($K_f = 10^{1.55}$ and $10^{1.46} \text{ M}^{-1}$, DN = 17.0 and 2.1 respectively) while pyridine ranked as the most stable adduct ($K_f = 10^{4.63} \text{ M}^{-1}$, DN = 33.1).

2.4 – General Remarks

Of course, one critical feature of the solvent is that it can dissolve the metalloporphyrin and the charged core transition metal complex. The charged transition metal complexes exhibit low solubilities in non-polar hydrocarbon and chlorinated solvents, while ruthenium(II) carbonyl porphyrins are very soluble in chloroform, dichloromethane, benzene, and toluene. The ruthenium(II) carbonyl metalloporphyrins greatly enhance the solubility of the charged transition metal complex, which make up the core of the axially coordinated arrays. The axially coordinated arrays are soluble in non-polar hydrocarbon and chlorinated solvents. It was found that using combinations of acetone or nitromethane mixed with dichloromethane provided the best results for studying axial coordination at varying complex concentrations. Due to increased solubility, the charged arrays were also studied in solvents such as dichloromethane and toluene, which do not compete and keep the pyridine adduct intact at lower concentrations.

These solvent mixtures were used in ^1H NMR, UV/Vis, IR, and ESI-MS studies. The IR studies were also performed on solid samples and, in doing so, the associated solvent effects of solution IR studies are eliminated. ESI mass spectrometry was chosen because the metalloporphyrins were assembled around charged templates, and the template acts as a carrier matrix and avoids the need for harsh ionization and the risk of fragmentation. One important feature to the nature of the ESI spectrometer, is that, due to the limitations of the machine, the upper mass limit for obtaining high-resolution spectra was 1000 mass units. Because of the high molecular weights of the arrays, low-resolution

experiments were performed and the spectra's isotopic distribution patterns were compared to the calculated patterns. However, in the absence of X-ray crystal structures, the array's final structure and composition was determined by combining the ESI-MS results with ^1H NMR, UV/Vis, and IR spectroscopy using methods already prescribed in the literature for studying axially coordination and transition metal complexes.

In this chapter, the use of self-assembly synthesis to create linear, tetrahedral and octahedral porphyrin arrays that are held together by metal-chelation and axial coordination is described. The arrays are templated through the use of transition metal complexes that are designed to govern the final geometries of the assemblies.

2.5 – Linear Axially Coordinated Metalloporphyrin Arrays

This section of the thesis describes the unprecedented formation of three linear multicomponent arrays constructed around bis(terpyridyl) transition metal complexes (also referred to as the “cores” of the arrays). More specifically, core complexes of transition metal complexes of iron(II), ruthenium(II), and osmium(II) link two metalloporphyrins via axial coordination that are spatially separated by *ca.* 11 Å (Figure 4).

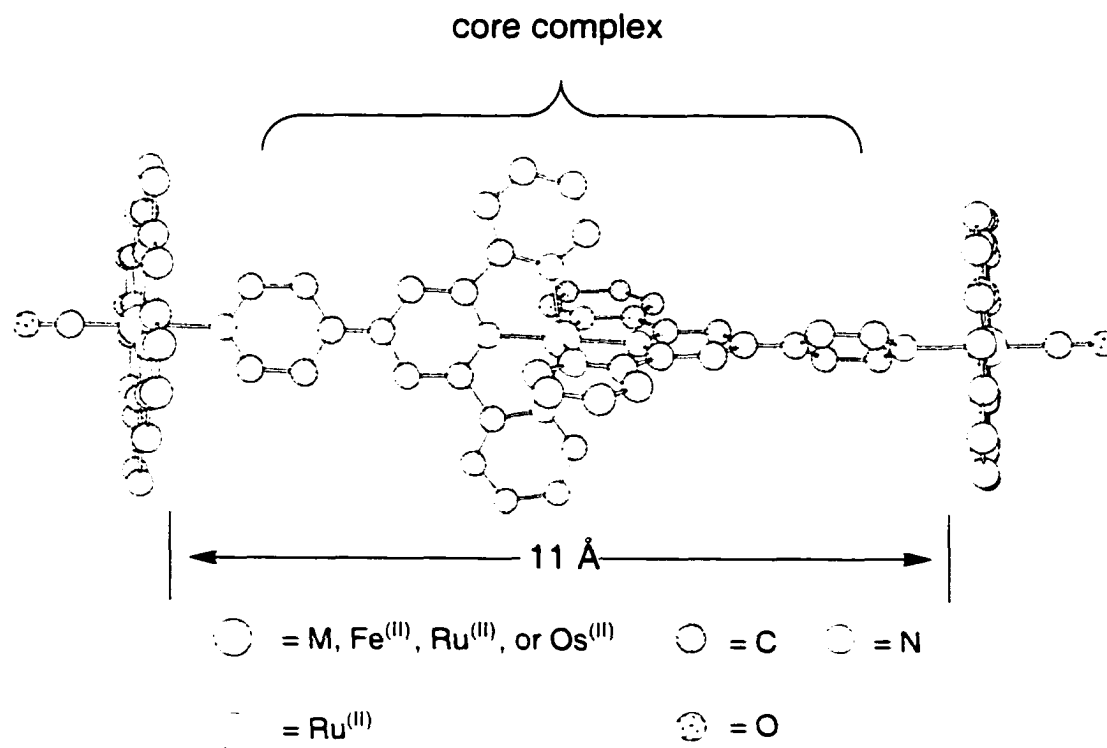


Figure 4. Molecular model that highlights the “core” of the porphyrin array. The porphyrins’ substituents have been omitted for clarity.

The molecular models of the core complexes and arrays presented in this section and in the following sections of this chapter of the thesis were adapted from crystal structures of the pyridyl adduct of ruthenium(II) carbonyl tetraphenylporphyrin and

bis(terpyridyl) octahedral transition metal complexes. Both of these structures can be found in the Cambridge Structure Database and were used, as is, without further minimization because the MacroModel program does not contain parameters suitable for transition metal atom types. Instead, the molecular models were created by simply connecting the metalloporphyrins' coordinated pyridine ligand to the central pyridine of the bis(terpyridyl) transition metal complex in the *para*-position. In doing so, the modeling program only applies the standard bond lengths and angles of a sp^2 carbon atom and does not alter the bond angles or bond lengths elsewhere in the complexes. In the absence of crystal structures, these molecular models provide a good representation of the overall topology of the linear arrays.

Initially, the design and synthesis of the important building blocks of the linear arrays will be discussed. Following this discussion, the self-assembly studies probed using ^1H NMR spectroscopy are highlighted. These studies serve to introduce the dramatic and characteristic upfield shifts seen in ^1H NMR spectra of the pyridine coordination to the axial site of ruthenium(II) carbonyl porphyrins. Lastly, the photophysical properties are presented. These properties show that there is intramolecular phosphorescence quenching for the ruthenium(II) and osmium(II) arrays in contrast to their molecular components which phosphoresce.

2.5.1 – Transition Metal Complex Design for Linear Templates

The design layout of the ambidentate ligand **1**⁷ is limited to forming linear arrays because it preferentially forms the stable bis-chelate complex and positions the

monodentate pyridine moiety as an extension of the two *trans*-coordination site vectors of the central metal (Figure 5).

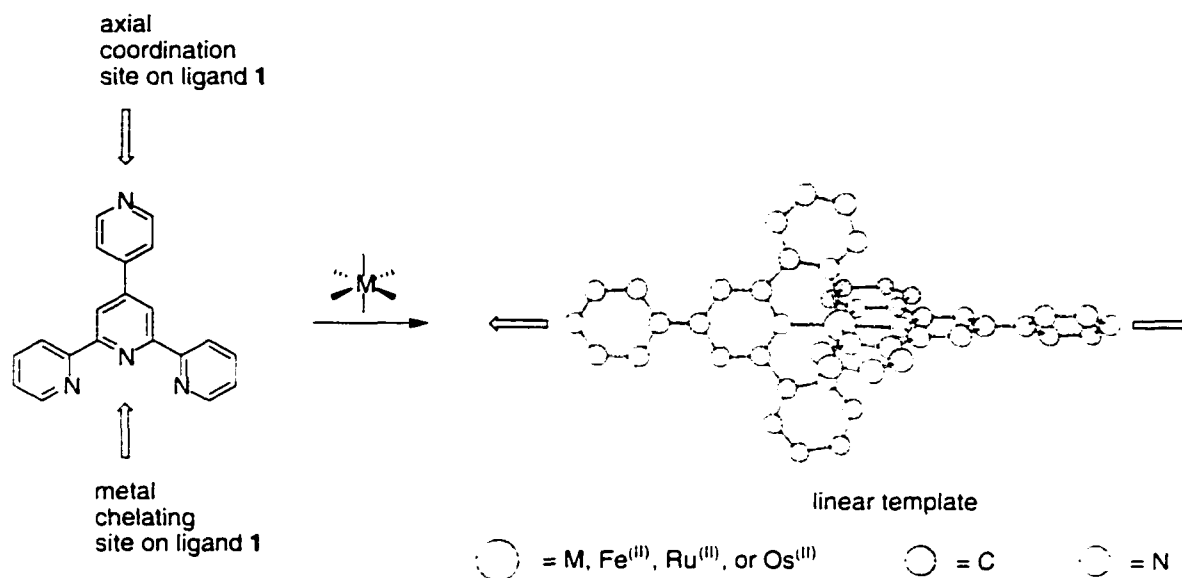


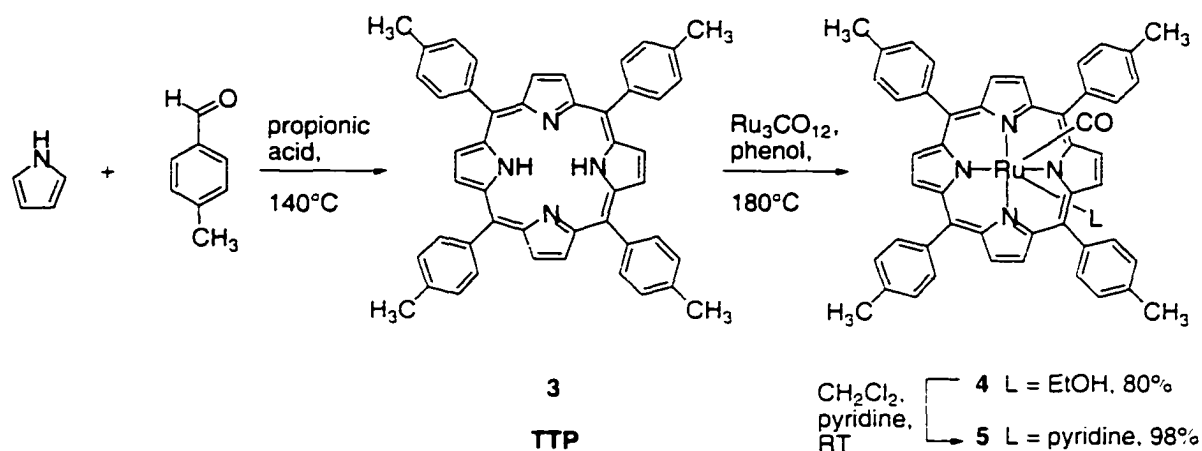
Figure 5. The design layout of the linear template. M = Fe^(III), Ru^(III), Os^(III).

Other advantages that terpyridines have in forming the central complex are: 1) a wide variety of substituents in the 4'-position can be easily introduced, and 2) because the *mer*-isomer is possible with a terpyridine ligand this eliminates stereoisomers that accompany the formation of mono-substituted bipyridine transition metal complexes.

2.5.2 – Results and Discussion

2.5.2.1 – Metalloporphyrin Synthesis

The *meso*-substituted porphyrin (**3**) (5,10,15,20-tetratolylporphyrin) was prepared following Alder's procedure by heating pyrrole with one molar equivalent of *p*-tolualdehyde in propionic acid at reflux (Scheme 1).⁸



Scheme 1.

The known metalloporphyrin Ru(TTP)(CO)(EtOH) (**4**) (TTP = 5,10,15,20-tetratolylporphyrinato dianion)⁹ was prepared using a slightly modified procedure of an earlier report by heating three molar equivalents of Ru₃CO₁₂ with one molar equivalent of **3** in phenol, instead of toluene, at reflux. Chromatographic purification was carried out using basic alumina (activity II-III) by sequentially changing the eluting solvents from non-coordinating to weakly coordinating. When eluting with dichloromethane, the metalloporphyrin strongly interacts with the solid support and allows the removal of any unreacted Ru₃CO₁₂ and free base porphyrin. The gradient addition of dichloromethane/ethanol (up to 95:5) decreases the metalloporphyrins' affinity towards the solid support and elutes it off the column as the ethanol adduct. Typically, after chromatography, a green band characteristic of chlorin impurity is retained on the column (Figure 6).^{9b} The amount of chlorin in the product can be assessed using UV/Vis spectroscopy, where the characteristic band associated with the chlorin impurity appears at 600 nm. If chlorin is present, it can be removed by repeating the purification procedure (basic alumina activity II-III) using a much slower gradient addition of dichloromethane/ethanol (up to 95:5).

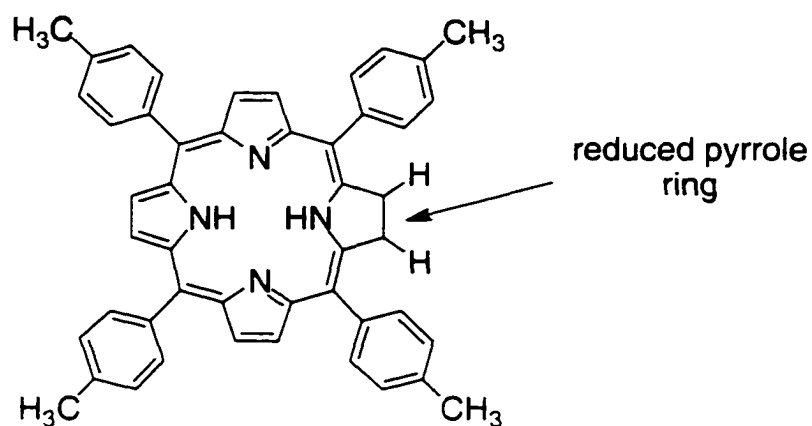
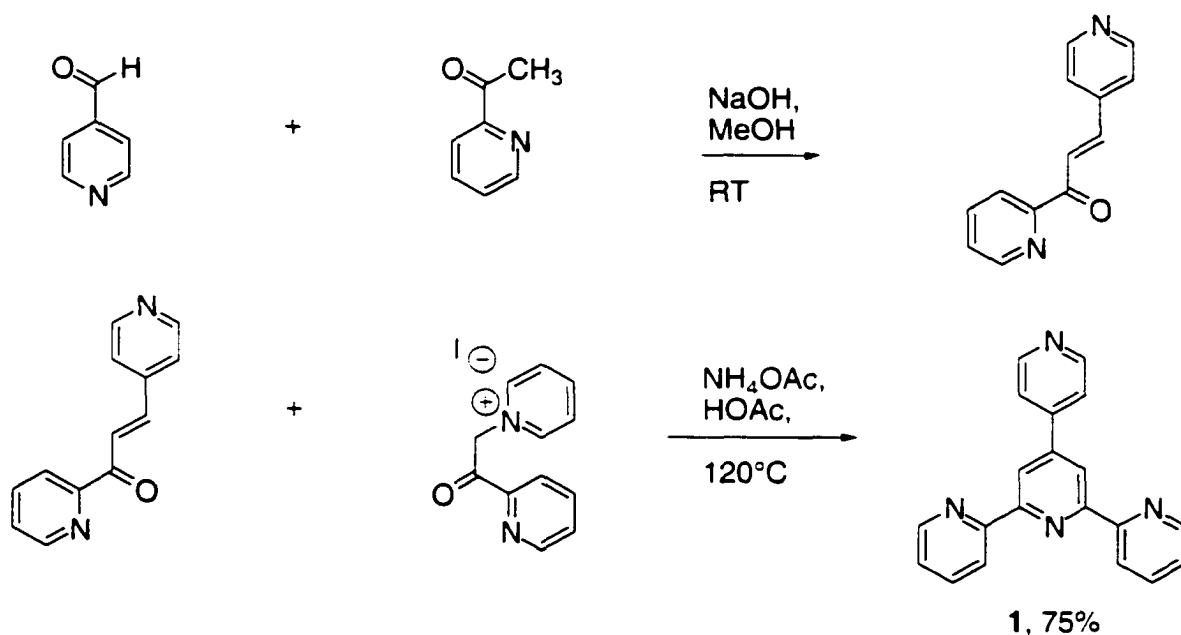


Figure 6. The reduced porphyrin macrocycle of Chlorin.

The labile ethanol ligand of **4** was replaced by adding pyridine to a dichloromethane solution containing Ru(TTP)(CO)(EtOH). The UV/Vis absorption spectrum, IR spectrum, and ^1H NMR spectrum of this metalloporphyrin product was consistent with the spectra previously reported in the literature.⁹ Removal of the solvent and recrystallization from hexane afforded the pyridine adduct Ru(TTP)(CO)(py) (**5**) in nearly quantitative yield. The solid state IR spectrum of Ru(TTP)(CO)(EtOH) showed that the ν_{CO} appears at 1946 cm^{-1} and when pyridine coordinates to the metal, the ν_{CO} shifted to 1933 cm^{-1} in **5**. The ^1H NMR spectrum of Ru(TTP)(CO)(py) (**5**) was also consistent with the pyridine ligand occupying the axial site by showing the expected upfield shifts for all pyridine proton resonances which experience the metalloporphyrin's anisotropic ring current.

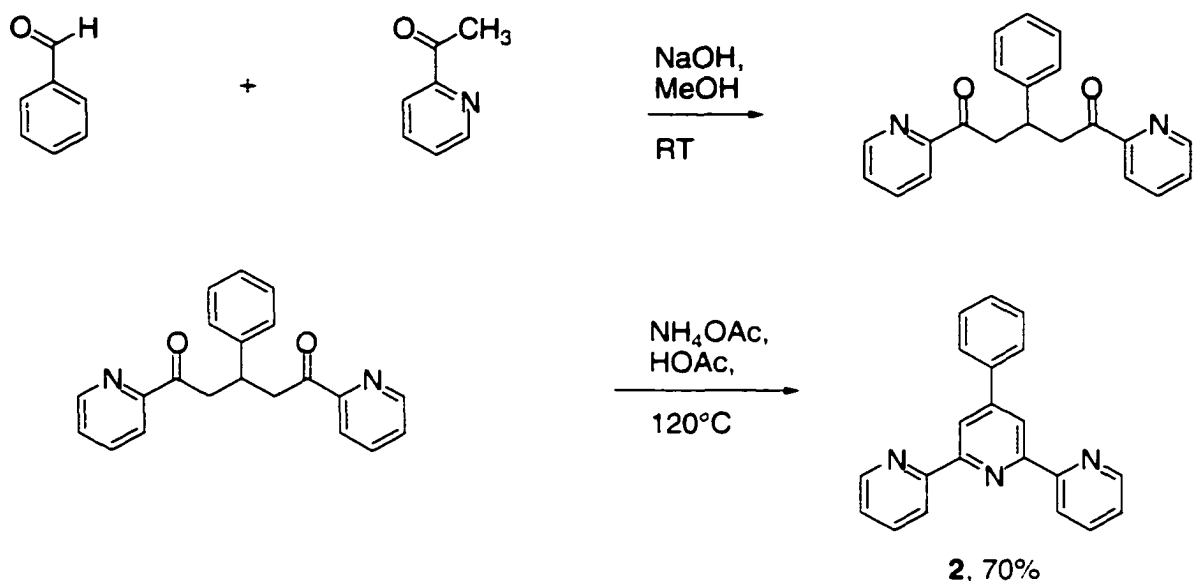
2.5.2.2 – Core Complex Ligand Synthesis

The central **pytpy** ligand (pytpy = 4'-(4'''-pyridyl)-2,2':6',2''-terpyridine, **1**)⁷ and **phtpy** ligand (phtpy = 4'-phenyl-2,2':6',2''-terpyridine, **2**)¹⁰ were prepared according to known methods described by Kröhnke (Scheme 2 for ligand **1**).¹¹ In Kröhnke's pyridine synthesis, the conjugate addition of a pyridinium ylide to an α,β -unsaturated carbonyl compound leads to the construction of a 1,5-diketone that cyclizes directly to a pyridine.



Scheme 2.

Alternatively, if the 1,5-diketone can be readily isolated, following a Hantzsch type reaction, the addition of ammonium acetate will lead to pyridine formation (Scheme 3 for ligand **2**).¹²



Scheme 3.

These are excellent routes to prepare large quantities of pyridines that have substituents in the 2-, 4-, and 6- positions and the products are usually readily purified by simple recrystallization.

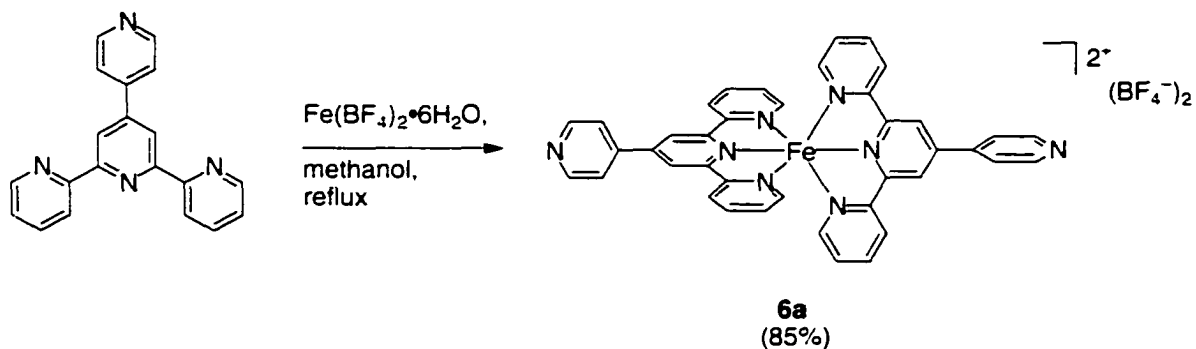
2.5.2.3 – The Synthesis of the Transition Metal Core Complexes

The core units of the linear arrays $[(M(\text{pytpy})_2)^{2+}]$, $\text{pytpy} = 4'-(4''\text{-pyridyl})-2,2':6'.2''\text{-terpyridine}$, $M = \text{Fe } \mathbf{6a}$, $\text{Ru } \mathbf{6b}$, $\text{Os } \mathbf{6c}$] and their phenyl substituted analogs $[(M(\text{phtpy})_2)^{2+}]$, $\text{phtpy} = 4'\text{-phenyl-}2,2':6'.2''\text{-terpyridine}$, $M = \text{Ru } \mathbf{7b}$, $\text{Os } \mathbf{7c}$] were prepared as their air-stable hexafluorophosphate or tetrafluoroborate salts according to previously reported literature procedures.^{7,13}

The iron(II) core **6a** complex was prepared in one step by heating $\text{Fe}(\text{BF}_4)_2 \cdot 6\text{H}_2\text{O}$ with two molar equivalents of **pytpy** in methanol at reflux (Equation 1).⁷ The lability of the iron(II) tetrafluoroborate synthon produced a diagnostic and immediate change in

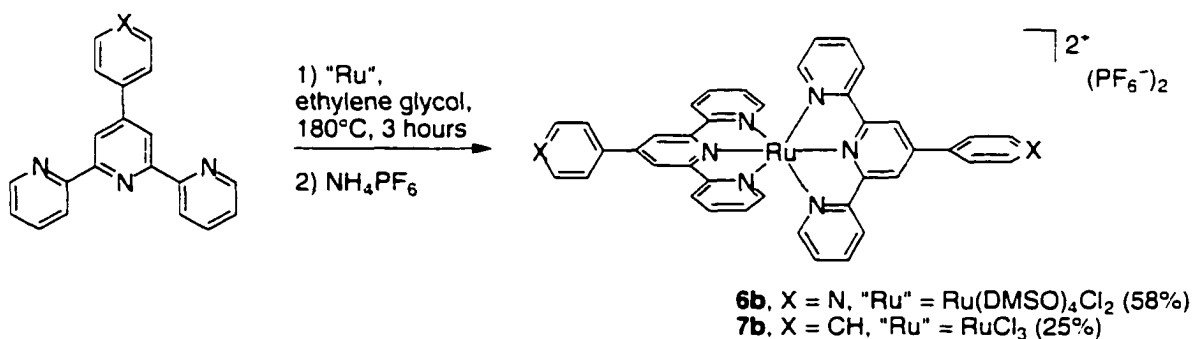
color from colorless to deep purple signifying the formation of the desired core complex.

The iron(II) core complex was purified by recrystallization from methanol.



Equation 1.

The ruthenium(II) core complexes **6b** and **7b** were prepared by heating $\text{Ru}(\text{DMSO})_4\text{Cl}_2$ or $\text{RuCl}_3 \cdot \text{H}_2\text{O}$ with two molar equivalents **pytpy** or **phtpy** in ethylene glycol at reflux producing deep red solutions (Scheme 4).¹³

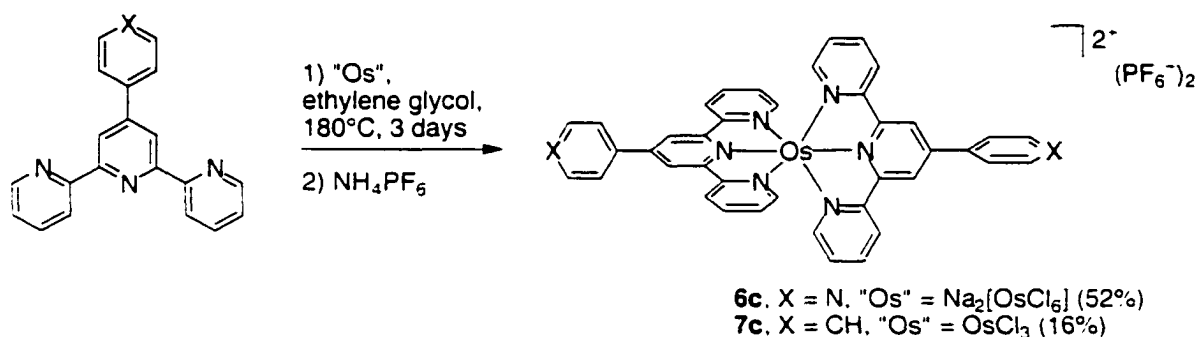


Scheme 4.

Using the dimethylsulfoxide complex as the source of ruthenium(II) is advantageous because it is non-acidic and, thus prevents the formation unwanted oxidized and protonated products. Also, the labile dimethylsulfoxide ligands are more easily displaced

than the chlorine ligands of $\text{RuCl}_3 \cdot x\text{H}_2\text{O}$, resulting in shorter reaction times with higher yields. The chloride counterions in the initially formed core complexes were exchanged by pouring the ethylene glycol solution into water and then adding a methanolic solution containing ammonium hexafluorophosphate to precipitate **6b** and **7b** as crude products. Purification was carried out using column chromatography through silica gel eluting the complexes with a mixture of water-acetonitrile-saturated potassium nitrate (7:1:0.5). This produced colorful columns that aided in product separation.

The osmium(II) core complexes **6c** and **7c** were prepared in an analogous manner using either basic $\text{Na}_2[\text{OsCl}_6]$ or acidic OsCl_3 , both of which produced dark brown solutions (Scheme 5).^{13a} The complexes were purified in an identical fashion as described for the ruthenium(II) terpyridine complexes.

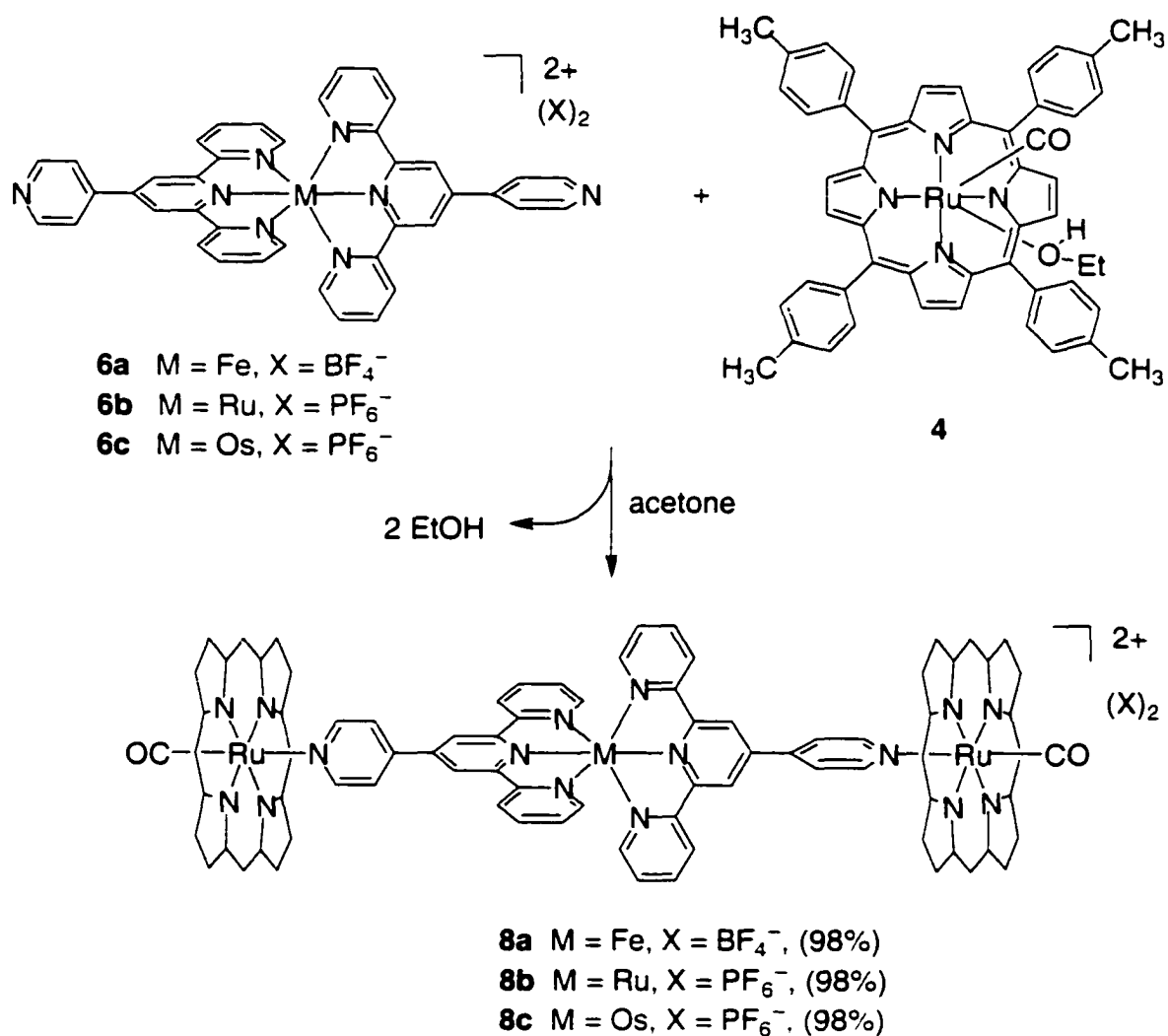


Scheme 5.

The formation of the osmium(II) core complexes required substantially longer reaction times (typically 3 days) compared to only 3 hours for the ruthenium(II) complex. The longer reaction times are a result of stronger metal-chloride bond in the case of osmium starting materials than that of ruthenium.

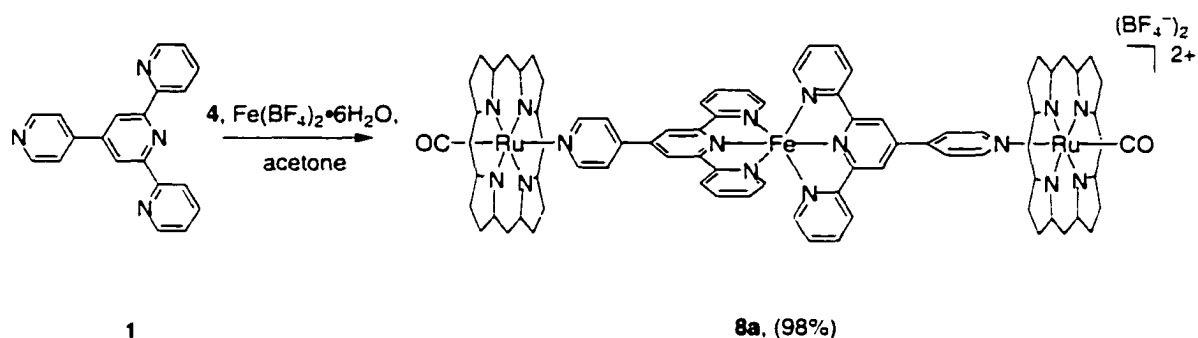
2.5.2.4 – Self-Assembly Synthesis of the Linear Porphyrin Arrays

The final triads **8a**, **8b** and **8c** were prepared in greater than 95% yield by adding two molar equivalents of Ru(TTP)(CO)(EtOH) (**4**) to one molar equivalent of the appropriate core complex M(pytpy)₂²⁺ in acetone and gently heating (Scheme 6). As an alternative to this procedure, the fully assembled arrays can be prepared at room temperature by adding an excess of the metalloporphyrin.



Scheme 6. The porphyrins' tolyl substituents and double bond representations have been omitted for clarity.

The iron triad **8a** can also be prepared in high yield (98%) using a one-pot procedure by dissolving a 2:2:1 solid mixture of metalloporphyrin **4**, terpyridine **1**, and $\text{Fe}(\text{BF}_4)_2 \cdot 6\text{H}_2\text{O}$ in acetone (Equation 2). The synthesis of the iron(II) array exemplifies the power of self-assembly synthesis to minimize the number of synthetic steps to form products in high yields.



Equation 2. The porphyrins' tolyl substituents and double bond representations have been omitted for clarity.

For all four syntheses, acetone was used as the solvent because it dissolves all the components and it is easy to remove, while at the same time does not significantly compete with axial coordination. Coordinating solvents may compete with the pyridyl group of the ligand for the metal of the metalloporphyrin which, if strong enough, favours dissociation of the array. In order to maximize the yields of the fully assembled linear arrays, acetone ($\text{DN} \approx 17$) was removed and replaced with dichloromethane ($\text{DN} = 0$), a non-competitive solvent.⁶ The addition of pentane to the dichloromethane solutions precipitated the fully assembled arrays and also removed any unreacted metalloporphyrin. In either case, the fully assembled triad complexes were isolated as red-purple (Fe), red (Ru), and red-brown (Os) solids and characterized by ^1H NMR

spectroscopy, UV/Vis spectroscopy, IR spectroscopy, ESI mass spectrometry, and ^{13}C NMR spectroscopy.

2.5.2.5 – Characterizations Using ^1H NMR Spectroscopy

^1H NMR spectroscopy proved to be a very diagnostic technique for studying self-assembly processes that involve axial coordination to metalloporphyrins (Figure 7). As mentioned in the introduction of this chapter, when a pyridine binds to a ruthenium(II) carbonyl metalloporphyrin, the heterocyclic ring experiences the porphyrin's anisotropic ring current and shifts the proton resonances upfield. For example, protons 'a' in Figure 7, which are closer to the porphyrin plane, are shifted further upfield than protons 'b' that are farther away.^{1,14}

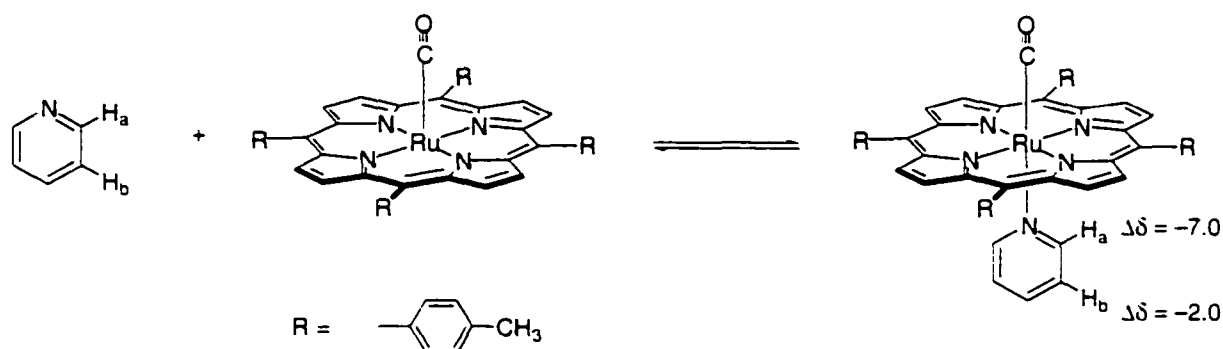


Figure 7. $\Delta\delta$ represents upfield shifts of the pyridine's resonances in ppm in its ^1H NMR spectrum.

The ^1H NMR spectra of all complexes **8a**, **8b**, and **8c** show significant upfield shifts for all hydrogen atoms of the $\text{M}(\text{pytpy})_2^{2-}$ core units as anticipated for protons lying within the close proximity of the porphyrin plane (Figure 8).^{1,14} Interestingly, the anisotropic effect never completely disappears and extends over the entire distance

spanned by the core unit (*ca.* 11 Å) and is attributed to an additive effect of both porphyrins forming the complex's walls. As expected, the protons immediately adjacent to the pyridine nitrogen of the core unit are the most affected and are seen to move as much as 7.5 ppm upfield upon complexation (protons H_a in Figure 8).

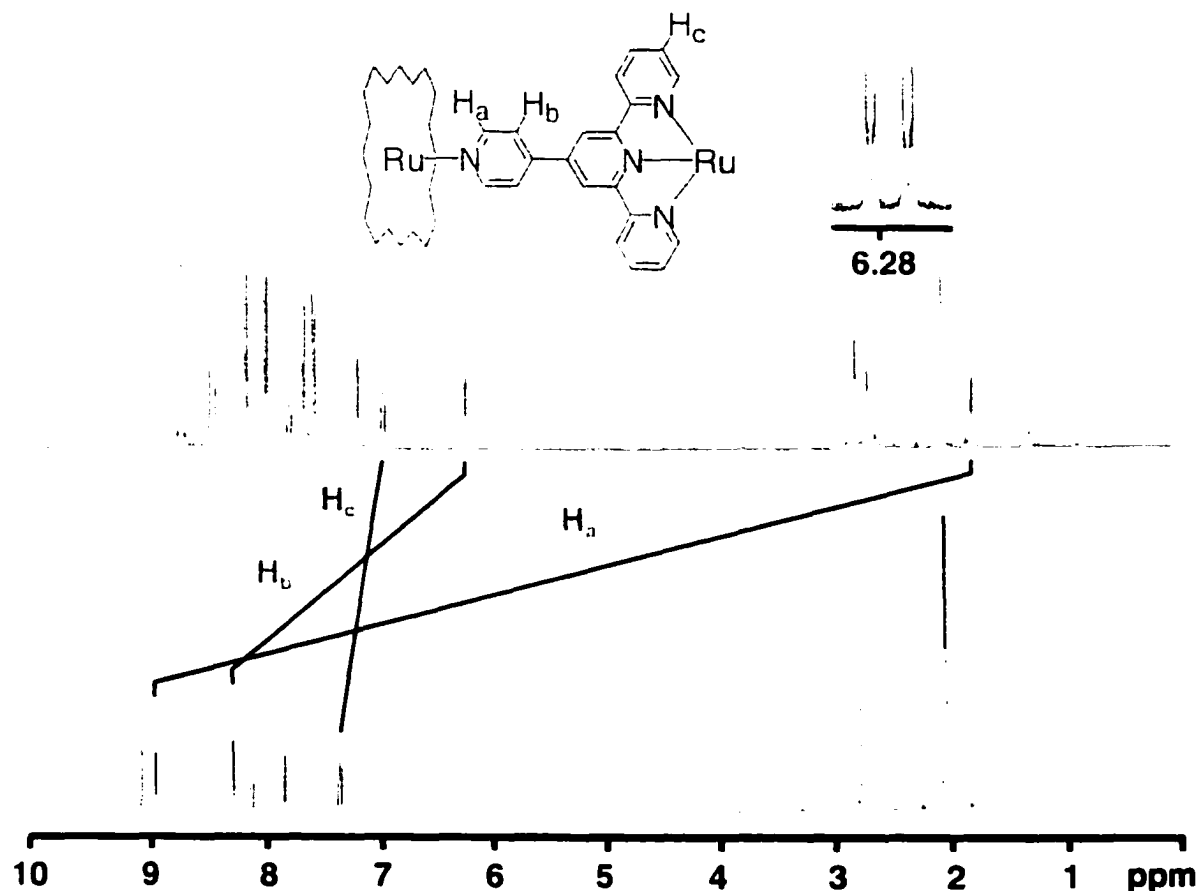


Figure 8. ¹H NMR (300 MHz, [D₆]acetone) spectra of [Ru(pytpy)₂](PF₆)₂ **6b** (bottom trace) and triad **8b** (top trace). The inset spectrum corresponds to protons H_b when only one molar equivalent of Ru(TTP)(CO)(EtOH) **4** was added showing both mono- (peaks on left) and bis-coordination (peaks on the right) arrays. The porphyrin is represented as a simple macrocycle.

The smallest, but still significant, shielding effect acts on the hydrogen atoms closest to the central metal which are shifted 0.5 ppm to higher field (protons H_c in Figure 8). The ¹H NMR studies revealed that, even in a competitive solvent such as acetone,

coordination to the metalloporphyrin is strong and ligand-exchange is slow on the NMR time scale, and sharp, unchanging peaks for the statistical mixture of non-, mono- and di-addition products were clearly visible when only one molar equivalent of Ru(TTP)(CO)(EtOH) (**4**) was added (Figure 8, inset). This observation is useful when preparing complexes *in situ* and is utilitarian when constructing larger porphyrin arrays because signals that correspond to the fully assembled array will be shifted the furthest upfield. This diagnostic tool will be very useful later in this chapter.

2.5.2.6 – Characterizations Using ESI Mass Spectrometry

The linear arrays **8a**, **8b**, and **8c** were also characterized by electrospray mass spectrometry (ESI-MS) using a CH₂Cl₂/nitromethane solvent mixture. The peak for the parent cation of **8a**, **8b**, and **8c** at $m/z = 1136, 1159, \text{ and } 1203 [M - 2X]^{2+}$ ($X = \text{counter ion PF}_6 \text{ or BF}_4$) was seen along with peaks corresponding to the consecutive loss of porphyrin units. The isotopic abundance of each peak matched the calculated values of double charged species.

2.5.2.7 – Characterizations Using IR Spectroscopy

The linear arrays **8a**, **8b**, and **8c** were also characterized in the solid state using IR spectroscopy. It should be remembered that when pyridine coordinated to Ru(TTP)(CO)(EtOH), the ν_{CO} shifted from 1946 cm^{-1} to 1933 cm^{-1} . For the linear arrays **8a**, **8b**, and **8c**, the ν_{CO} shifted to $1961, 1959, \text{ and } 1961 \text{ cm}^{-1}$ respectively. Since the ν_{CO} increases in frequency, this suggests that the amount of electron density back-bonded to CO is reduced when the core unit coordinates to Ru(TTP)(CO).

2.5.2.8 – Photophysical Properties of the Ruthenium(II) and Osmium(II) Triads

Initial photophysical studies show that the absorption spectra of complexes **8b** and **8c** in the UV/Vis region are essentially the sum of the absorption spectra of the triads' constituents (only **8c** and components are shown in Figure 9). This indicates that there is an absence of strong coupling between the different units of the assemblies and the chromophores behave independently.

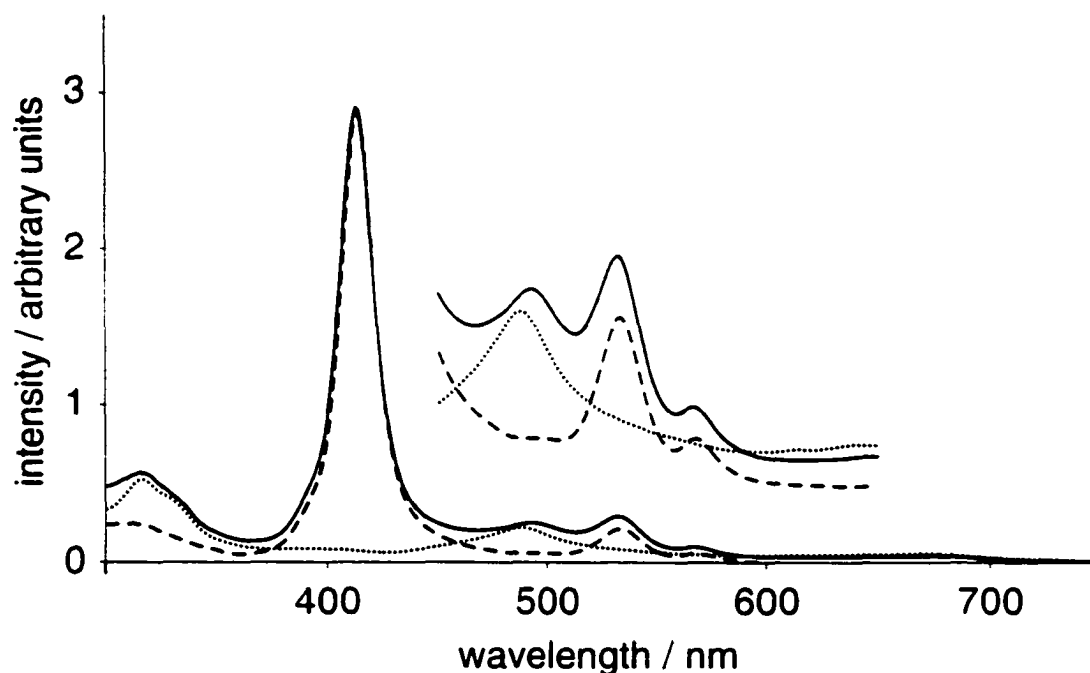


Figure 9. Overlay of absorption spectra of the osmium(II) array **8c** (solid line), Ru(TTP)(CO)(py) (**5**) (dashed line), and the osmium core complex [Os(pytpy)₂](PF₆)₂ (**6c**) (dotted line).

The steady-state emission properties of the triad complexes, however, differ greatly from those of their building blocks. In order to evaluate the photoemission properties of each of the triads' building blocks without complications from other luminescent species, the triads composed of the two different core units **6b** and **6c** were investigated independently.

The osmium core unit **6c** phosphoresces from its triplet excited state at room temperature in CH_2Cl_2 ,¹⁵ but the phosphorescence of the triad **8c** is significantly quenched (trace (b) and (c) in Figure 10 respectively). Here, the substantial reduction in phosphorescence intensity of the core unit on going from **6c** to **8c** can most likely be ascribed to ligation-induced quenching, where the porphyrin is acting as a Lewis acid for the monodentate pyridine of **6c**. This claim is supported by the complete luminescence quenching of **6c** upon *in situ* protonation with two equivalents of trifluoroacetic acid, although, at this stage, intramolecular triplet energy transfer from the core complex to the porphyrin cannot be completely ruled out.¹⁶

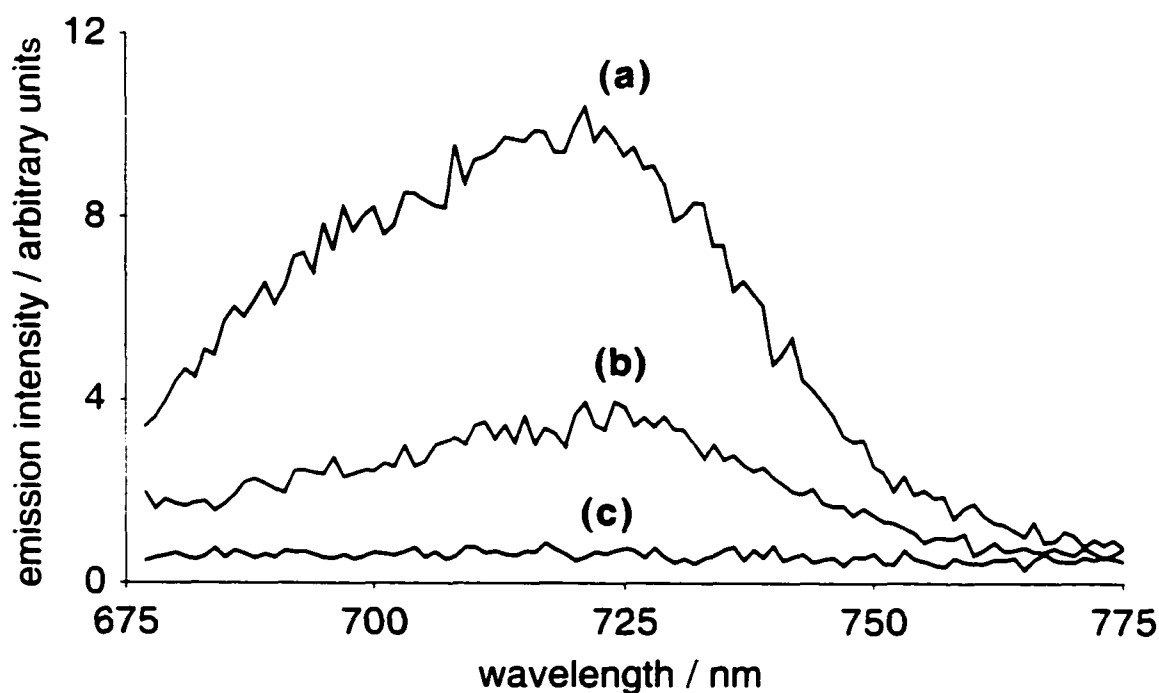


Figure 10. Emission spectra of CH_2Cl_2 solutions of the osmium(II) series (a) $[\text{Os}(\text{phtpy})_2](\text{PF}_6)_2$ (**7c**) ($\lambda_{\text{ex}} = 670 \text{ nm}$), (b) $[\text{Os}(\text{pytpy})_2](\text{PF}_6)_2$ (**6c**) ($\lambda_{\text{ex}} = 670 \text{ nm}$), (c) Osmium(II) array **8c** ($\lambda_{\text{ex}} = 670 \text{ nm}$). All spectra were run in dry deoxygenated solvent.

The lack of room temperature photoemission of the bis(terpyridine)ruthenium core unit **6b** enabled the study of the porphyrin unit, which shows substantially weaker phosphorescence intensity at room temperature in comparison with the osmium core unit **6c**.¹⁷ Again, significant phosphorescence quenching was observed for triad **8b** in comparison with the free pyridine-coordinated porphyrin species Ru(TTP)(CO)(py) (**5**) (trace (c) and (a) in Figure 11 respectively).

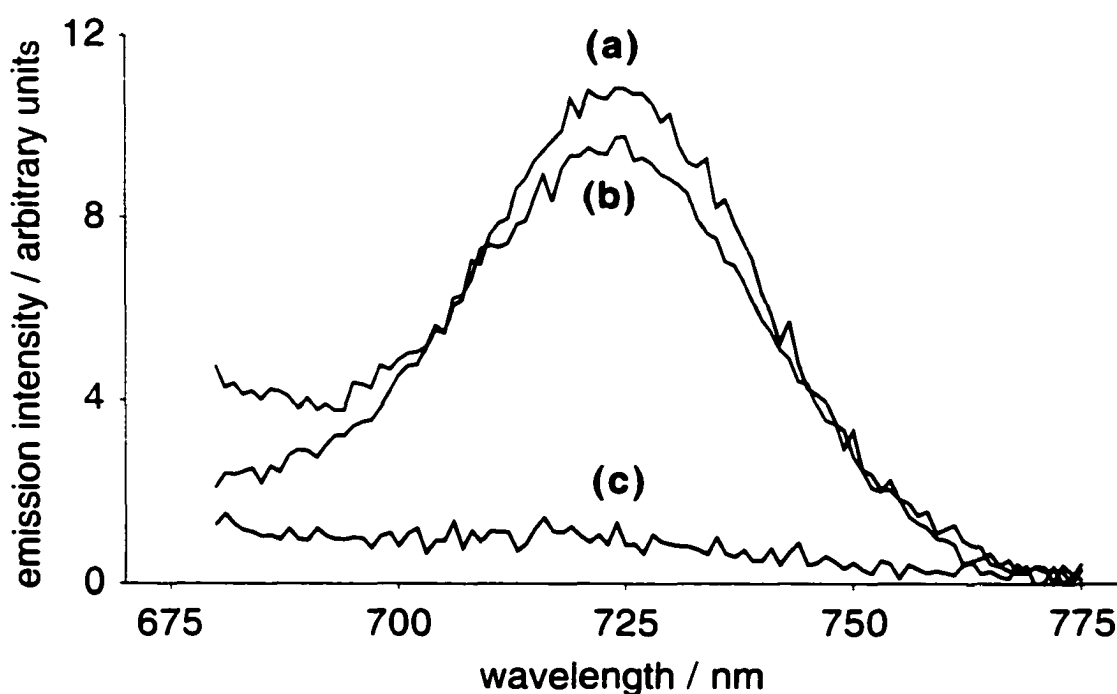


Figure 11. Emission spectra of CH₂Cl₂ solutions of (a) Ru(TTP)(CO)(py) (**5**) ($\lambda_{\text{ex}} = 530$ nm), (b) 2:1 mixture of **5** and [Ru(phtpy)₂](PF₆)₂ (**7b**) ($\lambda_{\text{ex}} = 530$ nm), (c) Ruthenium(II) array **8b** ($\lambda_{\text{ex}} = 530$ nm). All spectra were run in dry deoxygenated solvent.

In order to rule out the existence of intermolecular phosphorescence quenching between non-coordinated chromophores, the phenyl analog of **6b**, [Ru(phtpy)₂]²⁻ (phtpy = 4'-phenyl-2,2':6',2''-terpyridine) **7b**, which cannot axially coordinate to the metalloporphyrin, was examined. There was no observable intermolecular quenching of

the excited state of porphyrin chromophore **5** when treated with two molar equivalents of **7b**, clearly indicating that the luminescence quenching occurs only when the metalloterpyridine complex is intimately coordinated to the porphyrin (trace (b) in Figure 11). The conclusion that can be drawn from these observations is that there is effective electronic communication between chromophores within the assembled triad. A possible explanation for the luminescence quenching is that photoinduced electron transfer occurs from the metalloporphyrins to the core complex, followed by non-radiative decay of a charge-separated species.^{15,16b}

2.6 – Tetrahedral Axially Coordinated Metalloporphyrin Arrays

This section of the thesis describes the formation of novel tetrahedral multicomponent arrays through the self-assembly of a central bis(bipyridyl) transition metal complex linking four metalloporphyrins *via* axial coordination. Initially, the design and synthesis of the important building blocks of the tetrahedral array will be described. Following this, the probing of the self-assembly studies using ^1H NMR spectroscopy will be discussed. Revealed in these studies is the importance of having a properly matched ligand/metal pair, which plays a critical role in the stability of the core complex and, thus, the resulting porphyrin array. It is because of this component-matching that only one fully-assembled tetrahedral array can be isolated as an air-stable solid and characterized by ^1H NMR spectroscopy, UV/Vis spectroscopy, IR spectroscopy, ESI mass spectrometry, and ^{13}C NMR spectroscopy.

2.6.1 – Transition Metal Complex Design for Tetrahedral Templates

In order to extend the metal coordination strategy into the third dimension, the divergent central tetrapyrridyl copper(I) chelating ligand **dpybpy** (dpybpy = 4,4'-di(4''-pyridyl)-2,2'-bipyridine, **9**)¹⁸ was examined (Figure 12). All molecular models of the core complexes and arrays presented in this section were adapted from the crystal structure of the pyridyl adduct of tetraphenylporphyrin ruthenium(II) carbonyl and the bis(bipyridyl)copper(I) complexes. Both of these structures can be found in the Cambridge Structure Database and were used as is. As in the case of the terpyridyl

complexes described in last section of the thesis, the molecular models were created by simply connecting the metalloporphyrins' coordinated pyridine ligands to the pyridines of the bis(bipyridyl) transition metal complex in the appropriate *para*-positions. In the absence of crystal structures of the tetrahedral arrays, these molecular models provide a good representation of the overall topology of the tetrahedral arrays.

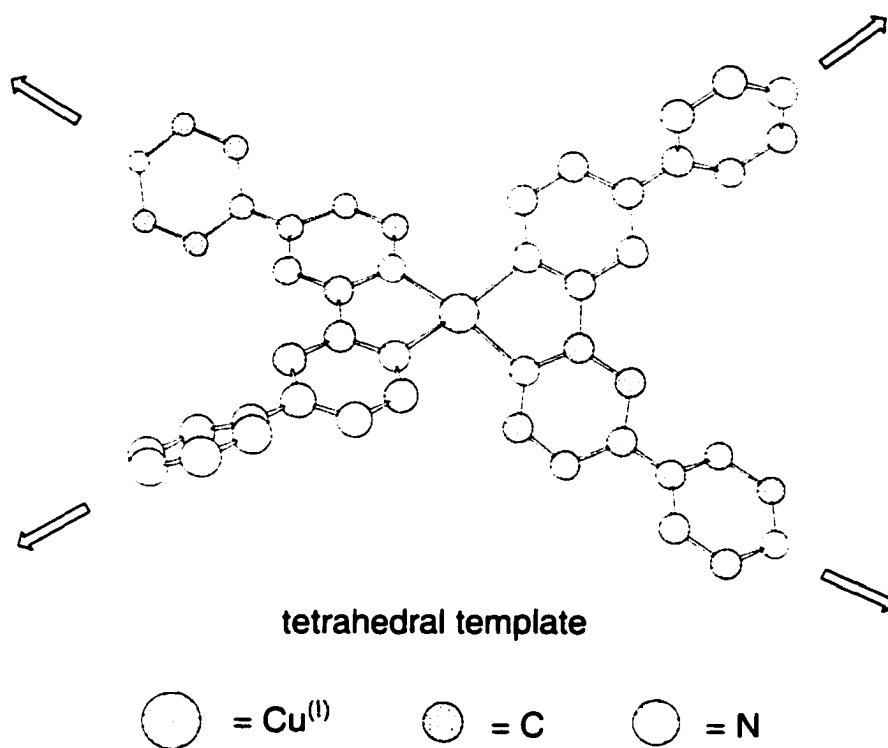


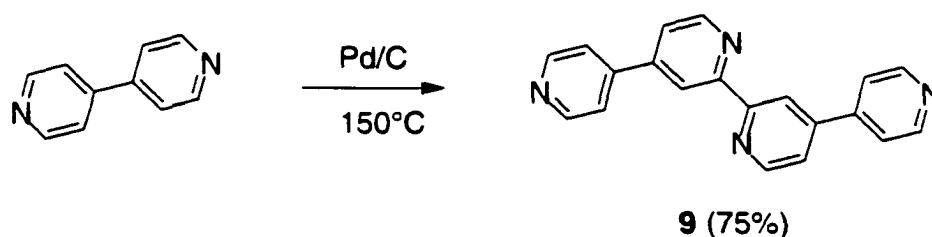
Figure 12. Design layout of the tetrahedral template highlighting the four divergent axial coordination sites provided by ligand **9** and Cu(I).

The central diimine nitrogens of the ligand **9** can chelate Cu(I) to position the terminal σ -donating nitrogens into an extended tetrahedral geometry that can axially coordinate to four units of Ru(TTP)(CO)(EtOH) (**4**) (Figure 12).

2.6.2 – Results and Discussion

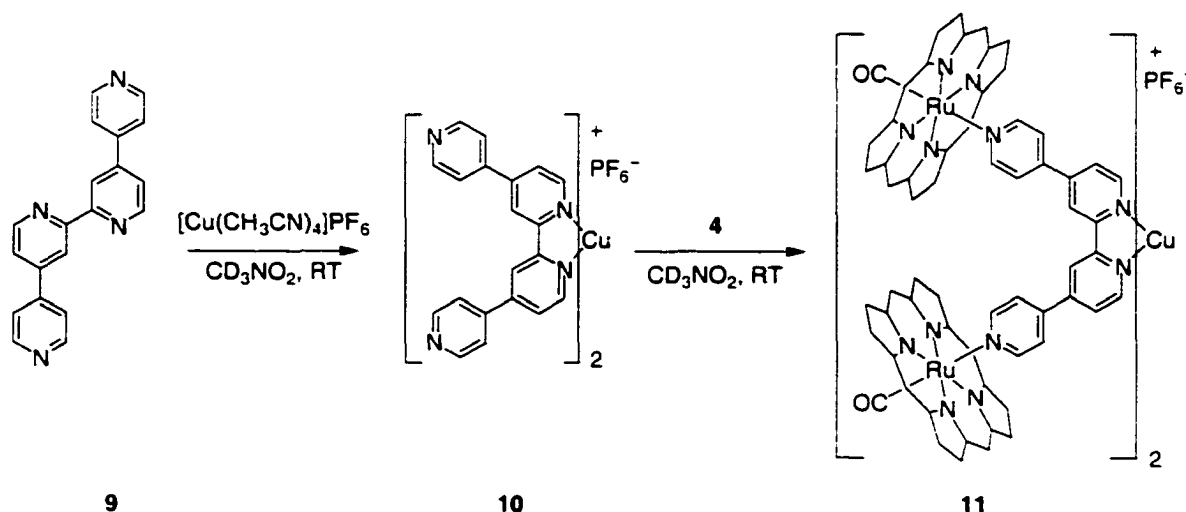
2.6.2.1 – Self-Assembly Synthesis of a Tetrahedral Porphyrin Array

Multigram quantities of the central **dpybpy** ligand (**9**) were conveniently prepared following a literature procedure in one step using a palladium catalyzed dehydrogenative coupling of 4,4'-bipyridine (Equation 3).¹⁸



Equation 3.

The tetrahedral core complex $[\text{Cu}(\mathbf{9})_2]\text{PF}_6$ (**10**) was generated *in situ* by reacting **9** with $[\text{Cu}(\text{CH}_3\text{CN})_4]\text{PF}_6$ in a 2:1 molar ratio in deuterated nitromethane at room temperature until the desired core complex was evident by ^1H NMR spectroscopy (Scheme 7).



Scheme 7. The porphyrins' tolyl substituents and double bond representations have been omitted for clarity.

It is especially attractive to use $[\text{Cu}(\text{CH}_3\text{CN})_4]\text{PF}_6$ as the source of the central transition metal because the metal-ligand bond is labile, eliminating extra synthetic steps to prepare the core complex. Because the core complex can be generated rapidly and with minimal side reactions, it can also be generated *in situ* and the self-assembly pathway can be monitored using ^1H NMR spectroscopy. With this in mind, ligand **9** must undergo a conformation change in order to bind Cu(I) and this change in conformation was monitored by comparing the initial positions of the resonances for the uncomplexed ligand with the ^1H NMR spectra generated *in situ*. However this was a difficult task because the spectra were complicated by the production of extremely broad resonances. The broad signals might be a resultant of three possibilities: 1) an oxidation of diamagnetic Cu(I) to paramagnetic Cu(II), 2) a ligand exchange process, or 3) polymer formation *via* the involvement of the divergent pyridines. Instead of isolating the tetrahedral core complex, the fully-assembled tetrahedral array **11** was immediately prepared by the addition of four equivalents of $\text{Ru}(\text{TTP})(\text{CO})(\text{EtOH})$ (**4**) directly to the NMR sample (Scheme 7). Signals that are diagnostic, although extremely broad, for axial coordination include the protons of the core unit which are significantly shielded as they lie directly over the porphyrin's anisotropic ring current. Another, and perhaps the most convenient, testament to successful axial coordination is the appearance of signals corresponding to the ethanol that is released from $\text{Ru}(\text{TTP})(\text{CO})(\text{EtOH})$ upon complexation. But in this case, complexes **10** and **11** could not be isolated even when rigorously anhydrous and anaerobic conditions were maintained. Use of anhydrous and anaerobic conditions should eliminate the amount of Cu(I) oxidized to Cu(II). This was

not the case, however, and the results suggest that the ligand was improperly designed to bind Cu(I). This ligand/metal pair mismatch is discussed in the next section.

2.6.2.2 – Stabilized Bipyridine Complexes of Copper(I)

All difficulties encountered in attempting to isolate the core fragment **10** and the tetrahedral array **11** can be attributed to improper metal/ligand pairing between Cu(I) and **dpybpy** which influences the complex's stability. It has been suggested that this metal/ligand pair will often result in Cu(I) complexes of low stability that are prone to oxidation of the metal ion.¹⁹ This instability is most likely due to the absence of bulky non-coordinating groups adjacent to the diimine nitrogen atoms on the ligand.¹⁹ In the absence of these substituents, the Cu(I) metal atom can be accessed by a Lewis base from an axial approach resulting in a distortion of the initial tetrahedral geometry to square pyramidal (Figure 13).

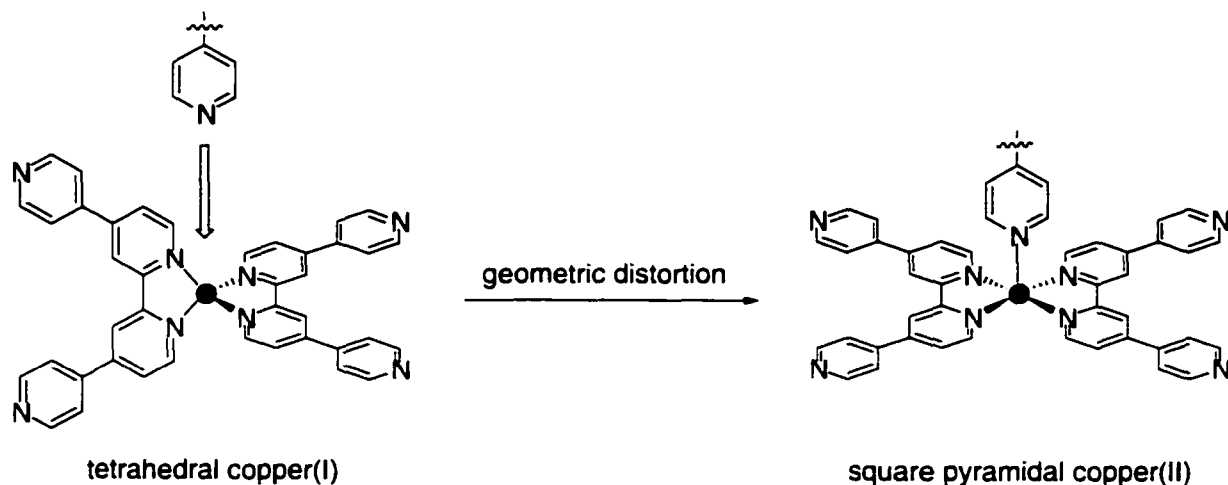


Figure 13. Schematic representation of the geometric distortion of copper(I) that promotes the oxidation of copper(I) to copper(II).

This distortion promotes the oxidation of the diamagnetic d^{10} Cu(I) to paramagnetic d^9 Cu(II) species. Considering the Lewis base strengths of all species in solution, the axial site was more than likely being accessed by the terminal pyridines of the ligand (DN \approx 33.1) and not the nitromethane solvent (DN \approx 2.7) molecules.⁶ In the presence of bulky non-coordinating groups in the 6,6'-positions on the bipyridine ligand, the axial site is blocked and the geometric distortion is prevented because severe inter-ligand repulsions occur which prevent this process (Figure 14).¹⁹

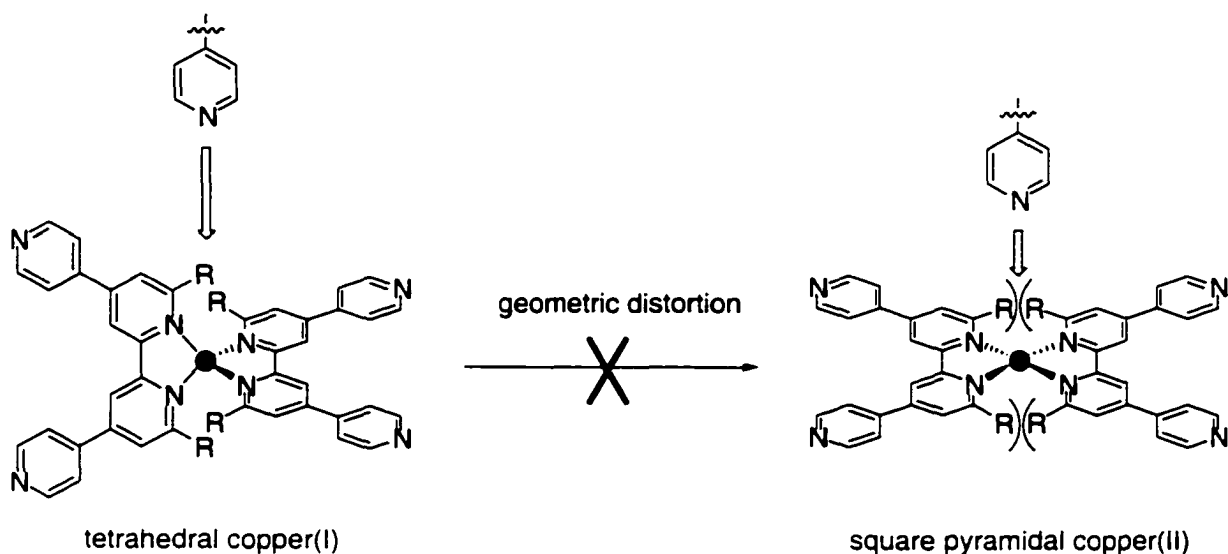
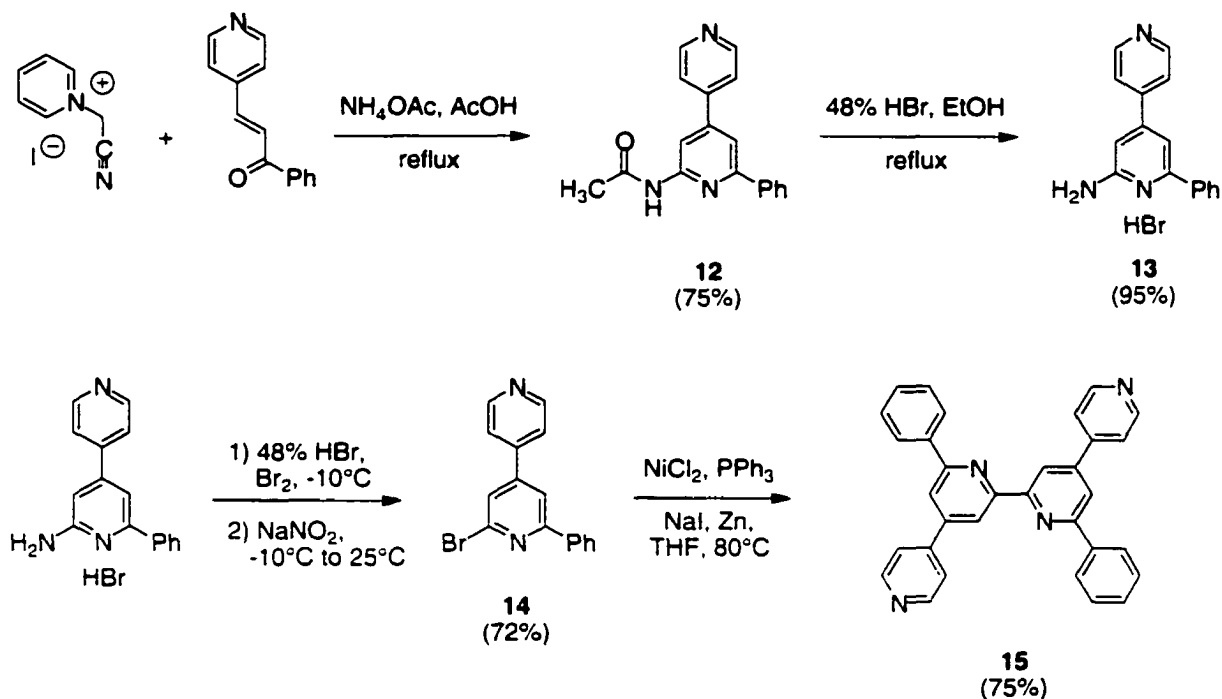


Figure 14. Schematic representation of preventing the solvent assisted oxidation of copper(I) to copper(II).

To overcome the ligand/metal pair mismatch described for the core complex **10**, the unknown bis(phenyl)bipyridine ligand **15** was synthesized (Scheme 8). Cyclocondensation of the known ketopyridine with 1-cyanomethylpyridinium iodide²⁰ using the protocol described by Kröhnke afforded gram quantities of the acetamidobipyridine **12**.¹¹ The acetamide was hydrolyzed with 48% hydrobromic acid

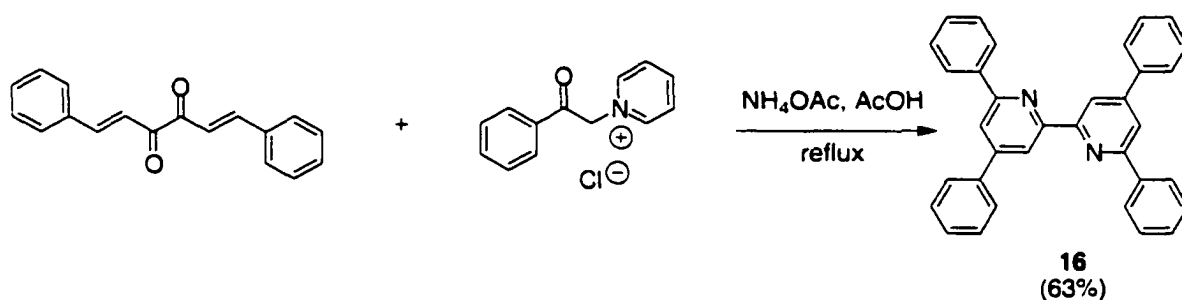
into the known amine salt **13**,¹¹ which was cleanly converted to bromide **14** using Sandmeyer conditions followed by nickel(II)-catalyzed coupling to yield the final tetrapyridine **15**.²¹



Scheme 8.

The *in situ* generation of the tetrahedral core complex $[\text{Cu}(\mathbf{15})_2]\text{PF}_6$ was monitored using ^1H NMR spectroscopy when ligand **15** was reacted with $[\text{Cu}(\text{CH}_3\text{CN})_4]\text{PF}_6$ in a 2:1 molar ratio in deuterated nitromethane. Surprisingly, instead of suggesting the clean conversion into the $\text{Cu}(\text{I})$ complex, the resulting spectrum consisted of broad signals. Also, the expected change in color from colorless to red-brown which is evidence for proper $\text{Cu}(\text{I})$ chelation, did not occur. Instead, the reaction produced a light green solution containing a green precipitate.

In order to determine the origin of these unexpected problems concerning the stability of the tetrahedral complex using this suitably substituted bipyridine, the known tetraphenylbipyridine **16** analog was synthesized (Equation 4).¹¹ By following the protocol described by Kröhnke, the conjugate addition of a pyridinium ylide to the bis- α,β -unsaturated carbonyl compound afforded gram quantities of the tetraphenylbipyridine **16**.



Equation 4.

When subjected to the same protocol as already described for the formation of the tetrahedral complex $[\text{Cu}(\mathbf{15})_2]\text{PF}_6$, ligand **16** readily reacted with $[\text{Cu}(\text{CH}_3\text{CN})_4]\text{PF}_6$ producing a red-brown solution which supports the formation of the tetrahedral Cu(I) complex $[\text{Cu}(\mathbf{16})_2]\text{PF}_6$. The higher stability of complex $[\text{Cu}(\mathbf{16})_2]\text{PF}_6$ provided single crystals suitable for X-ray analysis shown in Figure 15. The structure confirms the anticipated bis-ligand formulation of the Cu(I) complex. The structure also reveals that, in the solid state, the copper(I) complex adopts a distorted tetrahedral geometry (pseudotetrahedral). Each bipyridine ligand coordinates in a bidentate manner *via* the pyridines, but the dihedral angle between the planes defined by copper and each set of bipyridyl nitrogens is *ca.* 65° , and is far from being perpendicular.

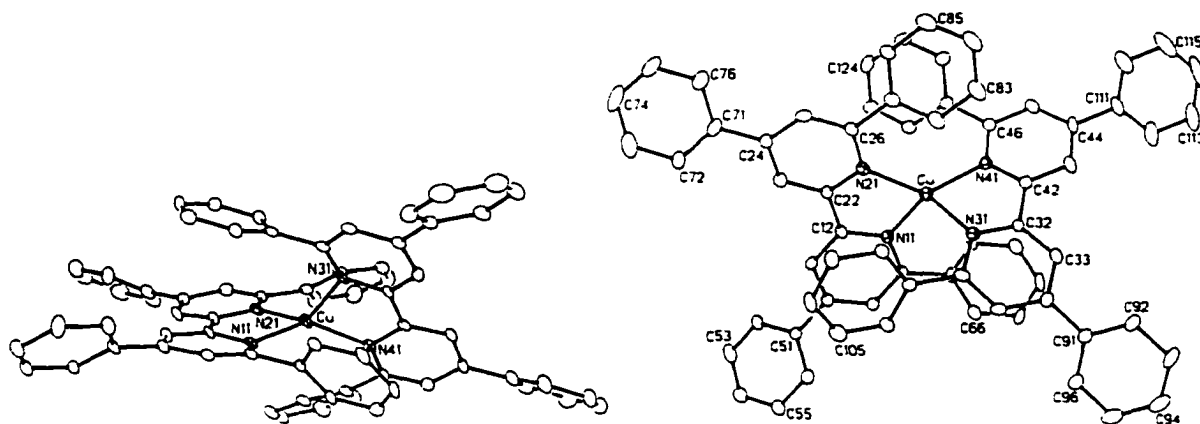


Figure 15. Molecular structure of $[\text{Cu}(\mathbf{16})_2]\text{PF}_6$ in the crystal. Non-hydrogen atoms are represented by Gaussian ellipsoids at the 20% probability level.

The distortion is partly due to how the bipyridine ligands impose small bite angles for the two N–Cu–N chelates of *ca.* 82° , which causes the other N–Cu–N angles to vary between 103° and 132° (Figure 16). These angles force a geometry around Cu(1) that is appreciably distorted from regular tetrahedral, at least in the solid state, and the distortion allows potential access to the metal center by incoming ligands.

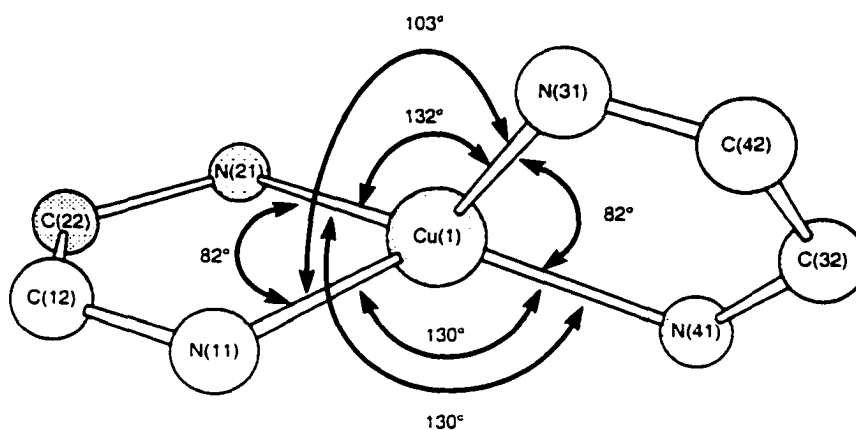
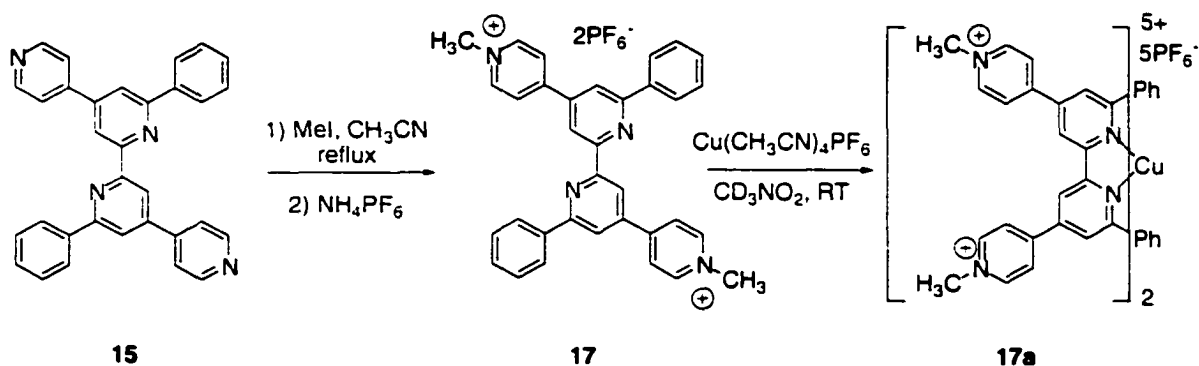


Figure 16. Selected bond angles of the distorted tetrahedral complex $[\text{Cu}(\mathbf{16})_2]\text{PF}_6$.

The pronounced distortion and greater stability of complex $[\text{Cu}(\mathbf{16})_2]\text{PF}_6$ also stems from multiple intramolecular face-to-face aryl interactions between aryl-aryl and aryl-pyridyl rings. These interactions compress the dihedral angle but also prevent Cu(I) oxidation by blocking the axial approach, and to a greater extent, prevent further distortion of the complex. In light of this, the problems encountered with ligand **15** suggest that the terminal pyridines on the ligand were initially coordinating to $[\text{Cu}(\text{CH}_3\text{CN})_4]\text{PF}_6$ before the diimine portion could properly form the stable chelated copper(I) complex. In order to support this observation, the unknown protected bis(methyl)-bipyridinium **17** was synthesized and isolated as the hexafluorophosphate salt (Scheme 9). The methylated ligand effectively removes the terminal pyridine fragments from coordinating to copper(I). The protected ligand readily reacted with $[\text{Cu}(\text{CH}_3\text{CN})_4]\text{PF}_6$ in deuterated nitromethane to form the stable $[\text{Cu}(\mathbf{17})_2](\text{PF}_6)_5$ complex (Figure 17).



Scheme 9.

The higher stability of the Cu(I) complex of ligand **17** is highlighted using ^1H NMR spectroscopy by the immediate formation of the desired pseudotetrahedral complex

when only 0.25 molar equivalents of $[\text{Cu}(\text{CH}_3\text{CN})_4]\text{PF}_6$ was added (Figure 17). After the addition, the signals are sharp, unchanging, and the only product that is formed is the bis-coordinated Cu(I) complex. The chemical shifts of the signals for complexed and uncomplexed ligand are easily distinguished which account for fourteen aromatic resonances in the spectrum. Also revealed are the face-to-face π -stacking interactions in the spectrum. Also revealed are the face-to-face π -stacking interactions centred on the phenyl rings as these signals are shifted 0.5 ppm upfield.

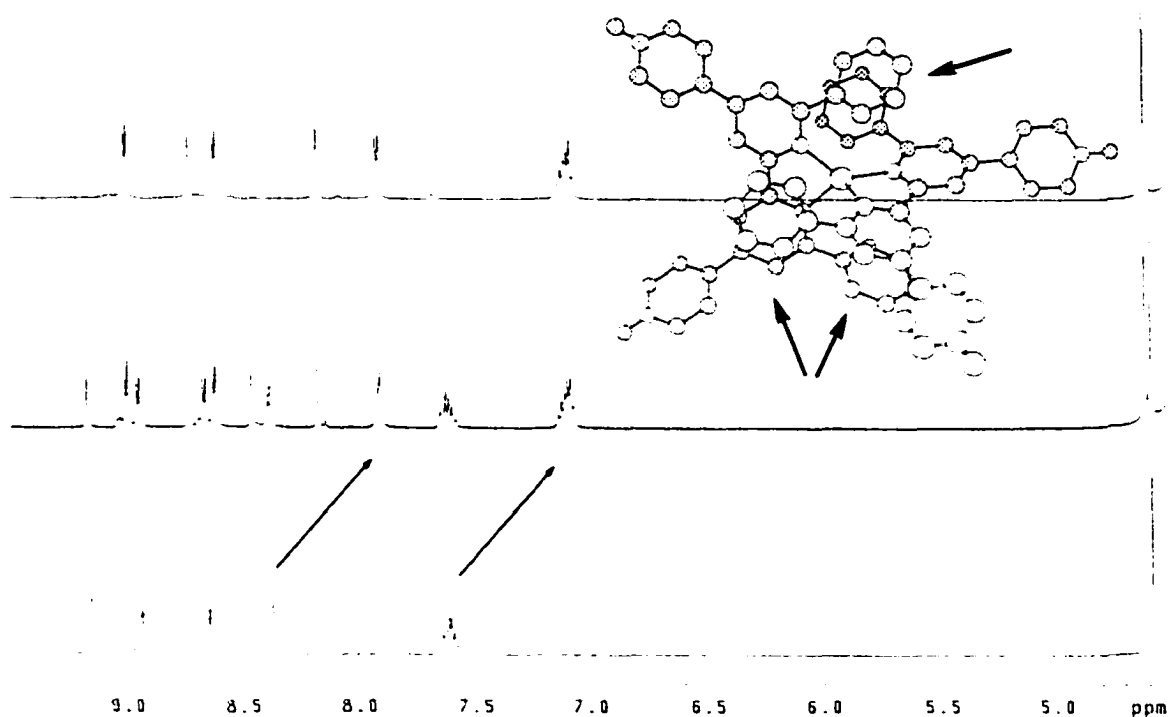
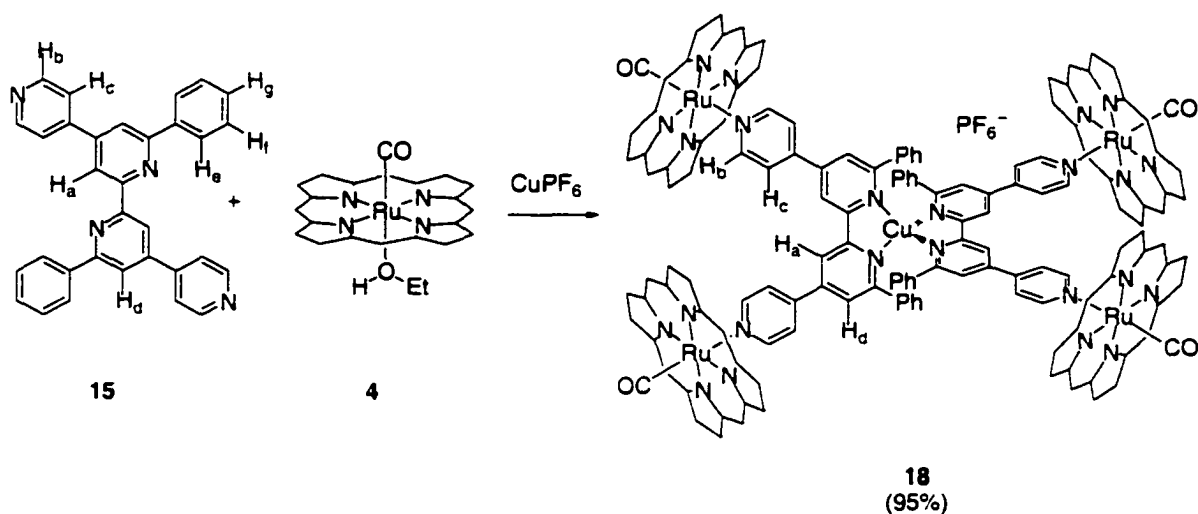


Figure 17. ^1H NMR (500 MHz, $[\text{D}_6]$ nitromethane) spectra of **17** (bottom trace), **17** + 0.25 molar equivalents $[\text{Cu}(\text{CH}_3\text{CN})_4]\text{PF}_6$ (middle trace), and **17** + 0.5 molar equivalents $[\text{Cu}(\text{CH}_3\text{CN})_4]\text{PF}_6$ (top trace) at room temperature. A molecular model highlights the important face-to-face π -stacking interactions of ligand **17** and which are labeled with arrows (inset).

Having a better understanding of the coordination algorithm of ligand **15**, the final tetrahedral array **18** could be formed and isolated as a purple air-stable solid following a

one-pot protocol. The previous observations suggested that the terminal pyridines were involved in the coordination algorithm of ligand **15** and to copper(I). Therefore, pre-assembling the ruthenium porphyrin units onto the terminal pyridine nitrogens prior to assembling the final array will effectively protect these nitrogens and prevent their coordination to copper. Thus, treatment of **15** with two molar equivalents of Ru(TTP)(CO)(EtOH) (**4**) followed by 0.5 molar equivalents of [Cu(CH₃CN)₄]PF₆ immediately formed assembly **18** in greater than 95% yield (Scheme 10 and Figure 18). The synthesis of the copper(I) pseudotetrahedral array also exemplifies the power of self-assembly synthesis to limit additional synthetic steps and rapidly form products in high yields. The addition of pentane to a concentrated dichloromethane solution containing **18** precipitated the fully assembled array.



Scheme 10. The porphyrins' tolyl substituents and double bond representations have been omitted for clarity. CuPF₆ is used as an abbreviation for the copper(I) source [Cu(CH₃CN)₄]PF₆.

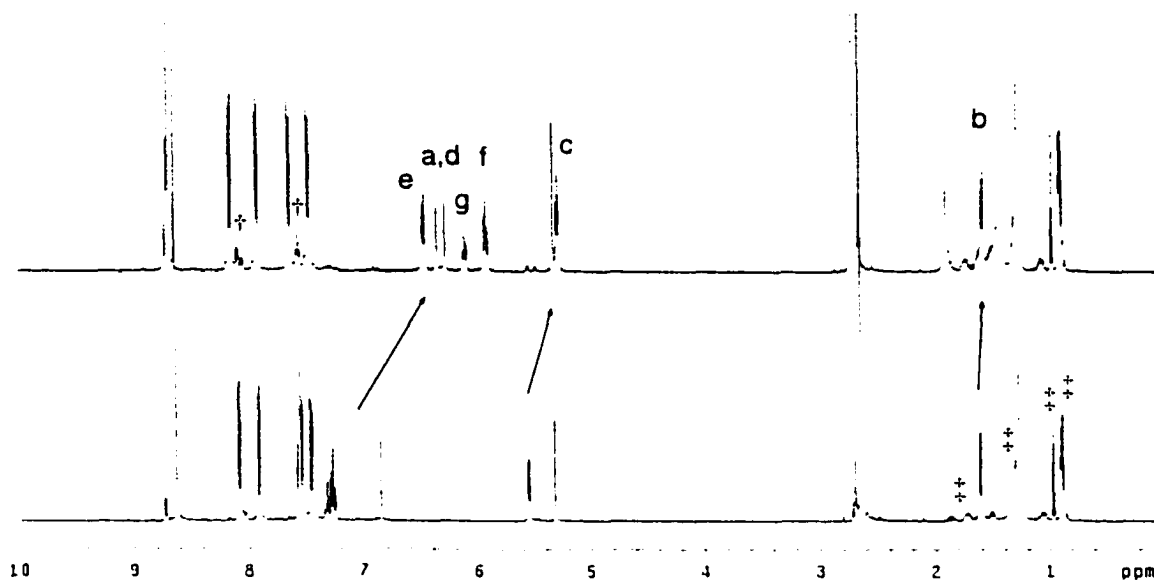
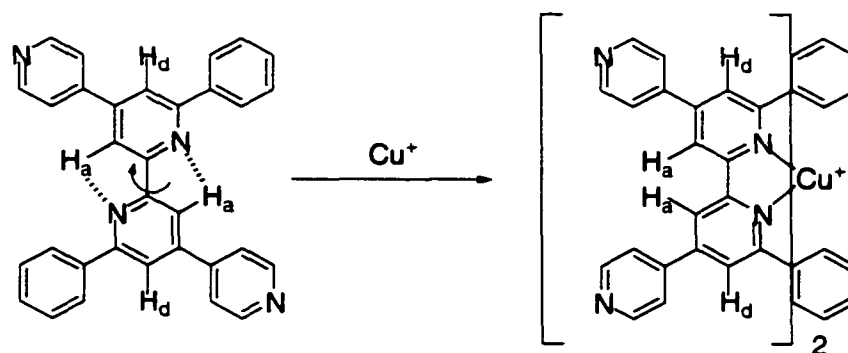


Figure 18. ^1H NMR (400 MHz, CD_2Cl_2) spectra of **15** + 2 molar equivalents $\text{Ru}(\text{TTP})(\text{CO})(\text{EtOH})$ (**4**) (bottom trace), and after the addition of 0.5 molar equivalent $[\text{Cu}(\text{CH}_3\text{CN})_4]\text{PF}_6$ (top trace) at room temperature. Peak assignments correspond to the atom labels in Scheme 10. The symbol † refers to free $\text{Ru}(\text{TTP})(\text{CO})(\text{EtOH})$ and the symbol ‡ refers to residual pentane in the sample.

The copper(I) binding event results in the shifting of the resonances due to the central core complex (protons H_a , H_d , H_e , H_f , and H_g in Scheme 10) into a visible region of the spectrum that are well separated from neighboring signals. Their final chemical shifts result from a combination of three effects: 1) the bond rotation around the central 2,2'-bipyridine and, thus, the breaking of two $\text{C}-\text{H}\cdots\text{N}$ hydrogen bonds between the 3,3'-hydrogens and the imine nitrogens (Equation 5), 2) the additive effect of the anisotropic ring currents of the four metalloporphyrins that point towards the core of the complex (Figure 19), and 3) the introduction of multiple face-to-face π -stacking effects between the flanking aromatic rings. The combination of these three effects results in shifting all of the signals for the core complex upfield from their original chemical shifts.



Equation 5. The bond rotation that forms the chelate pocket.

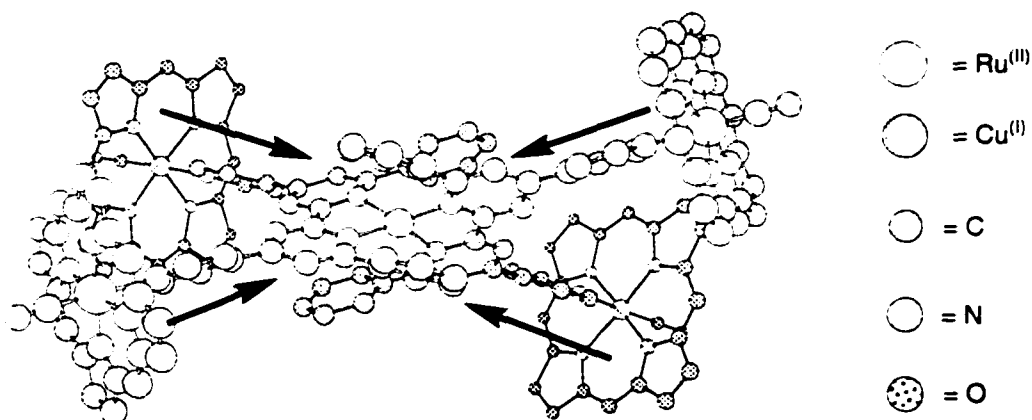
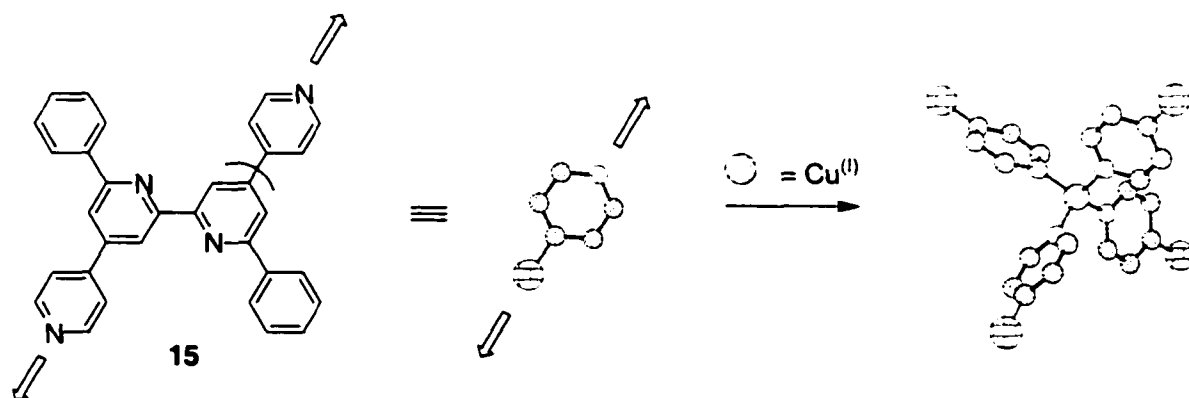


Figure 19. The additive anisotropic ring currents directed into the core tetrahedral template. The porphyrins' tolyl substituents have been omitted for clarity.

Interestingly, the air-stable copper complex $[\text{Cu}(\mathbf{15})_2](\text{PF}_6)$ can be isolated and characterized further as the porphyrin caps are cleaved from the core fragment by adding four molar equivalents of a Lewis basic solvent such as pyridine. This observation lends support to the argument that the inability to prepare the core unit directly is due to the terminal monodentate nitrogen atoms.

In light of the copper(I) metal binding studies, the inability to directly prepare the core unit $[\text{Cu}(\mathbf{9})_2]^+$ and $[\text{Cu}(\mathbf{15})_2]^+$ can be attributed to competitive binding events between the monodentate and the chelating nitrogen atoms of these ligands. It is also

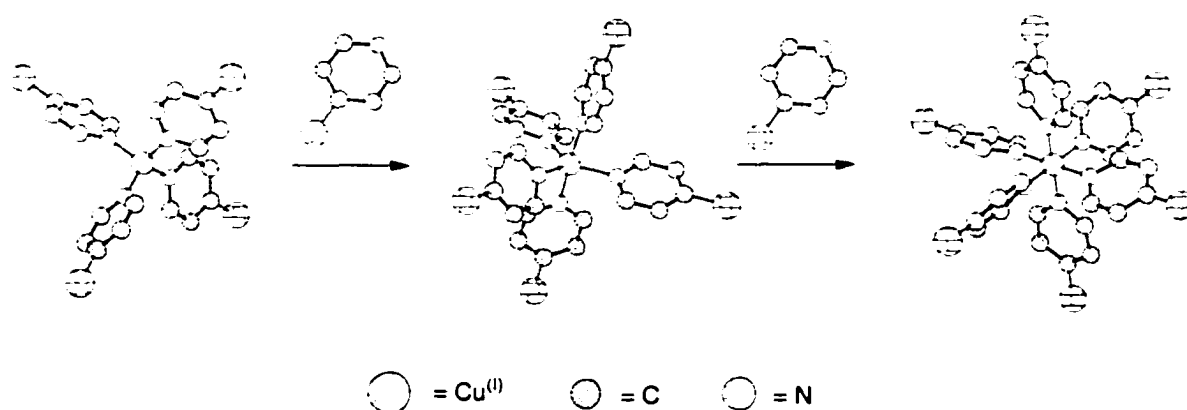
well known that phenanthrolines derivatives have a higher tendency than bipyridine ligands towards forming chelate complexes with copper(I).¹⁹ The lower affinities in the case of bipyridine ligands are a result of the additional bond rotation around the 2,2'-bond required for these ligands to form the proper chelate pocket. Coordination to the divergent monodentate pyridines, before the 2,2'-bond rotation, can result in forming polymeric species $[\text{Cu}_n(\mathbf{9})_n]^{n+}$ and $[\text{Cu}_n(\mathbf{15})_n]^{n+}$ which effectively remove copper from the binding algorithm (Scheme 11).



Scheme 11. The unproductive binding algorithm of ligand **15**. Only one of the terminal pyridines of ligand **15** is represented in the molecular model. The brick-walled atom type refers to the rest of ligand **15**.

Alternatively, the formation of tetrakis-, pentakis-, or hexakis-coordination compounds will result in the direct oxidation of copper(I) to copper(II) (Scheme 12). The reasoning follows that if tetrakis-coordination compounds were formed first through the monodentate pyridines, the metal atom would not be protected against subsequent ligand attacks. The additional attacking ligands can distort the complex and promote the oxidation of d^{10} copper(I) to d^9 copper(II). The presence of these competitive reactions

reduces the amount of the desired chelated copper(I) compound formed. The addition of phenyl appendages does, in fact, greatly enhance the stability of the copper(I) complexes as the coordination compounds based on ligands **16** and **17**, which lack the monodentate Lewis-basic sites, are rapidly formed. For these two ligands, the phenyl rings fully enclose the metal and prevent an axial approach by coordinating solvent molecules which invoke the distortion from tetrahedral to square pyramidal resulting in a solvent-assisted oxidation of copper(I) to copper(II).



Scheme 12. The unproductive binding algorithm of ligand **15**. Only one of the terminal pyridines of ligand **15** is represented in the molecular model. The brick-walled atoms refer to the rest of ligand **15**.

2.6.2.3 – Characterization Using ESI Mass Spectrometry

The tetrahedral array **18** was also characterized by electrospray mass spectrometry (ESI-MS) using a CH₂Cl₂/nitromethane solvent mixture (Figure 20). The peak for the parent cation at $m/z = 4180 [M - PF_6]^-$ was seen along with peaks corresponding to consecutive loss of porphyrin units ($m/z = 3383, 2584, \text{ and } 1789$). The isotopic abundance of each peak displayed the typical 1.0 peak separation of singly charged species.

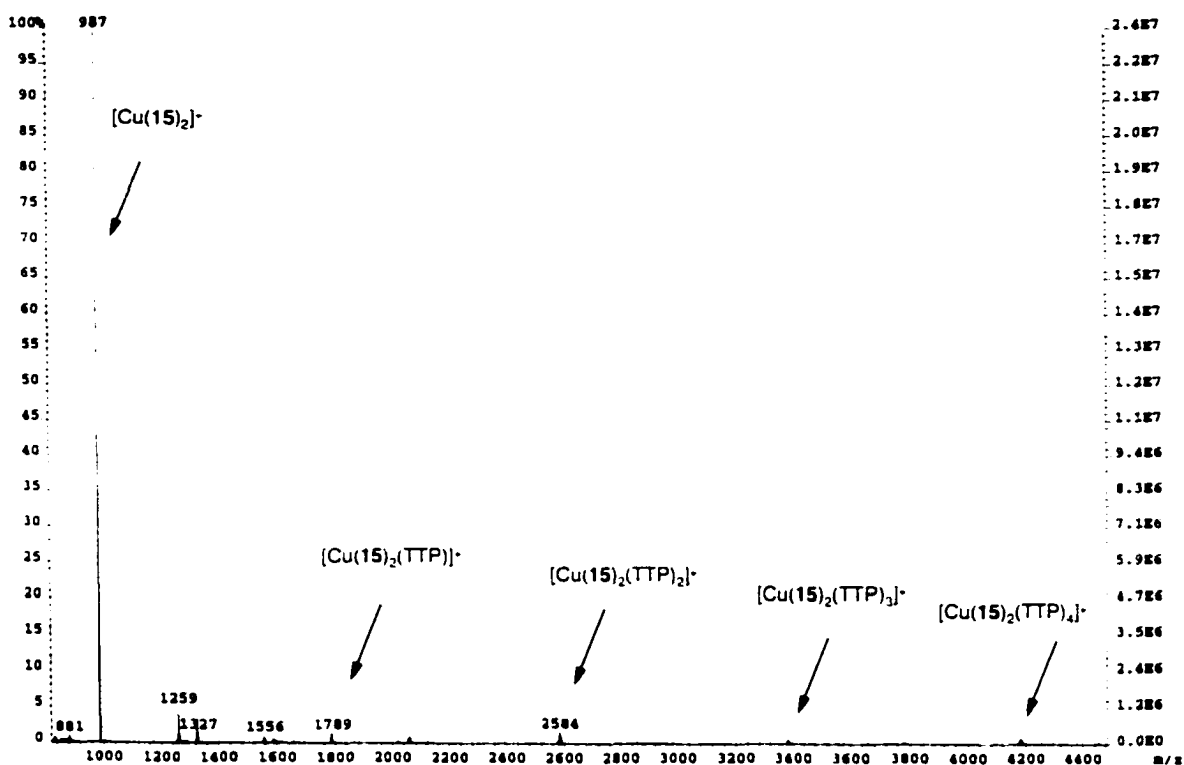


Figure 20. ESI mass spectrum of $[\text{Cu}(\mathbf{15})_2(\text{TTP})_4]^+$ in $\text{CH}_2\text{Cl}_2/\text{nitromethane}$.

2.6.2.4 – Characterization Using IR Spectroscopy

The pseudotetrahedral array **18** was also characterized in the solid state using IR spectroscopy. Recall that when pyridine coordinates to $\text{Ru}(\text{TTP})(\text{CO})(\text{EtOH})$ the ν_{CO} shifted from 1946 cm^{-1} to 1933 cm^{-1} . In the case of the tetrahedral array **18** the ν_{CO} shifted to 1950 cm^{-1} . Since the ν_{CO} increases in frequency, this suggests that the terminal pyridines on the core complex $[\text{Cu}(\mathbf{15})_2](\text{PF}_6)$ reduce the amount of electron density back-bonded to CO when they coordinate to the ruthenium(II) metal in $\text{Ru}(\text{TTP})(\text{CO})$.

2.6.2.5 – Characterization Using UV/Vis Spectroscopy

Initial photophysical studies show that the absorption spectra in the UV/Vis region of assembly **18** are essentially the same as the pyridyl adduct **5** (only **18** and

Ru(TTP)(CO)(py) (**5**) are shown in Figure 21). In order to compare the absorption spectra of the array and the arrays' constituents, the UV/Vis spectrum of the core complex is required. A complete comparison of the arrays' constituents was not made because an appropriate method to readily isolate the core complex of assembly **18** was not fully investigated. These results seem to indicate that there is an absence of strong coupling between the different units of the structure and the chromophores behave independently.

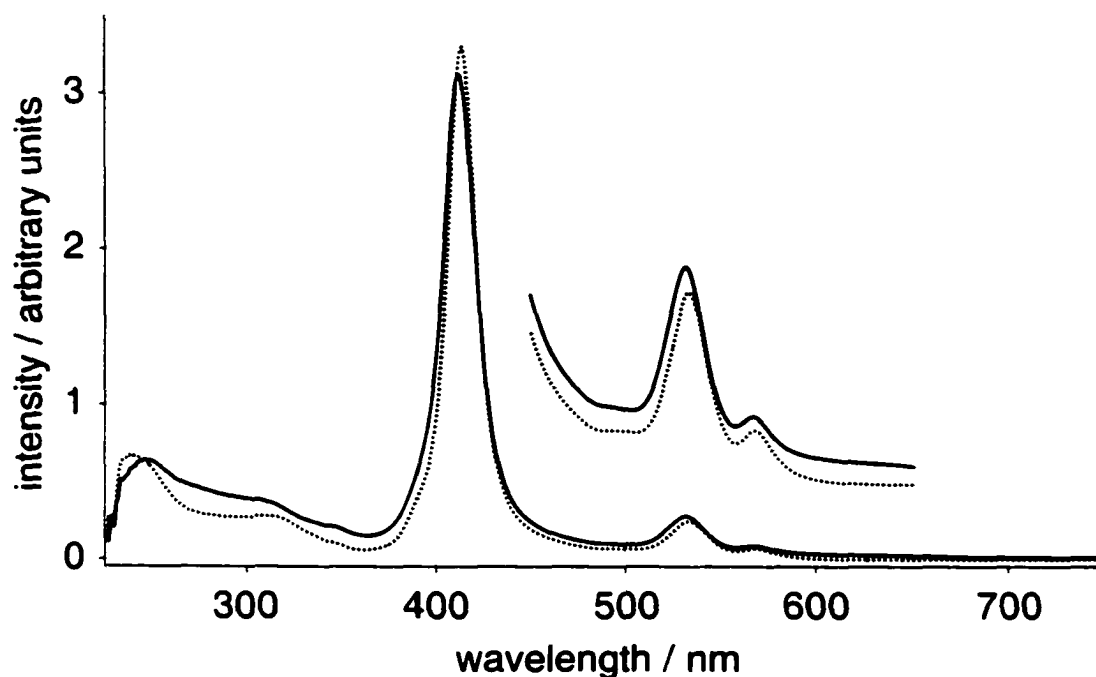


Figure 21. Overlay of absorption spectra of the pseudotetrahedral array **18** (solid line) and Ru(TTP)(CO)(py) (**5**) (dotted line) in dry deoxygenated dichloromethane. Both spectra are normalized to have the same porphyrin concentration of 1.45×10^{-5} M.

2.7 –Octahedral Axially Coordinated Metalloporphyrin Arrays

This section of the thesis describes the formation of novel octahedral metalloporphyrin arrays originally used to model the metal-directed templated synthesis of a porphyrin cube. The octahedral arrays are formed around two different central tris(bipyridyl) transition metal complexes of iron(II) and ruthenium(II) linking six metalloporphyrins *via* axial coordination. Initially, the design and synthesis of the important building blocks of the arrays will be described. After this description, the self-assembly studies, probed using ^1H NMR spectroscopy, will be discussed. Highlighted in this discussion is how the iron(II) arrays are constructed from their constituent parts in a one-pot procedure which follows a metal-directed self-assembly template synthesis. Included in this discussion is a comparison of the rates of octahedral array formation that incorporate the tris(bipyridyl)ruthenium(II) core complex using two different ruthenium(II) carbonyl metalloporphyrins. Also included in this section, are the initial photophysical properties of two different tris(bipyridyl)ruthenium(II) octahedral arrays. The results suggest that energy transfer may occur between the arrays' components because, after excitation, emission from the two octahedral arrays is detected. These arrays behave quite differently from their linear array counterparts. The fully assembled octahedral arrays are isolated as air-stable solids and characterized by ^1H NMR spectroscopy, UV/Vis spectroscopy, IR spectroscopy, ESI mass spectrometry, and ^{13}C NMR spectroscopy.

2.7.1 – Transition Metal Complex Design for Octahedral Templates

A ligand displaying multiple, divergent Lewis basic sites that provides a means to extend the metal coordination self-assembly strategy to the third dimension is the already described tetrapyridyl ligand (4,4'-di(4''-pyridyl)-2,2'-bipyridine, **9**)¹⁸ (Figure 22). This ligand was not suited to form stable tetrahedral copper complexes as explained in the previous section, but is well suited to generate stable iron(II) and ruthenium(II) octahedral complexes. The resulting tris(bipyridyl) octahedral template positions six Lewis basic lone pair vectors as extensions of the central metal-ligand complex's geometry and can axially coordinate to six metalloporphyrins.

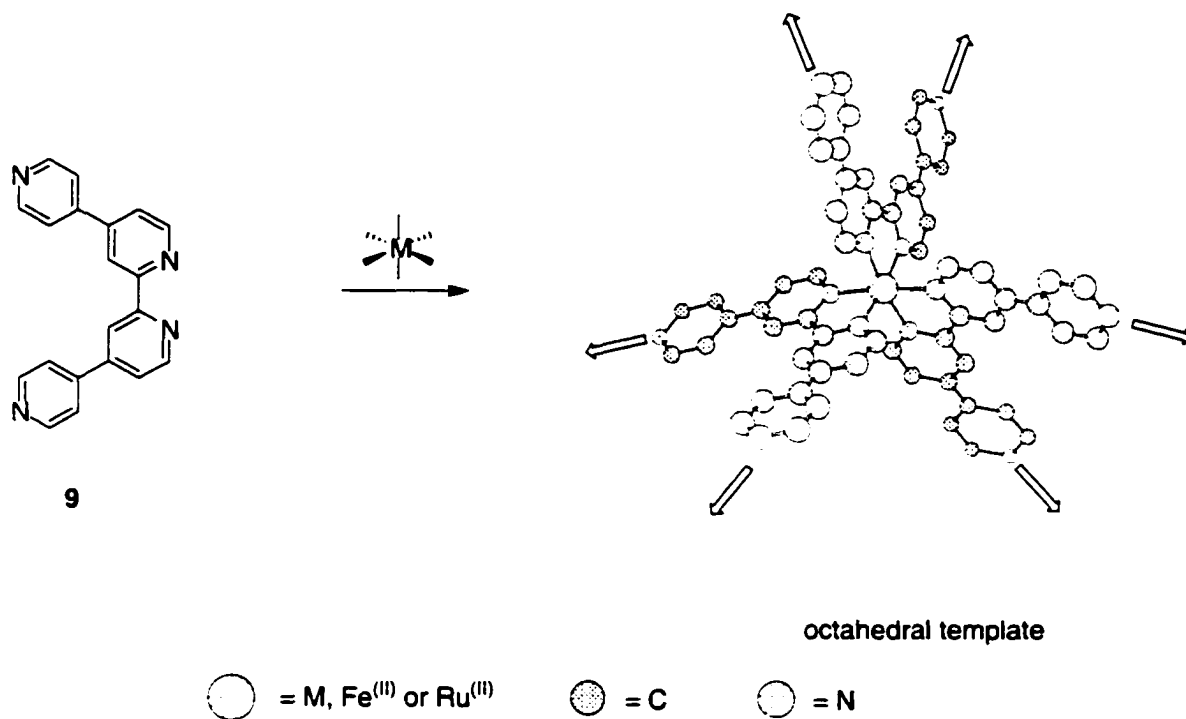


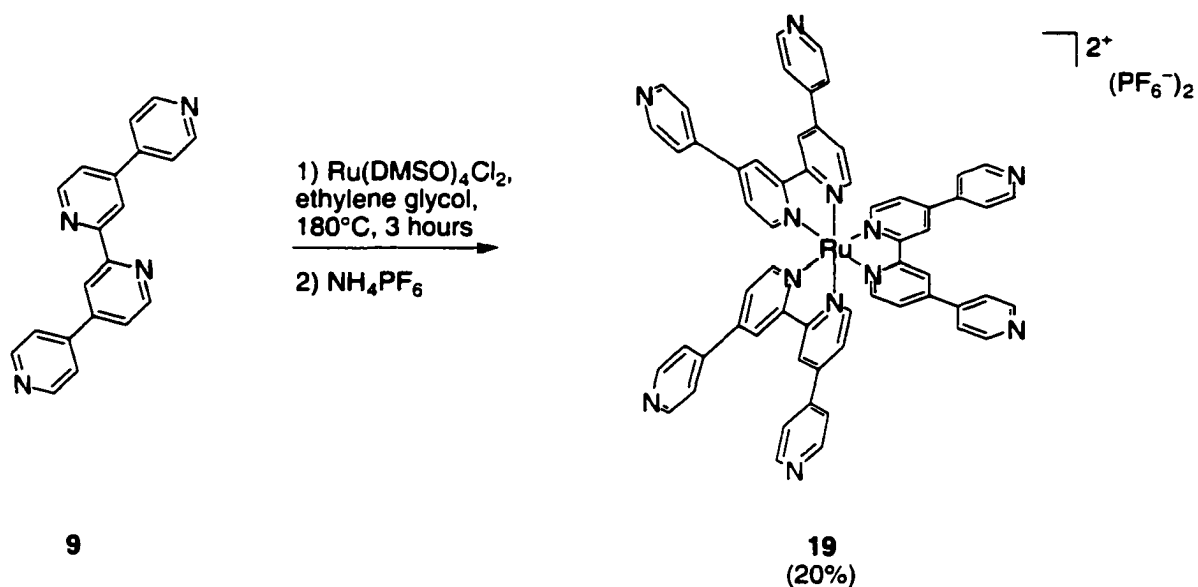
Figure 22. Design layout of the octahedral template.

All molecular models of the core complexes and arrays presented in this section were adapted from the crystal structure of the pyridyl adduct of tetraphenylporphyrin ruthenium(II) carbonyl and the tris(bipyridyl) octahedral complexes. Both of these structures can be found in the Cambridge Structure Database and were used as is. As in the case of the bipyridyl and terpyridyl complexes described in the previous sections of this thesis, the molecular models were created by simply connecting the metalloporphyrins' coordinated pyridine ligands to the pyridines of the tris(bipyridyl) transition metal complex in the appropriate *para*-positions. In the absence of crystal structures of the octahedral arrays, these molecular models provide a good representation of the overall topology of the octahedral arrays.

2.7.2 – Results and Discussion

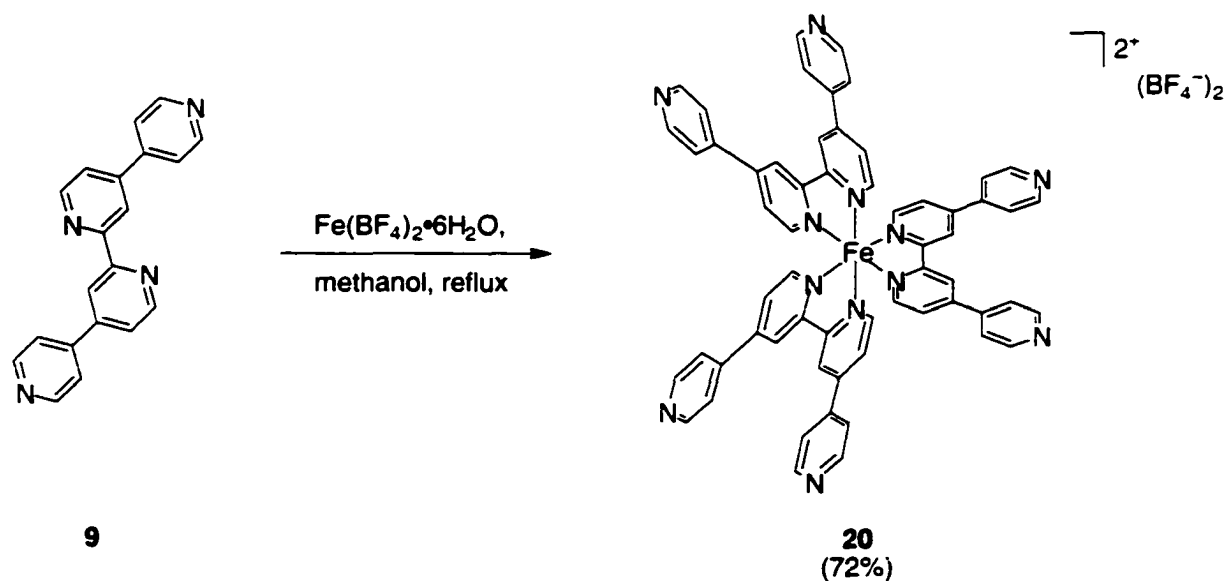
2.7.2.1 – Synthesis of the Transition Metal Core Complexes

The known octahedral ruthenium core unit **19** was prepared by heating $\text{Ru}(\text{DMSO})_4\text{Cl}_2$ or $\text{RuCl}_3 \cdot x\text{H}_2\text{O}$ with three molar equivalents of **9** and was isolated as its hexafluorophosphate salt (Scheme 13).²² The chloride counterions were exchanged by pouring the ethylene glycol solution into water and then adding a methanolic solution containing ammonium hexafluorophosphate, which precipitates the crude product which was collected by filtration. The complex was purified using column chromatography through silica gel eluting with a mixture of water-acetonitrile-saturated potassium nitrate (7:1:2) affording an orange solid.



Scheme 13.

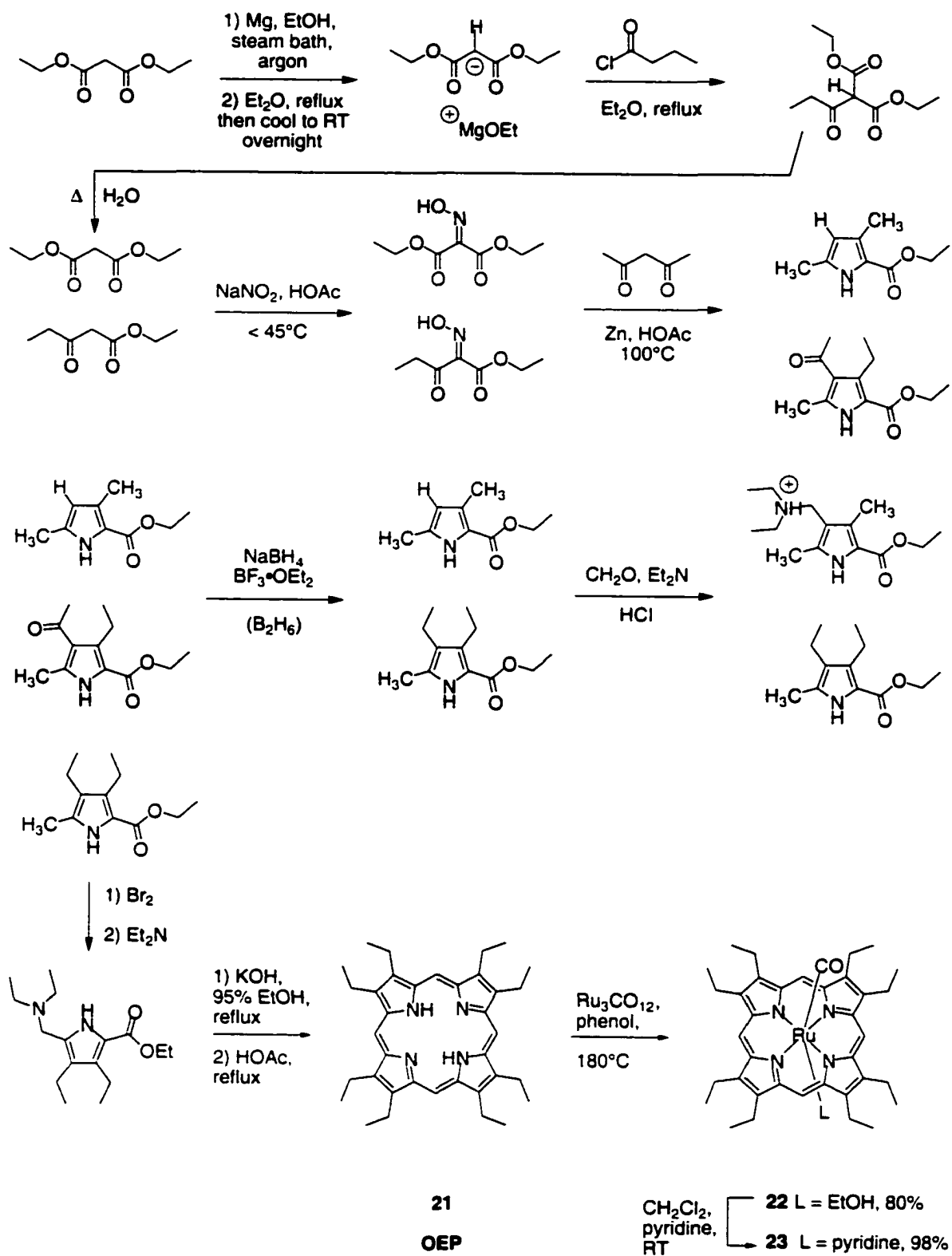
The known iron(II) core complex **20** was prepared in one step by adding $\text{Fe}(\text{BF}_4)_2 \cdot 6\text{H}_2\text{O}$ to three molar equivalents of ligand **9** in methanol at reflux (Equation 6).¹⁸ Again, the lability of iron(II) tetrafluoroborate produces a diagnostic and immediate change in color from colorless to red signifying the formation of the desired core complex.



Equation 6.

2.7.2.2 – Synthesis of Another Metalloporphyrin

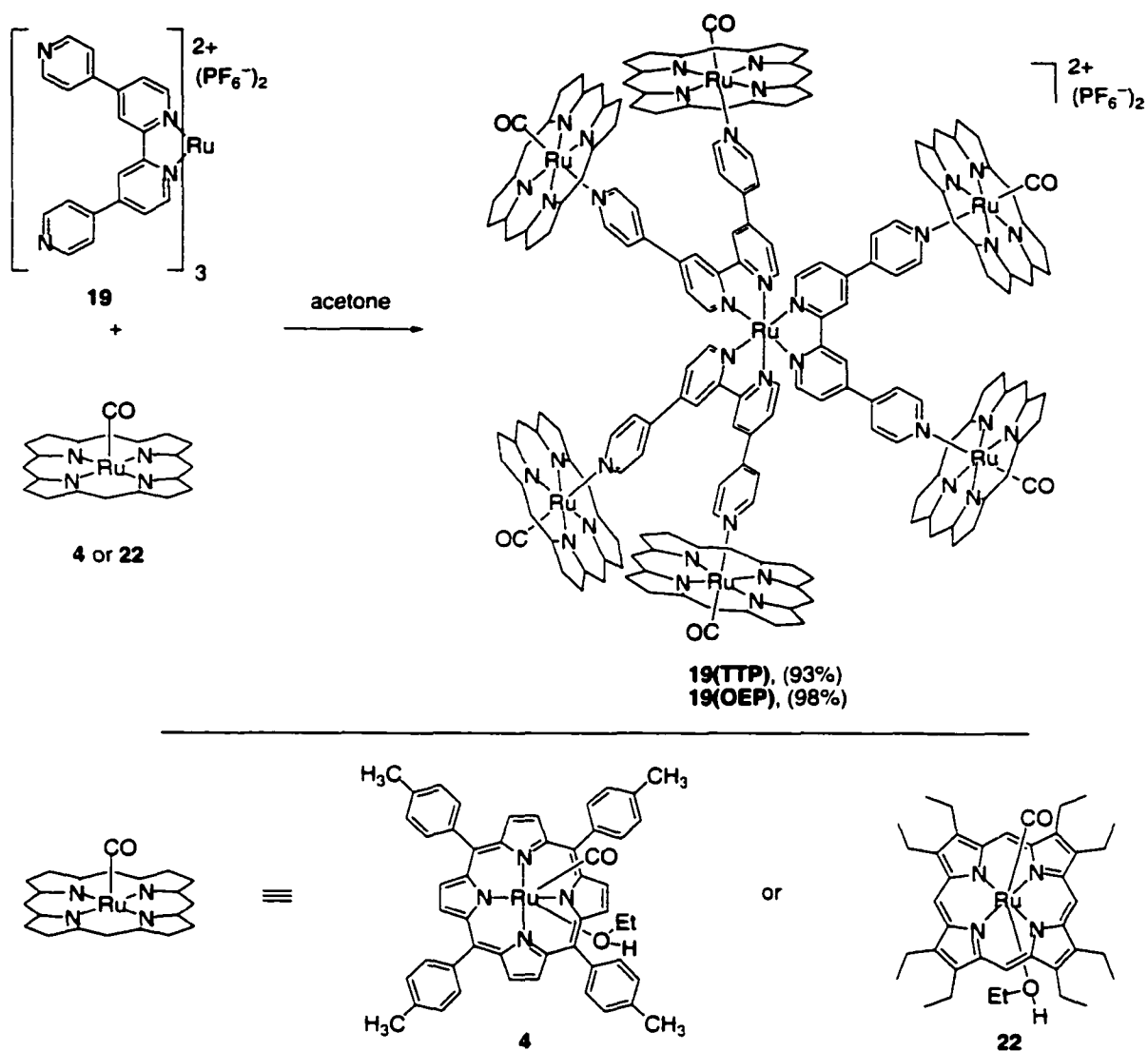
In order to provide insight into the nature of the self-assembly process and how the size of the building blocks affect the process, the smaller octaethylporphyrin (**21**) was prepared according to known methods described by Dolphin (Scheme 14).²³ Following this procedure, diethylmalonate was first converted into the ethoxymagnesium salt and then reacted with propionyl chloride, all in the same reaction vessel, to give diethylpropionyl malonate. This crude product was subject to steam distillation, which produces a mixture of the desired ethylpropionylacetate and diethylmalonate in a ratio of 80:20. This mixture was then converted, in the same pot, into the corresponding oximes and reacted with 2,4-pentanedione following the standard Knorr procedure to produce a mixture of pyrroles.²⁴ The desired acetylpyrrole was isolated as a mixture of two pyrroles and reduced with diborane. The unreactive dimethylpyrrole was removed during work-up as it was converted and extracted into water as the Mannich base. The diethylpyrrole was then treated with bromine followed by diethylamine to give the pyrrolylmethylamine. This heterocycle was finally converted into its potassium salt and then treated *in situ* with an excess of acetic acid at reflux with a stream of air to give octaethylporphyrin (**21**). The known metalloporphyrin Ru(OEP)(CO)(EtOH) (OEP = 2,3,7,8,12,13,17,18-octaethylporphyrinato dianion, **22**)²⁵ was prepared using a modified procedure of an earlier report by heating three molar equivalents of Ru₃CO₁₂ with one molar equivalent of **21** in phenol at reflux (Scheme 14).



Chromatographic purification was carried out through basic alumina (activity II-III) by sequentially changing the eluting solvents from dichloromethane to dichloromethane /ethanol (up to 95:5) which afforded the metalloporphyrin ethanol adduct. The labile ethanol ligand was replaced by adding pyridine to a dichloromethane solution containing Ru(OEP)(CO)(EtOH). Removal of the solvent and recrystallization from hexane afforded the known pyridine adduct Ru(OEP)(CO)(py) (**23**) in nearly quantitative yield.^{26a} When pyridine was coordinated to Ru(OEP)(CO)(EtOH), the ν_{CO} shifted from 1936 cm^{-1} to 1934 cm^{-1} .²⁶ Since the ν_{CO} remains relatively the same, this suggests that the pyridine removes approximately the same amount of electron density that it adds when it coordinates to the ruthenium(II) metal in Ru(OEP)(CO).

2.7.2.3 –Synthesis of the Ruthenium(II) Octahedral Arrays

Arrays **19(TTP)** and **19(OEP)** were synthesized by treating the core template **19** with six equivalents of Ru(TTP)(CO)(EtOH) (**TTP = 4**) and Ru(OEP)(CO)(EtOH) (**OEP = 22**), respectively, in acetone with gentle heating (Scheme 15). Arrays **19(TTP)** and **19(OEP)** were isolated as air-stable red solids in greater than 90% yields by adding pentane to concentrated dichloromethane solutions, which precipitated the fully assembled arrays.



Scheme 15. The porphyrins' substituents and double bond representations have been omitted for clarity.

Both arrays exhibit significant upfield shifts of the signals in their ^1H NMR spectra corresponding to the protons on the core unit which are completely surrounded by the shielding cones of as many as six porphyrin building blocks (Figure 23). The most significant shift corresponds to the protons directly adjacent to the axially directed nitrogen atoms ($\Delta\delta$ as much as 8.1 ppm upfield) as it is these hydrogen atoms that are

buried deepest within each porphyrin's shielding cone and experience the greatest anisotropic effect.²⁷

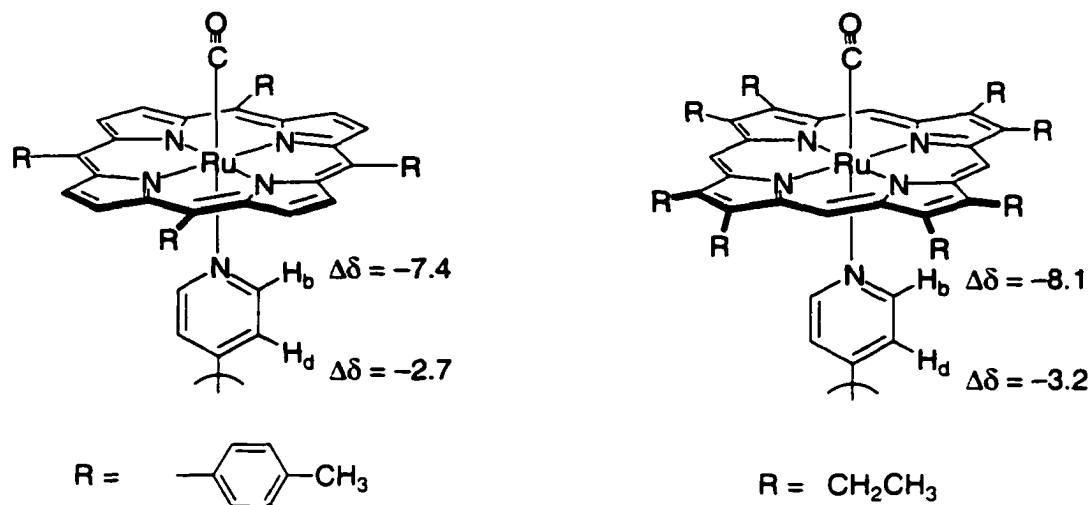


Figure 23. Characteristic upfield shifts for pyridyl protons labeled 'b' and 'd' from this thesis work.²⁷

There is also an apparent difference in the additive effects of the two different metalloporphyrins' anisotropic ring currents on the octahedral core with greater upfield shifts observed for **19(OEP)** than for **19(TTP)** (protons labeled 'b' and 'd' in Figure 23). This phenomenon can be attributed to the differences in the electron density located on the porphyrin ring and, hence, on the metal.¹ X-ray structure determinations of *meso*-phenyl substituted metalloporphyrins have generally shown that the phenyl rings adopt 90° angles to the porphyrin plane.^{2b} In solution, the aromatic *meso*-substituents are rotationally restricted and electron density is removed away from the metal and the porphyrin ring system through moderate π induction and conjugation.²⁸ Thus, the electron density of the octaethylporphyrin is not removed and is largely centered on both the ring and on the metal and a stronger anisotropic ring current is produced.

The most notable feature of the self-assembly process arises from the steric bulk expressed by the porphyrinic building blocks and is highlighted by the different rates at which **19(TTP)** and **19(OEP)** form in solution (Figure 24).

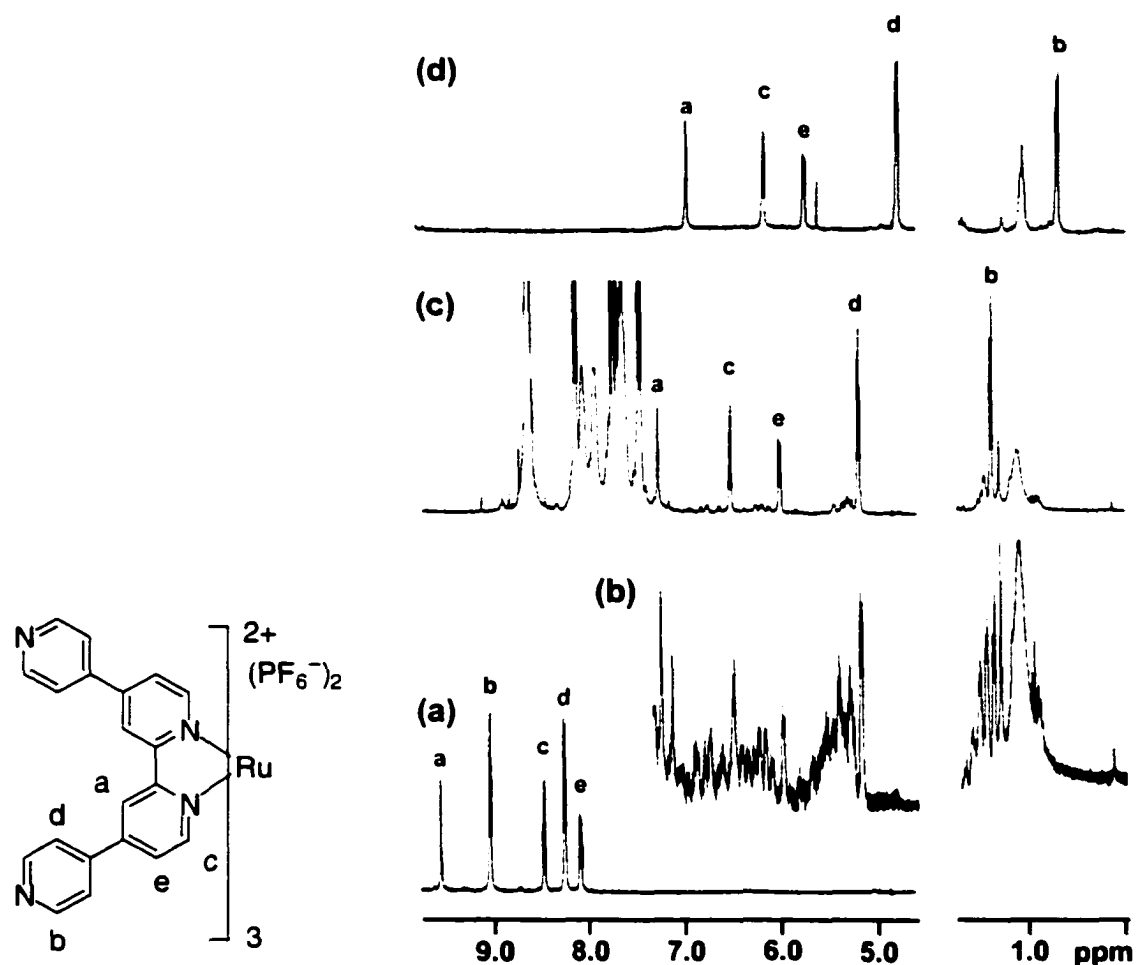


Figure 24. ^1H NMR (300 MHz, $[\text{D}_6]$ acetone) spectra of (a) **19**, (b) **19** + 6 equivalents $\text{Ru}(\text{TTP})(\text{CO})(\text{EtOH})$ (**4**) before and (c) after heating at 45°C for 2 h, and (d) **19** + 6 equivalents $\text{Ru}(\text{OEP})(\text{CO})(\text{EtOH})$ (**22**) at room temperature.

^1H NMR studies of **19(TTP)** reveal that the self-assembling process is slow on the NMR time scale and sharp peaks for the statistical mixture of fully assembled and lower-generation arrays were clearly visible even when six molar equivalents of

Ru(TTP)(CO)(EtOH) (4) were added (Figure 24b). Only upon heating to 45°C did the spectrum simplify to signals that correspond to **19(TTP)** alone (Figure 24c). On the other hand, despite the fact that the ruthenium atom in the octaethylporphyrin is a weaker Lewis acid,^{1a} complex **19(OEP)** assembles at a significantly greater rate than **19(TTP)** as illustrated by the immediate appearance of major signals for the fully assembled array (Figure 24d). The octaethylporphyrin is less Lewis acidic because it contains four electron-rich pyrroles and lacks *meso*-substituents. Thus, the electron density of the octaethylporphyrin is not removed and is largely centered on both the ring and on the metal. Based solely on Lewis acidity, it might be expected that the **TTP** array would form faster than the **OEP** array. However, the Lewis acidity differences contradict the observed rates by which the arrays **19(TTP)** and **19(OEP)** form and these phenomena can be attributed to the relative steric bulk of the tolyl and ethyl groups.

The need to input additional energy in the case of **19(TTP)** can be explained by the fact that the tetratolylporphyrin traces out a circle of a diameter that is significantly larger than that inscribed by the octaethyl analog (18.5 Å vs 12.7 Å) (Figure 25a). The result is that the CH₃- groups on the phenyl ring overlap with those on adjacent porphyrin rings in **19(TTP)** (Figure 25b). Molecular modeling also revealed that these steric interactions are not equally shared between the six porphyrins. Since bipyridine ligands have small bite angles, this places porphyrins on the same ligand closer together than those on adjacent ligands (Figure 25c). Based on information from the self-assembly studies and molecular modeling, the construction of arrays with larger porphyrins using this octahedral template will be difficult.

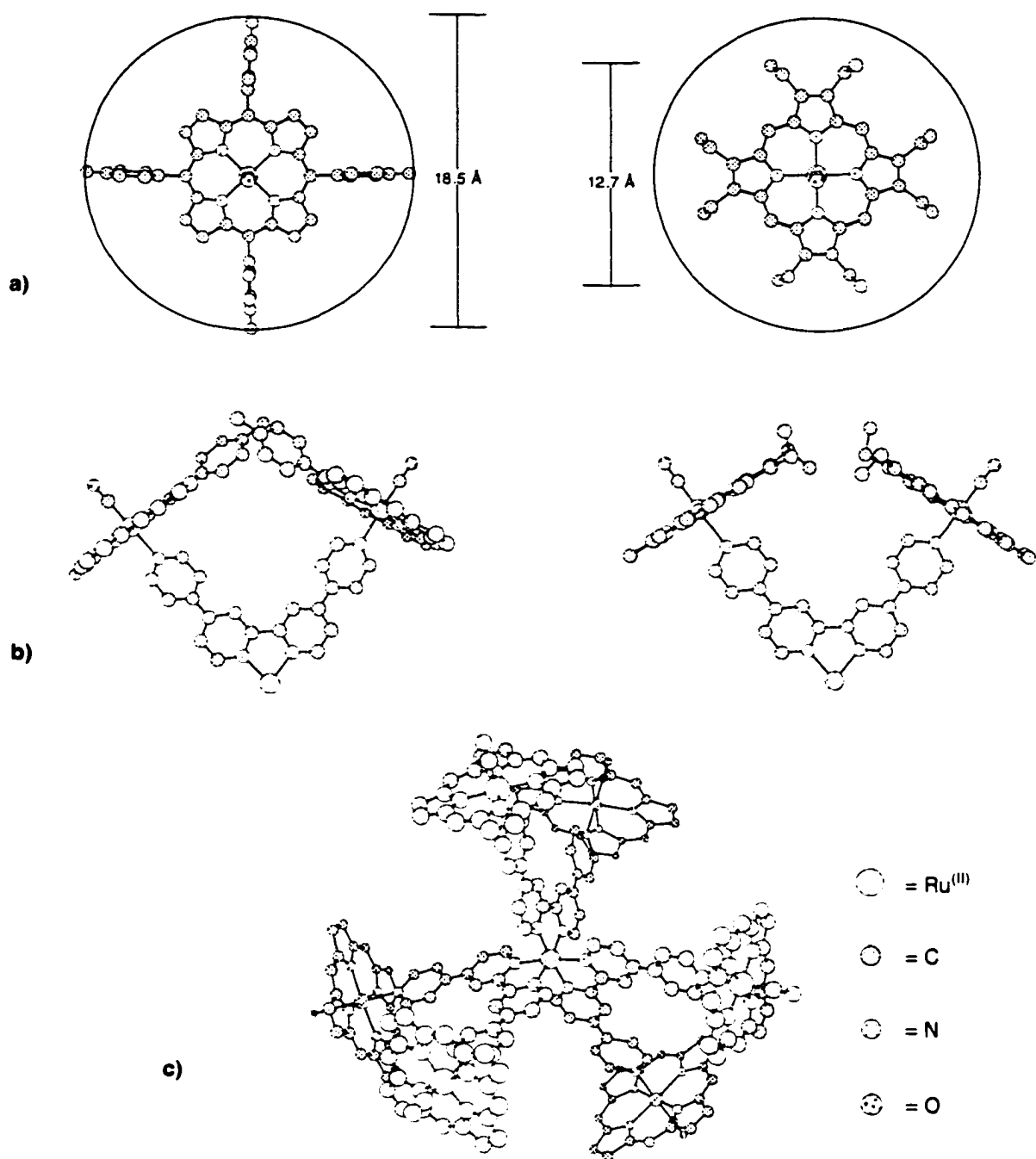
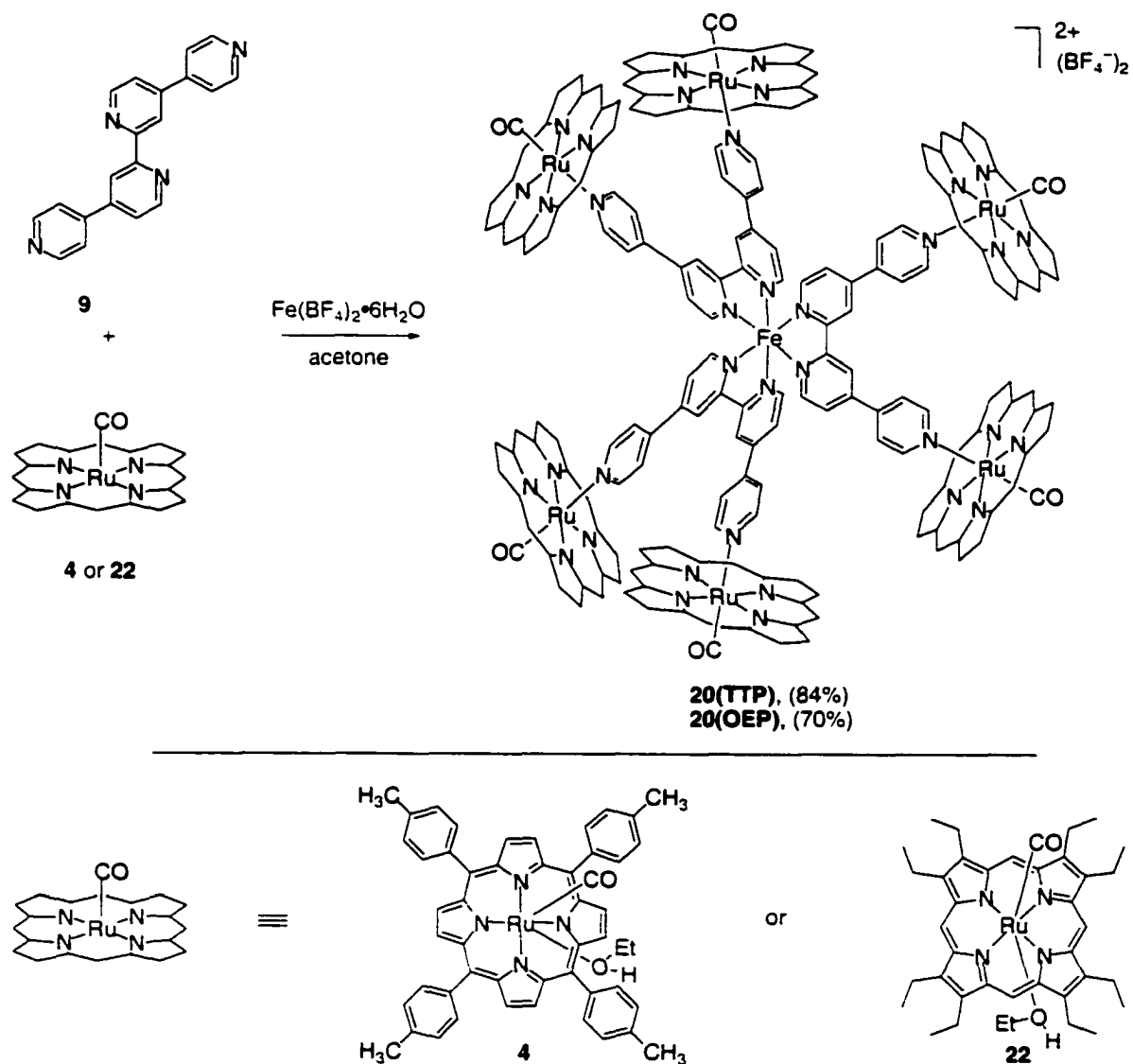


Figure 25. Molecular models of the components that highlight the (a) size restrictions of the two porphyrins, (b) steric interactions between porphyrins on the same ligand, (c) how the distorted octahedral template places the porphyrins in space. The porphyrins' substituents have been omitted for clarity.

2.7.2.4 –Self-Assembly Synthesis of the Iron(II) Octahedral Arrays

The octahedral iron analogs **20(TTP)** and **20(OEP)** were readily synthesized in greater than 70% isolated yield in one step when a 1:2 mixture of solid **9** and solid Ru(TTP)(CO)(EtOH) (**4**) or Ru(OEP)(CO)(EtOH) (**22**) were dissolved in an [D₆]acetone/CD₂Cl₂ solution of Fe(BF₄)₂•6H₂O (0.33 molar equivalents) with gentle heating (Scheme 16).



Scheme 16. The porphyrins' substituents and double bond representations have been omitted for clarity

The iron(II) arrays were isolated by adding pentane to concentrated dichloromethane solutions and filtering the precipitate. Again, this particular iron synthon was chosen for these studies because the highly labile nature of the metal's ligands allows for the rapid generation of the octahedral core fragment in high purity at room temperature, avoiding the harsh conditions required to form the ruthenate counterpart. Here, ten molecular species must organize and form twelve dative metal-ligand bonds in this assembly pathway. It is clear that, under these conditions, the self-assembly process results from the reading of both ruthenium and iron's inherent coordination algorithms and from the binding information stored in ligand **9**.

2.7.2.5 – Characterizations Using IR Spectroscopy

The octahedral arrays **19(TTP)**, **19(OEP)**, **20(TTP)**, and **20(OEP)** were also characterized in the solid state using IR spectroscopy. Recall that when pyridine coordinates to Ru(TTP)(CO)(EtOH) the ν_{CO} shifted from 1946 cm^{-1} to 1933 cm^{-1} . For the octahedral arrays **19(TTP)** and **20(TTP)**, the ν_{CO} of Ru(TTP)(CO) appeared at 1968 and 1953 cm^{-1} respectively. Since the ν_{CO} increases in frequency, this suggests that the terminal pyridines on complex **19** reduce the amount of electron density back-bonded to CO when they coordinate to the ruthenium(II) metal in Ru(TTP)(CO). Recall that when pyridine coordinates to Ru(OEP)(CO)(EtOH) (**23**), the ν_{CO} shifted from 1936 cm^{-1} to 1934 cm^{-1} . For the octahedral arrays **19(OEP)** and **20(OEP)**, the ν_{CO} of Ru(OEP)(CO) appeared at 1942 and 1941 cm^{-1} respectively. Since the ν_{CO} increases in frequency, this suggests that the terminal pyridines on complex **19** reduce the amount of electron density back-bonded to CO when they coordinate to the ruthenium(II) metal in Ru(OEP)(CO).

2.7.2.6 – Characterizations Using ESI Mass Spectrometry

The octahedral arrays **19(TTP)**, **19(OEP)**, **20(TTP)**, and **20(OEP)** were also characterized by electrospray mass spectrometry (ESI-MS) using a CH₂Cl₂/nitromethane solvent mixture. The peak for the parent cation of **19(TTP)**, **19(OEP)**, **20(TTP)**, and **20(OEP)** at $m/z = 2909, 2503, 2888,$ and $2479 [M - 2X]^+$ ($X = \text{counter ion PF}_6 \text{ or BF}_4$) were seen along with peaks corresponding to consecutive loss of porphyrin units (a representative mass spectrum of **19(TTP)** is shown in Figure 26). The isotopic abundance of each peak matched the calculated values of double charged species.

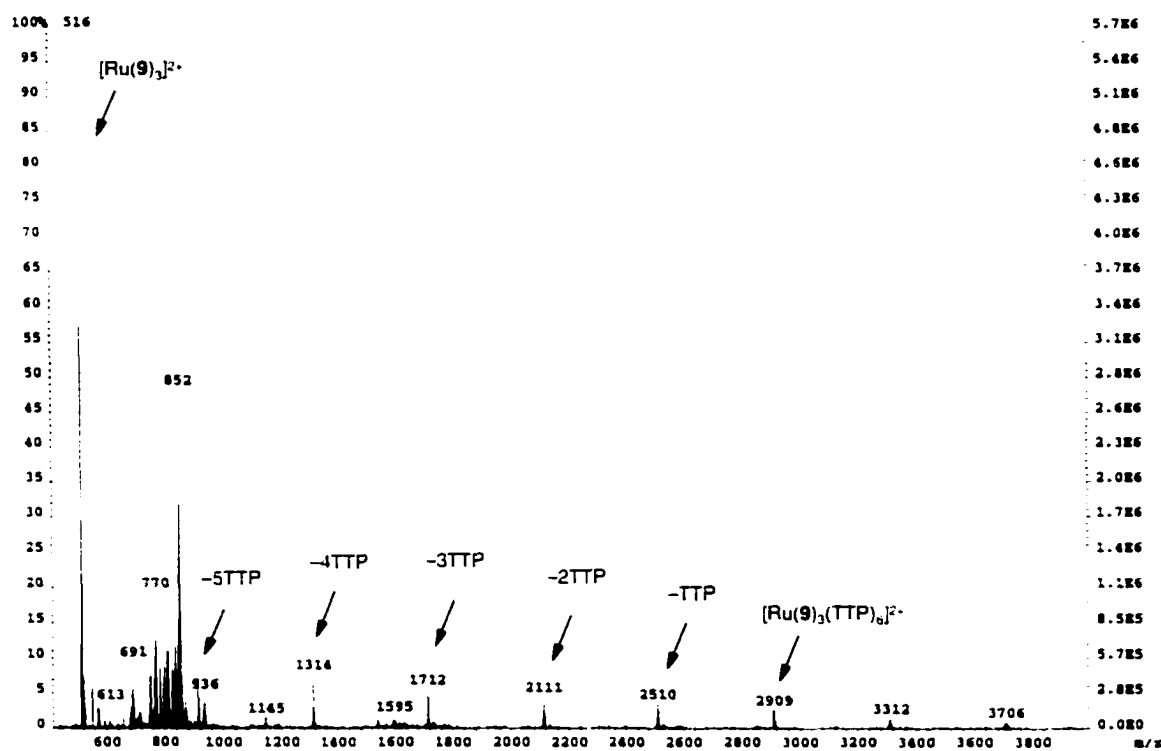


Figure 26. ESI mass spectrum of **19(TTP)** in CH₂Cl₂/nitromethane.

2.7.2.7– Photophysical Properties of the Ruthenium(II) Octahedral Arrays

The absorption spectra in the UV/Vis region of **19(TTP)**, **19(OEP)**, **20(TTP)**, and **20(OEP)** are essentially the sums of the spectra of the arrays' constituents. This indicates that there is an absence of strong coupling between the different units of the structure and the chromophores behave independently (only **19(TTP)** and **19(OEP)** are shown in Figures 27 and 28).

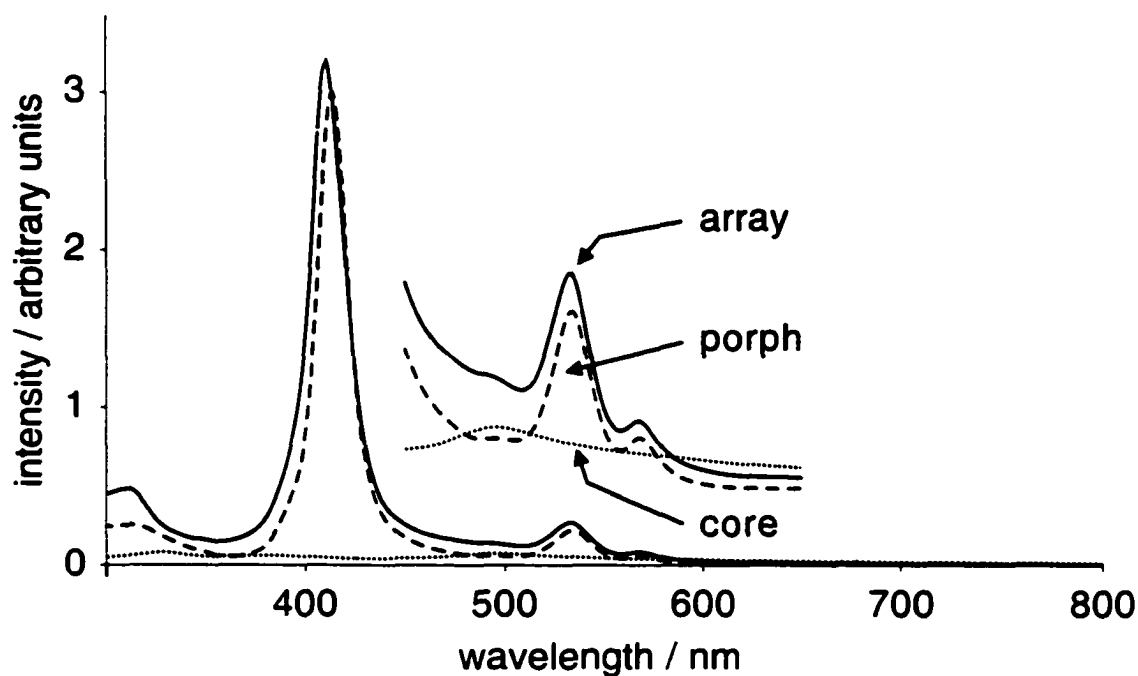


Figure 27. Overlay of absorption spectra of **19(TTP)** (solid line), Ru(TTP)(CO)(py) (**5**) (dashed line), and the octahedral core complex **19** (dotted line).

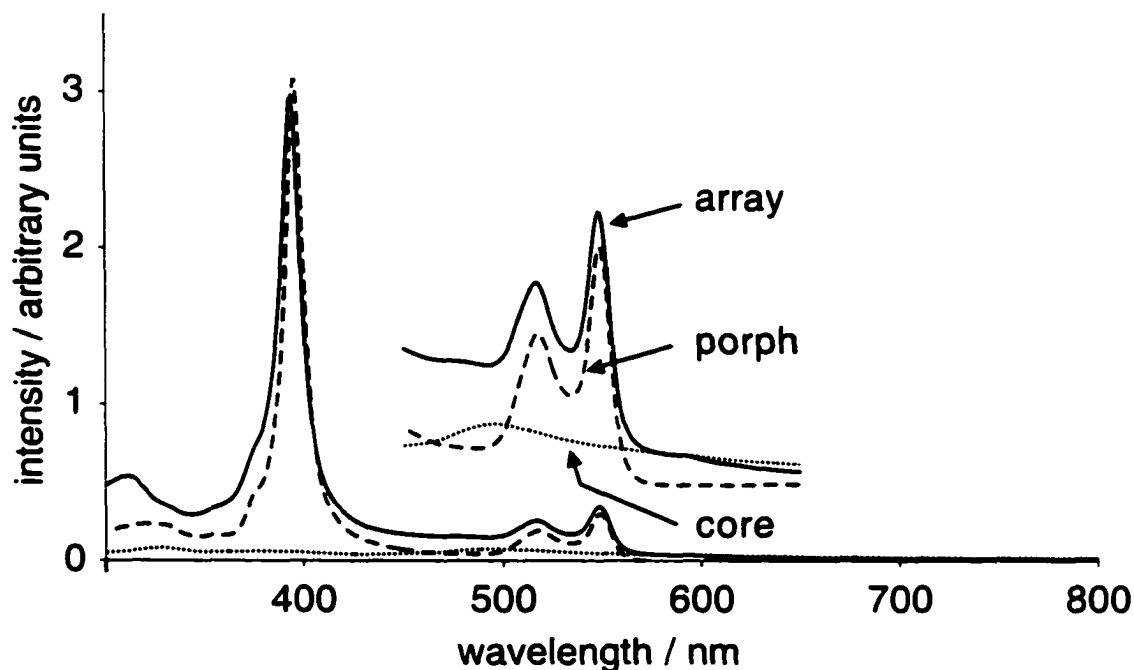


Figure 28. Overlay of absorption spectra of **19(OEP)** (solid line), Ru(OEP)(CO)(py) (**23**) (dashed line), and the octahedral core complex **19** (dotted line).

Only the ruthenium(II) core complexes **19(TTP)** and **19(OEP)** were studied by luminescence spectroscopy because of the production of a long-lived excited state of Ru(bpy)_3^{3+} type coordination compounds at room temperature (trace (b) in Figures 29 and 30).⁵ The iron(II) analogs, on the other hand, possess excited states that are too short lived to monitor conveniently. Monitoring the phosphorescence of **19(TTP)** and **19(OEP)** can, in the presence of appropriate quenchers, be used to evaluate possible energy and/or electron transfer processes. The excited states of metalloporphyrins are known to exhibit photoredox behaviour involving both oxidative and reductive quenching. Normally, ruthenium(II) metalloporphyrins lack fluorescence at room temperature because of strong orbital coupling provided by the metal. This leads to very fast intersystem crossing from the singlet to the triplet state and subsequent phosphorescence.²⁹ The spatial arrangement of the arrays' components, with the core

being completely surrounded by six porphyrins, may lead to efficient energy or electron transfer processes in the assembled array. The initial steady-state emission spectra of these complexes argue that there are significant differences between the excited states of each array and their building blocks. In order to evaluate the photoemission properties of each octahedral array, the arrays composed of the same core unit but with different porphyrins were investigated independently. The solutions containing the fully assembled octahedral arrays were “optically mismatched” to contain less than the total concentration of metalloporphyrin when compared to concentrations of the solutions containing Ru(TTP)(CO)(py) (**5**) or Ru(OEP)(CO)(py) (**23**). For instance, the solutions containing arrays **19(TTP)** and **19(OEP)** were prepared at 1.67×10^{-6} M, and since there are six metalloporphyrins in the array, the solution had an effective total pyridyl coordinated metalloporphyrin concentration of 1.00×10^{-5} M ($6 \times 1.67 \times 10^{-6}$ M). When comparing these effective total concentrations with the pyridyl adduct control solutions Ru(TTP)(CO)(py) (**5**) or Ru(OEP)(CO)(py) (**23**), which were prepared at 1.67×10^{-5} M, the arrays contained 40% less pyridyl coordinated metalloporphyrin, and are termed “optically mismatched”. The difference in concentrations will help to evaluate the arrays’ ability to harness the available light for possible photoinduced electron or energy transfer reactions. For example, if in the excited state, the arrays’ component compounds do not communicate and behave independently, then the control solutions of Ru(TTP)(CO)(py) (**5**) and Ru(OEP)(CO)(py) (**23**) would expectantly emit more light.

Exciting the core unit **19** at 530 nm resulted in the appearance of an emission centred at 625 nm corresponding to phosphorescence (trace (b) in Figure 29).²² Exciting

the porphyrin unit **5** at 530 nm resulted in the appearance of a band centred at 725 nm also corresponding to phosphorescence (trace (a) in Figure 29).

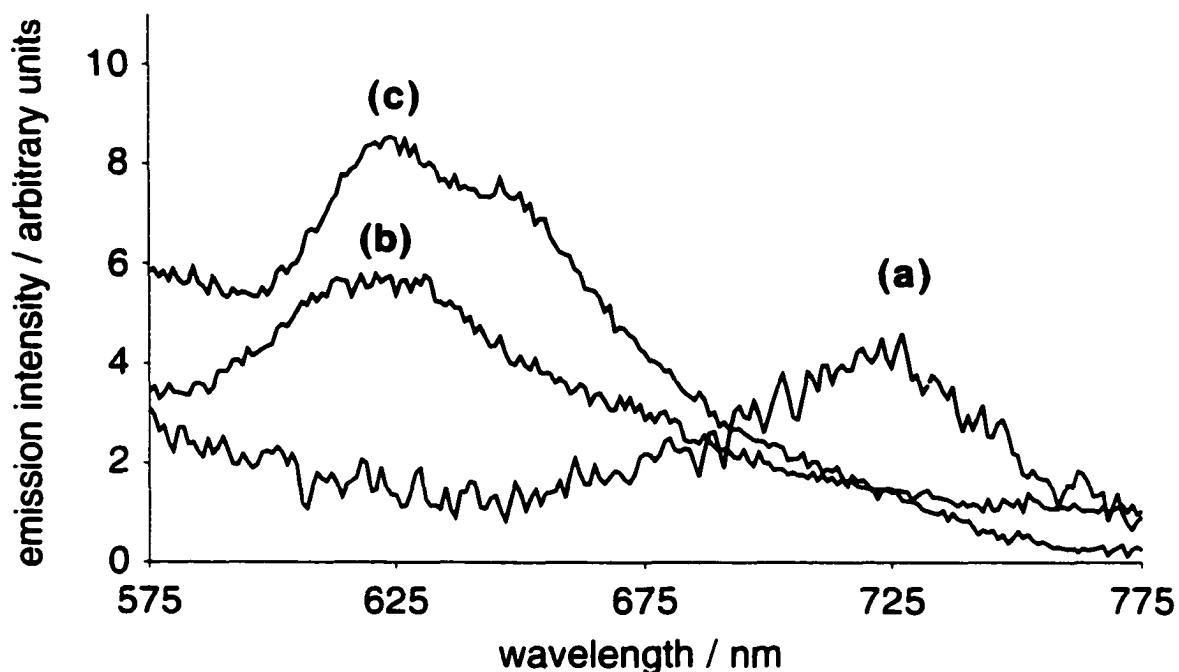


Figure 29. Emission spectra of CH₂Cl₂ solutions of (a) **5** ($\lambda_{\text{ex}} = 530$ nm) run at 1.67×10^{-5} M, (b) **19** ($\lambda_{\text{ex}} = 530$ nm) run at 2.04×10^{-5} M, (c) **19(TTP)** ($\lambda_{\text{ex}} = 530$ nm) run at 1.67×10^{-6} M. All spectra were run in dry deoxygenated solvent.

However, exciting the array **19(TTP)** at 530 nm resulted in the appearance of a band centred at 625 nm that closely resembles emission from the core unit (trace (c) in Figure 29). It should be recalled that excitation of the linear porphyrin arrays **8b** and **8c** resulted in the quenching of the porphyrins' phosphorescence through a non-radiative process and the inability to monitor any secondary emissions was due to the non-emissive properties of the central transition complex at room temperature. Thus, the absence of the porphyrin's phosphorescence for the octahedral array can be explained by considering the presence of a non-radiative process, but this does not account for the emission at 625 nm. This suggests that the core unit **19** does, in fact, emit light while the porphyrins do not

when assembled in the array. The band at 625 nm may be a result of a double electron transfer that follows the Dexter mechanism or an energy transfer that follows the Förster mechanism (see Chapter 1 of this thesis) between the core unit and porphyrins. Both mechanisms can produce the triplet excited state of **19** which is protected from external collision quenching because the core complex is completely surrounded by six porphyrins. The free energy for photoinduced electron transfer calculated using the Rehm–Weller equation³⁰ for **19(TTP)** (-12.17 kcal mol⁻¹) indicates, that for a Dexter energy transfer mechanism, the first electron transfer reaction from the porphyrin to the core unit is thermodynamically favourable. However, a Förster type energy transfer mechanism cannot be completely ruled out because non-zero overlap integrals between the absorption and emission spectra of the components exist. Also because of the close proximity of the components it is expected that there would be significant orbital overlap. If this occurs, the intensity of the emission will depend on two competitive pathways. One pathway proceeds through a non-productive charge recombination and the second produces the excited state of the core.

The steady-state emission studies of array **19(OEP)** showed that there exists a dramatic difference between the excited states of the array and building blocks. Exciting the porphyrin unit **23** at 515 nm resulted in the appearance of two intense bands at 572 and 621 nm (trace (a) in Figure 30). Exciting the array **19(OEP)** resulted in the appearance of three bands centred at 572, 621, and 666 nm (trace (c) in Figure 30). The two high-energy bands overlap well with the two bands of the free porphyrin unit Ru(OEP)(CO)(py) (**23**) and it is reasonable to assume that they arise from either coordinated or non-coordinated porphyrins that are not completely quenched. In a

suggested future study, the addition of an excess of Ru(OEP)(CO)(EtOH) (**22**) to the solution of **19(OEP)** may increase the intensity of the lower energy bands and would answer whether these emissions are from coordinated or non-coordinated Ru(OEP)(CO).

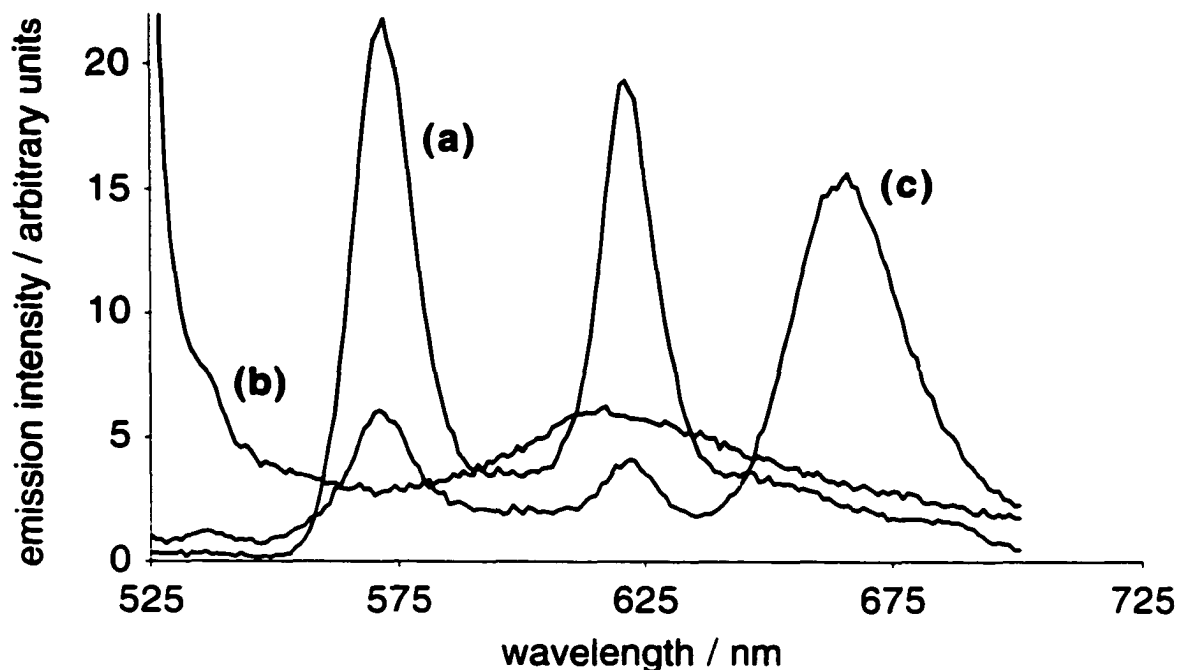


Figure 30. Emission spectra of CH_2Cl_2 solutions (a) **23** ($\lambda_{\text{ex}} = 515 \text{ nm}$) run at $1.58 \times 10^{-5} \text{ M}$, (b) **19** ($\lambda_{\text{ex}} = 515 \text{ nm}$) run at $2.04 \times 10^{-5} \text{ M}$, (c) **19(OEP)** ($\lambda_{\text{ex}} = 515 \text{ nm}$) run at $1.58 \times 10^{-6} \text{ M}$. All spectra were run in dry deoxygenated solvent.

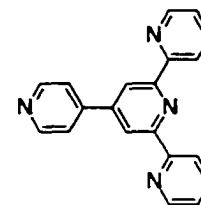
The substantial reduction in intensity of the porphyrin bands originally centred at 575 and 625 nm seems to be coupled to the new emission that appears at longer wavelengths (trace (c) in Figure 30). Taking into account the relative absorptivities and the emission intensities of each component, this new emission can be viewed as a function of the sums of the parts and attributed to an energy transfer between the porphyrins and the core. The free energy for photoinduced electron transfer calculated using the Rehm–Weller equation³⁰ for **19(OEP)** ($-15.88 \text{ kcal mol}^{-1}$) indicates that for a double electron transfer that follows the Dexter mechanism the first electron transfer reaction is

thermodynamically favourable. However, a Förster type energy transfer mechanism cannot be completely ruled out because non-zero overlap integrals between the absorption and emission spectra exist. Also because of the close proximity of the components it is expected that there would be significant orbital overlap. Again, a possible explanation is that two electron-transfers occur between the porphyrins into low lying *d*-orbitals on the core metal center, which are protected from recombination and the array emits light efficiently.

2.8 – Experimental

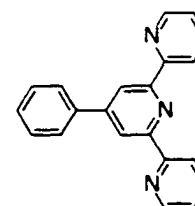
General Remarks: All solvents (Caledon) were distilled prior to use. Solvents used for UV/Vis spectroscopy were deoxygenated by bubbling argon through the solvent. Solvents for NMR spectroscopic analysis (Cambridge Isotope Laboratories) were used as received. All reagents and starting materials were purchased from Aldrich. 4'-(4'''-pyridyl)-2,2':6',2''-terpyridine (**1**),⁷ 4'-phenyl-2,2':6',2''-terpyridine (**2**),¹⁰ 5,10,15,20-tetratolylporphyrin (**3**),⁸ Ru(TTP)(CO)(EtOH) (TTP = 5,10,15,20-tetratolylporphyrinato dianion, **4**),⁹ [Fe(pytpy)₂][BF₄]₂ (**6a**),⁷ [Ru(pytpy)₂][PF₆]₂ (**6b**),¹³ and [Os(pytpy)₂][PF₆]₂ (**6c**)¹³ (pytpy = 4'-(4'''-pyridyl)-2,2':6',2''-terpyridine, **1**), [Ru(phtpy)₂][PF₆]₂ (**7b**),¹³ [Os(phtpy)₂][PF₆]₂ (**7c**)¹³ (phtpy = 4'-phenyl-2,2':6',2''-terpyridine, **2**), 1-cyanomethylpyridinium iodide,²² 2-acetamido-6-phenyl-4,4'-bipyridine (**12**),¹¹ 2-amino-6-phenyl-4,4'-bipyridine (**13**),¹¹ 4,4':6,6'-tetraphenyl-2,2'-bipyridine (**16**),¹¹ [Ru(dpybpy)₃][PF₆]₂ (**19**)²² (dpybpy = 4,4'-di(4''-pyridyl)-2,2'-bipyridine), [Fe(dpybpy)₃][BF₄]₂ (**20**)¹⁸ (dpybpy = 4,4'-di(4''-pyridyl)-2,2'-bipyridine), 4,4'-di(4''-pyridyl)-2,2'-bipyridine (**9**)¹⁸, 2,3,7,8,12,13,17,18-octaethylporphyrin (**21**),²³ Ru(OEP)(CO)(EtOH) (OEP = 2,3,7,8,12,13,17,18-octaethylporphyrinato dianion, **22**),²⁵ Ru(OEP)(CO)(py) (OEP = 2,3,7,8,12,13,17,18-octaethylporphyrinato dianion, **23**),^{26a} and [Ru(DMSO)₄Cl₂]³¹ were prepared as described in the literature. ¹H NMR spectroscopic characterizations were performed on a Varian Inova-500 instrument, working at 499.92, on a Varian Inova-400 instrument, working at 399.96, or on a Varian

Inova-300 instrument, working at 299.96 MHz. Chemical shifts (δ) are reported in parts per million relative to tetramethylsilane using the residual solvent peak as a reference standard. FT-IR measurements were performed using a Nicolet Magna-IR 750 on solid samples using a microscope unless otherwise stated. UV/Vis measurements were performed using a Varian Cary 400 Scan spectrophotometer. Steady-state phosphorescence spectra were recorded on a PTI spectrofluorimeter. Electrospray ionization mass spectra were recorded on a Micromass ZabSpec Hybrid Sector-TOF with positive mode electrospray ionization. The liquid carrier was infused into the electrospray source by means of a Harvard syringe pump at a flow rate of 10 μ L/minute. The sample solution, in the same solvent, was introduced *via* a 1 μ L-loop-injector. Purified nitrogen gas was used as a pneumatic aid and filtered air as the bath gas, heated at *ca.* 80°C. For low resolution, the mass spectra were acquired by magnet scan at a rate of 5 seconds/decade at *ca.* 1000 resolution. For exact mass measurements, the spectra were obtained by voltage scan over a narrow mass range at *ca.* 10000 resolution. Data acquisition and processing was achieved by using the OPUS software package on a Digital Alpha station with VMS operating system.



4'-(4''-pyridyl)-2-,2':6',2''-terpyridine (pytpy) (1)⁷: 2-Acetylpyridine (12.5 mL, 0.11 mol) was added dropwise to a stirred emulsion of 4-pyridinecarboxaldehyde (11 mL, 0.11 mol) in ethanol (100 mL) and aqueous sodium hydroxide solution (75 mL, 1.5 M). The mixture was then stirred for 24 h at ambient temperature, after which period the precipitate was collected by filtration. The light yellow solid was washed with ethanol (25 mL). This solid was carried on to the next step without further purification. (3-pyridacyl)-pyridinium iodide (1.6 g, 0.0049 mol), 1-(2-pyridyl)-3-(4-pyridyl)-1-oxopropene-2-ene (0.75 g, 0.0036 mol), and ammonium acetate (6.3 g) were boiled for 3 h in acetic acid (3 mL). The acetic acid was removed and the residue dissolved in hot methanol. The product precipitates on cooling. Yield: 75%.

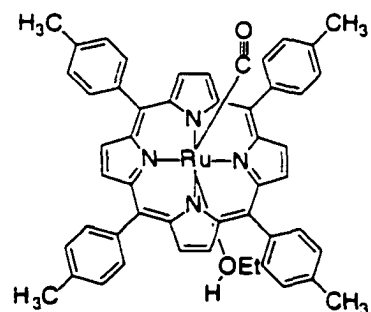
¹H NMR (300 MHz, CDCl₃, 22°C): δ = 8.73 (s, 2 H), 8.71 (dd, 2 H), 8.65 (td, 2 H), 7.88 (m, 4 H), 7.48 (dd, 2 H), 7.37 (ddd, 2 H).



4'-(4''-phenyl)-2-,2':6',2''-terpyridine (phtpy) (2)¹⁰: 2-Acetylpyridine (25 mL, 0.22 mol) was added dropwise to a stirred emulsion of benzaldehyde (11 mL, 0.11 mol) in ethanol (200 mL) and aqueous sodium hydroxide solution (150 mL, 1.5 M). The mixture

was then stirred for 24 h at ambient temperature, after which period the precipitate was collected by filtration. The white solid was washed with ethanol (50 mL). This solid was carried on to the next step without further purification. A suspension of 3-phenyl-1,5-bis(2-pyridyl)-1,5-pentanedione (0.75 g, 0.0036 mol) and ammonium acetate (6.3 g) in acetic acid (3 mL) was heated at reflux for 3 h. The acetic acid was removed under reduced pressure and the residue dissolved in hot methanol. The product precipitates on cooling. Yield: 70%.

^1H NMR (300 MHz, CDCl_3 , 22°C): δ = 8.75 (s, 2 H), 8.71 (m, 2 H), 8.66 (td, 2 H), 8.30 (m, 2 H), 8.20 (m, 2 H), 7.88 (dt, 2 H), 7.68 (t, 1 H), 7.36 (ddd, 2 H).



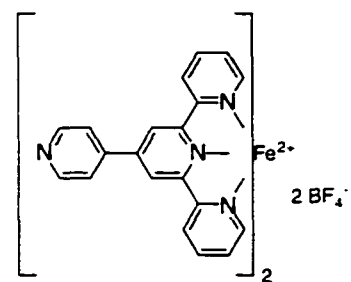
Ru(TTP)(CO)(EtOH) (4)⁹: *Meso*-tetratolylporphyrin (0.500 g, 0.746 mmol) and triruthenium dodecacarbonyl (0.750 g, 1.17 mmol) were heated in phenol (2.0 g) at reflux for 45 min. The solution was then cooled and EtOH (1 mL) was added. The crude product was precipitated by the addition of water then collected by vacuum filtration and washed with water. The residue was chromatographed through Alumina (neutral, activity II-III) eluting first with CH_2Cl_2 and finally with a mixture of EtOH/ CH_2Cl_2 (5/95) which

removed a red band. The red band was concentrated to dryness to give a red solid which was recrystallized from ethanol. Yield: 0.456 g (73%).

^1H NMR (300 MHz, CD_2Cl_2 , 22°C): δ = 8.72 (s, 8 H), 8.09 (d, $J=7.8$ Hz, 4 H), 7.75 (d, $J=7.8$ Hz, 4 H), 7.56 (d, $J=8.5$ Hz, 4 H), 7.54 (d, $J=8.1$ Hz, 4 H), 2.69 (s, 12 H), 0.49 (bs, 3 H), -0.48 (bs, 2 H); ^{13}C NMR (125.7 MHz, CD_2Cl_2 , 22°C): δ = 182.2, 144.5, 139.8, 137.6, 134.5, 134.3, 132.0, 127.7, 127.6, 122.4, 21.6; Selected IR (microscope): ν = 1946 (CO) cm^{-1} .

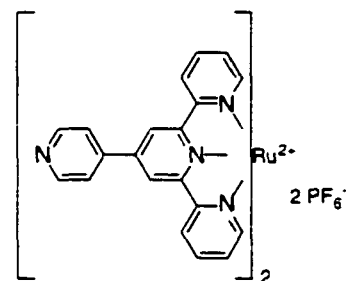
Ru(TTP)(CO)(py) (5): Ru(TTP)(CO)(EtOH) (4) (25 mg, 0.031 mmol) was dissolved in CH_2Cl_2 (5 mL) and pyridine (0.5 mL) was added. The solution was evaporated to dryness under reduced pressure and hexanes (5 mL) was added, the residue was sonicated and then filtered then washed with hexanes. Yield: 26 mg (98%).

^1H NMR (500 MHz, CD_2Cl_2 , 22°C): δ = 8.64 (s, 8 H), 8.09 (dd, $J=2.0, 7.5$ Hz, 4 H), 7.92 (dd, $J=2.0, 7.5$ Hz, 4 H), 7.55 (d, $J=8.0$ Hz, 4 H), 7.50 (d, $J=8.0$ Hz, 4 H), 6.13 (tt, $J=1.5, 7.5$ Hz, 1 H), 5.23 (dd, $J=1.5, 5.5$ Hz, 2 H), 1.50 (dt, $J=1.5, 5.5$ Hz, 2 H), 2.69 (s, 12 H); UV/Vis (CH_2Cl_2): λ_{max} / nm ($\log \epsilon / \text{M}^{-1}\text{cm}^{-1}$) = 238 (4.66), 312 (4.29), 414 (5.36), 534 (4.23), 568 (3.66); Selected IR (microscope): ν = 1933 (CO) cm^{-1} .



[Fe(pytpy)₂][BF₄]₂ (6a)⁷: To a hot solution of pytpy (1) (120 mg, 0.387 mmol) in methanol (5 mL) was added Fe(BF₄)₂·6H₂O (28 mg, 0.116 mmol), and the resulting deep purple solution was stirred at reflux for 30 min. Upon cooling the product precipitates from the solution and was collected by filtration and recrystallized from methanol. Yield: 110 mg (85%).

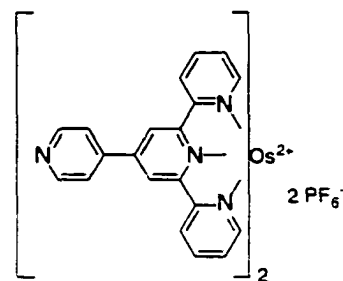
¹H NMR (300 MHz, [D₆]acetone, 22°C): δ = 9.60 (s, 4 H), 9.08 (d, *J*=8.1 Hz, 4 H), 8.95 (dd, *J*=1.8, 4.8, Hz, 4 H), 8.25 (dd, *J*=1.8, 4.8 Hz, 4 H), 8.00 (dd, *J*=1.5, 7.8 Hz, 4 H), 7.73 (d, *J*=5.1 Hz, 4H), 7.30 (dd, *J*=1.5, 5.7 Hz, 4 H).



[Ru(pytpy)₂][PF₆]₂ (6b)¹³: A solution of pytpy (1) (pytpy = 4'-(4'''-pyridyl)-2-.2':6'.2''-terpyridine) (73 mg, 0.24 mmol) and Ru[DMSO]₄Cl₂ (37 mg, 0.078 mmol) in ethylene glycol (5 mL) was heated at reflux for 3 h. The reaction mixture was cooled to room temperature, diluted with water (3 mL) and treated with excess of a methanolic solution of NH₄PF₆. The resulting dark red precipitate was collected by filtration on a

Celite pad, washed with water and the crude product was removed by eluting with acetonitrile. The crude mixture was concentrated to 5 mL and then chromatographed through silica gel with acetonitrile-saturated aqueous potassium nitrate-water (7:1:0.5) as eluent. After discarding the initial yellow band, the red-orange band was collected and concentrated until a precipitate formed. The precipitate was collected by filtration, redissolved in acetonitrile and treated with excess NH_4PF_6 . The red product was precipitated by the addition of ether, collected by filtration and washed with water to remove excess NH_4PF_6 . Yield: 45 mg, (57%).

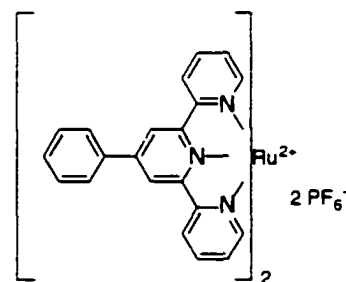
^1H NMR (300 MHz, $[\text{D}_6]$ acetone, 22°C): $\delta = 9.58$ (s, 4 H), 9.08 (d, $J=8.1$ Hz, 4 H), 8.95 (dd, $J=1.8, 4.8$ Hz, 4 H), 8.29 (dd, $J=1.8, 4.8$ Hz, 4 H), 8.46 (dd, $J=1.5, 7.8$ Hz, 4 H), 7.84 (d, $J=5.1$ Hz, 4 H), 7.40 (dd, $J=1.5, 5.7$ Hz, 4 H); MS (ESI+): $m/z = 361.0$ $[\text{M} - 2\text{PF}_6]^{2+}$, 867.0 $[\text{M} - \text{PF}_6]^+$.



$[\text{Os}(\text{pytpy})_2][\text{PF}_6]_2$ (6c)¹³: A solution of pytpy (1) (pytpy = 4'-(4''-pyridyl)-2',2':6',2''-terpyridine) (150 mg, 0.483 mmol) and $\text{Na}_2[\text{OsCl}_6]$ (70 mg, 0.161 mmol) in ethylene glycol (5 mL) was heated at reflux for 3 days. The reaction mixture was cooled to room temperature, diluted with water (3 mL) and treated with excess of a methanolic solution of NH_4PF_6 . The resulting dark brown precipitate was collected by filtration on a

Celite pad, washed with water and the crude product was removed by eluting with acetonitrile. The crude mixture was concentrated to 5 mL and then chromatographed through silica gel with acetonitrile-saturated aqueous potassium nitrate-water (7:1:0.5) as eluent. After discarding the initial yellow band, the brown band was collected and concentrated until a precipitate formed. The precipitate was collected by filtration, redissolved in acetonitrile and treated with excess NH_4PF_6 . The brown product was precipitated by the addition of ether, collected by filtration and washed with water to remove excess NH_4PF_6 . Yield: 92 mg (52%).

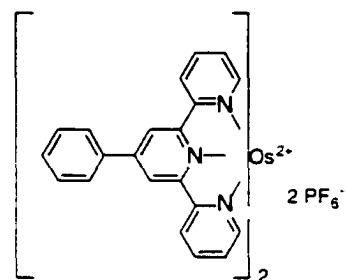
^1H NMR (300 MHz, $[\text{D}_6]$ acetone, 22°C): δ = 9.60 (s, 4 H), 9.08 (d, $J=8.1$ Hz, 4 H), 8.95 (dd, $J=1.8, 4.8$ Hz, 4 H), 8.25 (dd, $J=1.8, 4.8$ Hz, 4 H), 8.00 (dd, $J=1.5, 7.8$ Hz, 4 H), 7.73 (d, $J=5.1$ Hz, 4H), 7.30 (dd, $J=1.5, 5.7$ Hz, 4 H); MS (ES+): m/z = 406.0 $[\text{M} - 2\text{PF}_6]^{2+}$, 957.0 $[\text{M} - \text{PF}_6]^+$.



$[\text{Ru}(\text{phtpy})_2][\text{PF}_6]_2$ (**7b**)¹³: A solution of phtpy (**2**) (phtpy = 4'-(4'''-phenyl)-2-,2':6',2''-terpyridine) (120 mg, 0.387 mmol) and $\text{RuCl}_3 \cdot \text{H}_2\text{O}$ (28 mg, 0.116 mmol) in ethylene glycol (5 mL) was heated at reflux for 3 h. The reaction mixture was cooled to room temperature, diluted with water (3 mL) and treated with excess of a methanolic solution of NH_4PF_6 . The resulting dark red precipitate was collected by filtration on a

Celite pad, washed with water and the crude product was removed by eluting with acetonitrile. The crude mixture was concentrated to 5 mL and then chromatographed through silica gel with acetonitrile-saturated aqueous potassium nitrate-water (7:1:0.5) as eluent. After discarding the initial yellow band, the red-orange band was collected and concentrated until a precipitate formed. The precipitate was collected by filtration, redissolved in acetonitrile and treated with excess NH_4PF_6 . The red product was precipitated by the addition of ether, collected by filtration and washed with water to remove excess NH_4PF_6 . Yield: 30 mg (25%).

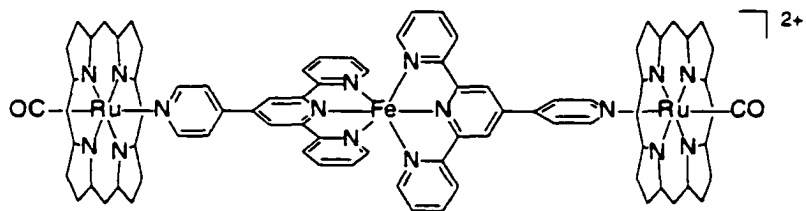
^1H NMR (300 MHz, $[\text{D}_6]$ acetone, 22°C): δ = 9.44 (s, 4 H), 9.07 (d, $J=8.1$ Hz, 4 H), 8.33 (dd, $J=1.8, 4.8$ Hz, 4 H), 8.10 (dd, $J=1.5, 7.8$ Hz, 4 H), 7.84 (d, $J=5.1$ Hz, 4 H), 7.74 (m, 8 H), 7.30 (dd, $J=1.5, 5.7$ Hz, 4 H).



$[\text{Os}(\text{phtpy})_2][\text{PF}_6]_2$ (7c)¹³: A solution of phtpy (**2**) (phtpy = 4'-(4'''-phenyl)-2-,2':6',2''-terpyridine) (120 mg, 0.387 mmol) and $\text{OsCl}_3 \cdot \text{H}_2\text{O}$ (28 mg, 0.116 mmol) in ethylene glycol (5 mL) was heated at reflux for 3 h. The reaction mixture was cooled to room temperature, diluted with water (3 mL) and treated with excess of a methanolic solution of NH_4PF_6 . The resulting dark brown precipitate was collected by filtration on a Celite pad, washed with water and the crude product was removed by eluting with

acetonitrile. The crude mixture was concentrated to 5 mL and then chromatographed through silica gel with acetonitrile-saturated aqueous potassium nitrate-water (7:1:0.5) as eluent. After discarding the initial yellow band, the brown band was collected and concentrated until a precipitate formed. The precipitate was collected by filtration, redissolved in acetonitrile and treated with excess NH_4PF_6 . The brown product was precipitated by the addition of ether, collected by filtration and washed with water to remove excess NH_4PF_6 . Yield: 20 mg (16%).

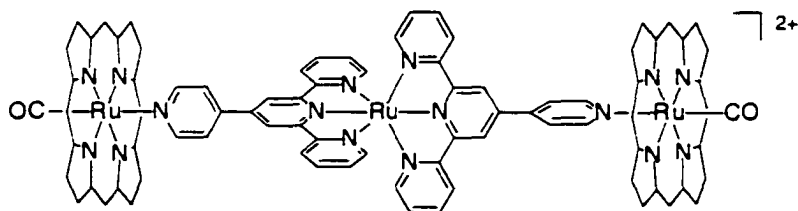
^1H NMR (300 MHz, $[\text{D}_6]$ acetone, 22°C): $\delta = 9.47$ (s, 4 H), 9.08 (d, $J=8.1$ Hz, 4 H), 8.30 (dd, $J=1.8, 4.8$ Hz, 4 H), 7.97 (dd, $J=1.5, 7.8$, Hz, 4 H), 7.78 (t, $J= 8.1$ Hz, 4 H), 7.70 (d, $J=5.1$ Hz, 4 H), 7.60 (t, $J=8.1$ Hz, 2 H), 7.25 (dd, $J=1.5, 5.7$ Hz, 4 H). UV/Vis ($\text{CH}_2\text{Cl}_2/\text{Acetone}$): $\lambda_{\text{max}} / \text{nm}$ ($\log \epsilon / \text{M}^{-1}\text{cm}^{-1}$) = 315 (4.72), 490 (4.23), 561 (3.74), 668 (3.62).



[Fe(pytpy) $_2$][BF $_4$] $_2$ [Ru(TTP)(CO)] $_2$ (8a): A solution of pytpy (1) (13.0 mg, 4.19×10^{-2} mmol) in acetone (5.0 mL) was treated with 1.1 molar equivalents of Ru(TTP)(CO)(EtOH) (4) (40 mg, 4.74×10^{-2} mmol) followed by Fe(BF $_4$) $_2 \cdot 6\text{H}_2\text{O}$ (7.0 mg, 2.08×10^{-2} mmol) and stirred at ambient temperature for 22 h. The solvents were evaporated to dryness and the resulting solid was dissolved in CH_2Cl_2 . The product was

precipitated by adding a mixture of Et₂O/pentane (20:80) and collected by filtration. The product was washed with a mixture of Et₂O/pentane (20:80) and dried under vacuum. Yield: 50.0 mg (98%).

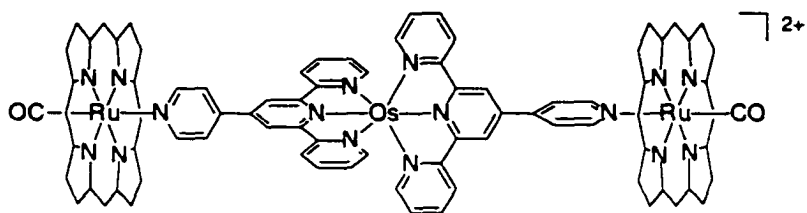
M.p. >300°C (decomp); ¹H NMR (500 MHz, [D₆]acetone/CH₂Cl₂, 22°C): δ = 8.66 (s, 16 H), 8.26 (s, 4 H), 8.19 (d, *J*=7.0 Hz, 4 H), 8.08 (d, *J*=7.0 Hz, 8 H), 7.96 (d, *J*=7.0 Hz, 8 H), 7.53 (m, 12 H), 7.48 (d, *J*=7.0 Hz, 8 H), 6.72 (m, *J*=5.1 Hz, 4 H), 6.59 (m, 4 H), 6.11 (d, *J*=5.5 Hz, 4 H), 2.63 (s, 24 H), 1.77 (d, *J*=4.5 Hz, 4 H); ¹³C NMR (125.7 MHz, [D₆]acetone/CH₂Cl₂, 22°C) (21 of 22 signals): δ = 181.1, 160.6, 157.7, 152.9, 145.7, 145.5, 144.3, 140.0, 139.1, 137.6, 134.6, 134.4, 132.3, 127.9, 127.8, 127.6, 124.5, 122.2, 121.1, 120.4, 21.4; MS (ESI⁺): *m/z* = 1136 [2%, M – 2BF₄]²⁺, 737 [4%, M – TTP, 2BF₄]²⁺; UV/Vis (CH₂Cl₂): λ_{max} / nm (log ε / M⁻¹cm⁻¹) = 246 (4.99), 279 (4.97), 287 (5.04), 323 (4.86), 414 (5.68), 533 (4.67), 572 (4.55); Selected IR (microscope): ν = 1961 (CO) cm⁻¹.



[Ru(pytpy)₂][PF₆]₂[Ru(TTP)(CO)]₂ (8b): A solution of [Ru(pytpy)₂][PF₆]₂ (**6b**) (17.0 mg, 1.68×10⁻² mmol) in acetone (5.0 mL) was treated with 2.5 molar equivalents of Ru(TTP)(CO)(EtOH) (**4**) (35 mg, 4.20×10⁻² mmol) and stirred at ambient temperature for 22 h. The solvents were evaporated to dryness and the resulting solid was dissolved in

CH₂Cl₂. The product was precipitated by adding a mixture of Et₂O/pentane (20:80) and collected by filtration. The product was washed with a mixture of Et₂O/pentane (20:80) and dried under vacuum. Yield: 43.0 mg (98%).

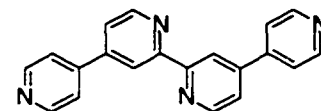
M.p. >300°C (decomp); ¹H NMR (500 MHz, [D₆]acetone/CH₂Cl₂, 22°C): δ = 8.66 (s, 16 H), 8.27 (d, *J*=8.1 Hz, 4 H), 8.16 (s, 4 H), 8.08 (dd, *J*=2.1, 7.8 Hz, 8 H), 7.93 (dd, *J*=1.8, 7.8 Hz, 8 H), 7.62 (ddd, *J*=1.5, 1.5, 7.8, 4 H), 7.55 (d, *J*=8.5 Hz, 8 H) 7.47 (d, *J*=8.1 Hz, 8 H), 6.91 (d, *J*=5.1 Hz, 4 H), 6.85 (dd, *J*=1.5, 5.7 Hz, 4 H), 6.00 (d, *J*=7.5 Hz, 4 H), 2.64 (s, 24 H), 1.72 (d, *J*=7.0 Hz, 4 H); ¹H NMR (300 MHz, [D₆]acetone, 22°C): δ = 8.70 (s, 16 H), 8.44 (d, *J*=8.1 Hz, 4 H), 8.40 (s, 4 H), 8.14 (dd, *J*=2.1, 7.8 Hz, 8 H), 7.96 (dd, *J*=1.8, 7.8 Hz, 8 H), 7.74 (dd, *J*=1.5, 7.8 Hz, 4 H), 7.63 (d, *J*=8.5 Hz, 8 H) 7.55 (d, *J*=8.1 Hz, 8 H), 7.16 (d, *J*=5.1 Hz, 4 H), 6.94 (dd, *J*=1.5, 5.7 Hz, 4 H), 6.20 (dd, *J*=1.8, 4.8 Hz, 4 H), 2.64 (s, 24 H), 1.79 (dd, *J*=1.8, 4.8 Hz, 4 H); ¹³C NMR (125.7 MHz, [D₆]acetone/CH₂Cl₂, 22°C) (19 of 22 signals): δ = 157.5, 155.4, 153.1, 145.2, 144.1, 139.8, 138.3, 137.4, 134.4, 134.2, 132.1, 128.0, 127.7, 127.3, 124.9, 122.0, 121.1, 120.1, 21.3; MS (ESI+): *m/z* = 1664 [5%, M – TTP, PF₆]¹⁺, 1159 [12%, M – 2PF₆]²⁺, 867 [100%, M – 2TTP, PF₆]⁺, 760 [15%, M – TTP, 2PF₆]²⁺; UV/Vis (CH₂Cl₂): λ_{max} / nm (log ε / M⁻¹cm⁻¹) = 278 (4.93), 286 (4.93), 314 (4.89), 413 (5.59), 494 (4.54), 532 (4.58), 567 (4.07); Selected IR (microscope): ν = 1959 (CO) cm⁻¹.



[Os(pytpy)₂][PF₆]₂[Ru(TTP)(CO)]₂ (8c): A solution of [Os(pytpy)₂][PF₆]₂ (**6c**) (11.0 mg, 1.00×10⁻² mmol) in acetone (5.0 mL) was treated with 3.0 molar equivalents of Ru(TTP)(CO)(EtOH) (**4**) (25 mg, 3.00×10⁻² mmol) and stirred at ambient temperature for 22 h. The solvents were evaporated to dryness and the resulting solid was dissolved in CH₂Cl₂. The product was precipitated by adding a mixture of Et₂O/pentane (20:80) and collected by filtration. The product was washed with a mixture of Et₂O/pentane (20:80) and dried under vacuum. Yield: 9.0 mg (98%).

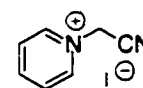
M.p. >300°C (decomp); ¹H NMR (500 MHz, [D₆]acetone/CH₂Cl₂, 22°C): δ = 8.66 (s, 16 H), 8.33 (d, *J*=8.1 Hz, 4 H), 8.26 (s, 4 H), 8.08 (dd, *J*=2.1, 7.8 Hz, 8 H), 7.93 (dd, *J*=1.8, 7.8 Hz, 8 H), 7.57 (d, *J*=8.5 Hz, 8 H), 7.52 (ddd, *J*=1.5, 1.5, 7.8 Hz, 4 H), 7.48 (d, *J*=8.1 Hz, 8 H), 6.87 (d, *J*=5.1 Hz, 4 H), 6.81 (dd, *J*=1.5, 5.7 Hz, 4 H), 6.03 (d, *J*=1.5, 4.8 Hz, 4 H), 2.64 (s, 24 H), 1.72 (dd, *J*=1.5, 4.8 Hz, 4 H); ¹H NMR (300 MHz, [D₆]acetone, 22°C): δ = 8.70 (s, 16 H), 8.44 (d, *J*=8.1 Hz, 4 H), 8.40 (s, 4 H), 8.14 (dd, *J*=2.1, 7.8 Hz, 8 H), 7.96 (dd, *J*=1.8, 7.8 Hz, 8 H), 7.74 (dd, *J*=1.5, 7.8 Hz, 4 H), 7.63 (d, *J*=8.5 Hz, 8 H), 7.55 (d, *J*=8.1 Hz, 8 H), 7.16 (d, *J*=5.1 Hz, 4 H), 6.94 (dd, *J*=1.5, 5.7 Hz, 4 H), 6.20 (dd, *J*=1.8, 4.8 Hz, 4 H), 2.64 (s, 24 H), 1.79 (dd, *J*=1.8, 4.8 Hz, 4 H); ¹³C NMR (125.7 MHz, [D₆]acetone/CH₂Cl₂, 22°C) (19 of 22 signals): δ = 159.5, 154.9, 152.2, 145.1, 144.3, 140.0, 138.4, 137.6, 134.6, 134.3, 132.3, 128.2, 127.9, 127.5, 125.2,

122.2, 120.5, 120.2, 21.4; MS (ESI+): $m/z = 1203$ [25%, $M - 2PF_6$]²⁺, 957 [5%, $M - 2TTP, PF_6$]⁺, 805 [45%, $M - TTP, 2PF_6$]²⁺, 406 [100%, $M - 2TTP, 2PF_6$]²⁺; UV/Vis (CH₂Cl₂): λ_{max} / nm ($\log \epsilon / M^{-1}cm^{-1}$) = 242 (4.89), 279 (4.97), 286 (4.98), 316 (4.95), 413 (5.66), 493 (4.60), 532 (4.66), 567 (4.19); Selected IR (microscope): $\nu = 1961$ (CO) cm^{-1} .



2,2':4,4'':4',4'''-quaterpyridyl (dpybpy) (9)¹⁸: A solid mixture of 4,4'-bipyridine (7.5 g 48 mmol) and 10 % palladium on carbon (1.0 g) was heated in a 10 mL round bottom flask at 160°C for 3 days at which time a precipitate had formed. The crude product was dissolved in hot EtOH and filtered to remove an insoluble solid. The mother liquor was treated with decolorizing charcoal then filtered hot. The mother liquor was concentrated until a precipitate formed and refrigerated overnight. The product was collected by vacuum filtration and dried under vacuum. Yield: 5.6 g (75%).

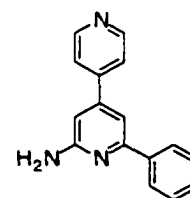
¹H NMR (300 MHz, CDCl₃, 22°C): $\delta = 8.81$ (dd, $J=0.6, 5.1$ Hz, 2 H), 8.78 (m, 6 H), 7.71 (dd, $J=1.8, 4.8$ Hz, 4 H), 7.60 (dd, $J=2.1, 5.1$ Hz, 2 H); HRMS (EI) Calcd for M (C₂₀H₁₄N₄). 310.1219. Found: 310.1218.



[(Cyanomethyl) Pyridinium Iodide]²²: 2-chloroacetonitrile (45.0 g, 596 mmol) and KI (110 g, 662 mmol) were heated in methanol at reflux for 4 h. The mixture was then cooled

to ambient temperature and concentrated to dryness. The residual oil was dissolved in CH_2Cl_2 (100 mL) and filtered to remove inorganic salts. The filtrate was dried over MgSO_4 and filtered, and pyridine (200 mL) was added dropwise over a period of 1 h. The mixture was stirred at ambient temperature overnight. The resulting yellow precipitate was collected by filtration, washed with Et_2O and dried under vacuum. Yield: 113 g (75%).

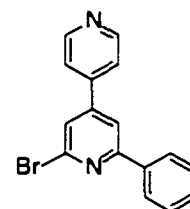
^1H NMR (300 MHz, $[\text{D}_6]\text{DMSO}$, 22°C): $\delta = 9.20$ (m, 2 H), 8.75 (m, 1 H), 8.28 (m, 2 H), 6.03 (s, 2 H).



2-amino-6-phenyl-4,4'-bipyridine (13)¹¹: To a solid suspension containing 1-phenyl-3-(4'-pyridyl)-2-propenone (4.5 g, 21.7 mmol) and cyanomethylpyridinium iodide (5.4 g, 22.0 mmol) was added an acetic acid solution (10 mL) containing NH_4OAc (8.0 g, 104 mmol) and the reaction mixture was heated at reflux for 15 h. The solution was cooled and concentrated to give a tar. The residue was sonicated with $\text{MeOH}/\text{H}_2\text{O}$ (50:50) until a solid appeared which was collected by vacuum filtration and washed with $\text{MeOH}/\text{H}_2\text{O}$ to afford the acetamido derivative as a beige solid (1.90 g). The filtrate was concentrated to dryness and redissolved in absolute EtOH (10 mL) and treated with 48% HBr (6 mL) and heated under reflux for 3 h. The reaction mixture was refrigerated producing a solid which was collected by vacuum filtration and washed with cold EtOH followed by ether to give

the hydrobromide derivative as a yellow-brown solid (2.5 g). The acetamido derivative was treated with 48 % HBr in EtOH following the same procedure as mentioned above to yield 2.5 g of the hydrobromide. Combined yield: 5.0 g (70%).

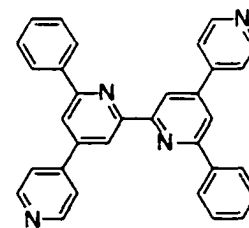
Mp. 118-119°C; ¹H NMR (300 MHz, CDCl₃, 22°C): δ = 8.70 (dd, *J*=1.8, 6.3 Hz, 2 H), 7.96 (m, 2 H), 6.58 (d, *J*=7.0 Hz, 1 H), 7.51 (dd, *J*=1.5, 6.3 Hz, 2 H), 7.40 (m, 2 H), 7.28 (d, *J*=1.5 Hz, 1 H) 6.65 (d, *J*=1.5 Hz, 1 H), 4.65 (bs, 2 H); ¹H NMR (300 MHz, D₂O, 22°C) (HBr salt): δ = 8.88 (dd, *J*=1.8, 6.3 Hz, 2 H), 8.32 (dd, *J*=1.5, 6.3 Hz, 2 H), 7.74 (m, 2 H), 7.56 (m, 3 H), 7.39 (d, *J*=1.5 Hz, 1 H) 7.29 (d, *J*=1.5 Hz, 1 H); ¹H NMR (300 MHz, CDCl₃, 22°C) (acetamide): δ = 8.75 (dd, *J*=1.8, 6.3 Hz, 2 H), 8.45 (br s, 1 H), 8.13 (br s, 1 H), 7.98 (m, 2 H), 7.69 (d, *J*=1.5 Hz, 1 H), 7.63 (dd, *J*=1.5, 6.3 Hz, 2 H), 7.50 (m, 3H) 2.24 (s, 3H); HRMS (EI) Calcd for M (C₁₆H₁₃N₂). 247.1110. Found: 247.1110; IR (microscope): ν = 3423, 3278, 3149, 3062, 2208, 1623, 1594, 1579, 1538, 1516, 1498, 1438, 1466, 1406, 1376, 1325, 1293, 1249, 1071, 1000, 823, 778, 695, 668, 621 cm⁻¹.



2-bromo-6-phenyl-4,4'-bipyridine (14): Using a mechanical stirrer (teflon paddle) 2-amino-6-phenyl-4,4'-bipyridine (**13**) (2.5 g, 7.65 mmol) was added to a 48% HBr (5 mL) and cooled to -20°C using a dryice-acetone bath. To this stirred solution was added bromine (1 mL) which caused the solution to thicken and was stirred at -20°C for 45 min.

Over a period of 2h the mixture was then allowed to warm to ambient temperature and then cooled back down to -20°C . An aqueous solution of NaNO_2 (2 mL) was added dropwise and kept at -20°C until bubbles formed (1 h). Over a period of 2 h the solution was allowed to warm to ambient temperature and the dark red solution was stirred for an additional 2 h. The mixture was cooled to and maintained at -15°C and powdered NaOH was added until the solution was at a pH of 9 (indicator paper). The solution turned bright yellow and a beige tar was left on the stirring paddle and was stirred for 2 h. Stirring was stopped and the yellow solution was decanted and discarded. The paddle and tar were sonicated in water until a solid was produced and the solid was collected by filtration. The solid was then dissolved in CH_2Cl_2 (200 mL), transferred to a separatory funnel and washed with 5% NaOH (2×100 mL), the organic layer was then dried (Na_2SO_4) and evaporated. Column chromatography (activity II Al_2O_3 , 1:1 CH_2Cl_2 /Hexanes) afforded the bromide as a white solid. Yield: 1.70 g (72%).

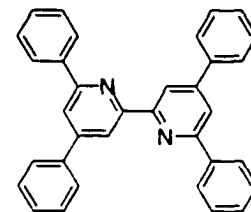
Mp $124\text{--}126^{\circ}\text{C}$; ^1H NMR (300 MHz, CD_2Cl_2 , 22°C): $\delta = 8.75$ (d, $J=6.3$ Hz, 2 H), 8.05 (m, 2 H), 7.93 (d, $J=1.5$, 1 H), 7.68 (d, $J=1.5$ Hz, 1 H) 7.53 (m, 5 H); ^{13}C NMR APT (75.5 MHz, CD_2Cl_2 , 22°C): $\delta = 159.5$ (C), 151.2 (CH), 149.7 (C), 144.8 (C), 143.2 (C), 137.7 (C), 130.4 (CH), 129.3 (CH), 127.4 (CH), 124.5 (CH), 121.8 (CH), 117.7 (CH); HRMS (EI) Calcd for M ($\text{C}_{16}\text{H}_{11}\text{N}_2^{81}\text{Br}$) 312.0085; ($\text{C}_{16}\text{H}_{11}\text{N}_2^{79}\text{Br}$) 310.0106. Found: 312.0075; 310.0099; IR (microscope): $\nu = 3064, 3041, 2990, 1587, 1560, 1523, 1497, 1418, 1385, 1309, 1259, 1226, 1189, 1153, 1097, 1075, 1052, 1026, 999, 980, 915, 870, 816, 790, 776, 724, 696, 690, 669, 648, 632, 619, 612, 589$ cm^{-1} .



4,4':6,6'-(4'',4'''-dipyridyl)-(diphenyl)-2,2'-bipyridine (dpyphbpy) (15) : All of the following manipulations require anhydrous and inert conditions. To a stirred solution of thionyl chloride (2 mL) was added $\text{NiCl}_2 \cdot 6\text{H}_2\text{O}$ and the mixture was heated at reflux until the solid changed from green to yellow in color. The thionyl chloride was removed under reduced pressure and was dried under vacuum (2 mmHg). The anhydrous NiCl_2 was placed under an inert atmosphere of argon. A mixture of NiCl_2 (330 mg, 1.40 mmol), PPh_3 (1.10 g, 4.20 mmol), Zn dust (823 mg, 12.59 mmol) and NaI (500 mg, 3.30 mmol) in freshly distilled THF (25 mL) was warmed to 50°C for 30 min, resulting in a blood red solution. To this solution was added 2-bromo-6-phenyl-4,4'-bipyridine (14) (870 mg, 2.81 mmol) in THF (10 mL) and the mixture heated at 60°C for 15 h. The mixture was quenched with 6 M HCl (50 mL), made basic with concentrated ammonia solution, filtered and extracted three times with CH_2Cl_2 . The combined organic layers were washed with brine, dried (MgSO_4) and evaporated to afford the crude product which was recrystallized from a mixture of EtOH and water. Yield: 487 mg (75%).

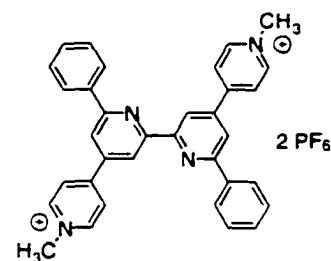
Mp $286\text{--}288^\circ\text{C}$; ^1H NMR (300 MHz, CDCl_3 , 22°C): δ = 8.86 (d, $J=1.5$ Hz, 2 H), 8.21 (dd, $J=1.5, 6.9$ Hz, 4 H), 8.21 (m, 4 H), 8.01 (d, $J=1.5$ Hz, 2 H), 7.73 (dd, $J=1.5, 6.9$ Hz, 4 H), 7.54 (m, 6 H); ^{13}C NMR (125.7 MHz, CD_2Cl_2 , 22°C): δ = 157.9, 156.9, 151.0, 148.1, 146.5, 139.3, 129.8, 129.2, 127.5, 122.1, 119.0, 118.0; HRMS (EI) Calcd for M

(C₃₂H₂₂N₄). 462.1845. Found: 462.1855; IR (microscope): $\nu = 3057, 3038, 1588, 1564, 1538, 1495, 1386, 1305, 1256, 1222, 1086, 1074, 1024, 995, 986, 891, 826, 775, 739, 694, 667, 637, 622, 613 \text{ cm}^{-1}$.



4,4':6,6'-tetraphenyl-2,2'-bipyridine (16)¹¹ : A suspension of 1-(phenacyl)-pyridinium chloride (or bromide) (2.0 g, 8.43 mmol), 1,6-diphenylhexa-1,5-diene-3,4-dione (0.6 g, 2.11 mmol), and ammonium acetate (6.8 g) in glacial acetic/propionic acid (5 mL/1 mL) was heated a reflux for 3 h. The acetic/propionic acid mixture was removed under reduced pressure and the residue dissolved in hot methanol. The product did not dissolve in hot methanol and was collected by filtration (0.62 g, 64%).

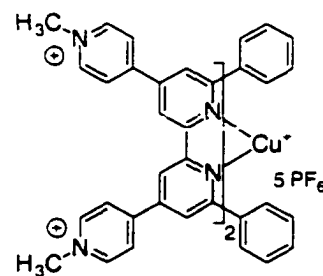
¹H NMR (300 MHz, CDCl₃, 22°C): $\delta = 8.86$ (d, $J=1.2$ Hz, 2 H), 8.21 (dd, $J=1.5, 6.9$ Hz, 4 H), 7.99 (d, $J=1.8$ Hz, 2 H), 7.83 (dd, $J=1.5, 6.9$ Hz, 4 H), 7.51 (m, 12 H).



4,4':6,6'-(1'',1'''-dimethyl-4'',4'''-dipyridinium)-(diphenyl)-2,2'-bipyridine hexafluorophosphate (medpyphbp) (17) : A solution of dpyphbpy (15) (50.0 mg, 1.09×10^{-1} mmol) in CH₃CN (10.0 mL) was treated with an excess of CH₃I (1 mL) and

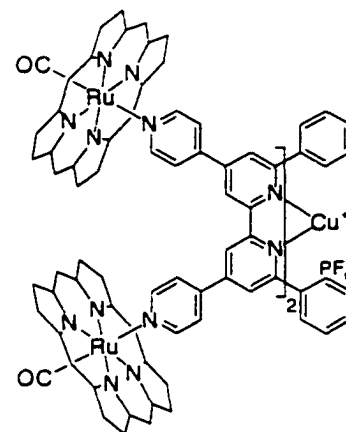
stirred at reflux for 22 h. The mixture was concentrated and the resulting solid product was suspended in CH_2Cl_2 and filtered. The solid was dissolved in water and treated with excess NH_4PF_6 which precipitated the product. The product was collected by filtration and recrystallized from a mixture of $\text{EtOH}/\text{CH}_3\text{CN}$. Yield: 63 mg (74 %).

Mp 345–346°C; ^1H NMR (500 MHz, CD_3NO_2 , 22°C): δ = 9.12 (d, J =1.5 Hz, 2 H), 8.91 (d, J =7.0 Hz, 4 H), 8.62 (d, J =7.0 Hz, 4 H), 8.42 (d, J =1.5 Hz, 2 H), 8.36 (d, J =7.0 Hz, 4 H), 7.61 (m, 6 H), 4.58 (s, 6 H); ^{13}C NMR (125.7 MHz, CD_3NO_2 , 22°C): δ = 159.8, 157.9, 155.9, 147.0, 145.6, 139.6, 131.5, 130.5, 128.6, 127.5, 120.6, 119.1, 49.4; HRMS (ESI+): m/z Calcd for M^+ ($\text{C}_{34}\text{H}_{28}\text{N}_4\text{F}_6\text{P}$) 637.1950. Found: 637.1956.



[Cu(medpyphbpy) $_2$][PF $_6$] $_5$ (17a) : To a stirred solution of medpyphbpy (17) (20.0 mg, 0.026 mmol) in CH_3NO_2 (5 mL) was added $\text{Cu}(\text{CH}_3\text{CN})_4\text{PF}_6$ (4.8 mg, 0.013 mmol) which was accompanied with an immediate change in color of the solution from colorless to brown-red. The solution was concentrated to 2 mL and ether was added to precipitate out the copper complex. The product was collected by vacuum filtration and washed with $\text{MeOH}/\text{Et}_2\text{O}$ (1:1) and was then dried under vacuum. Yield: 20.0 mg (92%).

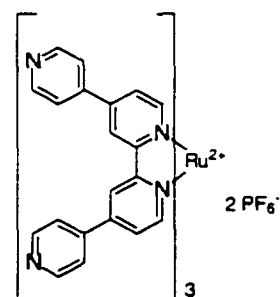
$^1\text{H NMR}$ (500 MHz, CD_3NO_2 , 22°C): $\delta = 9.00$ (d, $J=6.5$ Hz, 8 H), 8.72 (s, 4 H), 8.61 (d, $J=6.5$ Hz, 8 H), 8.17 (s, 4 H), 7.91 (d, $J=7.0$ Hz, 8 H), 7.08 (m, 12 H), 4.61 (s, 12 H);
 MS (ESI+): $m/z = 1627$ $[\text{M} - \text{PF}_6]^+$.



[Cu(dpyphbpy) $_2$][PF $_6$][Ru(TTP)(CO)] $_4$ (18) : A solution of dpyphbpy (15) (10.0 mg, 2.17×10^{-2} mmol) in 5% acetone/ CH_2Cl_2 (5.0 mL) was treated with 2.2 molar equivalents of Ru(TTP)(CO)(EtOH) (4) (37.0 mg, 4.35×10^{-2} mmol) followed by $\text{Cu}(\text{CH}_3\text{CN})_4\text{PF}_6$ (4.0 mg, 1.07×10^{-2} mmol) and stirred at ambient temperature for 22 h. The solvents were evaporated to dryness and the resulting solid was dissolved in CH_2Cl_2 . The product was precipitated by adding a mixture of Et_2O /pentane (20:80) and collected by filtration. The product was washed with a mixture of Et_2O /pentane (20:80) and dried under vacuum. Yield: 45 mg (97%).

M.p. $>300^\circ\text{C}$ (decomp); $^1\text{H NMR}$ (500 MHz, $[\text{D}_6]\text{acetone}/\text{CD}_2\text{Cl}_2$, 22°C): $\delta = 8.66$ (s, 32 H), 8.11 (dd, $J=1.5, 7.5$ Hz, 16 H), 7.84 (dd, $J=1.5, 7.5$ Hz, 16 H), 7.63 (d, $J=7.5$ Hz, 16 H), 7.45 (d, $J=7.5$ Hz, 16 H), 6.88 (s, 4 H), 6.55 (d, $J=7.5$ Hz, 8 H), 6.50 (s, 4 H), 6.06 (t, $J=7.5$ Hz, 4 H), 5.87 (t, $J=7.5$ Hz, 8 H), 5.45 (d, $J=7.0$ Hz, 8 H), 2.67 (s, 48 H),

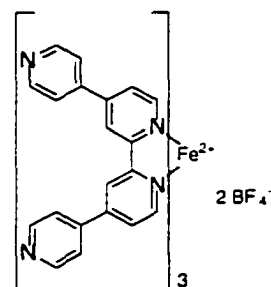
1.54 (d, $J=6.5$ Hz, 8 H); ^1H NMR (300 MHz, CD_2Cl_2 , 22°C): δ = 8.67 (s, 32 H), 8.13 (dd, $J=1.5, 7.5$ Hz, 16 H), 7.89 (dd, $J=1.5, 7.5$ Hz, 16 H), 7.63 (d, $J=7.5$ Hz, 16 H), 7.45 (d, $J=7.5$ Hz, 16 H), 6.45 (d, $J=7.5$ Hz, 8 H), 6.33 (s, 4 H), 6.28 (s, 4 H), 6.11 (t, $J=7.5$ Hz, 4 H), 5.92 (t, $J=7.5$ Hz, 8 H), 5.26 (d, $J=7.0$ Hz, 8 H), 2.70 (s, 48 H), 1.60 (d, $J=6.5$ Hz, 8 H); ^{13}C NMR (125.7 MHz, $[\text{D}_6]\text{acetone}/\text{CD}_2\text{Cl}_2$, 22°C) (22 of 23 signals): δ = 156.6, 152.5, 145.0, 144.9, 143.9, 142.6, 139.7, 137.5, 137.1, 134.6, 133.9, 132.0, 131.7, 128.7, 127.8, 127.3, 126.9, 126.8, 122.2, 119.6, 118.4, 21.2; MS (ESI+): m/z = 4180 [1%, $\text{M} - \text{PF}_6^-$], 3383 [1%, $\text{M} - \text{TTP}, \text{PF}_6^-$], 2584 [4%, $\text{M} - 2\text{TTP}, \text{PF}_6^-$], 1789 [5%, $\text{M} - 3\text{TTP}, \text{PF}_6^-$], 987 [100%, $\text{M} - 4\text{TTP}, \text{PF}_6^-$]; UV/Vis (CH_2Cl_2): λ_{max} / nm ($\log \epsilon$ / $\text{M}^{-1}\text{cm}^{-1}$) = 246 (5.25), 308 (5.02), 412 (5.93), 532 (4.88), 567 (4.37); Selected IR (microscope): ν = 1950 (CO) cm^{-1} .



$[\text{Ru}(\text{dpybpy})_3][\text{PF}_6]_2$ (19)²²: A solution of dpybpy (**9**) (120 mg, 0.387 mmol) and $\text{Ru}[\text{DMSO}]_4\text{Cl}_2$ (56 mg, 0.116 mmol) in ethylene glycol (5 mL) was heated at reflux for 3 h. The reaction mixture was cooled to room temperature, diluted with water (3 mL) and treated with an excess of a methanolic solution of NH_4PF_6 . The resulting dark red precipitate was collected by filtration on a Celite pad, washed with water and the crude product was removed by eluting with acetonitrile. The crude mixture was concentrated to

5 mL and then chromatographed through silica gel with acetonitrile-saturated aqueous potassium nitrate-water (7:1:2) as eluent. After discarding the initial band, the red-orange band was collected and concentrated until a precipitate formed. The precipitate was collected by filtration, redissolved in acetonitrile and treated with excess NH_4PF_6 . The product was precipitated as a red solid by the addition of ether, collected by filtration and washed 95% EtOH to remove excess NH_4PF_6 and was then dried under vacuum. Yield: 30 mg (20%).

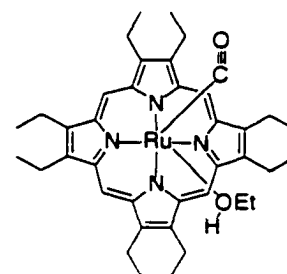
^1H NMR (500 MHz, $[\text{D}_6]$ acetone, 22°C): $\delta = 9.51$ (d, $J=1.5$ Hz, 6 H), 8.82 (d, $J=5.0$ Hz, 12 H), 8.42 (d, $J=5.5$ Hz, 6 H), 8.02 (dd, $J=2.0, 6.0$ Hz, 12 H), 7.94 (d, $J=6.0$ Hz, 6 H); ^{13}C NMR (125.7 MHz, $[\text{D}_6]$ acetone, 22°C): $\delta = 158.9, 153.6, 151.4, 148.1, 144.3, 126.5, 123.6, 122.5$; MS (ESI+): $m/z = 516$ $[\text{M} - 2\text{PF}_6]^{2+}$, 1177 $[\text{M} - \text{PF}_6]^+$; UV/Vis (1% $\text{CH}_3\text{NO}_2/\text{CH}_2\text{Cl}_2$): $\lambda_{\text{max}} / \text{nm}$ ($\log \epsilon / \text{M}^{-1}\text{cm}^{-1}$) = 328 (4.60), 381 (4.48), 496 (4.57).



$[\text{Fe}(\text{dpybpy})_3][\text{BF}_4]_2$ (20)¹⁸: A solution of dpybpy (9) (150 mg, 0.484 mmol) and $\text{Fe}(\text{BF}_4)_2 \cdot 6\text{H}_2\text{O}$ (54 mg, 0.161 mmol) in MeOH (25 mL) was heated at reflux for 3 h. The reaction mixture was cooled to room temperature and concentrated to dryness. The precipitate was suspended in 95% EtOH containing NaBF_4 . The product was precipitated as a purple solid by the addition of ether, collected by filtration and washed

with 95% EtOH to remove excess NaBF₄ and was then dried under vacuum. Yield: 135 mg (72%).

¹H NMR (300 MHz, [D₆]acetone/CD₃OD 22°C): δ = 9.45 (s, 6 H), 8.75 (d, *J*=5.7 Hz, 12 H), 7.96 (m, 24 H); ¹H NMR (300 MHz, [D₆]acetone, 22°C): δ = 9.00 (d, *J*=2.1 Hz, 6 H), 8.82 (dd, *J*=1.5, 4.8 Hz, 12 H), 7.98 (d, *J*=5.7 Hz, 6 H), 7.85 (dd, *J*=1.5, 4.8 Hz, 12 H), 7.94 (dd, *J*=2.1, 5.7 Hz, 6 H); MS (ESI+): *m/z* = 493 [M - 2BF₄]²⁺; UV/Vis (1% CH₃NO₂/CH₂Cl₂): λ_{max} / nm (log ε / M⁻¹cm⁻¹) = 328 (4.60), 381 (4.48), 496 (4.57).

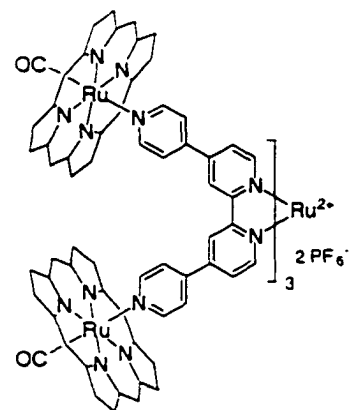


[Ru(OEP)(CO)(EtOH)] (21): Octaethylporphyrin (0.500 g, 0.935 mmol) and triruthenium dodecacarbonyl (0.75 g, 1.17 mmol) were heated in phenol (2.0 g) at reflux for 45 min. The solution was then cooled and EtOH (1 mL) was added. The crude product was precipitated by the addition of water then collected by vacuum filtration and washed with water. The residue was chromatographed through Alumina (neutral, activity II-III) eluting first with CH₂Cl₂ and finally with a mixture of EtOH/CH₂Cl₂ (5/95) which removed a red band. The red band was concentrated to dryness to give a red solid which was recrystallized from ethanol. Yield: 510 mg (82%).

^1H NMR (300 MHz, $[\text{D}_6]$ acetone, 22°C): $\delta = 10.04$ (s, 4 H), 4.07 (q, $J=7.8$ Hz, 16 H), 1.91 (t, $J=7.8$ Hz, 24 H); ^{13}C NMR (125.7 MHz, CD_2Cl_2 , 22°C): $\delta = 183.8$, 142.5, 141.9, 99.1, 55.4, 20.1, 18.7, 14.6; Selected IR (microscope): $\nu = 1936$ (CO) cm^{-1} .

[Ru(OEP)(CO)(py)] (22): Ru(OEP)(CO)(EtOH) (21) (25 mg, 0.0378 mmol) was dissolved in CH_2Cl_2 (5 mL) and pyridine (0.5 mL) was added. The solution was evaporated to dryness and hexanes (5 mL) was added, the residue was sonicated, filtered and then washed with hexanes. Yield: 27 mg (96%).

^1H NMR (500 MHz, CD_2Cl_2 , 22°C): $\delta = 9.90$ (s, 4 H), 5.89 (m, 1 H), 4.94 (m, 2 H), 4.02 (m, 16 H), 1.91 (t, $J=7.8$ Hz, 24 H), 0.84 (m, 2 H); UV/Vis (CH_2Cl_2): λ_{max} / nm ($\log \epsilon / \text{M}^{-1}\text{cm}^{-1}$) = 250 (4.27), 323 (4.20), 395 (5.31), 517 (4.10), 549 (4.30); Selected IR (microscope): $\nu = 1934$ (CO) cm^{-1} .



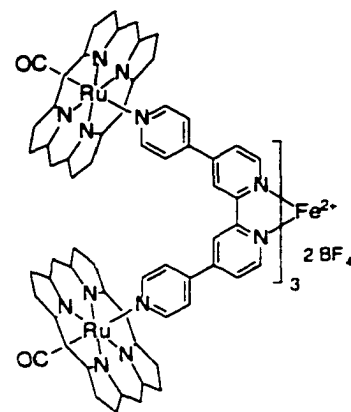
[Ru(dpybpy) $_3$][PF $_6$] $_2$ [Ru(TTP)(CO)] $_6$ 19(TTP): A solution of [Ru(dpybpy) $_3$][PF $_6$] $_2$ (19) (10.0 mg, 7.56×10^{-3} mmol) in acetone (5.0 mL) was treated with 6.3 molar equivalents of Ru(TTP)(CO)(EtOH) (4) (40.0 mg, 4.76×10^{-2} mmol) and stirred with gentle heating at

45°C for 22 h. The solvents were evaporated to dryness and the resulting solid was dissolved in CH₂Cl₂. The product was precipitated by adding a mixture of Et₂O/pentane (20:80) and collected by filtration. The product was washed with a mixture of Et₂O/pentane (20:80) and dried under vacuum. Yield: 43.0 mg (93%).

M.p. >300°C (decomp); ¹H NMR (300 MHz, [D₆]acetone, 22°C): δ = 8.62 (s, 48 H), 8.13 (dd, *J*=2.1, 7.8 Hz, 24 H), 7.75 (dd, *J*=1.8, 7.8 Hz, 24 H), 7.71 (d, *J*=8.5 Hz, 24 H), 7.45 (d, *J*=8.1 Hz, 24 H), 7.27 (d, *J*=1.8 Hz, 6 H), 6.53 (d, *J*=6.3 Hz, 6 H), 6.02 (dd, *J*=1.8, 6.0 Hz, 6 H), 5.16 (d, *J*=6.9 Hz, 12 H), 2.73 (s, 72 H), 1.37 (d, *J*=6.9 Hz, 12 H); ¹H NMR (300 MHz, CD₂Cl₂, 22°C): δ = 8.59 (s, 48 H), 8.09 (dd, *J*=2.1, 7.8 Hz, 24 H), 7.74 (dd, *J*=1.8, 7.8 Hz, 24 H), 7.61 (d, *J*=8.5 Hz, 24 H), 7.37 (d, *J*=8.1 Hz, 24 H), 6.42 (d, *J*=1.8 Hz, 6 H), 5.91 (d, *J*=6.3 Hz, 6 H), 5.81 (dd, *J*=1.8 Hz, 6.0 Hz, 6 H), 4.97 (dd, *J*=1.5, 6.9 Hz, 12 H), 2.71 (s, 72 H), 1.35 (dd, *J*=1.5, 6.9 Hz, 12 H); ¹³C NMR (125.7 MHz, CD₂Cl₂, 22°C) (19 of 19 signals): δ = 181.4, 156.8, 151.6, 145.2, 144.8, 144.5, 142.2, 140.3, 138.1, 134.9, 134.5, 132.2, 128.5, 128.0, 124.5, 122.5, 122.1, 120.1, 21.6; MS (ESI+): *m/z* = 2911 [10%, M – 2PF₆]²⁺, 2511 [13%, M – TTP, 2PF₆]²⁺, 2112 [12%, M – 2TTP, 2PF₆]²⁺, 1713 [10%, M – 3TTP, 2PF₆]²⁺, 1314 [12%, M – 4TTP, 2PF₆]²⁺, 915 [14%, M – 5TTP, 2PF₆]²⁺, 516 [100%, M – 6TTP, 2PF₆]²⁺; UV/Vis (CH₂Cl₂): λ_{max} / nm (log ε / M⁻¹cm⁻¹) = 248 (5.48), 311 (5.34), 411 (6.16), 533 (5.09), 568 (4.57); Selected IR (microscope): ν = 1968 (CO) cm⁻¹.

[Ru(dpybpy)₃][PF₆]₂[Ru(OEP)(CO)]₆ 19(OEP): A solution of [Ru(dpybpy)₃][PF₆]₂ (**19**) (10.0 mg, 7.56×10⁻³ mmol) in acetone (5.0 mL) was treated with 6.3 molar equivalents of Ru(OEP)(CO)(EtOH) (**21**) (35.0 mg, 4.76×10⁻² mmol) and stirred at ambient temperature for 22 h. The solvents were evaporated to dryness and the resulting solid was dissolved in CH₂Cl₂. The product was precipitated by adding a mixture of Et₂O/pentane (20:80) and collected by filtration. The product was washed with a mixture of Et₂O/pentane (20:80) and dried under vacuum. Yield: 40.0 mg (98%).

M.p. >300°C (decomp); ¹H NMR (300 MHz, [D₆]acetone, 22°C): δ = 9.93 (s, 24 H), 6.94 (s, 6 H), 6.15 (d, *J*=5.7 Hz, 6 H), 5.73 (d, *J*=6.0 Hz, 6 H), 4.77 (d, *J*=6.6 Hz, 12 H), 4.16 (m, 96 H), 1.93 (m, 144 H), 0.73 (d, *J*=6.0 Hz, 12 H); ¹H NMR (300 MHz, CD₂Cl₂, 22°C): δ = 9.93 (s, 24 H), 6.98 (s, 6 H), 6.53 (d, *J*=5.7 Hz, 6 H), 5.76 (dd, *J*=1.8, 6.3 Hz, 6 H), 4.81 (d, *J*=6.9 Hz, 12 H), 4.16 (m, 96 H), 1.93 (m, 144 H), 0.73 (d, *J*=6.0 Hz, 12 H); ¹³C NMR (125.7 MHz, CD₂Cl₂, 22°C) (14 of 14 signals): δ = 183.0, 156.5, 151.1, 145.1, 144.3, 142.9, 141.9, 141.4, 124.4, 121.3, 119.0, 98.9, 20.3, 19.0; MS (ESI+): *m/z* = 2503 [10%, M - 2PF₆]²⁺, 2171 [10%, M - OEP, 2PF₆]²⁺, 1839 [10%, M - 2OEP, 2PF₆]²⁺, 1509 [10%, M - 3OEP, 2PF₆]²⁺, 1178 [10%, M - 4OEP, 2PF₆]²⁺, 847 [15%, M - 5OEP, 2PF₆]²⁺, 516 [100%, M - 6OEP, 2PF₆]²⁺; UV/Vis (CH₂Cl₂): λ_{max} / nm (log ε / M⁻¹cm⁻¹) = 253 (5.37), 312 (5.33), 394 (6.07), 516 (5.00), 548 (5.14); Selected IR (microscope): ν = 1942 (CO) cm⁻¹.



[Fe(dpybpy)₃][BF₄]₂[Ru(TTP)(CO)]₆ 20(TTP): A solution of [Fe(dpybpy)₃][BF₄]₂ (**20**) (8.8 mg, 7.56×10⁻³ mmol) in acetone (5.0 mL) was treated with 6.3 molar equivalents of Ru(TTP)(CO)(EtOH) (**4**) (40.0 mg, 4.76×10⁻² mmol) and stirred with gentle heating at 45°C for 22 h. The solvents were evaporated to dryness and the resulting solid was dissolved in CH₂Cl₂. The product was precipitated by adding a mixture of Et₂O/pentane (20:80) and collected by filtration. The product was washed with a mixture of Et₂O/pentane (20:80) and dried under vacuum. Yield: 38 mg (84%).

M.p. >300°C (decomp); ¹H NMR (300 MHz, [D₆]acetone/CD₂Cl₂, 22°C): δ = 8.60 (s, 48 H), 8.08 (dd, *J*=2.1, 7.8 Hz, 24 H), 7.72 (dd, *J*=1.8, 7.8 Hz, 24 H), 7.62 (d, *J*=8.5 Hz, 24 H), 7.40 (d, *J*=8.1 Hz, 24 H), 7.13 (d, *J*= 1.8, 6 H), 5.98 (d, *J*=6.3 Hz, 6 H), 5.89 (dd, *J*=1.8, 6.0 Hz, 6 H), 5.08 (dd, *J*=1.5, 6.9 Hz, 12 H), 2.71 (s, 72 H), 1.33 (dd, *J*=1.5, 6.9 Hz, 12 H); ¹H NMR (300 MHz, CD₂Cl₂, 22°C): δ = 8.59 (s, 48 H), 8.09 (dd, *J*=2.1, 7.8 Hz, 24 H), 7.74 (dd, *J*=1.8, 7.8 Hz, 24 H), 7.61 (d, *J*=8.5 Hz, 24 H), 7.37 (d, *J*=8.1 Hz, 24 H), 6.42 (d, *J*= 1.8 Hz, 6 H), 5.91 (d, *J*=6.3 Hz, 6 H), 5.81 (dd, *J*=1.8, 6.0 Hz, 6 H), 4.97 (dd, *J*=1.5, 6.9 Hz, 12 H), 2.71 (s, 72 H), 1.35 (dd, *J*=1.5, 6.9 Hz, 12 H); MS

(ESI+): $m/z = 2889$ [10%, $M - 2BF_4$] $^{2+}$, 2489 [15%, $M - TTP, 2BF_4$] $^{2+}$, 2089 [20%, $M - 2TTP, 2BF_4$] $^{2+}$, 1689 [20%, $M - 3TTP, 2BF_4$] $^{2+}$, 1292 [20%, $M - 4TTP, 2BF_4$] $^{2+}$, 892 [25%, $M - 5TTP, 2BF_4$] $^{2+}$, 493 [100%, $M - 6TTP, 2BF_4$] $^{2+}$; UV/Vis (CH_2Cl_2): λ_{max} / nm ($\log \epsilon / M^{-1}cm^{-1}$) = 251 (5.44), 316 (5.26), 411 (6.05), 533 (5.05), 567 (4.71); Selected IR (microscope): $\nu = 1953$ (CO) cm^{-1} .

[Fe(dpybpy) $_3$][BF $_4$] $_2$ [Ru(OEP)(CO)] $_6$ 20(OEP): A solution of [Fe(dpybpy) $_3$][BF $_4$] $_2$ (**20**) (11.0 mg, 9.49×10^{-3} mmol) in acetone (5.0 mL) was treated with 6.3 molar equivalents of Ru(OEP)(CO)(EtOH) (**21**) (42.0 mg, 5.98×10^{-2} mmol) and stirred with gentle heating at 45°C for 22 h. The solvents were evaporated to dryness and the resulting solid was dissolved in CH_2Cl_2 . The product was precipitated by adding a mixture of Et $_2$ O/pentane (20:80) and collected by filtration. The product was washed with a mixture of Et $_2$ O/pentane (20:80) and dried under vacuum. Yield: 32 mg (70%).

M.p. >300°C (decomp); 1H NMR (500 MHz, [D $_6$]acetone, 22°C): $\delta = 9.96$ (s, 24 H), 6.95 (s, 6 H), 5.83 (d, $J=6.5$ Hz, 6 H), 5.72 (d, $J=6.0$ Hz, 6 H), 4.81 (d, $J=6.5$ Hz, 12 H), 4.10 (m, 96 H), 1.96 (m, 144 H), 0.69 (d, $J=7.0$ Hz, 12 H); 1H NMR (300 MHz, CD_2Cl_2 , 22°C): $\delta = 9.93$ (s, 24 H), 6.98 (s, 6 H), 6.53 (d, $J=5.7$ Hz, 6 H), 5.76 (dd, $J=1.8, 6.3$ Hz, 6 H), 4.81 (d, $J=6.9$ Hz, 12 H), 4.16 (m, 96 H), 1.93 (m, 144 H), 0.73 (d, $J=6.0$ Hz, 12 H); ^{13}C NMR (125.7 MHz, [D $_6$]acetone, 22°C) (14 of 14 signals): $\delta = 183.0, 158.5, 153.7, 145.1, 145.0, 142.9, 141.9, 141.4, 124.1, 120.8, 119.1, 98.9, 20.3, 19.0$; MS (ESI+): $m/z = 2479$ [10%, $M - 2BF_4$] $^{2+}$, 2146 [5%, $M - OEP, 2BF_4$] $^{2+}$, 1815 [10%, $M -$

2OEP, 2BF₄]²⁺, 1487 [5%, M – 3OEP, 2BF₄]²⁺, 1156 [10%, M – 4OEP, 2BF₄]²⁺, 825 [15%, M – 5OEP, 2BF₄]²⁺, 493 [100%, M – 6OEP, 2BF₄]²⁺; UV/Vis (CH₂Cl₂): λ_{max} / nm (log ε / M⁻¹cm⁻¹) = 252 (5.42), 315 (5.27), 394 (6.10), 517 (5.01), 548 (5.19); Selected IR (μscope): ν = 1941 (CO) cm⁻¹.

X-ray Crystallographic Study: The crystallographic data for the complex [Cu(**16**)₂]PF₆ is shown in Table 2. Crystals of [Cu(**16**)₂]PF₆ were grown from a CH₂Cl₂ solution. X-Ray data were collected on a Bruker PLATFORM/SMART 1000 CCD at 193 K using a graphite-monochromated Mo-K_α radiation (λ = 0.71073 Å) by taking ω scans at 0.2° intervals. The structures were solved by direct methods/fragment search using the computer program DIRDIF-96 and refined by full-matrix least-squares with anisotropic displacement parameters for the non-hydrogen atoms using the computer program SHELXL-93.³² Hydrogen atoms were introduced in their idealized positions as indicated by the sp² geometries of their attached carbon atoms.

Table 2. Crystallographic data for the Pseudotetrahedral Complex [Cu(16)₂]PF₆

Molecular Formula	C ₆₈ H ₄₈ CuF ₆ N ₄ P•0.5CH ₂ Cl ₂
Molecular Weight	M = 1172.08
Crystal size/mm	0.42 × 0.21 × 0.04
Crystal system	triclinic
Space group	<i>P</i> $\bar{1}$ (No. 2)
<i>a</i> /Å	14.579 (2)
<i>b</i> /Å	15.427 (5)
<i>c</i> /Å	16.578 (4)
α /°	73.012 (3)
β /°	66.023 (3)
γ /°	65.533 (3)
<i>Z</i>	2
\bar{V} /Å ³	3066.4 (8)
Density/g cm ⁻³	1.229
μ /mm ⁻¹	0.487
Data collection 2 θ limit/°	53.00
Total data collected	15340 (-10 ≤ <i>h</i> ≤ 18, -13 ≤ <i>k</i> ≤ 19, -20 ≤ <i>l</i> ≤ 20)
Independent reflections	12449 (<i>R</i> _{int} = 0.0538)
Observed data with <i>I</i> ≥ 2 σ (<i>I</i>)	4599
Absorption correction method	Gaussian integration (face indexed)
Range of transmission factors	0.9808–0.8215
Data/restraints/parameters	12449 / 5 ^b / 767
Goodness-of-fit on <i>F</i> ²	0.968
Final <i>R</i> indices [<i>I</i> ≥ 2 σ (<i>I</i>)] ^a	
<i>R</i> ₁ = [<i>F</i> _o ² ≥ 2 σ (<i>F</i> _o ²)]	0.1121
<i>wR</i> ₂ = [<i>F</i> _o ² ≥ 3 σ (<i>F</i> _o ²)]	0.3456
Largest difference peak and hole	1.772 and -1.812 e Å ⁻³

^a $R_1 = \frac{\sum ||F_o| - |F_c||}{\sum |F_o|}$; $wR_2 = \frac{\{\sum [w(F_o^2 - F_c^2)]\}}{\sum [w(F_o^4)]}^{1/2}$.

^b Distance within the disordered solvent dichloromethane molecule were assigned fixed idealized values: *d*(C11S–C1S) = *d*(C12S–C1S) = *d*(C13S–C1S) = 1.80 Å; *d*(C11S...C12S) = *d*(C11S...C13S) = 2.95 Å (C11S and C1S were refined with an occupancy factor of 0.5; C12S and C13S are two sites for the disordered half-occupancy chlorine atom, thus were each refined with an occupancy factor of 0.25).

2.9 – References

1. (a) S. S. Eaton and G. R. Eaton, *Inorg. Chem.*, **1977**, *16*, 72; (b) J. W. Faller, C. C. Chen, and C. J. Malerich, *J. Inorg. Biochem.*, **1979**, *11*, 151.
2. (a) G. M. Brown, F. R. Hopf, J. A. Ferguson, T. J. Meyer and D. G. Whitten, *J. Am. Chem. Soc.*, **1973**, *95*, 5939; (b) J. J. Bonnet, S. S. Eaton, G. R. Eaton, R. H. Holm and J. A. Ibers, *J. Am. Chem. Soc.*, **1973**, *95*, 2141.
3. (a) K. M. Kadish, D. J. Leggett and D. Chang, *Inorg. Chem.*, **1982**, *21*, 3618; (b) K. M. Kadish and D. Chang, *Inorg. Chem.*, **1982**, *21*, 3614; (c) L. M. A. Levine and D. Holten, *J. Phys. Chem.*, **1988**, *92*, 714.
4. J. K. M. Sanders, N. Bampos, Z. Clyde-Watson, S. L. Darling, J. C. Hawley, H.-J. Kim, C. C. Mak and S. J. Webb, in *The Porphyrin Handbook*, eds. K. M. Kadish, K. M. Smith and R. Guilard, Academic Press, New York, 2000, vol. 3, ch 15, p1.
5. (a) W. E. Jones, Jr., R. A. Smith, M. T. Abramo, M. D. Williams, and J. Van Houten, *Inorg. Chem.*, **1989**, *28*, 2281; (b) H.-B. Kim, N. Kitamura, and S. Tazuke, *J. Phys. Chem.*, **1990**, *94*, 1414; (c) M. J. Cook, A. P. Lewis, G. S. G. McAuliffe, V. Skarda, A. J. Thomson, J. L. Glasper, and D. J. Robbins, *J. Chem. Soc., Perkin Trans. II*, **1984**, 1293.
6. V. Gutmann, *Coord. Chem. Rev.*, **1976**, *18*, 225.
7. E. C. Constable and A. M. W. Cargill Thompson, *J. Chem. Soc., Dalton Trans.*, **1992**, 2947.
8. A. D. Alder, F. R. Longo, J. D. Finarelli, J. Goldmacher, J. Assour, and L. Koraskoff, *J. Org. Chem.*, **1967**, *32*, 476.

9. (a) S. S. Eaton and G. R. Eaton, *Inorg. Chem.*, **1977**, *16*, 72; (b) D. P. Rillema, J. K. Nagle, L. F. Barringer, Jr., and T. J. Meyer, *J. Am. Chem. Soc.*, **1981**, *103*, 56.
10. E. C. Constable, J. Lewis, M. C. Liptrot and P. R. Raithby, *Inorg. Chim. Acta*, **1990**, *178*, 47.
11. F. Kröhnke, *Synthesis*, **1976**, 1.
12. A. Sausins and G. Duburs, *Heterocycles*, **1988**, *27*, 269.
13. (a) E. C. Constable and A. M. W. Cargill Thompson, *J. Chem. Soc., Dalton Trans.*, **1994**, 1409; (b) E. C. Constable, A. M. W. Cargill Thompson, D. A. Tocher, and M. A. M. Daniels, *New. J. Chem.*, **1992**, *16*, 855; (c) M. Maestri, N. Armaroli, V. Balzani, E. C. Constable, and A. M. W. Cargill Thompson, *Inorg. Chem.*, **1995**, *34*, 2759.
14. For previous reports of this anisotropy see: (a) K. Funatsu, T. Imamura, A. Ichimura and Y. Sasaki, *Inorg. Chem.*, **1998**, *37*, 4986; (b) A. Prodi, M. T. Indelli, C. J. Kleverlaan, F. Scandola, E. Alessio, T. Gianferrara and L. G. Marzilli, *Chem. Eur. J.*, **1999**, *5*, 2668; (c) M. Ikonen, D. Guez, V. Marvaud and D. Markovitsi, *Chem. Phys. Lett.*, **1994**, *231*, 93 and references therein.
15. J.-P. Sauvage, J.-P. Collin, J.-C. Chambron, S. Guillerez, C. Coudret, V. Balzani, F. Barigelletti, L. De Cola and L. Flamigni, *Chem. Rev.*, **1994**, *94*, 993.
16. (a) J.-P. Collin, A. Harriman, V. Heitz, F. Odobel and J.-P. Sauvage, *J. Am. Chem. Soc.*, **1994**, *116*, 5679; (b) L. Flamigni, F. Barigelletti, N. Armaroli, J.-P. Collin, J.-P. Sauvage and J. A. Gareth Williams, *Chem. Eur. J.*, **1998**, *4*, 1744 and references cited therein.

17. For a detailed description of the triplet state phosphorescence of both components, see: L. M. A. Levine and D. Holten, *J. Phys. Chem.*, **1988**, *92*, 714 and reference 15.
18. R. J. Morgan and A. D. Baker, *J. Org. Chem.*, **1990**, *55*, 1986.
19. (a) M. Meyer, A.-M. Albrecht-Gary, C. O. Dietrich-Buchecker, J.-P. Sauvage, *Inorg. Chem.*, **1999**, *38*, 2279; (b) A. J. Pallenberg, K. S. Koenig, and D. M. Barnhart, *Inorg. Chem.*, **1995**, *34*, 2833; (c) P. J. Burke, D. R. McMillin, and W. R. Robinson, *Inorg. Chem.*, **1980**, *19*, 1211.
20. N. C. Fletcher, F. R. Keene, M. Ziegler, H. Stoeckli-Evans, H. Viebrock and A. von Zelewsky, *Helv. Chim. Acta*, **1996**, *79*, 1192.
21. For nickel(II) coupling reactions of related ligands, see: A. Ford, E. Sinn and S. Woodward, *J. Chem. Soc., Perkin Trans. I*, **1997**, 927.
22. H. Dürr, U. Thiery, P. P. Infelta, and A. M. Braun, *New J. Chem.*, **1989**, *13*, 575.
23. J. B. Paine III, W. B. Kirshner, D. W. Moskowitz, and D. Dolphin, *J. Org. Chem.*, **1976**, *41*, 3857.
24. (a) R. J. Sundberg, in *Comprehensive Heterocyclic Chemistry*, Vol. 4, Chapter 3.06, Pergamon Press, Oxford, 1984; (b) H. Fischer, *Org. Synth., Coll. Vol. 2*, **1943**, 202.
25. M. Barely, J. Y. Becker, G. Domazetis, D. Dolphin, and B. R. James, *Can. J. Chem.*, **1983**, *61*, 2389.
26. (a) M. Barely, D. Dolphin, B. R. James, C. Kirmaier, and D. Holten, *J. Am. Chem. Soc.*, **1984**, *106*, 3937; (b) K. M. Kadish, P. Tagliatesta, Y. Hu, Y. J. Mu, and L. Y. Bao, *Inorg. Chem.*, **1991**, *30*, 3737.
27. A. Antipas, J. W. Buchler, M. Gouterman, and P. D. Smith, *J. Am. Chem. Soc.*, **1978**, *100*, 3015.

28. F. A. Walker, D. Beroiz, and K. M. Kadish, *J. Am. Chem. Soc.*, **1976**, *98*, 3484.
29. A. Prodi, M. T. Indelli, C. J. Kleverlaan, F. Scandola, E. Alessio, T. Gianferrara and L. G. Marzilli, *Chem. Eur. J.*, **1999**, *5*, 2668.
30. D. Rehm and A. Weller, *Isr. J. Chem.*, **1970**, *8*, 259.
31. I. P. Evans, A. Spencer and G. Wilkinson, *J. Chem. Soc., Dalton*, **1973**, 204.
32. G. M. Sheldrick, *Acta Crystallogr.*, **1990**, *A46*, 467.

Chapter 3 – Axially Coordinated Metalloporphyrin Stoppers for Rotaxanes

3.1 – Introduction

Rotaxanes are molecules that consist of one or more wheel components that are localized on the axle of a dumbbell-shaped component (Figure 1).^{1,2} Pseudo-rotaxanes, which are precursors to rotaxanes, lack the bulky end-stoppers and, as a result, the wheel is free to move on and off the axle. To name rotaxanes and pseudo-rotaxanes, the number of interlocked components is allocated a numerical prefix so that, for example, one wheel trapped on a central axle would be termed a [2]rotaxane. The trapped wheel fragments in rotaxanes are able to freely move in relation to the axle because the components are non-covalently attached and are classified as being “mechanically interlocked”.²

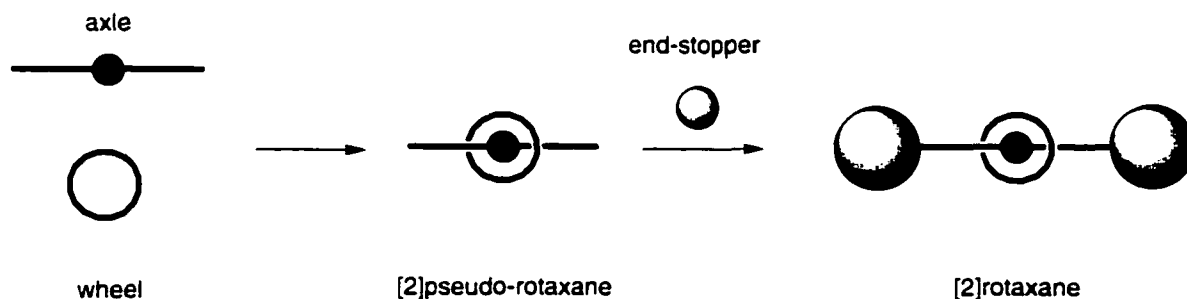


Figure 1. [2]Rotaxane formation.

The rotaxane motif has served as a conduit for designing multicomponent systems displaying novel chemical and physical properties. The unique mechanical association of these interlocked fragments is the impetus for using rotaxanes in prototypical molecular machines.² For example, light can be used to trigger the shuttling of the wheel between

two stations 'A' and 'B' of a [2]rotaxane which behaves like a molecular shuttle (Figure 2).^{3a} The [2]rotaxane in Figure 2 consists of a π -electron-donating wheel that can interact with two π -electron-accepting axle stations. The irradiation of the tris(2,2'-bipyridyl)ruthenium(II) complex is followed by a rapid electron transfer to station 'A' which reduces the dication axle. The reduction results in the disruption of the π -acceptor-donor interactions used to hold the wheel at station 'A'. As a result, the wheel is then shuttled to station 'B' because of stronger π -acceptor-donor interactions.

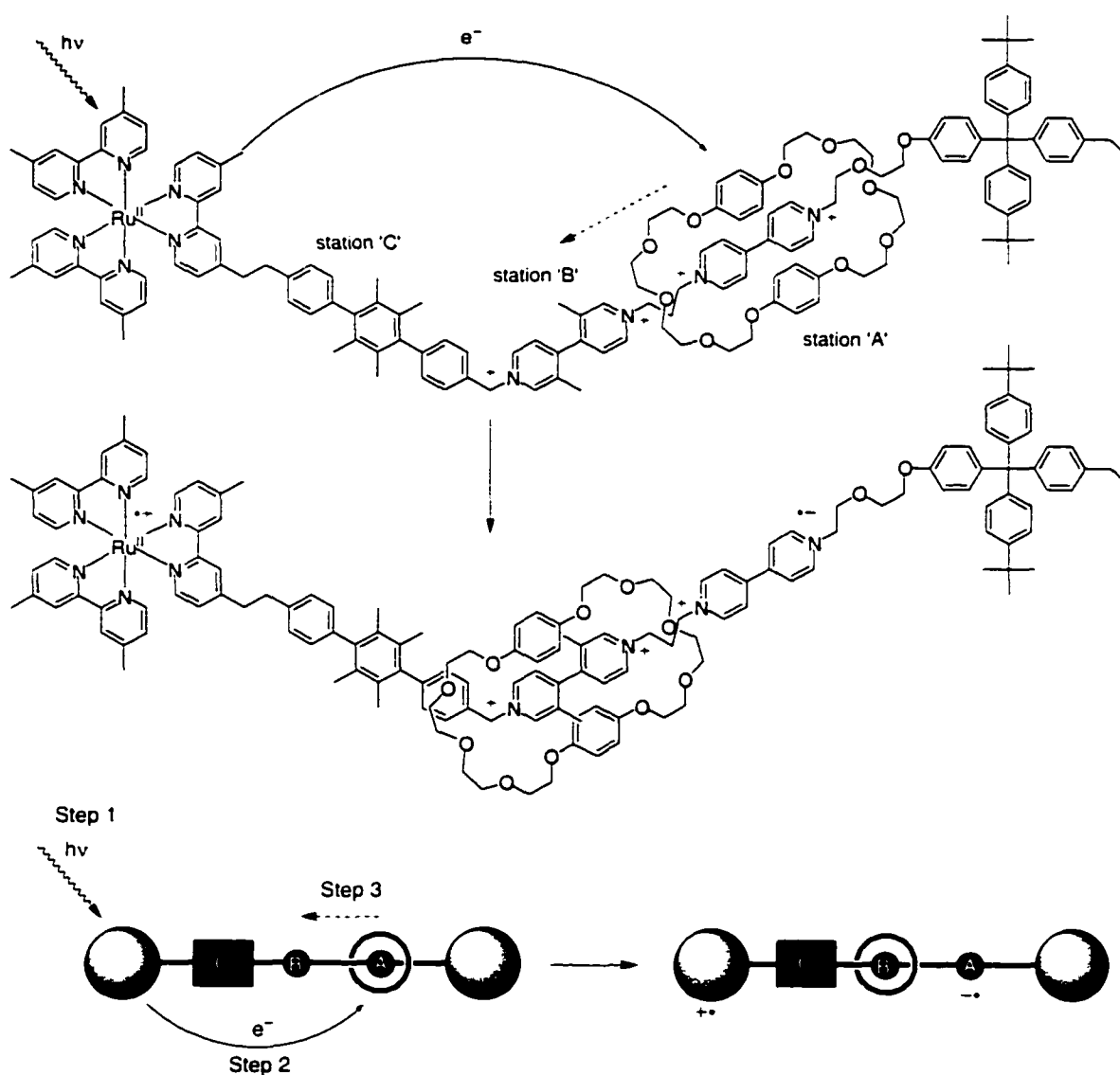


Figure 2. A molecular shuttle

3.1.1 – Methods in Rotaxane Synthesis

In order for rotaxanes to be used effectively as architectures when building nanoscale machines and new materials, the macrocyclic wheel, once threaded onto the molecular axle, must be held there to prevent the components from disassembling.¹ At present, there are several synthetic routes for fabricating rotaxanes that, based on the method used, are either formed under kinetic or thermodynamic control. These established synthetic routes can be grouped into three types of classes *clipping*, *slipping*, and *threading* (Figure 3).

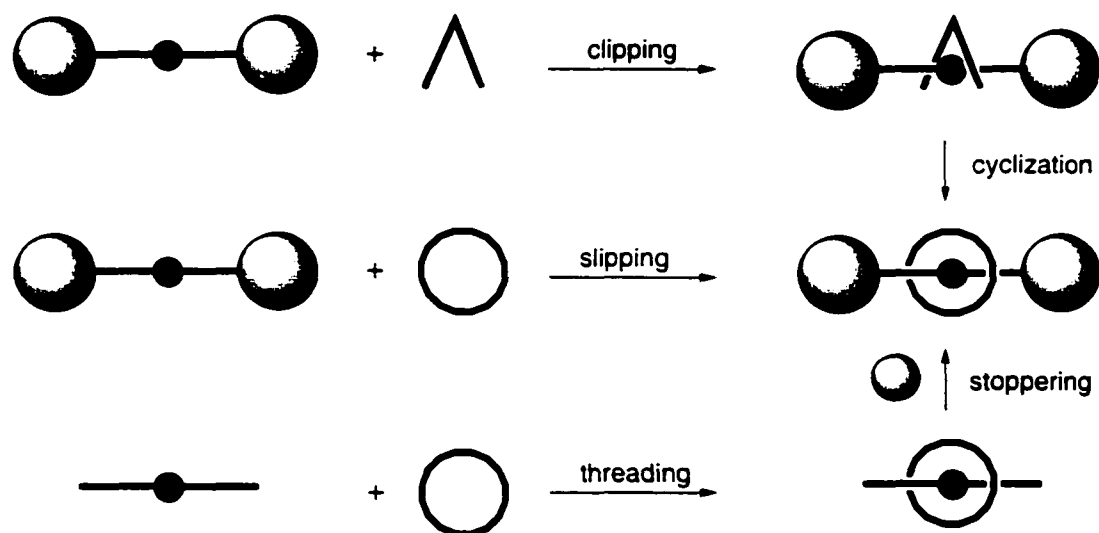


Figure 3. Three common strategies used to synthesize rotaxanes.

Clipping is accomplished by assembling a preformed dumbbell with a hemi-circular synthon and then reacting it with an agent causing cyclization. This strategy is challenged by finding appropriate cyclization methods to bring about macrocyclization of the pseudo-rotaxane, instead of polymerization and, thus, requires extra efforts in designing components that have compatible reactivity. The *slippage* strategy involves threading a presynthesized stoppered axle through the macrocyclic wheel with

appropriate heating.⁴ The *slippage* strategy is a thermodynamically controlled process because of the existence of a higher activation barrier for the dethreading process than the threading process. However, the harsh reaction conditions that tend to accompany this strategy may not be conducive for synthesizing rotaxanes containing highly sensitive molecular components. The *slippage* strategy is also limiting because rotaxanes can only be prepared from stoppered axles small enough to allow for the wheel to pass over them. The *threading* strategy, which is the most widely used route, involves threading an axle through a macrocycle wheel and finally fastening bulky end-stoppers to the pseudo-rotaxane. The *threading* strategy is the most versatile and widely used because it offers several ways to carry out the last step involving pseudo-rotaxane *stopping*.⁵ For example, a recently reported *stopping* method utilizes the dynamic nature of the imine bond to end-cap pseudo-rotaxanes under thermodynamic control (Figure 4).⁶ Unlike the *clipping* and *slipping* strategies, a thermodynamically controlled end-capping method has the advantage of greatly limiting the number of synthetic steps required to prepare the rotaxane and pseudo-rotaxane components.

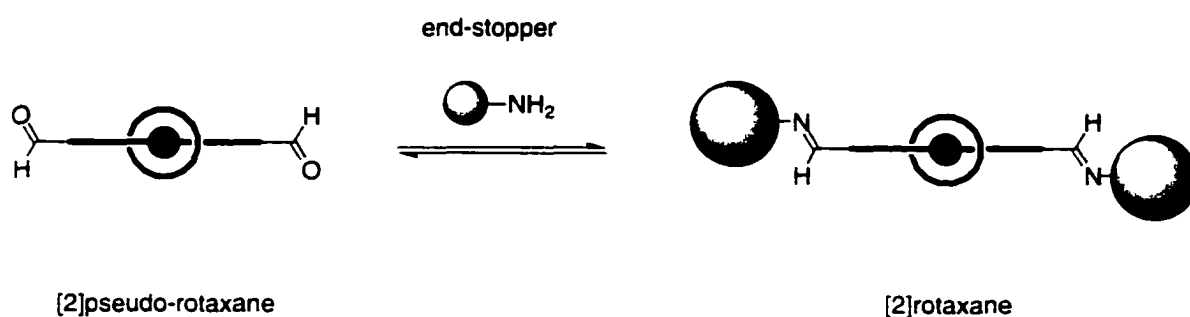


Figure 4. The reversible imine *stopping* method.

An alternative to using reversible carbon-heteroatom bond formation is to exploit metal-directed self-assembly synthesis which, as has been reiterated throughout this

thesis, has the advantage of being thermodynamically driven but is accomplished more rapidly and under milder conditions. Despite its being introduced almost two decades ago, there are few examples that utilize this approach to generate interlocking rotaxane structures (for example see Figure 5).⁷

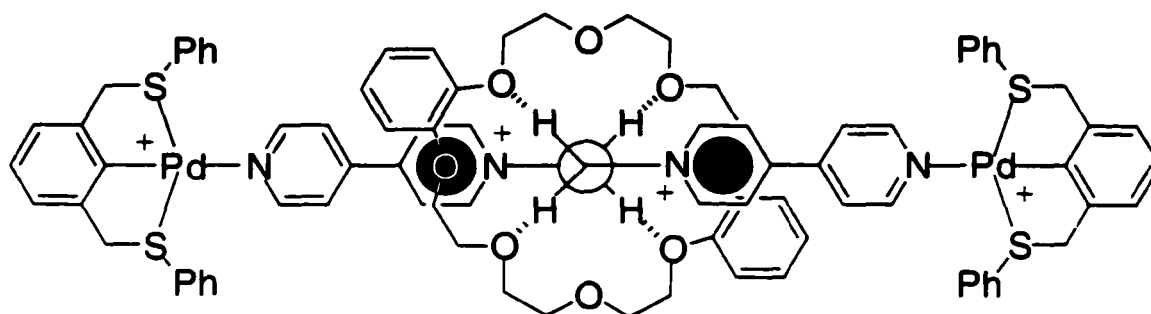


Figure 5. Metal-directed stoppering.

The synthetic strategies mentioned (*clipping*, *slipping*, and *threading*) can be further classified as *statistical*, *directed*, and *templated* based on the construction methodology (Figure 6).

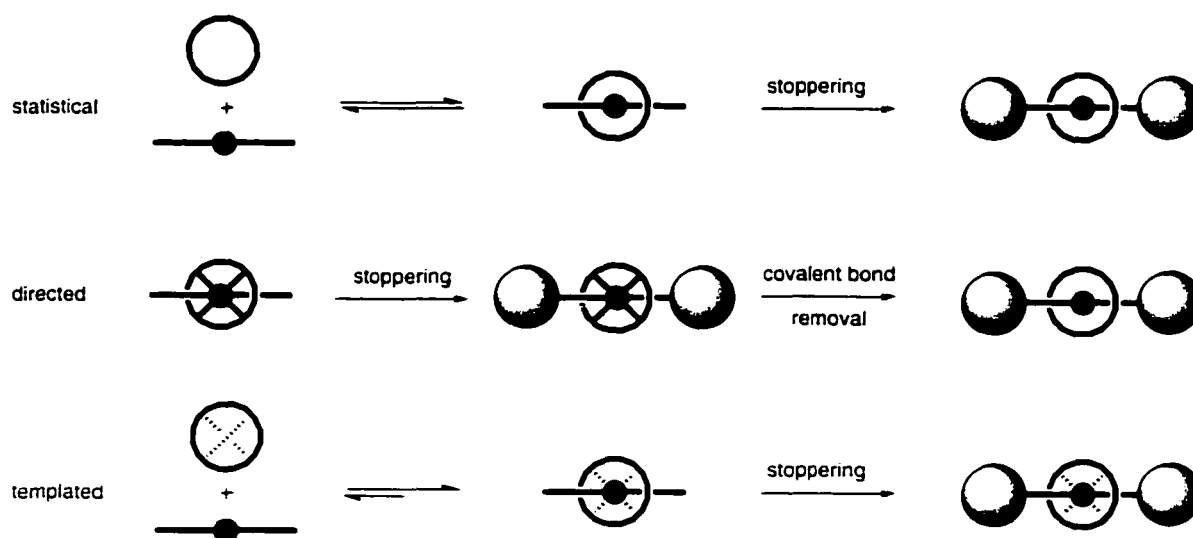


Figure 6. The alternative methods for assembling the axle and wheel.

The *statistical* method is less commonly used because the reaction is equilibrating and lacks any intermolecular interactions that can enhance the formation of the pseudo-rotaxane. This results in very low yields of the rotaxane. The *directed* and *templated* methods are preferred because they increase the amount of pseudo-rotaxane formed by using temporary covalent bonds or incorporating weak intermolecular forces, respectively. Examples of the *directed* method are few in their numbers because they rely on the cleavage of the covalent bonds that hold the wheel onto the axle. Again, systems of this type are plagued with the problem of finding compatible covalent synthetic steps to form and modify the linked axle and wheel. The *templated* method is the most widely used because it relies on easily incorporated and modified supramolecular glues into the components that are used to drive the *threading* process. The glues can be incorporated into a wide variety of axle and wheel components, and this affords a great deal of component versatility when building variants of the rotaxane structure. The types of supramolecular glue include π - π acceptor-donor interactions, hydrogen bonds, van der Waals forces, and metal-ligand associations. Of course, the interactions can also be used in combination.

The synthetic utility of the three synthetic methods is only realized after compiling their adaptability with the three strategies of *clipping*, *slipping* and *threading*. The *directed* method relies on covalent bond formation and can only be combined with the *clipping* approach. Also limited, but still more versatile than *clipping*, is the *statistical* method which can be combined with the *slipping* and *threading* approaches for rotaxane synthesis. Whereas, the *template* method can be combined with all three

approaches. It is because of this that it is the most widely used and accepted method for rotaxane synthesis.

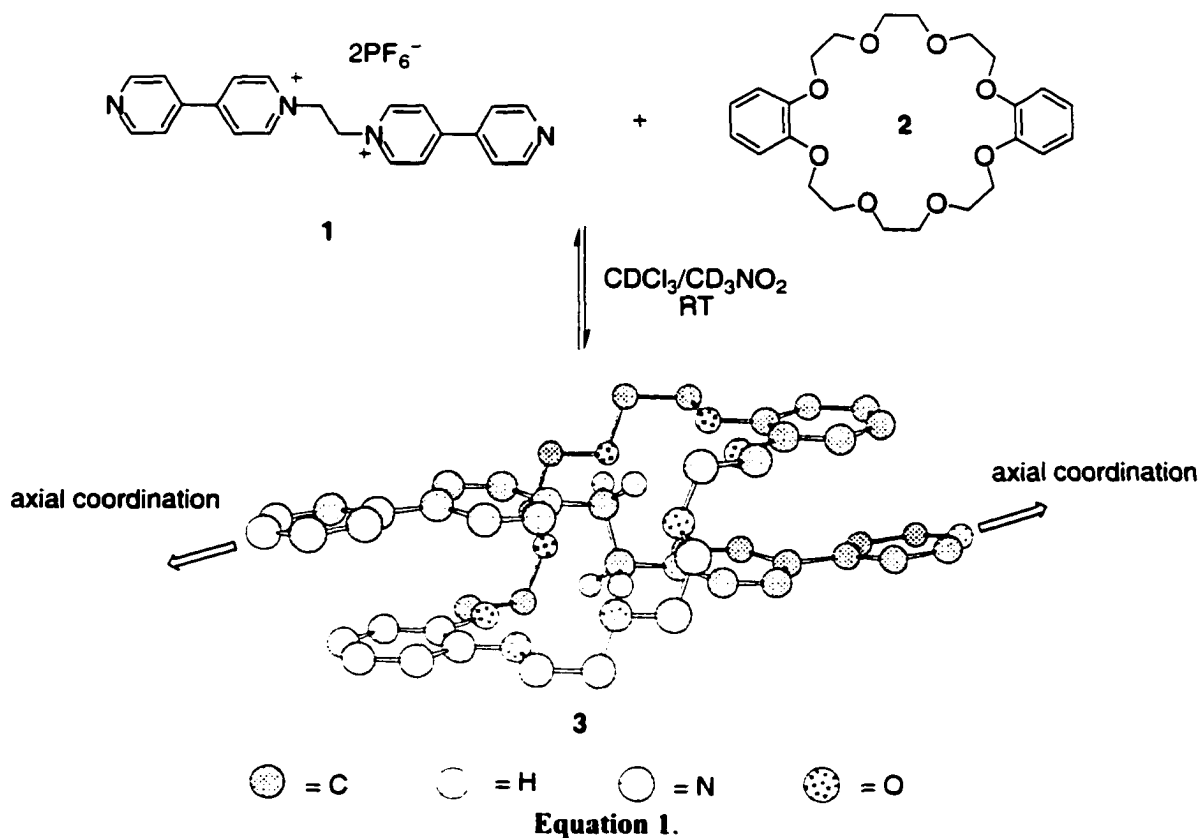
3.2 – Metalloporphyrin Stoppered Rotaxanes

The growing interest in rotaxanes containing chromophores as stoppers^{1,3a,7c,8} prompted the development of a mild porphyrin-based end-capping method. The incorporation of porphyrins as stoppers is particularly attractive not only because of their bulkiness, but also because of their rich electro- and photophysical properties, which have played important roles in synthetic electron and energy transfer systems as already discussed in previous chapters.^{1,8a,8b} In this study, axial coordination to the central metal of the metalloporphyrin Ru(TTP)(CO) (TTP = 5,10,15,20-tetratolylporphyrinato dianion) is used in combination with the *threading* strategy as a means to conveniently synthesize a porphyrin stoppered [2]rotaxane under thermodynamic control. A similar procedure surfaced in the literature after our initial publication. The strategy reported by Sanders and co-workers also takes advantage of axial coordination to a rhodium(III) metalloporphyrin using a slightly different wheel and axle components.⁹ Their results are similar to ours.

3.3 – Results and Discussion

3.3.1 – [2]Pseudo-Rotaxane Design

In order to effectively end-cap a pseudo-rotaxane *via* axial coordination, the pseudo-rotaxane must display divergent Lewis-basic sites appropriately distanced from the threaded wheel so as not to interfere with the self-assembly process. The 1,2-bis(4,4'-dipyridinium)ethane dication•dibenzo[24]crown-8 [2]pseudo-rotaxane (**3**) recently spot-lighted by Loeb^{7a,7b} provided the suitable model pseudo-rotaxane for this purpose (Equation 1).

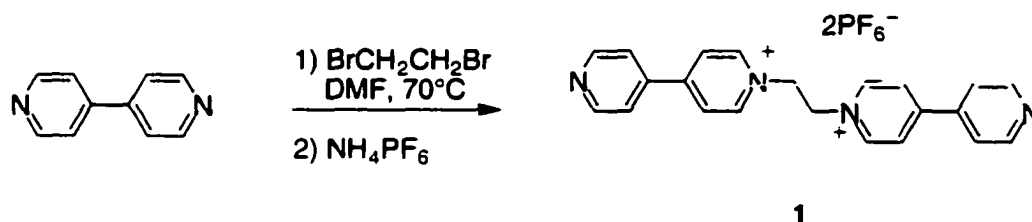


Within the [2]pseudo-rotaxane, the two divergent nitrogen atoms are positioned with an atom separation of approximately 17 Å that is ideally suited to axially coordinate

151

to Ru(TTP)(CO). The threading of the 1,2-bis(4,4'-dipyridinium)ethane dication (**1**) through dibenzo[24]crown-8 (DB24C8, (**2**)) forms the [2]pseudo-rotaxane (**3**) which is held together through three supramolecular glues: π - π acceptor-donor, C-H...O hydrogen bonding, and N^+ ...O ion-dipole. The importance of these glues will be highlighted in a more detailed discussion later in the Chapter.

Multigram quantities of the central 1,2-bis(4,4'-dipyridinium)ethane dication (**1**) were easily prepared according to known methods described by Summers.¹⁰ Following this procedure, a dimethylformamide solution containing 4,4'-bipyridine was treated with an excess of dibromoethane at 70°C. The dibromide salt precipitated from the reaction mixture and was recrystallized from water. The bromide counter ions were exchanged with organic soluble hexafluorophosphate ions (Scheme 1).



Scheme 1.

3.3.2 – Spontaneous Pseudo-Rotaxane Formation

Dissolving equimolar amounts of axle **1** and wheel **2** in a 1:1 mixture of $CDCl_3$ and CD_3NO_2 immediately generated [2]pseudo-rotaxane **3** as apparent by 1H NMR spectroscopy (Figure 7 and Figure 8). The direct evidence for the formation of [2]pseudo-rotaxane **3** is the observation of diagnostic down-field shifts of the methylene protons on the axle component as they are involved in C-H...O hydrogen bonds. There are also

characteristic upfield shifts of the aromatic protons on the axle and wheel components whose rings are involved in π - π stacking interactions. Both of these interactions are responsible for driving the threading process.^{7a,7b}

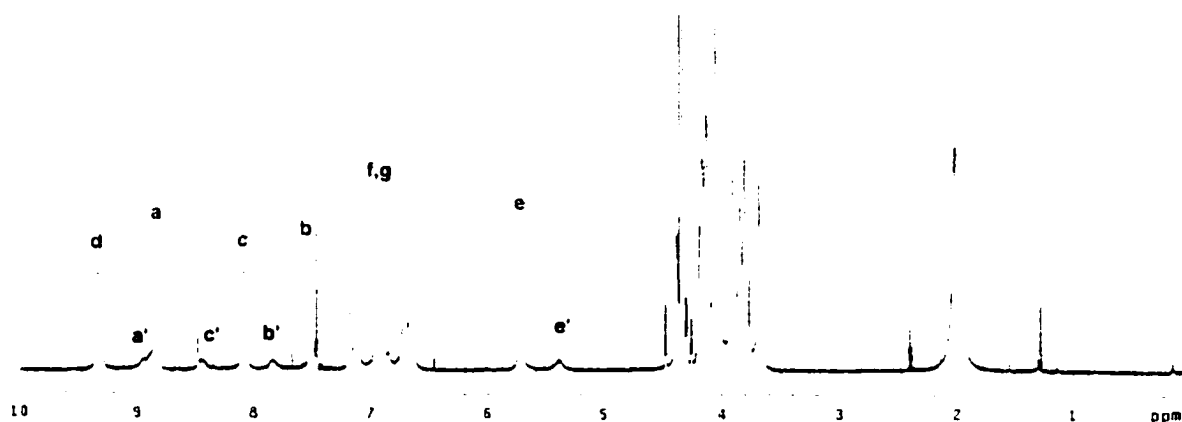


Figure 7. ^1H NMR (500 MHz) of [2]pseudo-rotaxane **3** formation (3 mM in 1:1 CDCl_3 - CD_3NO_2). For signal numbering refer to the structures in Figure 8. Primed (') signals correspond to unbound components.

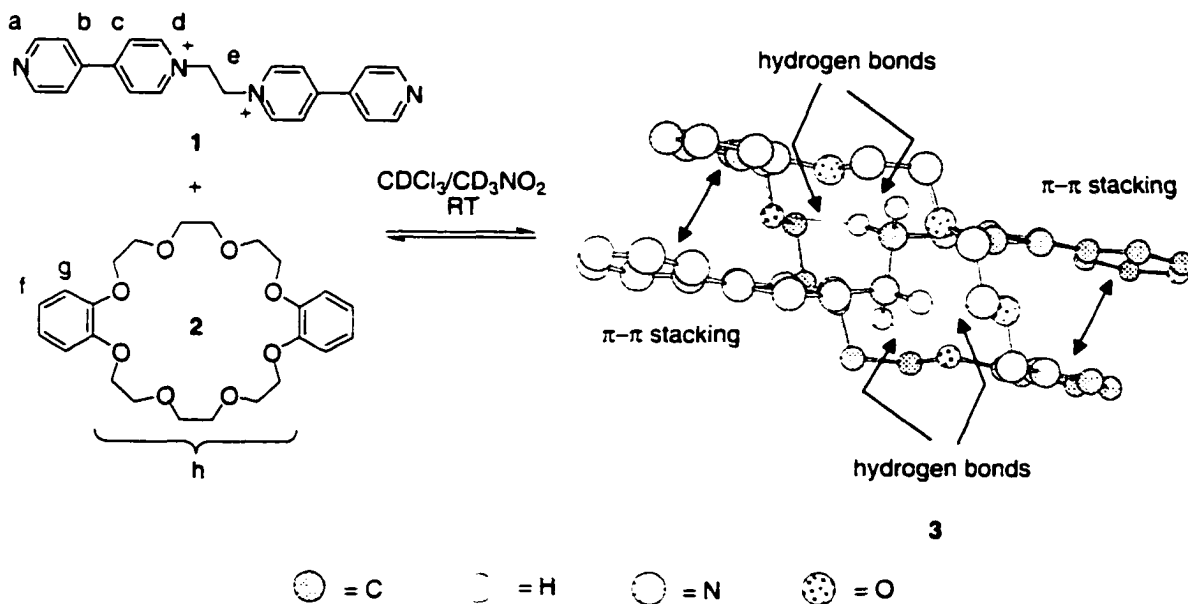


Figure 8.

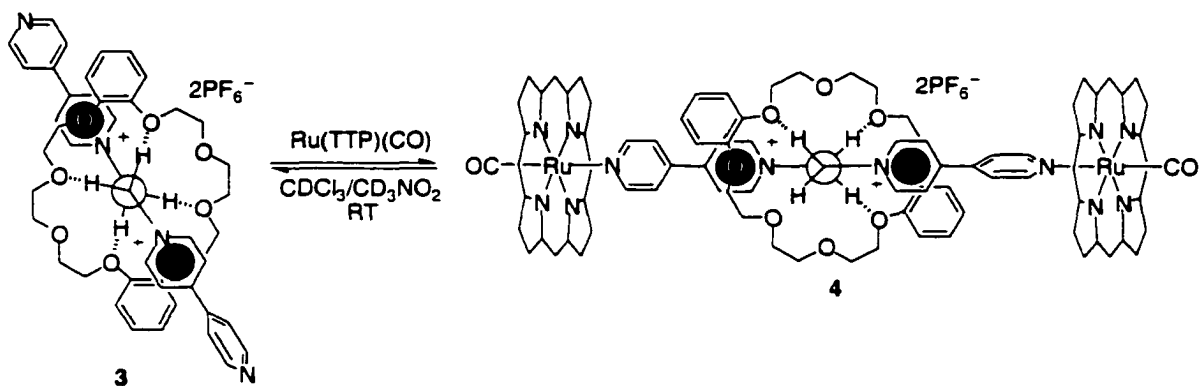
Although the [2]pseudo-rotaxane is soluble in two-component systems such as a mixture of nitromethane and acetonitrile, the poor solubility of Ru(TTP)(CO) in nitromethane alone eliminated the possibility of using this solvent. Acetonitrile was avoided as its nitrogen atom effectively competes as a Lewis base with those on **1** for coordinating to the transition metal. However, once formed and isolated, the [2]rotaxane **4** is freely soluble in single organic solvents alone such as CHCl₃ or CH₂Cl₂.

Integrating the area under the peaks corresponding to the methylene protons of free and bound **1** and **2** (signals labeled e' and e in Figure 7), both of which were clearly separated in the ¹H NMR spectrum, allowed for the facile determination of the association constant (K_a) in the slow-exchange threading process using the single point method.¹¹ This value was measured to be in the range of 3000-10000 M⁻¹ in the mixed-solvent system (1-3 mM in CDCl₃/CD₃NO₂ 1:1 solutions). The association constant K_a is reported as being within a range because the extent of threading was sensitive to the concentration of **1** and **2** in the sample, and the magnitude of the association constant increased as the concentration of both components were raised. This unexpected concentration dependency can be attributed to the trace amount of residual water in the solvents. Because the solvent shells surrounding all species (**1-3**) certainly can include water, it is reasonable to assume that the concentration of free and bound water would change throughout the complexation reaction at the low water concentrations found in these solutions. The result is that water cannot be eliminated from the thermodynamic equilibrium equation and will thus have a great effect on the ability to form the [2]pseudo-rotaxane **3**. The strength of the hydrogen bonds that are holding the axle in place is lowered because water is an effective hydrogen bond competitor. Also, it could

be expected that, along with the solvent shell, there are water molecules networked inside the cavity of any uncomplexed crown ether and these bonds must be broken to bind the axle. In this way, the slightly hydrous nature of the solvents used (and the difficult task of drying these solvents) affects the precision of K_a measurements. Support of this suggestion came in the observed lowering of K_a for solutions at any concentration when additional water was added to the sample. The association constants leveled out at 800-1000 M^{-1} when enough water (200-300 equivalents) was added so that its concentration remains unchanged during the threading process. Despite this, the strength of the interactions holding the interlocked components together compensates for the presence of such a competitive solvent like water.

3.3.3 – Metalloporphyrin Capping for [2]Rotaxane Formation

The [2]rotaxane **4** was immediately formed when 2 molar equivalents of $Ru(TTP)(CO)$ were added directly to the NMR sample of the pseudo-rotaxane (Equation 2 and Figure 9).



Equation 2. The porphyrins' substituents and double bond representations have been omitted for clarity.

Signals for all the hydrogen atoms of both **1** and **2** shift significantly upfield, as would be expected for protons that reside within the additive shielding cones of the porphyrin stoppers. This effect has already been described in detail in previous chapters. The pyridine hydrogen atoms immediately adjacent to the coordinating nitrogen are closest to the end-caps (2.7 Å average nitrogen-to-porphyrin distance) and are the most affected by the anisotropic effect (signals “a” in Figure 9 and Table 1). The shielding effect is minimally felt by the methylene protons on the dication axle (-CH₂, signals “e” in Figure 9) which are as far as 10.2 Å from the stoppers, although the shielding effect is still significant ($\Delta\delta = 0.72$ ppm). All protons on the crown ether are also shielded, the most effected being those on the phenyl ring which are 3.0 Å and 5.1 Å from the mean centre of the porphyrin planes.

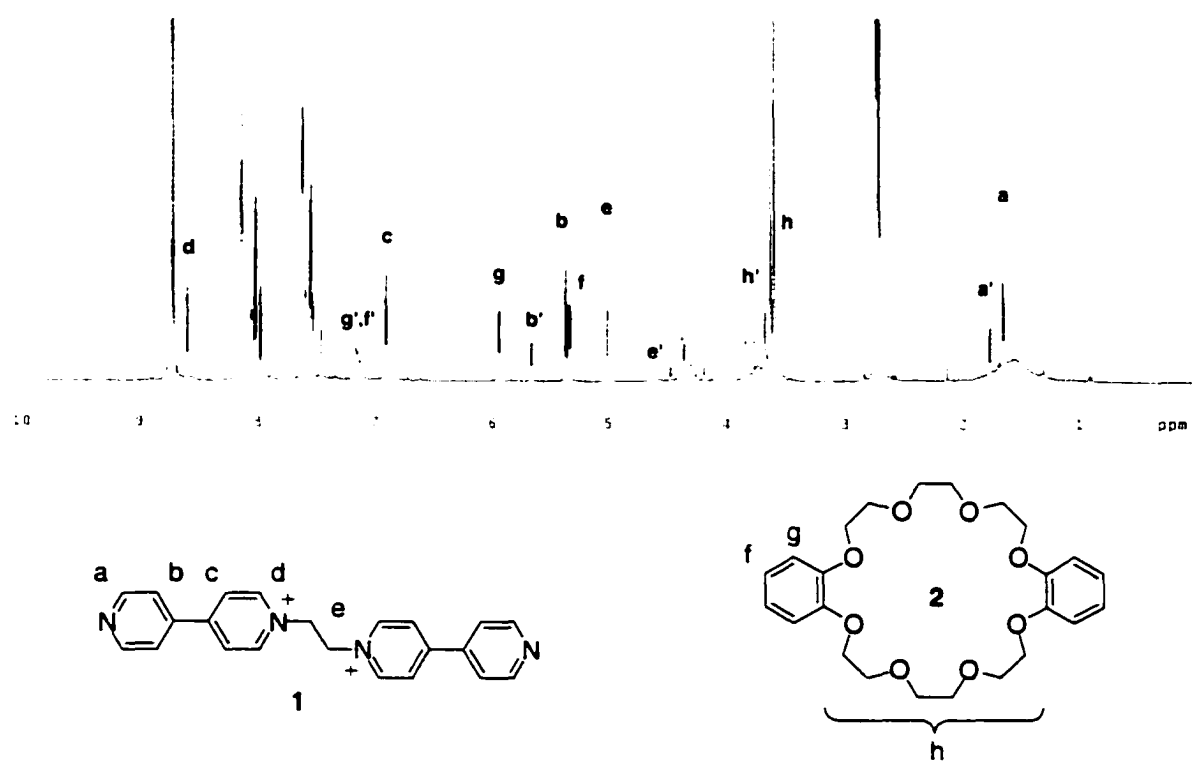


Figure 9. ¹H NMR (500 MHz) of [2]rotaxane **4** formation (3 mM in 1:1 CDCl₃-CD₃NO₂). Primed (') signals correspond to stoppered axle and unbound wheel component **2**.

Table 1 Selected ¹H NMR data (500 MHz) of **4** in 1:1 CDCl₃-CD₃NO₂

δ / ppm							
axle fragment				wheel fragment			
H(a) ^a	H(b)	H(c)	H(d)	H(e)	H(f)	H(g)	H(h)
1.65	5.36	6.91	8.60	5.01	5.33	5.94	3.67-3.59
(-7.18) ^b	(-2.14)	(-1.17)	(-0.72)	(-0.72)	(-1.37)	(-0.76)	(-0.48)

^a Atom numbering scheme refers to structures in Figure 9. ^b Refers to upfield shifts of the protons relative to those in the spectrum of [2]pseudo-rotaxane **3**.

At this time, it is important to consider the effects that axial coordination may have on the interactions responsible for holding the pseudo-rotaxane together. As a result of axial coordination, the Lewis acidic ruthenium metal will pull electron density away from the axle making the pyridine rings less electron rich thereby increasing the acidity of any protons involved in hydrogen bonding. Also effected are the electron poor pyridine rings on the axle as these rings will become even more electron poor after axial coordination. Considering these effects, it is safe to assume that the π - π stacking between the pyridines and the electron rich aromatic rings on the wheel and hydrogen bonding interactions used to hold the pseudo-rotaxane together will increase in their strengths. Overall, the result should be seen as an increase in stability of the axle and wheel components in the rotaxane.

3.3.4 – [2]Rotaxane X-Ray Crystal Structure

Crystals of [2]rotaxane **4** suitable for structure determination were obtained by treating acetone solutions of **1** with excess **2**, end-capping the *in situ* formed [2]pseudo-rotaxane **3** with two molar equivalents of Ru(TTP)(CO), followed by slow evaporation.

The crystal structure is consistent with the binding interactions observed in the ^1H NMR spectrum (Figure 10). All methylene protons of **1** are within hydrogen bond distances to the oxygen atoms of the crown ether (3.54 Å average $\text{C}\cdots\text{O}$ distance).

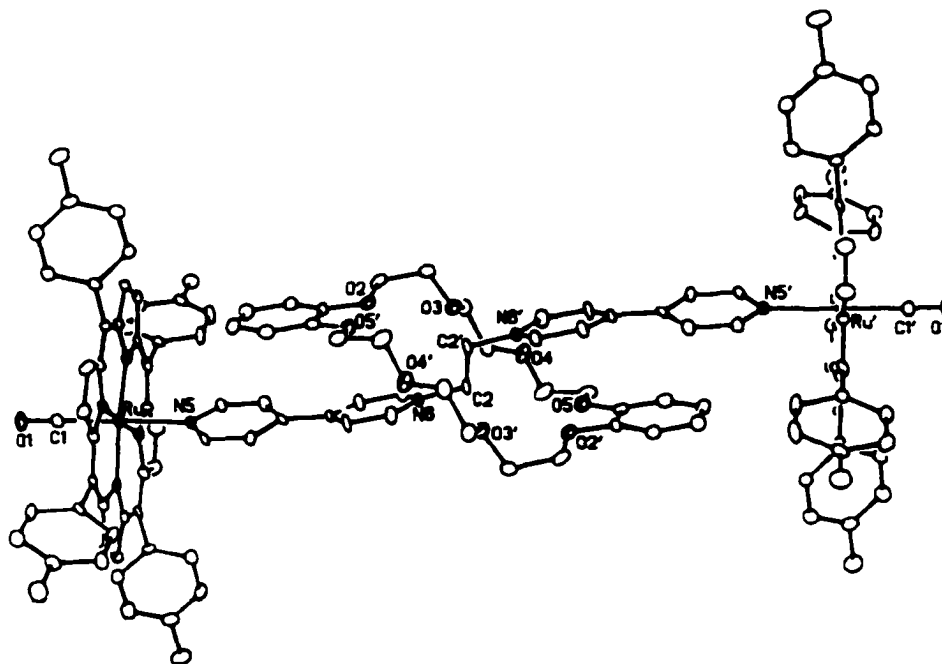


Figure 10. Molecular structure of [2]rotaxane **4** in the crystal. The thermal ellipsoids are drawn at the 20% probability level.

Also, the phenyl rings of the crown ether wheel are lying parallel to the heterocycles of the axle and are within π - π stacking range (3.4 Å mean Ph-Ph distance). Also revealed are the weak but important $\text{N}^-\cdots\text{O}$ ion-dipole interactions that range from 4.12 to 3.35 Å for all nitrogen atoms which are in close proximity to the crown ether's oxygen atoms.^{7a,7b} The crystal structure shows that the distance between the porphyrin stoppers (21.692(3) Å Ru(1)-Ru(2) distance) is just enough to accommodate the entire crown ether fragment without sacrificing any of the favourable π - π stacking interactions between the wheel and the axle.

3.3.5 – [2]Rotaxane Solution Dynamics

The most notable feature of [2]rotaxane **4** appears in the solution behaviour of the isolated complex. The thermodynamic properties of the [2]rotaxane are quite intriguing because they involve two reversible binding events, *threading/dethreading* and the *stopping*. Since the [2]rotaxane **4** was created using a reversible approach, it serves as an example of how the thermodynamic properties of the components are retained in the final assembled [2]rotaxane. This is highlighted in Figure 11, which compares the solution behaviour of **4** in two different solvent systems (CD_2Cl_2 and $\text{CD}_2\text{Cl}_2/[\text{D}_6]\text{acetone}$ 1:1). These solvents were chosen because they have varying degrees of competition with respect to axial coordination and hydrogen bonding. The signals that are highlighted with arrows in Figure 11 correspond to the NCH_2 protons on the central dication axle involved in hydrogen bonding with the crown ether wheel.

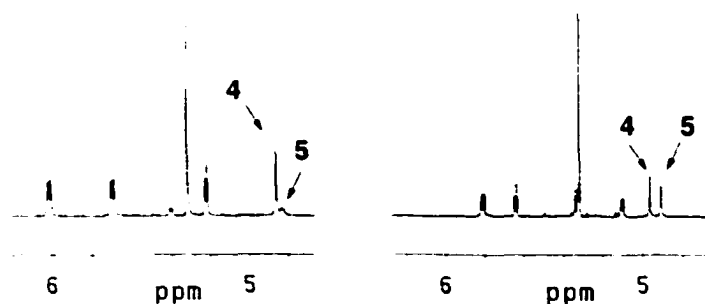
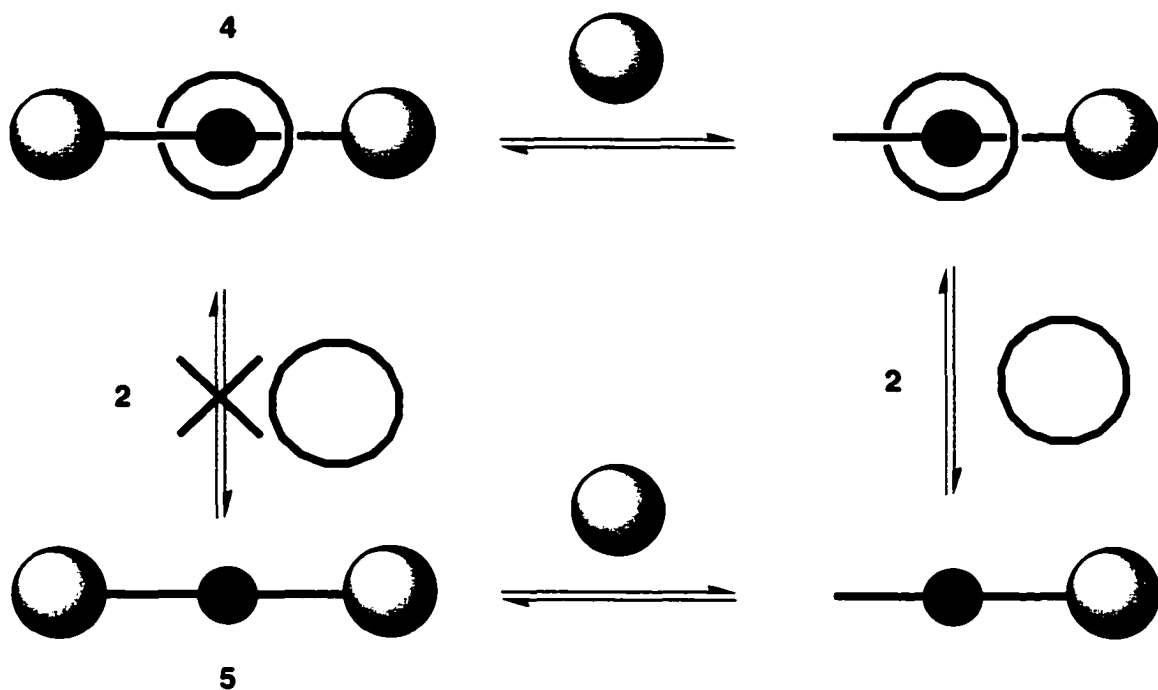


Figure 11. ^1H NMR (500 MHz) spectra of isolated [2]-rotaxane **4** highlighting the solvent dependency on the equilibrium mixture. The left trace was obtained in CD_2Cl_2 . The right trace was obtained in 1:1 $[\text{D}_6]\text{acetone}/\text{CD}_2\text{Cl}_2$. Both spectra were obtained at the same concentration of 0.80 mM. See Equation 3 for schematic representations of the peak assignments.

The signal that is shifted further down field corresponds to the [2]rotaxane **4**. In both cases, an equilibrium mixture of the components was produced and shows the dynamic nature of using axial coordination as a rotaxane end-capping method (Equation 3).



Equation 3. The schematic representation of the equilibria involved.

It was not unexpected that in acetone **4** was less favoured over **5** to a larger extent than it was in dichloromethane. Acetone therefore, effectively reduces the strength of axial coordination and hydrogen bonding which allows the wheel to slip off more easily. It is important to note that the equilibrium mixture of **4** and **5** may also result from unfavourable steric interactions that are present when the wheel bumps into one or both of the stoppers thus aiding in their removal. Even though the solid state structure suggests that there is enough room to accommodate the wheel, it only represents a static version of the [2]rotaxane. Integrating the area under the peaks corresponding to bound and free **4** and **5** in acetone, both of which were clearly separated in the ^1H NMR spectrum, allowed for the facile determination of the association constant (K_a) in the

slow-exchange threading process using the single point method (Figure 10). An association constant K_a of 2000 M^{-1} (0.80 mM in $\text{CD}_2\text{Cl}_2/[\text{D}_6]\text{acetone}$) was calculated for the acetone solvent system.

Changing the solvent to dichloromethane, which can be considered as being a non-competitive solvent for both axial coordination and hydrogen bonding, shows that the equilibrium favours the [2]rotaxane **4** (Equation 3 and Figure 11). By integrating the area under the peaks corresponding to bound and free, **4** and **5** respectively, an association constant K_a of 8000 M^{-1} (0.80 mM in CD_2Cl_2) was calculated for this solvent system. A comparison of this value to that for the acetone solution (2000 M^{-1} at 0.80 mM in $\text{CD}_2\text{Cl}_2/[\text{D}_6]\text{acetone}$) suggests that the interactions used to hold the wheel and axle together are stronger in dichloromethane and supports the solvent dependency of rotaxane formation. Even though axial coordination is strong, the [2]rotaxane still disassembles in dichloromethane lending support to the argument that the stoppers are exchanging and their removal might be assisted by interactions with the wheel. In light of this, the reversible and thermodynamically controlled assembly of this [2]rotaxane is revealed by the shifting of the dichloromethane equilibrium mixture to favour **4** after the addition of excess crown. Therefore, it is possible to alter the conditions necessary to enhance [2]rotaxane formation by simple mixing of the wheel, axle and stoppers in appropriate ratios. This should facilitate the rapid synthesis of more elaborate structures. Alternatively, addition of an excess of a competitive Lewis basic solvent such as pyridine to the dichloromethane solution containing **4** resulted in the quantitative displacement of the stoppers as $\text{Ru}(\text{TTP})(\text{CO})(\text{py})$ and the regeneration of the dynamic mixture of pseudo-rotaxane **3** and the non-threaded wheel and axle (Figure 12). Integration of the area

under the peaks in the ^1H NMR spectrum showed that the reaction mixture had 1:1:2 stoichiometry between components axle:wheel:porphyrin. This study reveals the dynamic nature of the end-capping process and will serve usefully when removable stoppers are desired.

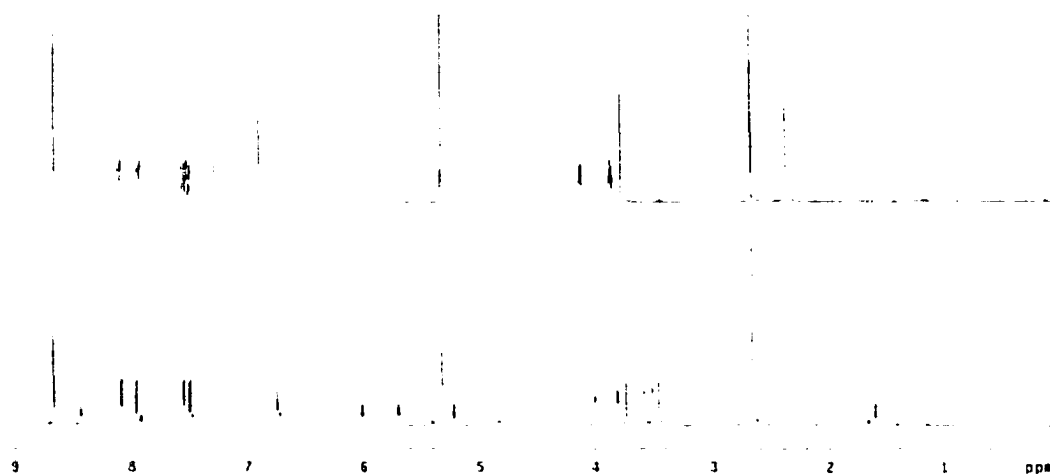
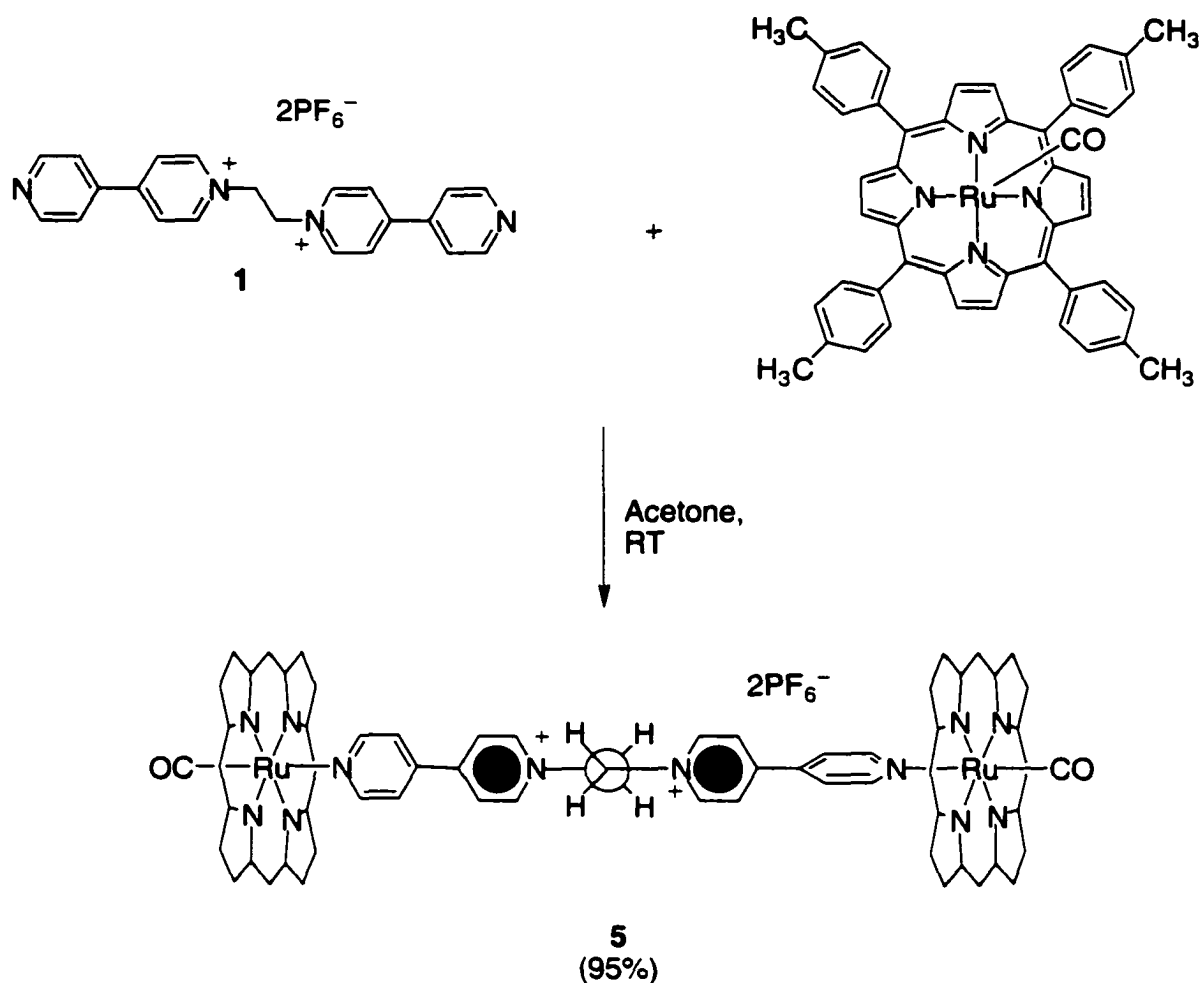


Figure 12. ^1H NMR (500 MHz, CD_2Cl_2) spectra of the isolated [2]rotaxane **4** (bottom trace) highlighting the ability to remove the porphyrin stoppers by adding pyridine (top trace).

3.3.6 – [2]Rotaxane Synthesis Using an Axially Coordinated Axle

The reversible and thermodynamically controlled self-assembly process was further probed by testing the ability to prepare the [2]rotaxane **4** from the preformed coordinated axle **5**. First, the axially coordinated axle was prepared in greater than 95% yield by adding 2.5 molar equivalents of $\text{Ru}(\text{TTP})(\text{CO})$ to an acetone solution of **1** at room temperature (Equation 4). The solvent was removed, replaced with dichloromethane and **5** precipitated by adding pentane.



Equation 4. The porphyrins' substituents and double bond representations have been omitted for clarity.

^1H NMR spectroscopy was then used to follow the progress of the self-assembly reaction involving the stoppered axle **5** and the wheel **2**. In this ^1H NMR study, aliquots of dibenzo[24]crown-8 were added to a $[\text{D}_6]$ acetone sample containing **5** and the disappearance of the signals corresponding to **5** was monitored (Figure 13). Acetone was chosen as the solvent because it dissolves all of the components and this competitive solvent should increase the exchange rate of the stoppers thus facilitating the addition of the wheel onto the axle. It is clear from Figure 13 that the addition of 5 μL (0.7 molar

equivalents) of dibenzo[24]crown-8 resulted in the formation of the [2]rotaxane **4** (signals labeled '†' in Figure 13).

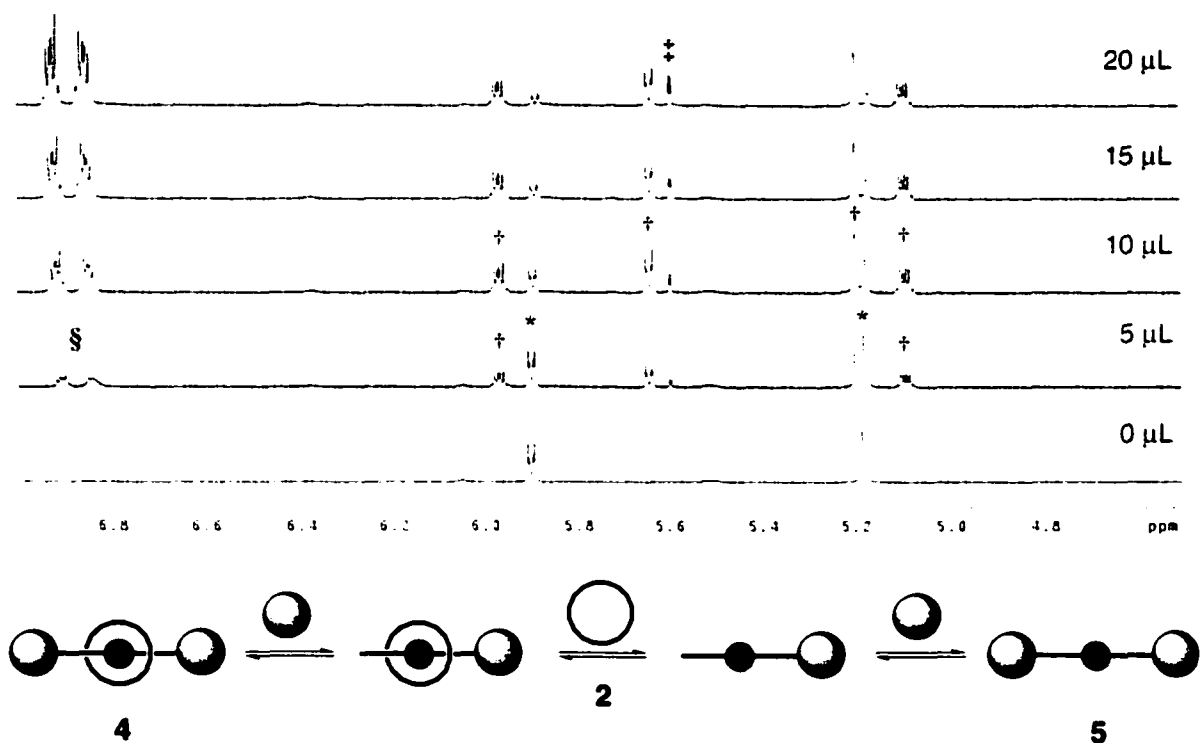


Figure 13. ^1H NMR (500 MHz) during the titration of capped axle **5** (0.75 mM) in $[\text{D}_6]$ acetone with aliquots of dibenzo[24]crown-8 **2** (85 mM) dissolved in CD_2Cl_2 forming [2]-rotaxane **4**. The symbol '§' refers to signals that correspond to excess dibenzo[24]crown-8, the symbol '*' refers to selected signals of unbound **5**, the symbol '†' refers to selected signals of bound [2]-rotaxane **4** and the symbol '‡' refers to residual solvent CH_2Cl_2 peak.

Evidence for [2]rotaxane **4** formation is supported by the diagnostic down-field shifts of C-H...O hydrogen bonds and the appearance of the crown ether's two phenyl ring resonances. It is not unexpected that the signals corresponding to the crown ether's phenyl rings are shifted dramatically upfield when they are associated on the axle because they lie within the porphyrins' anisotropic ring currents. The yield of [2]rotaxane **4** was calculated by comparing the area under the signals (signals labeled '†' and '*' in Figure 13) and was found to be 38% for this first addition. By adding more

dibenzo[24]crown-8 the yield of the [2]rotaxane increased and leveled off at 75% when 20 μL (2.67 molar equivalents) of dibenzo[24]crown-8 were added. An average association constant K_a of 2300 M^{-1} (0.80 mM in $[\text{D}_6]$ acetone) was calculated for each addition and again it reflects the solvent dependency of rotaxane formation in acetone. This study reveals the reversible nature of this stoppering method and demonstrates the ease at which the *threading* and *stoppering* of the axle can be monitored. The information obtained from this study can be used to calculate the amount of wheel required to maximize [2]rotaxane formation using a one step procedure.

All of the ^1H NMR studies mentioned in this chapter of the thesis have shown that axial coordination of porphyrins is an effective end-capping method to convert dynamic [2]pseudo-rotaxanes into dynamic [2]rotaxanes. The driving force for [2]rotaxane formation results from cooperative templating forces of π - π acceptor-donor interactions, C-H \cdots O hydrogen bonding, and N $^+$ \cdots O ion-dipole interactions. The importance and strength of these templating interactions and the reversible *stoppering* method was revealed by their dynamic solution state behaviour. A solvent dependency of these processes was found and highlighted by noticeable changes in the association constants calculated for pseudo-rotaxane and rotaxane formation. The reaction conditions can be altered to maximize rotaxane formation, and the stoppers can also be quantitatively removed under mild conditions by treating the [2]rotaxane **4** with the appropriate solvent.

3.3.7 – Characterization using ESI Mass Spectrometry

Attempts were also made to characterize the [2]rotaxane **4** by electrospray mass spectrometry (ESI-MS) using a CH_2Cl_2 /nitromethane solvent mixture. Unfortunately, the

spectrum was absent of the peaks that correspond to the singly or to the doubly charged species of the [2]rotaxane **4**. The spectrum contained a peak for the singly charged stoppered axle **5** at $m/z = 2080$ $[M - (DBZ24C8, PF_6)]^+$ along with a peak corresponding to the loss of a porphyrin unit. Also present in the spectrum was a peak for a singly charged species at $m/z = 1998$ which is consistent with $[M - (DBZ24C8, 2PF_6) + CH_3NO_2]^+$ along with a peak corresponding to the loss of a porphyrin unit. The isotopic abundance of each peak matched the calculated values of singly charged species.

3.3.8 – Characterizations using IR Spectroscopy

The [2]rotaxane **4** and stoppered axle **5** were also characterized in the solid state using IR spectroscopy. It should be remembered that when pyridine coordinated to Ru(TTP)(CO)(EtOH), the ν_{CO} shifted from 1946 cm^{-1} to 1933 cm^{-1} . For both the [2]rotaxane **4** and the stoppered axle **5**, the ν_{CO} appeared at 1959 cm^{-1} . Since the ν_{CO} increases in frequency, this suggests that the terminal pyridines on the axle component **1** reduce the amount of electron density back-bonded to CO when they coordinate to the ruthenium(II) metal in Ru(TTP)(CO). These results also suggest that when the crown ether is on the stoppered axle **5**, as in the [2]rotaxane **4**, the amount of electron density back-bonded to CO is not altered.

3.3.9 – Characterization Using UV/Vis Spectroscopy

Initial photophysical studies show that the absorption spectra in the UV/Vis region of [2]rotaxane **4** are essentially the same as the pyridyl adduct of Ru(TTP)(CO)(py) (Figure 14). In order to compare the absorption spectra of the

[2]rotaxane and its constituents, the UV/Vis spectrum of the [2]pseudo-rotaxane **3** and of the stoppered axle **5** are required.

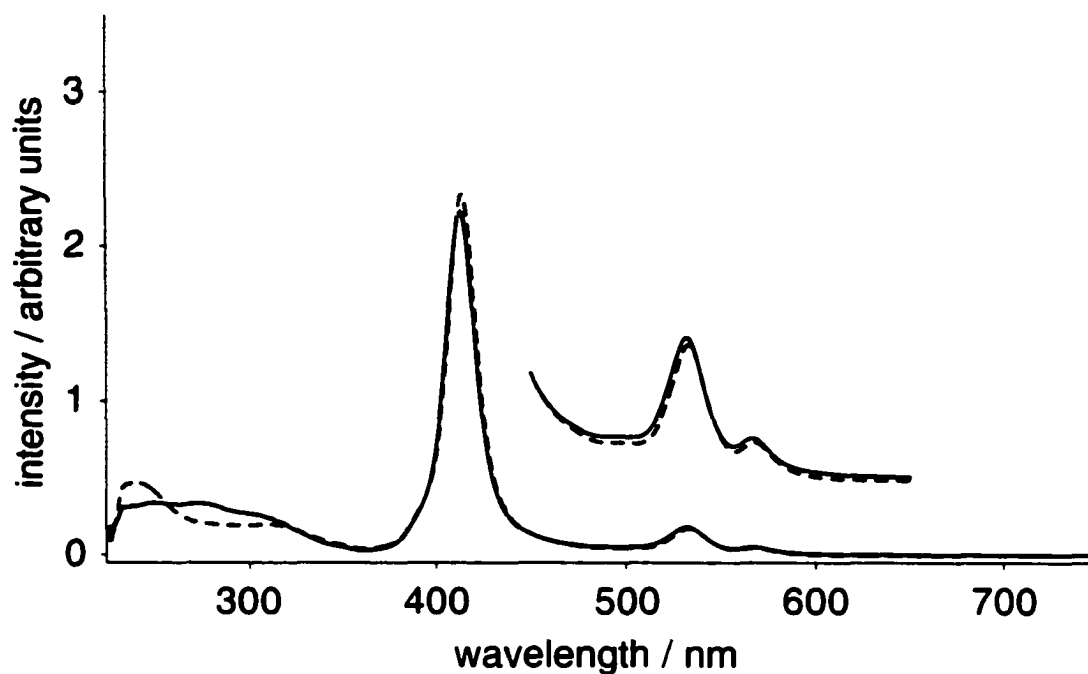


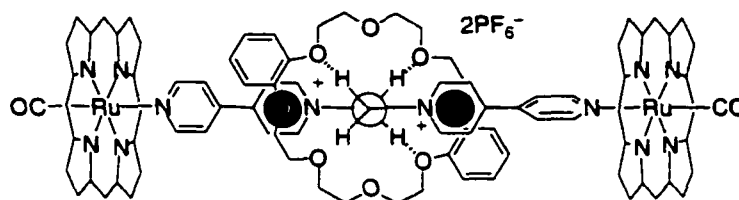
Figure 14. Overlay of absorption spectra of [2]rotaxane **4** (solid line) and Ru(TTP)(CO)(py) (dotted line) in dry deoxygenated dichloromethane. Both spectra are normalized to have the same porphyrin concentration of 1.00×10^{-5} M.

These results seem to indicate that there is an absence of strong coupling between the different units of the structure and the chromophores behave independently.

3.4 – Experimental

General Remarks: All solvents (Caledon) were distilled prior to use. Solvents used for UV/Vis spectroscopy were deoxygenated by bubbling argon through the solvent. Solvents for NMR spectroscopic analysis (Cambridge Isotope Laboratories) were used as received. All reagents and starting materials were purchased from Aldrich. ^1H NMR spectroscopic characterizations were performed on a Varian Inova-500 instrument, working at 499.92 or on a Varian Inova-300 instrument, working at 299.96 MHz. Chemical shifts (δ) are reported in parts per million relative to tetramethylsilane using the residual solvent peak as a reference standard. FT-IR measurements were performed on solid samples using a Nicolet Magna-IR 750 equipped with a microscope. UV/Vis measurements were performed using a Varian Cary 400 Scan spectrophotometer. Electrospray ionization mass spectra were recorded on a Micromass ZabSpec Hybrid Sector-TOF with positive mode electrospray ionization. The liquid carrier was infused into the electrospray source by means of a Harvard syringe pump at a flow rate of 10 $\mu\text{L}/\text{minute}$. The sample solution, in the same solvent, was introduced *via* a 1 μL -loop-injector. Prepurified nitrogen gas was used as a pneumatic aid and filtered air as the bath gas, heated at *ca.* 80°C. For low resolution, the mass spectra were acquired by magnet scan at a rate of 5 seconds/decade at *ca.* 1000 resolution. For exact mass measurements, the spectra were obtained by voltage scan over a narrow mass range at *ca.* 10000 resolution. Data

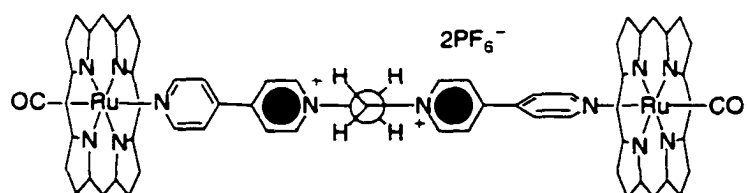
acquisition and processing was achieved by using the OPUS software package on a Digital Alpha station with VMS operating system.



[Ru(TTP)(CO)]₂[PF₆]₂[2]rotaxane (4) : A solution of 1,2-bis(4,4'-dipyridinium)ethane dication (**1**)¹⁰ (15.0 mg, 2.38×10⁻² mmol) in CH₃NO₂/CH₂Cl₂ (1:1) (5.0 mL) was treated with 3.0 molar equivalents of dibenzo-24-crown-8 (32.0 mg, 7.14×10⁻² mmol) and stirred at ambient temperature for 5 min. To this mixture was added 2.1 molar equivalents of Ru(TTP)(CO)(EtOH) (44 mg, 5.23×10⁻² mmol) and stirred for an additional 30 min. The reaction mixture was poured into ether (15 mL) and the resulting solid was collected by filtration and was washed with a mixture of Et₂O/pentane (20:80) and dried under vacuum. Yield: 49 mg (77%).

M.p. >300°C (decomp); ¹H NMR (500 MHz, CD₂Cl₂, 22°C) (primed signals (') refer to unbound components): δ = 8.67 (s, β-pyrrole CH), 8.65 (s, β-pyrrole' CH), 8.57 (br s, bpy' CH₂ and CH₆), 8.43 (d, *J*=7.0 Hz, bpy CH₂ and CH₆), 8.08 (m, *meso*-aromatic CH), 7.96 (dd, *J*=1.5, 7.5 Hz, *meso*-aromatic CH), 7.91 (dd, *J*=1.5, 7.5 Hz, *meso*-aromatic' CH), 7.55 (m, *meso*-aromatic CH), 7.49 (m, *meso*-aromatic CH), 7.03 (d, *J*=7.0 Hz, bpy' CH₃ and CH₅), 6.75 (d, *J*=7.0 Hz, bpy CH₃ and CH₅), 6.69 (br s,

catechol'), 6.65 (br s, catechol'), 6.03 (dd, $J=3.0, 9.5$, catechol), 5.72 (dd, $J=3.0, 9.5$, catechol), 5.46 (d, $J=7.0$ Hz, bpy' CH3' and CH5'), 5.22 (dd, $J=1.5, 5.8$ Hz, bpy CH3' and CH5'), 4.86 (br s, ethyl CH₂), 4.74 (br s, ethyl' CH₂), 3.95 (br s, ether' OCH₂), 3.78 (t, $J=4.5$ Hz, ether' OCH₂), 3.72 (s, ether' OCH₂), 3.59 (m, ether OCH₂), 3.51 (m, ether OCH₂), 3.59 (s, ether OCH₂), 2.66 (s, *meso*-aromatic CH₃), 1.70 (dd, $J=1.5, 5.0$ Hz, bpy' CH₂' and CH6'), 1.60 (dd, $J=1.5, 5.0$ Hz, bpy CH₂' and CH6'); ¹³C NMR (125.7 MHz, CD₂Cl₂, 22°C): $\delta = 181.2, 152.2, 149.3, 146.8, 145.9, 145.7, 145.6, 144.1, 139.8, 138.6, 137.5, 134.62, 134.57, 134.3, 132.2, 127.8, 127.5, 125.5, 123.9, 122.1, 121.8, 121.5, 120.0, 119.7, 114.6, 112.1, 71.4, 71.0, 70.5, 70.3, 69.5, 67.9, 57.8, 21.5$; MS (ESI+): $m/z = 2879 [M + CH_3NO_2, PF_6]^-$, 2080 [2%, $M - (DBZ24C8, PF_6)]^-$, 1998 [5%, $M - (DBZ24C8, 2PF_6) + CH_3NO_2]^+$, 1282 [4%, $M - (TTP, DBZ24C8, PF_6)]^-$ 1200 [5%, $M - (TTP, DBZ24C8, 2PF_6) + CH_3NO_2]^+$; UV/Vis (CH₂Cl₂): $\lambda_{max} / nm (\log \epsilon / M^{-1}cm^{-1}) = 250 (4.44), 273 (4.43), 413 (5.25), 533 (4.16), 567 (3.62)$; Selected IR (microscope): $\nu = 1959 (CO) cm^{-1}$.



[Ru(TTP)(CO)]₂[PF₆]₂[2]rotaxane (5) : A solution of 1,2-bis(4,4'-dipyridinium)ethane dication (**1**) (15.0 mg, 2.38×10^{-2} mmol) in acetone (5.0 mL) was treated with 2.1 molar

equivalents of Ru(TTP)(CO)(EtOH) (44 mg, 5.23×10^{-2} mmol) and stirred for 30 min. The reaction mixture concentrated to dryness and redissolved in dichloromethane (2 mL). The resulting solution was diluted with pentane (15 mL) and the resulting solid was collected by filtration and was washed with a mixture of Et₂O/pentane (20:80) and dried under vacuum. Yield: 56 mg (95%).

M.p. >300°C (decomp); ¹H NMR (500 MHz, [D₆]acetone, 22°C): δ = 8.67 (s, 16H), 8.59 (d, *J*=7.0 Hz, 4H), 8.11 (dd, *J*=2.0, 7.5 Hz, 8H), 7.89 (dd, *J*=2.0, 7.5 Hz, 8H), 7.63 (d, *J*=7.5 Hz, 8H), 7.51 (d, *J*=7.5 Hz, 8H), 7.49 (d, *J*=7.5 Hz, 4H), 5.90 (dd, *J*=1.5, 5.5 Hz, 4H), 5.17 (s, 4H), 2.68 (s, 24H), 1.72 (dd, *J*=1.5, 5.5 Hz, 4H); ¹³C NMR (125.7 MHz, [D₆]acetone, 22°C): δ = 146.1, 145.9, 144.6, 140.3, 138.1, 134.9, 134.6, 132.7, 128.4, 128.0, 126.5, 122.6, 121.0, 60.1, 21.5; MS (ESI+): *m/z* = 2080 [5%, M – PF₆]⁺, 1282 [5%, M – (TTP, PF₆)]⁻; Selected IR (microscope): ν = 1959 (CO) cm⁻¹.

X-ray Crystallographic Study: The crystallographic data for [2]rotaxane **4** is shown in Table 2. Crystals of [2]rotaxane **4** were grown from acetone. X-Ray data were collected on a Bruker PLATFORM/SMART 1000 CCD at 193 K using a graphite-monochromated *Mo-K_α* radiation (λ = 0.71073 Å) by taking ω scans at 0.2° intervals. The structures were solved by direct methods/fragment search using the computer program DIRDIF-96 and refined by full-matrix least-squares with anisotropic displacement parameters for the non-hydrogen atoms using the computer program SHELXL-93.¹² Hydrogen atoms were

introduced in their idealized positions as indicated by the sp^2 or sp^3 geometries of their attached carbon atoms.

Table 2. Crystallographic data for the [2]Rotaxane **4**

Molecular Formula	$C_{166.5}H_{169}F_{12}N_{12}O_{17.5}P_2Ru_2$
Molecular Weight	$M = 3110.22$
Crystal size/mm	$0.59 \times 0.08 \times 0.05$
Crystal system	monoclinic
Space group	$P2_1/n$ (a nonstandard setting of $P2_1/c$ [No. 14])
$a/\text{\AA}$	11.655 (2)
$b/\text{\AA}$	30.385 (5)
$c/\text{\AA}$	24.340 (4)
$\beta/^\circ$	103.745 (3)
Z	2
$V/\text{\AA}^3$	8373 (2)
Density/ g cm^{-3}	1.234
μ/mm^{-1}	0.276
Data collection 2θ limit/ $^\circ$	53.10
Total data collected	41325
Independent reflections	17184
Observed data with $I \geq 2\sigma(I)$	4929
Absorption correction method	SADABS
Range of transmission factors	0.9803–0.5738
Data/restraints/parameters	17184 / 0 / 976
Goodness-of-fit on F^2	0.864
Final R indices [$I \geq 2\sigma(I)$] ^a	
$R_1 = [F_o^2 \geq 2\sigma(F_o^2)]$	0.0877
$wR_2 = [F_o^2 \geq -3\sigma(F_o^2)]$	0.2673
Largest difference peak and	1.418 and $-0.901 \text{ e \AA}^{-3}$

$$^a R_1 = \sum ||F_o| - |F_c|| / \sum |F_o|; wR_2 = \{ \sum [w(F_o^2 - F_c^2)^2] / \sum [w(F_o^4)] \}^{1/2}.$$

3.5 – References

1. (a) M.-J. Blanco, M. C. Jiménez, J.-C. Chambron, V. Heitz, M. Linke and J.-P. Sauvage, *Chem. Soc. Rev.*, **1999**, 28, 293; (b) L. Flamigni, N. Armaroli, F. Barigelletti, J.-C. Chambron, J.-P. Sauvage and N. Solladie, *New J. Chem.*, **1999**, 23, 1151 and references therein.
2. For a review on rotaxanes and other molecular machines: V. Balzani, A. Credi, F. M. Raymo and J. F. Stoddart, *Angew. Chem. Int. Ed.*, **2000**, 39, 3348 and references therein.
3. (a) P. R. Ashton, R. Ballardini, V. Balzani, A. Credi, K. R. Dress, E. Ishow, C. J. Kleverlaan, O. Kocain, J. A. Preece, N. Spencer, J. F. Stoddart, M. Venturi and S. Wenger, *Chem. Eur. J.*, **2000**, 6, 3558. For other examples of light driven motions see: (b) A. M. Brouwer, C. Frochot, F. C. Gatti, D. A. Leigh, L. Mottier, F. Paolucci, S. Roffia and G. W. H. Wurpel, *Science*, **2001**, 291, 2124; (c) N. Armaroli, V. Balzani, J.-P. Collin, P. Gaviña, J.-P. Sauvage and B. Ventura, *J. Am. Chem. Soc.*, **1999**, 121, 4397.
4. F. M. Raymo, K. N. Houk and J. F. Stoddart, *J. Am. Chem. Soc.*, **1998**, 120, 9318.
5. Previously employed stoppers include: phosphines, (a) S. J. Rowan and J. F. Stoddart, *J. Am. Chem. Soc.*, **2000**, 122, 164; calixarenes, (b) C. Fischer, M. Nieger, O. Mogck, V. Bohmer, R. Ungaro and F. Vogtle, *Eur. J. Org. Chem.*, **1998**, 155; fullerenes, (c) N. Armaroli, F. Diederich, C. O. Dietrich-Buchecker, L. Flamigni, G. Marconi, J.-F. Nierengarten and J.-P. Sauvage, *Chem. Eur. J.*, **1998**, 4, 406; ferrocene, (d) A. C. Benniston, A. Harriman and V. M. Lynch, *J. Am. Chem. Soc.*, **1995**, 117, 5275;

- saccharides, C. Kauffmann, W. M. Muller, F. Vogtle, S. Weinman, S. Abramson and B. Fuchs, *Synthesis*, **1999**, 849; (e) T. Schmidt, R. Schmieder, W. M. Muller, B. Kiupel and F. Vogtle, *Eur. J. Org. Chem.*, **1998**, 2003; dendrimers, (f) D. B. Amabilino, P. R. Ashton, V. Balzani, C. L. Brown, A. Credi, J. M. J. Frechet, J. W. Leon, F. M. Raymo, N. Spencer, J. F. Stoddart and M. Venturi, *J. Am. Chem. Soc.*, **1996**, *118*, 12012; trityl, (g) M. C. Jiménez, C. Dietrich-Buchecker and J.-P. Sauvage, *Angew. Chem. Int. Ed.*, **2000**, *39*, 3284; (h) C. Heim, A. Affeld, M. Nieger and F. Vogtle, *Helv. Chim. Acta.*, **1999**, *82*, 746.
6. (a) S. J. Rowan and J. F. Stoddart, *Org. Lett.*, **1999**, *1*, 1913; (b) S. J. Cantrill, S. J. Rowan and J. F. Stoddart, *Org. Lett.*, **1999**, *1*, 1363.
7. For examples of using coordination chemistry to interlock rotaxanes, see: (a) S. J. Loeb and J. A. Wisner, *Chem. Commun.*, **1998**, 2757; (b) S. J. Loeb and J. A. Wisner, *Angew. Chem. Int. Ed.*, **1998**, *37*, 2838; (c) D. J. Cárdenas, P. Gaviña and J.-P. Sauvage, *Chem. Commun.*, **1996**, 1915; (d) A. P. Lyon and D. H. Macartney, *Inorg. Chem.*, **1997**, *36*, 729 and references therein. For examples to interlock catenanes, see: (e) C. Dietrich-Buchecker, N. Geum, A. Hori, M. Fujita, S. Sakamoto, Kentaro and J.-P. Sauvage, *Chem. Commun.*, **2001**, 1182; (f) M. Fujita, *Acc. Chem. Res.*, **1999**, *32*, 53; (g) A. C. Try, M. M. Harding, D. G. Hamilton and J. K. M. Sanders, *Chem. Commun.*, **1998**, 723. For examples to link rotaxanes into oligomers and necklaces, see: (h) S.-G. Roh, K.-M. Park, G.-J. Park, S. Sakamoto, K. Yamaguchi and K. Kim, *Angew. Chem. Int. Ed.*, **1999**, *38*, 638; (i) D. Whang, K.-M. Park, J. Heo, P. Ashton and K. Kim, *J. Am. Chem. Soc.*, **1998**, *120*, 4899.

8. (a) M. Andersson, M. Linke, J.-P. Chambron, J. Davidsson, V. Heitz, J.-P. Sauvage, L. Hammarström, *J. Am. Chem. Soc.*, **2000**, *122*, 3526; (b) N. Solladie, J.-C. Chambron and J.-P. Sauvage, *J. Am. Chem. Soc.*, **1999**, *121*, 3684; (c) F. Vogtle, F. Ahuis, S. Baumann and J. L. Sessler, *Liebigs Ann. Rec.*, **1996**, 921; (d) R. Ishin and A. E. Kaifer, *J. Am. Chem. Soc.*, **1991**, *113*, 8188.
9. M. J. Gunter, N. Bampos, K. D. Johnstone and J. K. M. Sanders, *New J. Chem.*, **2000**, *25*, 166.
10. M. I. Attalla, N. S. McAlpine and L. A. Summers, *Z. Naturforsch., Teil B*, **1984**, *39*, 74.
11. J. C. Adrian and C. S. Wilcox, *J. Am. Chem. Soc.*, **1991**, *113*, 678.
12. G. M. Sheldrick, *Acta Crystallogr.*, **1990**, *A46*, 467.

Chapter 4 – Ruthenium(II)salophen Assemblies Using Axial Coordination

This chapter of the thesis introduces ruthenium(II) carbonyl salophen complexes as new synthons for supramolecular chemistry. The discussion will focus on the synthesis, properties and application of a series of unprecedented mononuclear and binuclear ruthenium(II) carbonyl complexes with N_2O_2 Schiff base ligands based on 3,5-di-*tert*-butyl-salicylaldehyde and three different *ortho*-diamines. The mononuclear metallosalophen complex acts as a versatile supramolecular synthon as illustrated by the fact that it spontaneously forms linear and three-dimensional assemblies through axial coordination to pyridyl Lewis bases. Using this motif, neutral and charged assemblies are prepared and characterized in the same manner as the metalloporphyrin arrays described in Chapter 2. The mononuclear carbonyl complex either exists as a non-rigid molecule or as a species that is involved in an exchange process with an unidentified axial ligand at room temperature. These processes are prevented when a Lewis base occupies the axial coordination site. The versatility of the salophen ligand is highlighted by the preparation of novel bimetallic ruthenium(II) carbonyl salophen complexes from 1,2,4,5-tetraaminobenzene and 2,3,7,8-tetraaminodibenzo[1,4]dioxin which are compared to the analogous bimetallic porphyrin complex. The bimetallic complexes are isolated as a mixture of *cis*- and *trans*-diastereomers with respect to the spatial relationship between the two axially bound carbon monoxide ligands. The electronic spectral and electrochemical properties of the ruthenium(II) carbonyl mono- and bis(salophen) pyridyl adducts are compared. These studies reveal that the central tetraamino linker regulates the

communication between the two metal centres. Also presented are preliminary self-assembly studies using the novel bimetallic salophen and porphyrin complexes with pyridyl Lewis bases to construct molecular rectangles and a three dimensional triangular prism.

4.1 – Introduction

As discussed in Chapters 2 and 3, the use of vacant axial coordination sites on metalloporphyrins in conjunction with substituted pyridines to create supramolecular assemblies with well-defined architectures and novel properties has been well exploited and extensively documented.¹ The construction of more elaborate porphyrin-based assemblies would provide access to new materials with tunable optical and electrochemical properties suitable for modeling photosynthetic functions such as energy capture and transfer reactions as well as new photonic devices such as solar cells and gated molecular circuitry.² There are, however, significant shortcomings in the utility of substituted porphyrins. The syntheses tend to provide the macrocycles in low yields and the macrocycles are tedious to isolate and purify, making the “design-to-realization” period of highly functionalized porphyrinic building blocks lengthy. Alternative molecular platforms that provide free binding sites suitable for axial coordination, but are more conducive to convenient synthesis, modification and isolation, need to be explored.

4.1.1 – Metallosalens and Metallosalophens in Supramolecular Chemistry

Metallosalens (salen = *N,N'*-bis(salicylidene)ethylenediamine, (1)) and metallosalophens (salophen = *N,N'*-bis(salicylidene)-1,2-phenylenediamine, (2)) have received little attention as sources of planar supramolecular building blocks (Figure 1).

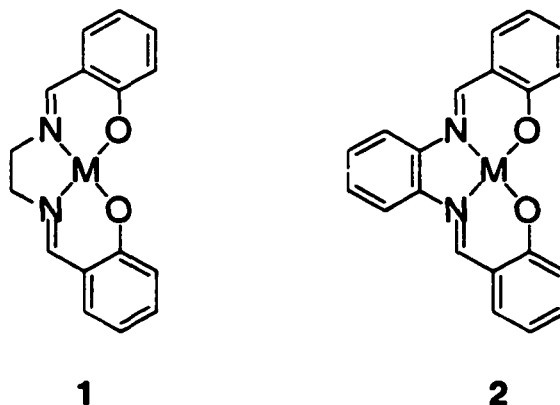


Figure 1.

These tetradentate ligands are particularly attractive for several reasons: 1) they are conveniently prepared in a single synthetic step by condensing substituted *ortho*-diamines with salicylaldehyde and, as a result, can be readily tailored by modifying the substituents on the diamine synthon, 2) they form stable, easily isolated coordination compounds with a wide variety of metals, and 3) if the appropriate metal is inserted into the ligands, the resulting complexes brandish accessible axial Lewis-acidic sites. Despite this appeal, there is only one report describing the use of metallosalens or metallosalophens to construct multicomponent supramolecular assemblies through axial coordination. In it, the authors describe how 4,4'-bipyridine axially coordinates to two methylcobalt(III) salen complexes to produce a linear three-component assembly.³

The success in constructing multicomponent assemblies using axial coordination to ruthenium(II) carbonyl porphyrin synthons⁴ prompted the evaluation of ruthenium(II) carbonyl salophen analogues in supramolecular chemistry. The reported examples of axial coordination to ruthenium(II) carbonyl salen and ruthenium(II) carbonyl salophen complexes are limited in their scope and have certainly not been given the same degree of attention as their porphyrin counterparts.

The remaining sections of this chapter describe the synthesis, properties and application of the Ru(BSP)(CO) building block **4** (BSP = *N,N'*-bis(3,5-di-*tert*-butylsalicylidene)-1,2-phenylenediamine) and the bimetallic complexes [Ru₂(BS2P)(CO)₂] **14** (BS2P = *N,N'',N''',N''''*-tetra-(3,5-di-*tert*-butylsalicylidene)-1,2,4,5-phenylenetetraamine) and [Ru₂(BS2DP)(CO)₂] **16** (BS2DP = *N,N'',N''',N''''*-tetra-(3,5-di-*tert*-butylsalicylidene)-2,3,7,8-dibenzo[1,4]dioxin-tetraamine) to the generation of supramolecular assemblies.

4.2 – Results and Discussion

4.2.1 – Synthesis of the Ruthenium(II) Carbonyl Salophen Building Block

In an early report of metal-carbonyl insertion into salens, Calderazzo and coworkers describe the reaction of the unsubstituted ligand **1** (M = 2H) with Ru₃(CO)₁₂ to produce a metallosalen dimer in high yield.⁵ Owing to the insolubility of this dimeric product, it was characterized primarily using elemental analysis techniques which gave

the correct 1:1 metal-to-ligand stoichiometry for the coordination compound but not its three-dimensional structure. The authors postulated that the dimer is held together through axial coordination to the ruthenium center of each monomer by one of the Lewis basic oxygen atoms of the other. This claim was based on the fact that analogous iron(III) coordination compounds have been characterized in the solid-state which possess this bridged arrangement (Figure 2).⁶

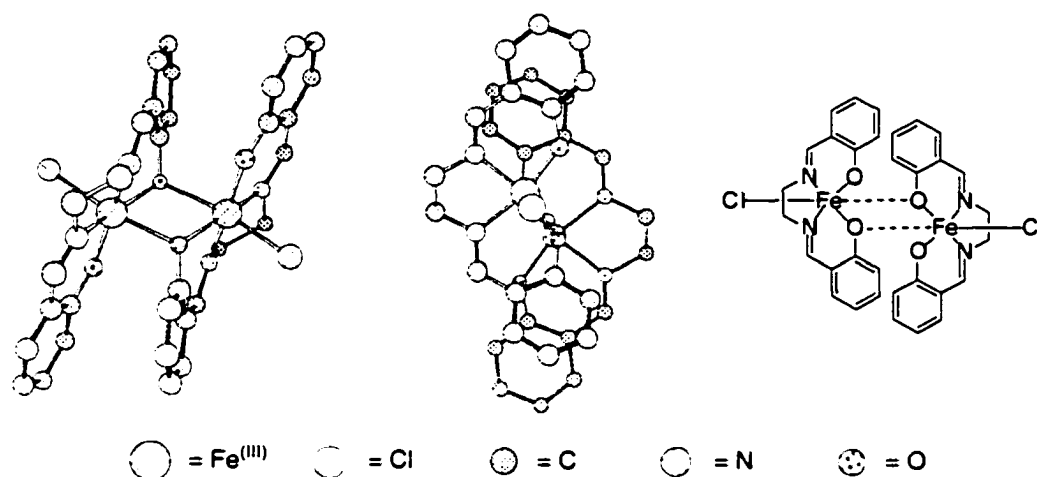
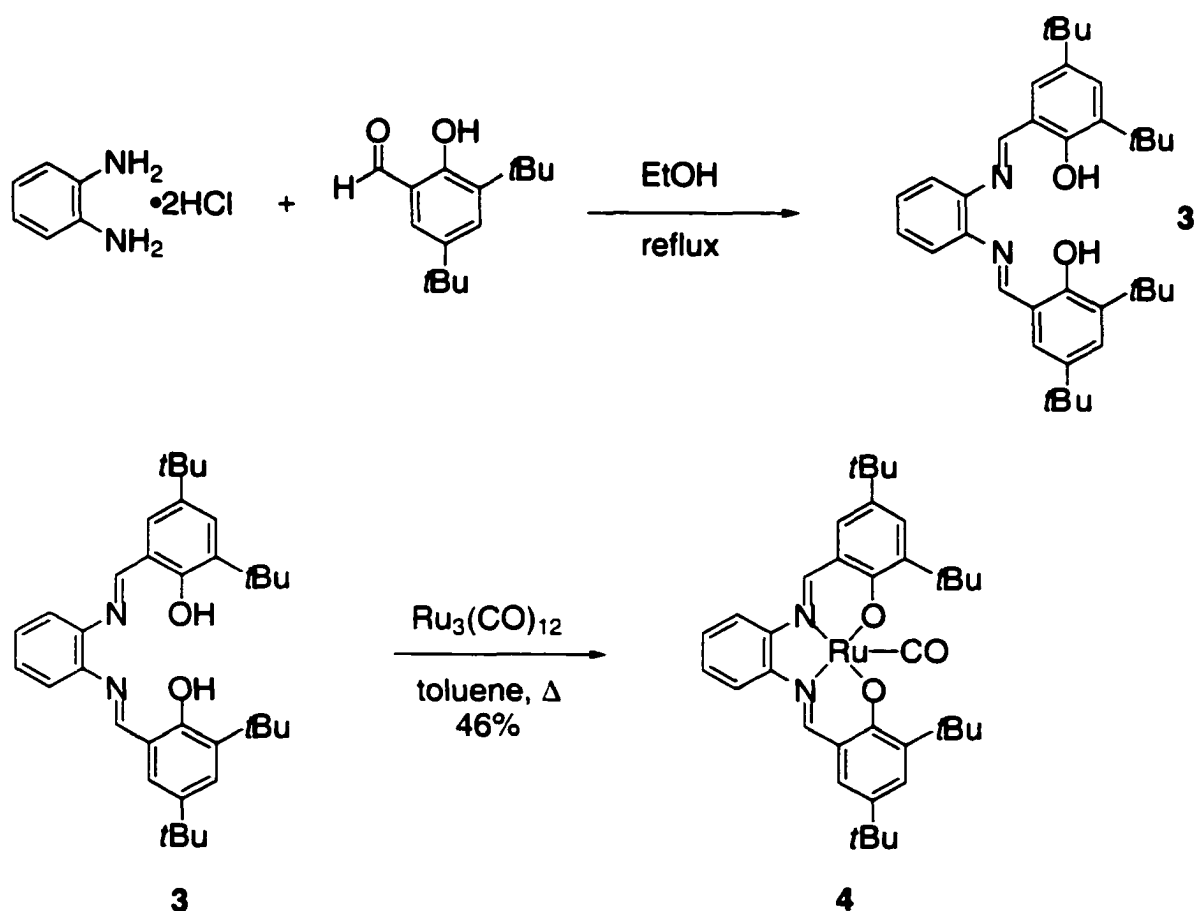


Figure 2. An example of an iron(III) salen dimer.

In a later report, Farrell and coworkers describe how the $[\text{Ru}(\text{1})(\text{CO})_2]$ dimer can be broken into its monomeric fragments only when heated in pyridine, where it dissociates to yield the pyridine-coordinated metallosalen monomer $\text{Ru}(\text{salen})(\text{CO})(\text{py})$.⁷ Khan and coworkers described an alternative, milder approach to metal-carbonyl insertion whereby a variety of chloro- and methoxy-substituted salens and salophens were reacted with $\text{Cs}_2[\text{RuCl}_4(\text{CO})(\text{H}_2\text{O})]$.⁸ However, the axial coordinating behaviour of these chloro- and methoxy-substituted ruthenium(II) Schiff base complexes have not been reported.

In light of the dimerization product described by Calderazzo and Farrell, and the less than satisfactory structural and binding information for the reported metallo-Schiff base complexes, a more soluble salophen ligand that is amenable to characterization in self-assembly processes was desired. Based on these requirements the decision was made to use the known *N,N*-bis(3,5-di-*tert*-butylsalicylidene)-1,2-phenylenediamine (**3**), which precipitates as a yellow solid when 3,5-di-*tert*-butylsalicylaldehyde and 1,2-diaminobenzene are condensed in hot ethanol.⁹ Metal insertion was accomplished by heating ligand **3** with an excess of $\text{Ru}_3(\text{CO})_{12}$ in toluene (Scheme 1).



Scheme 1.

Ru(BSP)(CO) (**4**) was isolated as a burgundy air-stable solid by a combination of column chromatography through alumina (activity II-III) and recrystallization from aqueous ethanol. The isolation of **4** as a monomer was first suggested by the absence of signals in the positive ion ESI mass spectrum corresponding to higher aggregates or multiply-charged species, and then by the ease of forming axially-coordinated supramolecular assemblies. In addition to peaks corresponding to the parent ion ($m/z = 668$) and the loss of carbon monoxide ($m/z = 640$), the ESI mass spectrum of a nitromethane solution of **4** contained peaks corresponding to the hydrated ($m/z = 686$) and solvated ($m/z = 729$ for $[M + \text{CH}_3\text{NO}_2]^+$) coordination compounds. It is reasonable to assume that, under these conditions, the solvent molecule (CH_3NO_2 or H_2O) most likely occupies the axial site on the metal center. It can be postulated that the presence of the bulky *tert*-butyl substituents on the salophen ligand inhibits the dimerization of Ru(BSP)(CO) (**4**). Similar results have been reported for the zinc(II) analogues of these types of coordination compounds.^{10a} However, an example of a dimer was reported for the group 13 aluminum(III) analogue that used a similar salophen ligand to that of **3** (Figure 3).^{10b}

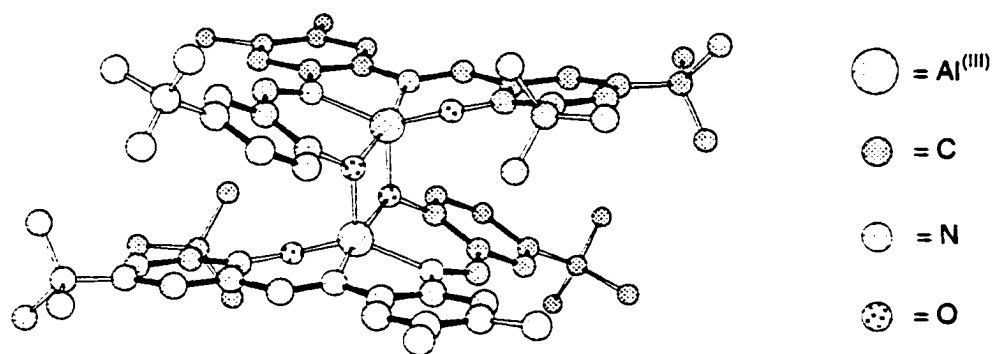


Figure 3. An example of an aluminum(III) salophen dimer.

In this case, the dimer crystallized after the metallosalophen complex ejected two of the eight bulky *tert*-butyl substituents *via* a Friedel-Crafts dealkylation process at -30°C . This observation suggests that Ru(BSP)(CO) (**4**) could form an oxygen-bridged dimer. Computer-assisted molecular modeling of **4**, derived from the crystal structures of [Fe(I)(Cl)]₂ and the aluminum(III) complex, revealed that the sterically demanding *tert*-butyl substituents hinder the metallosalophens from approaching each other, enough to impede the formation an analogous dimer as that originally reported by Calderazzo.

4.2.2 – ¹H NMR Solution Studies of the Ruthenium(II) Carbonyl Salophen

Investigations using ¹H NMR spectroscopy showed that **4** exists at room temperature as either a structurally non-rigid molecule or as a species that is involved in a fast exchange process on the NMR time scale with an unidentified axial ligand in deuterated dichloromethane (a non-coordinating solvent). The broad signals in the spectrum sharpened after the addition of Lewis basic solvents such as acetone or pyridine (Figure 4). In the presence of these Lewis basic solvents, the axial site will be occupied and a rigid hexacoordinate metallosalophen complex will be formed. It was also apparent that these Lewis basic solvents coordinate strongly enough to prevent the unidentified ligand from competing in the coordination process.

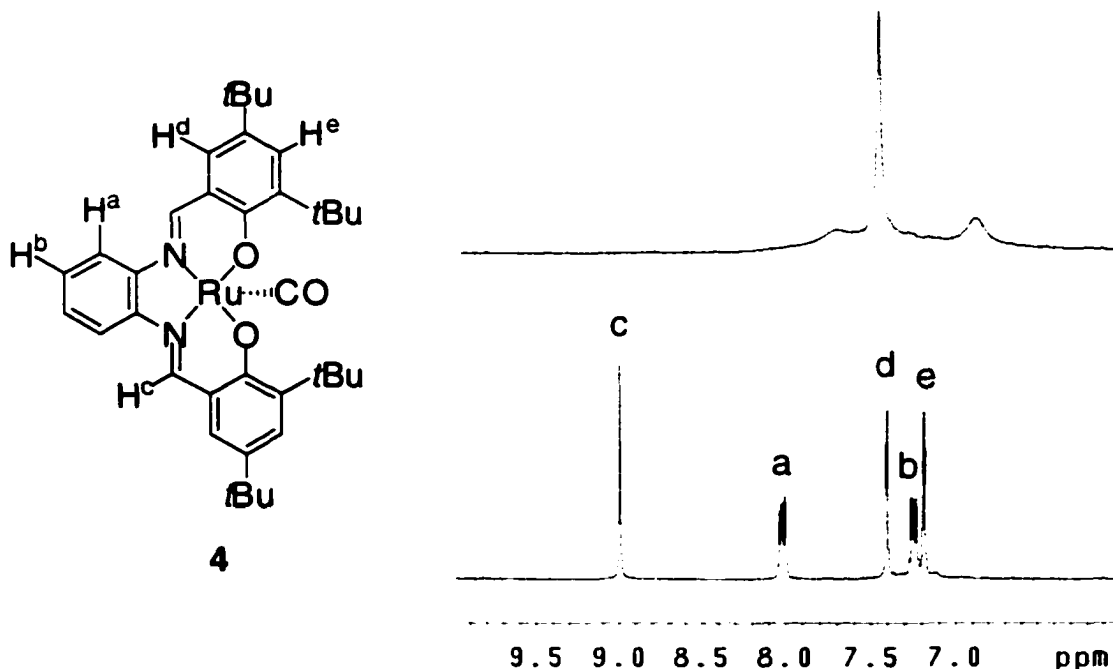


Figure 4. ^1H NMR (500 MHz) experiment of the aromatic region of **4** in CD_2Cl_2 (top) and after the addition of excess $[\text{D}_6]\text{acetone}$ (bottom). Spectra were recorded at room temperature. Peak assignments correspond to the atoms labels of structure **4**.

4.2.3 – ^1H NMR Variable-Temperature Studies

The coordination event was also studied by performing variable-temperature ^1H NMR, two-dimensional COSY, and NOESY experiments on dichloromethane samples of **4** prepared under inert nitrogen atmosphere and anhydrous conditions. The variable-temperature ^1H NMR study was repeated with the same sample and the same spectra were reproduced. This suggested that the coordination of the unidentified ligand was reversible. For the variable-temperature study, the samples were first heated to 40°C and at this temperature there were no observable changes (sharpening of the signals) in their spectra. This suggested that the proton resonances were in coalescence at room temperature and appeared as two very broad resonances at $\delta = 7.8$ and 6.8 ppm with one

sharper signal at $\delta = 7.4$ ppm (Figure 5). The samples were then cooled from 27°C down to -50°C and the spectra generated are shown in Figure 5. Upon cooling the sample from 27°C to 20°C, the resonances changed in their appearance with one signal splitting ($\delta = 6.8$ ppm) and the sharp signal broadening ($\delta = 7.4$ ppm). Upon cooling to 0°C, the signals eventually separated into five domains that consisted of unresolved and resolved signals.

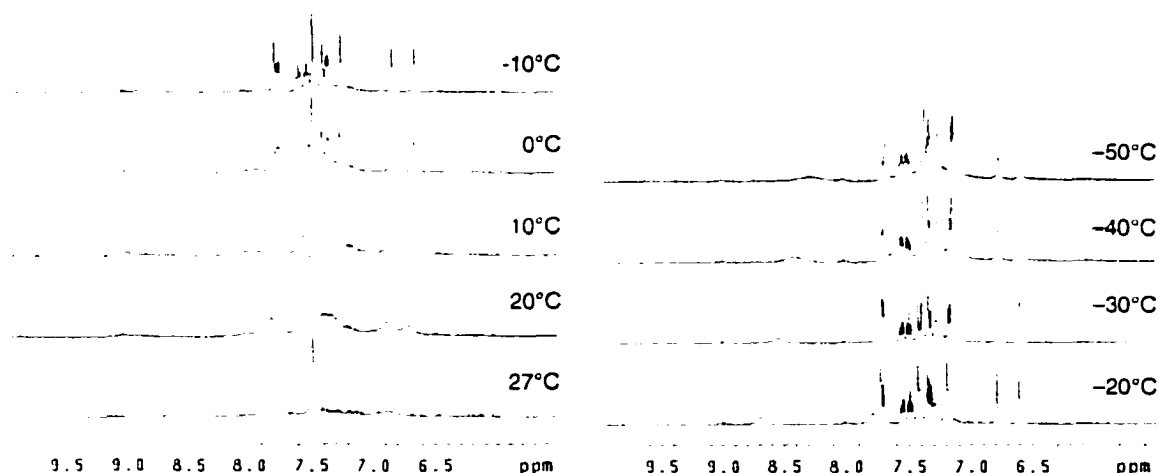


Figure 5. Variable-temperature ^1H NMR (500 MHz) experiment of the aromatic region of **4** in CD_2Cl_2 .

The spectra obtained at -10°C to -30°C consisted of fifteen signals in total: five broad signals, two triplets ($J = 7.5$ Hz), two doublets ($J = 7.5$ Hz), four doublets ($J = 1.5$ Hz), and two singlets (Figure 5 and Figure 6). The positions of these signals shifted as the temperature was lowered from -10°C to -30°C. Based on these shifts, the relative positions of the ten sharp signals (signals labeled 1-10 in Figure 6) and the five broad signals (signals labeled a-e in Figure 6) in each spectrum were located. The areas under the ten sharp peaks were integrated and had values that were consistently equal to one proton. The five broad signals were consistent with a C_s symmetric **4**, which will also

display five signals in the aromatic region. The broad signals in each spectrum were assigned and located by comparing their positions to the spectrum of **4** obtained in $\text{CD}_2\text{Cl}_2/[\text{D}_6]\text{acetone}$.

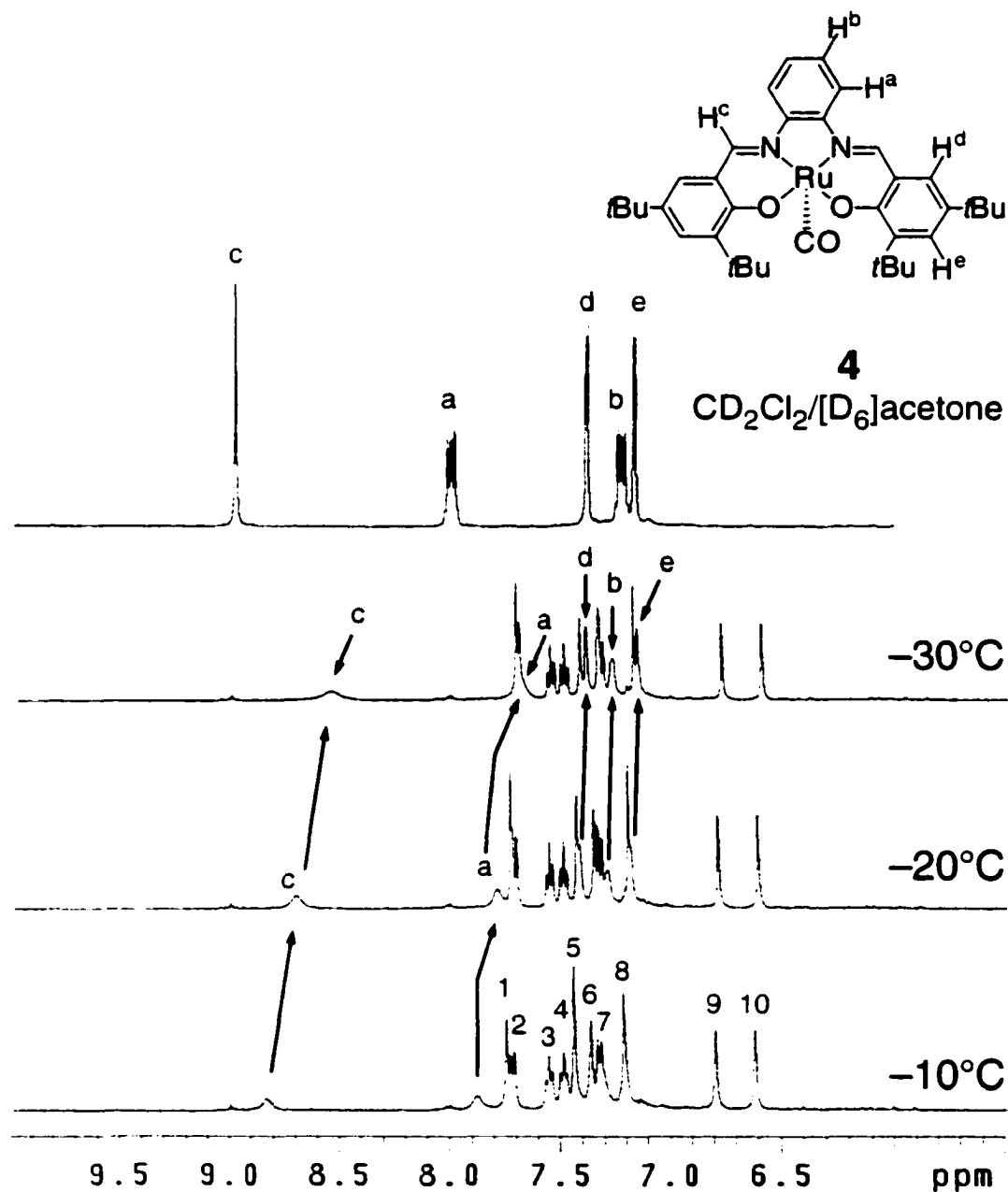


Figure 6. ^1H NMR (500 MHz) spectrum of the aromatic region of **4** in $\text{CD}_2\text{Cl}_2/[\text{D}_6]\text{acetone}$ (top trace). ^1H NMR (500 MHz) spectra of the aromatic region of **4** at -10°C , -20°C , and -30°C in CD_2Cl_2 (bottom traces). The arrows highlight the shifts and positions of the 5 broad signals as labeled in the structure of **4** (top). The sharp signals are labeled with numbers '1' through '10' (bottom trace).

The two signals for the *ortho*-diamine fragment of a C_2 symmetric **4** appeared as an AA'BB' pattern ($J = 7.5$ Hz) (signals labeled 'a' and 'b' for **4** in the top trace of Figure 6). At -20°C these signals were split into four unique signals that were consistent with a dissymmetric ABCD pattern comprised of two doublets and two triplets ($J = 7.5$ Hz) (signals labeled 2, 3, 4 and 7 in the bottom trace of Figure 6). The four signals labeled 5, 6, 9 and 10 in the trace obtained at -10°C sharpened and were separated from neighbouring signals at -20°C and -30°C . The traces obtained at -20°C and -30°C revealed that these signals were doublets ($J = 1.5$ Hz) and were consistent with protons that reside on the *tert*-butyl substituted phenyl rings. From these observations it was postulated that **4** might be interconverting between two non-rigid trigonal bipyramidal (**4a** and **4b**) penta-coordinate complexes (Figure 7). In this extreme case, the ^1H NMR spectrum would consist of five aromatic resonances because structures **4a** and **4b** are C_2 -symmetric.

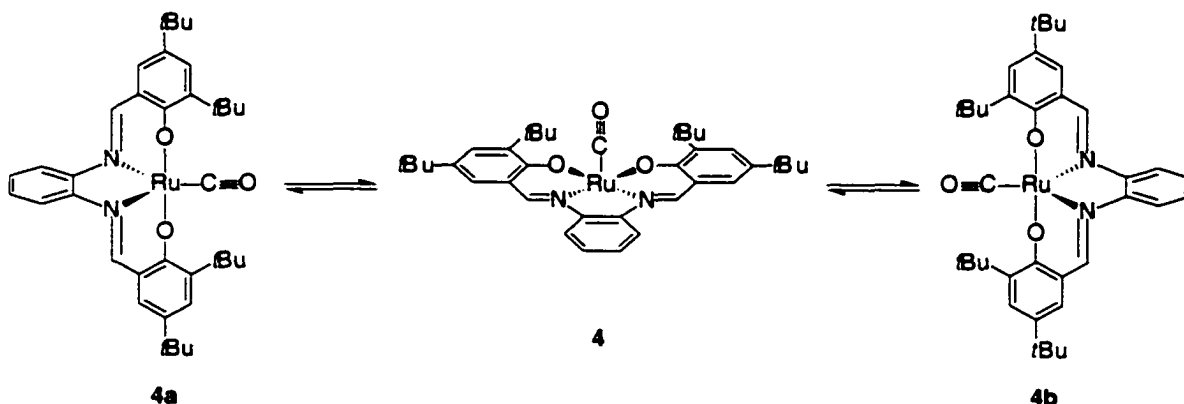


Figure 7. Two trigonal pyramidal isomers **4a** and **4b** interconvert through square pyramidal **4**.

Penta-coordinate metallocalophen complexes prefer the square pyramidal geometry because the salophen ligand does not provide enough flexibility to attain the

trigonal bipyramidal geometry.¹⁰ In light of this, a distorted geometry between square bipyramidal and trigonal bipyramidal could produce 10 aromatic resonances for a dissymmetric **4** as seen in the ¹H NMR spectra (structures **4c** and **4d** in Figure 8).

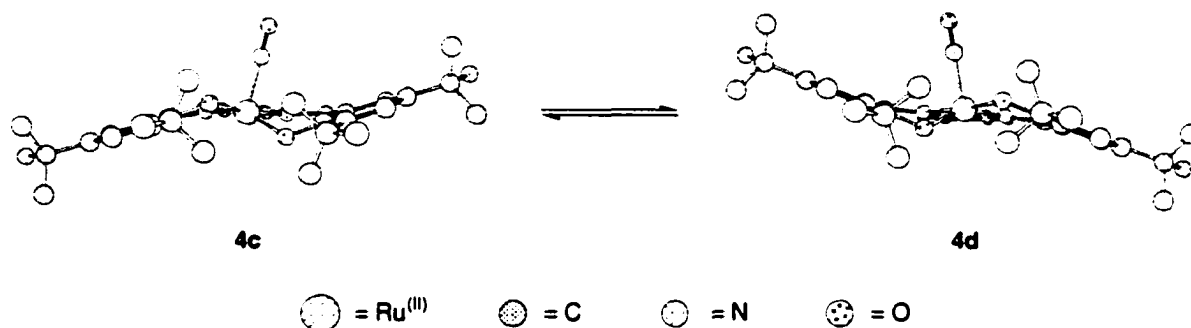


Figure 8. Molecular models of two distorted square pyramidal isomers **4c** and **4d** as obtained by MM2 calculations.

The modeled structures **4c** and **4d** reveal that this distortion introduces dissymmetry that might lead to ten signals in the aromatic region of the ¹H NMR spectrum. The plane of symmetry that bisects the Schiff base is lost and the tilted carbon monoxide can differentiate the two *tert*-butyl substituted phenyl rings. It is possible that the shielding region of the tilted carbon monoxide is close to one of these phenyl rings and will shift the phenyl ring's proton resonances upfield from the other signals in the spectrum (signals labeled 9 and 10 in Figure 6). If the two forms **4c** and **4d** were frozen out at -20°C , with some unchanged **4** still present, this would lead to the production of fifteen aromatic signals in its ¹H NMR spectrum. One other possibility remains. At colder temperatures there may be a higher propensity for **4** to form a dimer of the type known for iron(III) salens (Figure 9). This would also produce fifteen aromatic signals, five signals for the free monomer and ten signals for the dimer assuming the process is

slow on the NMR time scale. The dimer introduces dissymmetry and results in nonequivalent proton resonances because the metallosalophen complexes are offset. The presence a dimer would also explain why the two doublets at *ca.* 6.7 ppm ($J = 1.5$ Hz), are shifted upfield because it is possible that these protons might be positioned above the shielding regions of an aromatic ring resulting in an upfield shifting of the proton resonances.

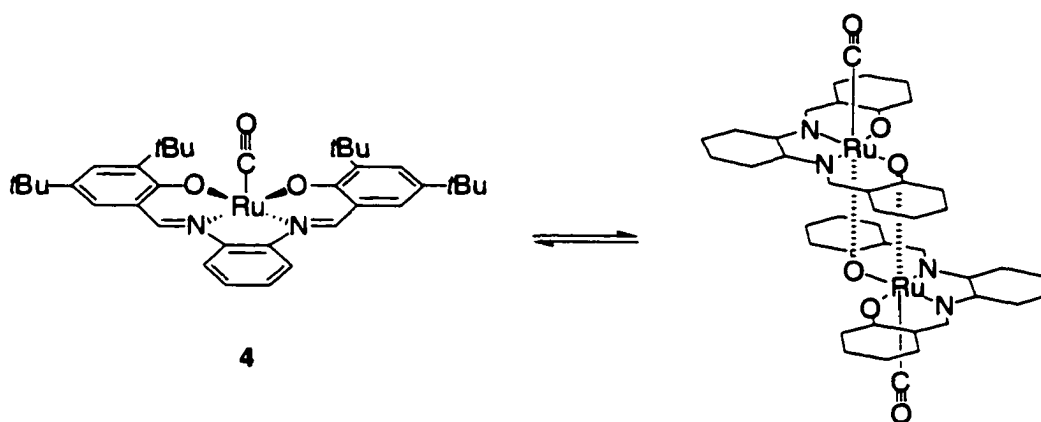


Figure 9. Schematic representation of the oxygen-bridged dimer of complex **4**. The substituents and double bond representations of the dimer have been omitted for clarity.

The assignment of the signals of **4** in the aromatic region of the ^1H NMR spectrum could provide some detailed information about the molecular structure of **4** at lower temperatures. Therefore, two-dimensional ^1H NMR measurements were performed.

4.2.4 – Two-Dimensional ^1H NMR COSY and NOESY Studies

A COSY experiment performed on samples cooled to -20°C allowed the sharp resonances in the region of 6.5–7.8 ppm to be assigned to the ring system of **4**. The COSY map is presented in Figure 10. The cross-peaks **a** and **b** between the aromatic *tert*-butyl phenyl protons identified the resonances at 6.8 and 6.6 ppm to be the protons

located on rings **A** and **B** of the structure shown in Figure 10. If these resonances corresponded to the protons located on the same ring then they should have displayed cross-peaks. The cross-peaks **c** and **d** allowed the connectivity pattern between aromatic protons on the *ortho*-diamine fragment to be identified. The two sharp singlets at 7.8 and 7.2 ppm did not show cross-peaks and were identified as the imine proton resonances of **4** (signals labeled '+' in Figure 10).

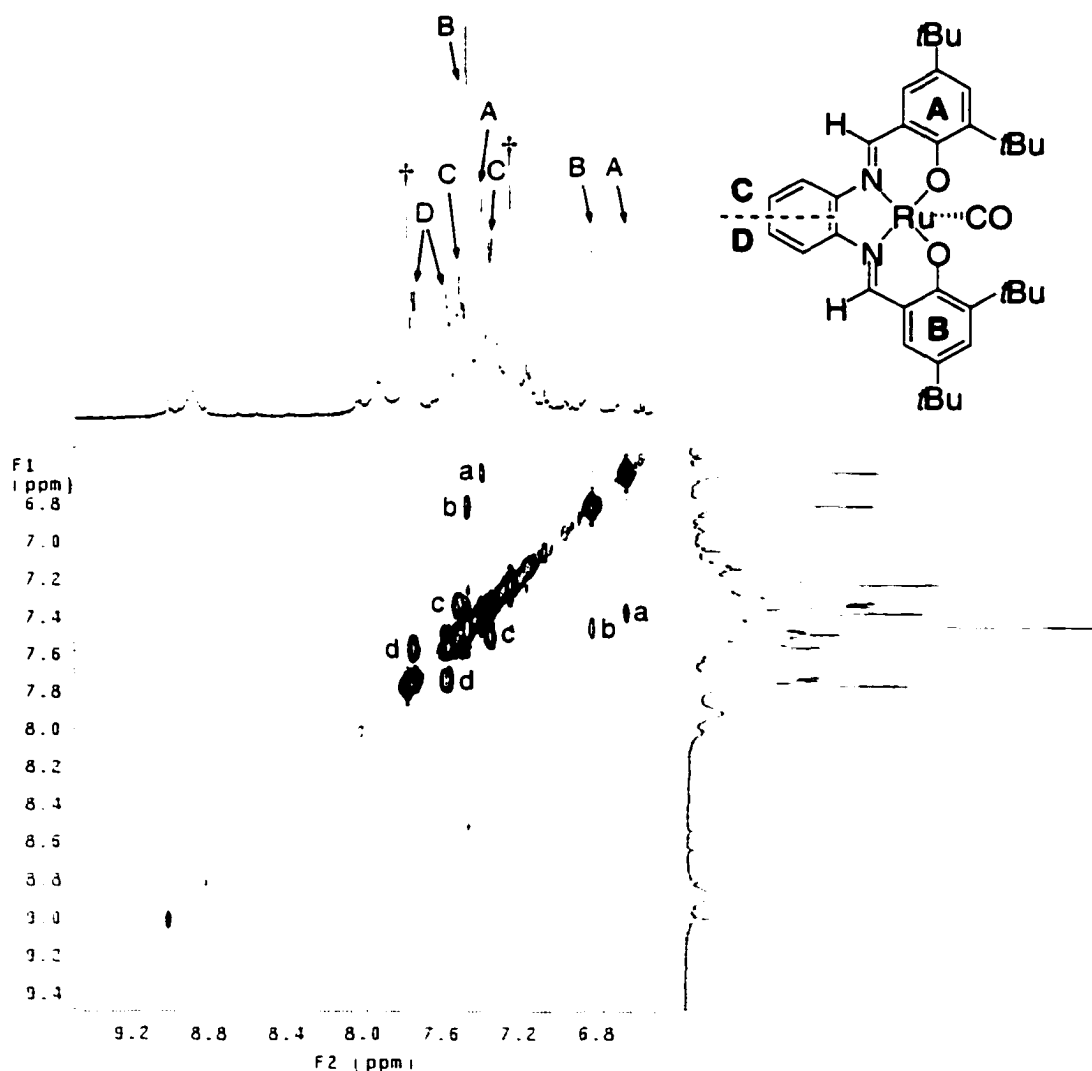


Figure 10. The COSY (500 MHz) map of **4** cooled to -20°C . The aromatic resonances labeled 'A', 'B', and 'C' refers to the ring they reside as shown in the inset structure. The symbol '+' refers to the imine proton resonances.

The connectivity pattern of **4** could not be confirmed by the presence of NOE cross-peaks obtained in a NOESY experiment performed on samples cooled to -20°C (Figure 11). At this temperature, the five broad signals exchanged with the ten sharp signals and produced strong exchange peaks instead of peaks that are related to close proximity effects.

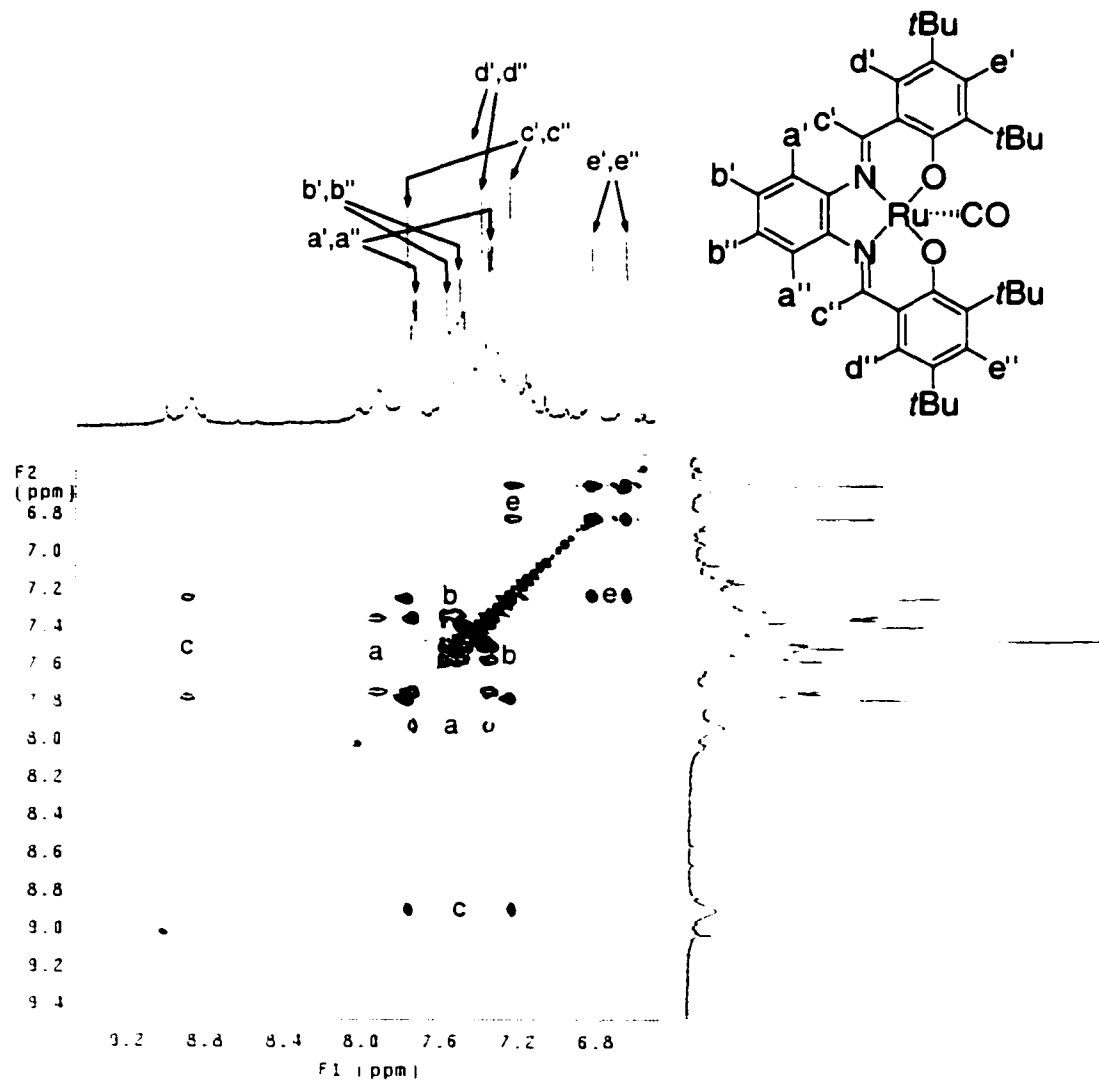
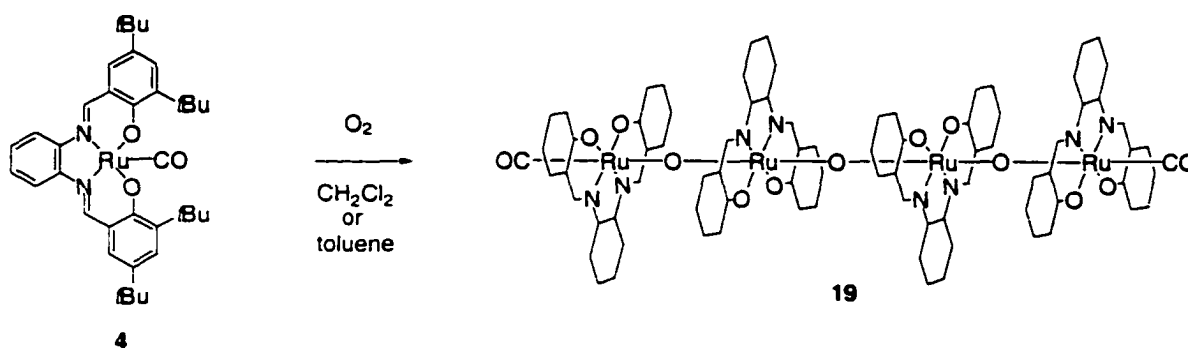


Figure 11. The NOESY spectrum (500 MHz) of **4** cooled to -20°C . The cross-peak labels a-e refer to the proton resonances of a symmetrical monomer **4**. The signals with primed labels refer to the protons resonances of a dissymmetric **4** as labeled in the structure.

This observation possibly suggests that a monomer/dimer exchange process was occurring. The exchange peaks provided an additional route to identify the resonances of the ring system of **4** at -20°C .

4.2.5 – X-Ray Crystallographic Analysis of the Ruthenium(II) Carbonyl Salophen

In order to provide information that might support or shed light on the variable temperature ^1H NMR solution studies of **4**, attempts were made to determine its solid state structure. Unfortunately, suitable crystals for these studies were not obtained from samples dissolved in THF, hexanes, toluene, or combinations of the three that were allowed to slowly evaporate inside a nitrogen atmosphere glove box kept at room temperature. Instead, an oxidation product was formed after the solvent (dichloromethane or toluene) was allowed to slowly evaporate from solutions containing **4** that were not protected from the atmosphere. Single crystals of this oxidation product suitable for structural determination were obtained from both of these solutions. The crystal structure shows that this product was an oxo-bridged ruthenium(salophen) tetramer **19** (Equation 1 and Figure 12).



Equation 1. The substituents and double bond representations of **19** have been omitted for clarity.

The X-ray structure shows that each Ru(BSP) unit is slightly puckered due to adjacent ligand–ligand repulsions. All aromatic protons of **19** are lying within the anisotropic ring current of the adjacent salophen complex (Figure 12).

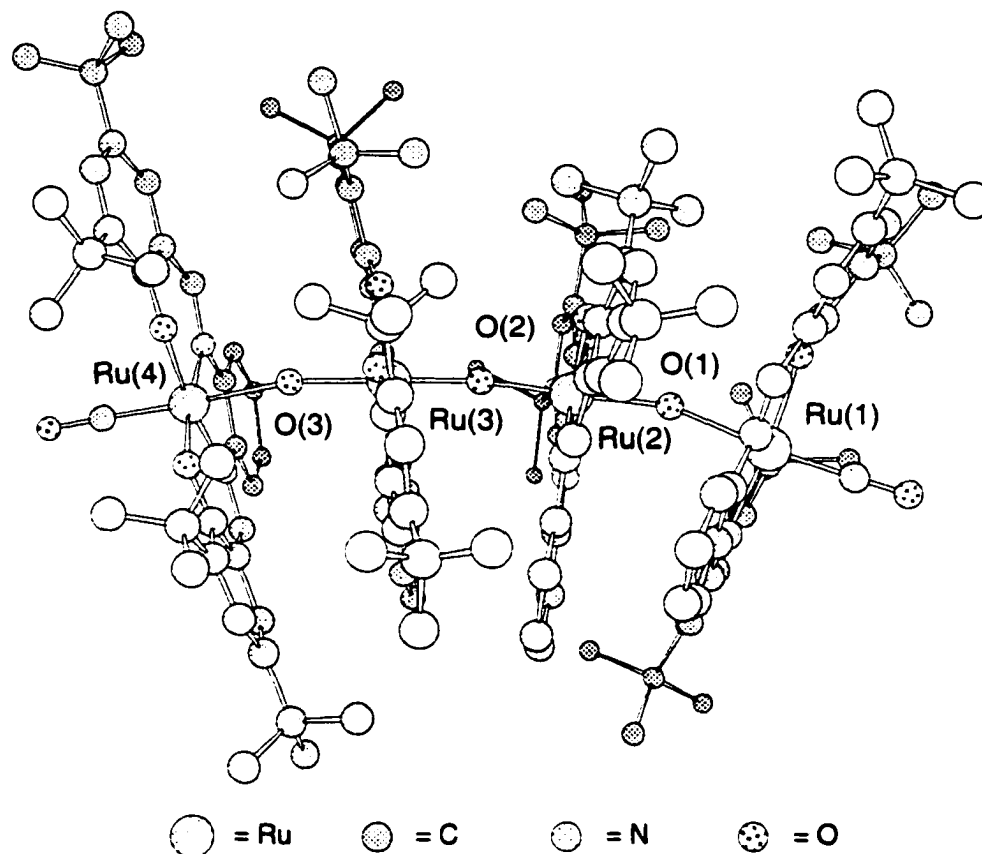


Figure 12. Molecular structure of **19** in the crystal.

The phenyl rings of the ligands are lying parallel to each other within π - π stacking range (3.5 Å mean Ph-Ph distance). The crystal structure shows that the distance between the metal centres is just enough to accommodate these π - π stacking interactions (Ru(1)-Ru(2) = 4.098, Ru(2)-Ru(3) = 3.631, and Ru(3)-Ru(4) = 4.098 Å). Another feature of the crystal structure is that each Ru(BSP) fragment is slightly tilted with respect to its neighboring Ru(BSP) ligand with bond angles of 160.6° (Ru(1)-O(1)-Ru(2)),

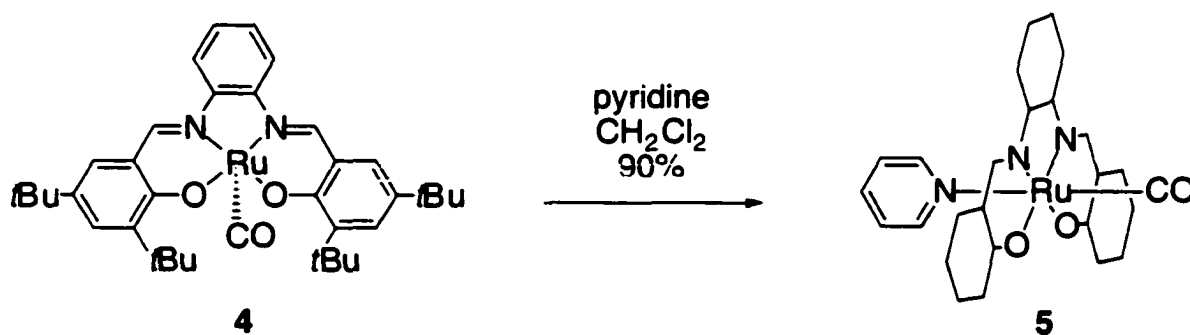
171.4° (Ru(2)-O(2)-Ru(3)), and 158.6° (Ru(3)-O(3)-Ru(4)). The most striking feature arises from the steric constraints of the *tert*-butyl substituents that results in the adoption of a twisted geometry with half a helical turn. Similar oxo-bridged dimers have been reported for iron(III) analogues.¹¹ This is the first observed instance of a tetrameric oxo-bridged ruthenium(III/IV) salophen complex. The reversible binding of dioxygen to ruthenium(III) carbonyl and iron(II) salophen complexes have been previously described in the literature.¹² For ruthenium(III) salophens, the binding results in the reversible oxidation of Ru(III) to Ru(IV) that is accompanied by the reduction of O₂ to the unstable superoxide ion O₂⁻. The superoxide ion further degrades and forms the presumed Ru(V)(O) complex. Based on these reports, the tetrameric structure **19** could have formed *via* the reduction of molecular oxygen dissolved in solution or oxygen scavenged from the air/dichloromethane interface. Since oxo ligands are formally O²⁻, then the outer most ruthenium atoms must have an oxidation state of Ru(III), while the two central ruthenium atoms should have an oxidation state of Ru(IV).

Redissolving a sample of the crystals in dichloromethane generated a very complex ¹H NMR spectrum with greater than 30 resonances due to the disymmetry of the tetrameric complex **19**. The spectrum contained four doublets ($J = 1.5$ Hz) located in the aromatic region between ($\delta = 6.1$ and 6.7 ppm). The chemical shifts of these four doublets were similar to the two doublets ($J = 1.5$ Hz) found in the same region of the variable-temperature ¹H NMR spectra generated between -10°C and -30°C for complex **4**. These results can only suggest that the spectra generated from the ¹H NMR

temperature studies using nitrogen purged samples might result from the formation of a weakly bridged dinitrogen dimer or an oxygen-bridged dimer. In light of the literature example that describes the formation of an analogous aluminum(III) salophen dimer at -30°C , these results would suggest that a weakly associated oxygen-bridged dimer was probably formed at colder temperatures.

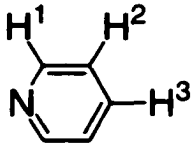
4.2.6 – Synthesis of the Ruthenium(II) Carbonyl Salophen Pyridyl Adduct

The pyridine adduct $\text{Ru}(\text{BSP})(\text{CO})(\text{py})$ (**5**) was obtained when **4** (0.9 molar equivalent) was added to pyridine in dichloromethane (Equation 2).



Equation 2. The salophen's substituents and double bond representations of **5** have been omitted for clarity.

Compound **5** was isolated as a purple solid by filtering the solution through silica gel which effectively removed any unchanged **4** as the pyridyl adduct is the only compound that elutes with CH_2Cl_2 . The formation of **5** was confirmed by the upfield shifts ($\Delta\delta = -0.6$ to -0.1 ppm) for the protons on the coordinated pyridine, which lie within the shielding regions of the aromatic rings of the salophen (Table 1 and Equation 2).

Table 1. Selected ^1H NMR spectroscopic data of **5** prepared in this study

Compound	δ / ppm ($\Delta\delta$) ^a		
	H ¹	H ²	H ³
5 ^b	8.12 (-0.46)	7.09 (-0.18)	7.59 (-0.10)

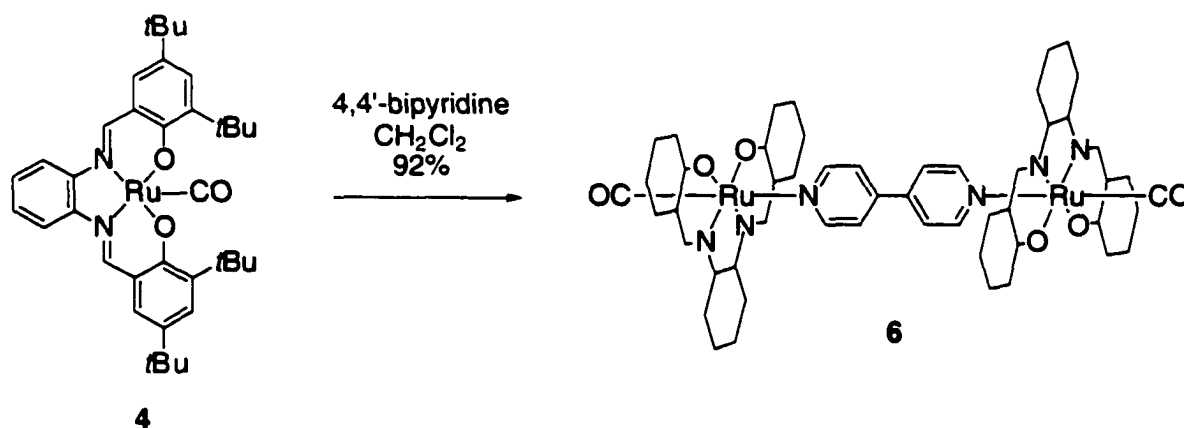
^a Upfield shifts of the signals for the protons in the assemblies relative to those in free pyridine for complex **5**. ^b In CD_2Cl_2 .

The generation of **5** using such mild conditions clearly indicates that, although the bulkiness of the *tert*-butyl substituents might inhibit the dimerization of **4**, they do not impede the approach of Lewis bases such as pyridine towards the metal center. The ESI mass spectrum of **5** was comprised of the parent ion peak ($m/z = 747$) as well as peaks corresponding to the loss of pyridine ($m/z = 668$) and both axial ligands ($m/z = 640$). A peak corresponding to the solvated compound (CH_3NO_2) was also present ($m/z = 729$). The intense band for ν_{CO} in the IR spectrum of **5** was shifted to higher frequency (1944 cm^{-1}) from the value for **4** (1931 cm^{-1}) as expected for the strengthening of the CO bond upon addition of a π -acid.¹³ It is well known that aromatic imine ligands can accept electron density into empty π^* -orbitals from electron rich metals which, in effect, increases the stability of the metal–carbonyl dative bond. This type of back-bonding aids in the removal of electron density from the metal and also from any other ligands present on the metal that are acting as π -acids, and especially those that are *trans*- to the incoming π -acid. It is, therefore, expected that the ν_{CO} would increase if the pyridine ligand acts, to some degree, as a π -acid. The magnitude of this shift is comparable to that reported for

the ν_{CO} of the flexible dimer salen complex $[\text{Ru}(\text{I})(\text{CO})]_2$ when it is converted to its pyridine adduct $\text{Ru}(\text{I})(\text{CO})(\text{py})$.⁷

4.2.7 – Construction of Neutral Assemblies

The use of the novel metallocalophen **4** as a supramolecular synthon was studied using ^1H NMR spectroscopy and then by the isolation of several air-stable multicomponent assemblies. A minimalist linear trimeric assembly $[\text{Ru}(\text{BSP})(\text{CO})]_2(4,4'\text{-bpy})$ (**6**) was prepared by treating a dichloromethane solution of 4,4'-bipyridine with 2.2 equivalents of $\text{Ru}(\text{BSP})(\text{CO})$ (**4**) in the same solvent (Equation 3).



Equation 3. The salophens' substituents and bond representations of **6** have been omitted for clarity.

The ^1H NMR spectrum of **6**, whether generated in situ or isolated as described for **5**, showed the expected upfield shifts for the signals assigned to the protons of the coordinated 4,4'-bipyridine fragment (Figure 13 and Table 2). These initial studies revealed that ligand-exchange is slow on the NMR time scale and sharp unchanging peaks

for the statistical mixture of mono- and di-addition products were visible when one molar equivalent of **4** was added (Figure 13).

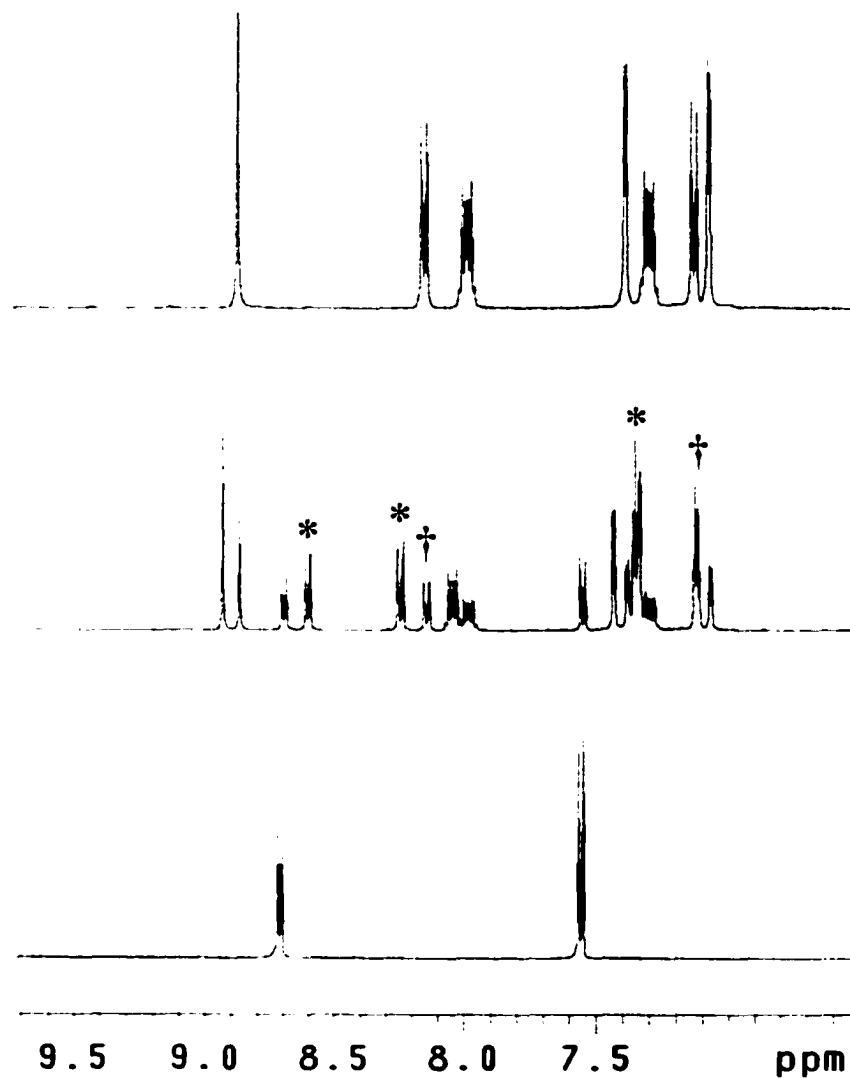
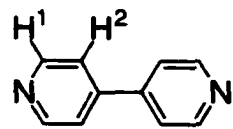


Figure 13. ¹H NMR (300 MHz) spectra of 4,4'-bipyridine (bottom trace), **4** + 1.0 equivalent of 4,4'-bipyridine (middle trace), and **4** + 0.5 equivalents of 4,4'-bipyridine (top trace). Signals corresponding to the protons of 4,4'-bipyridine for both the mono- (*) and the di-coordination (†) assemblies are highlighted. All spectra were run in CD₂Cl₂.

Table 2. Selected ^1H NMR spectroscopic data of **6** prepared in this study

Compound	δ / ppm ($\Delta\delta$) ^a	
	H ¹	H ²
 6 ^b	8.12 (-0.46)	7.09 (-0.18)

^a Upfield shifts of the signals for the protons in the assemblies relative to those in free 4,4'-bipyridine for assembly **6**.

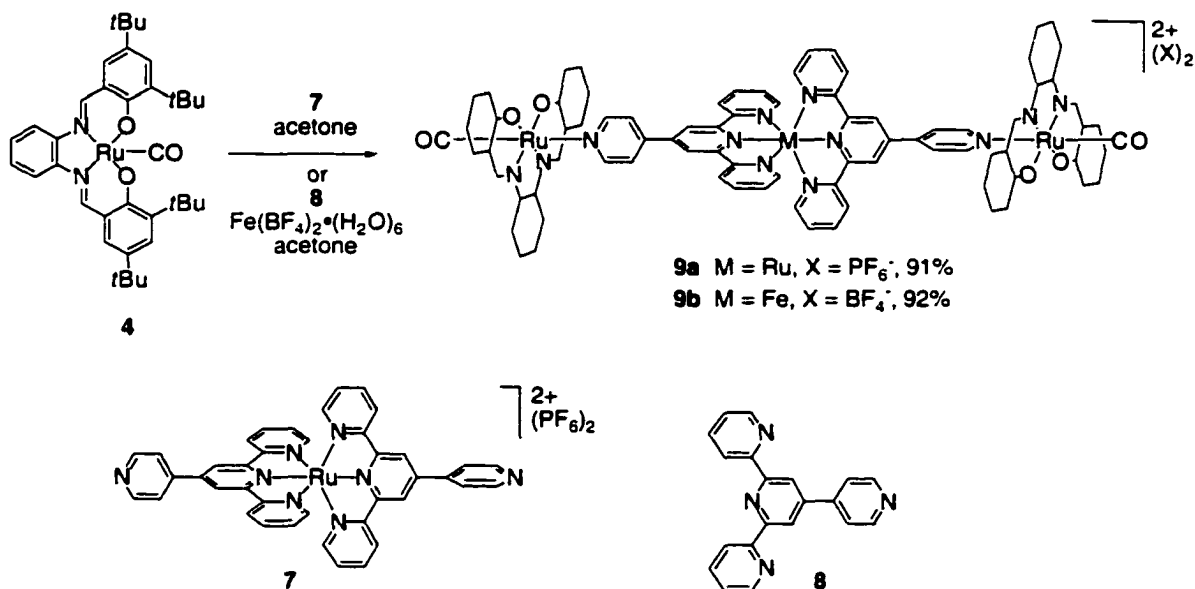
^b In CD_2Cl_2 .

The ESI mass spectrum of **6** exhibits a parent ion peak ($m/z = 1492$) as well as a peak ($m/z = 824$) corresponding to the loss of one metallosalophen. The spectrum also contained peaks that correspond to the fragmentation of the metallosalophen as previously seen for **4** and **5**. The IR spectrum of toluene solutions of **6** exhibits an intense band for ν_{CO} at 1947 cm^{-1} .

4.2.8 – Construction of Charged Assemblies

Metallosalophen assemblies incorporating coordination compounds as the central fragments were also prepared in an identical fashion as their porphyrin counterparts described in Chapter 2 (Scheme 2). Addition of two molar equivalents of $\text{Ru}(\text{BSP})(\text{CO})$ (**4**) to bis(4'-(4'''-pyridyl)-2,2':6',2''-terpyridine)ruthenium (**7**)¹⁴ in acetone afforded the triad **9a**, which was isolated as a purple solid by precipitation with pentane. The iron analogue **9b** was readily synthesized from its simplest building blocks in a single self-assembly process when equal parts of 4'-(4'''-pyridyl)-2,2':6',2''-terpyridine (**8**)¹⁵ and

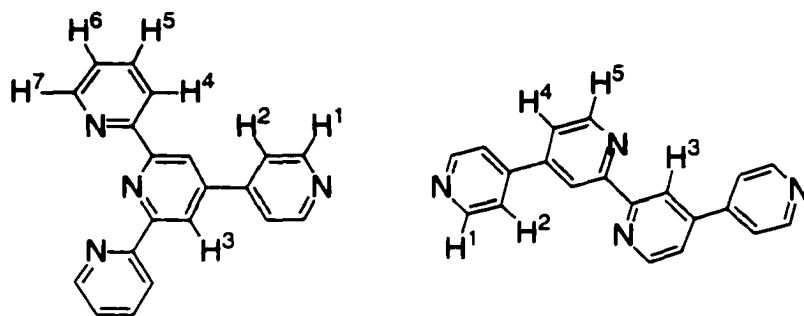
Ru(BSP)(CO) (**4**) are added to a acetone solution containing 0.5 molar equivalents of $\text{Fe}(\text{BF}_4)_2 \cdot (\text{H}_2\text{O})_6$.



Scheme 2. The salophens' substituents and double bond representations of **9a** and **9b** have been omitted for clarity.

The ^1H NMR spectrum of **9a** and **9b**, whether generated in situ or isolated, showed the expected upfield shifts for the signals assigned to the protons of the coordinated 4'-(4'''-pyridyl)-2,2':6',2''-terpyridine fragment (Table 3). The ESI mass spectra of both **9a** and **9b** each show parent ion peaks ($m/z = 1028$ for $[\text{M} - 2\text{PF}_6]^{2+}$ and 1006 for $[\text{M} - 2\text{BF}_4]^{2+}$, respectively) as well as peaks corresponding to the loss of one metallosalophen ($m/z = 695$ for $[\text{M} - 4 - 2\text{PF}_6]^{2+}$ and 672 for $[\text{M} - 4 - 2\text{BF}_4]^{2+}$, respectively). The IR spectrum for **9a** and **9b** obtained in the solid-state exhibits intense bands for ν_{CO} at 1933 and 1934 cm^{-1} , respectively.

Table 3. Selected ^1H NMR spectroscopic data of assemblies **9a**, **9b**, **12a**, and **12b** prepared in this study

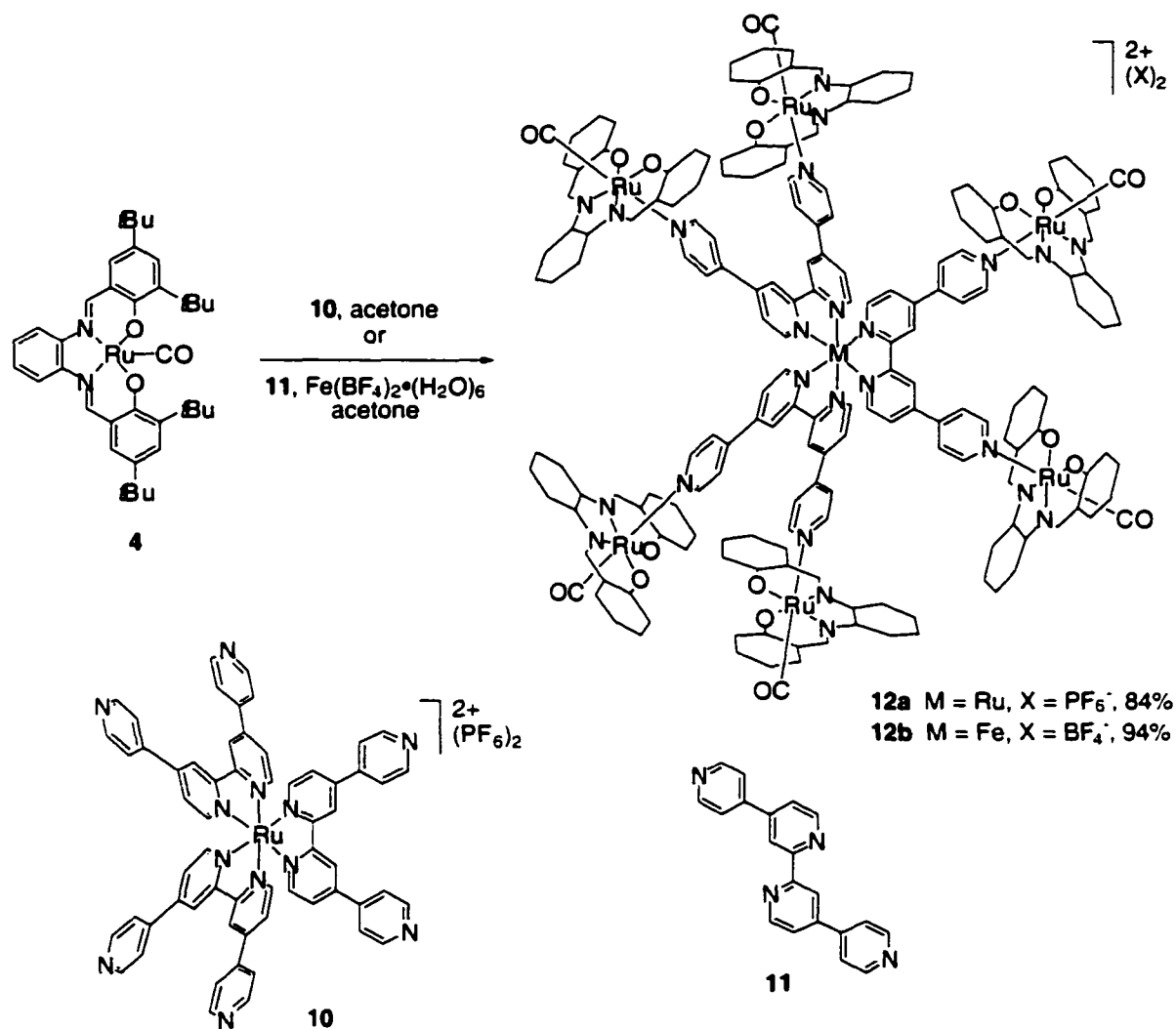


Compound	δ / ppm ($\Delta\delta$) ^a						
	H ¹	H ²	H ³	H ⁴	H ⁵	H ⁶	H ⁷
9a^b	8.48 (-0.48)	8.16 (-0.13)	9.39 (-0.17)	7.63 (-0.20)	8.00 (-0.13)	7.21 (-0.15)	8.91 (-0.17)
9b^b	8.53 (-0.47)	8.27 (-0.12)	9.55 (-0.20)	7.38 (-0.21)	7.95 (-0.13)	7.11 (-0.15)	8.27 (-0.12)
12a^b	8.23 (-0.79)	7.58 (-0.66)	9.04 (-0.49)	7.45 (-0.62)	7.88 (-0.58)		
12b^b	8.24 (-0.56)	7.59 (-0.33)	9.03 (-0.52)	7.56 (-0.47)	7.54 (-0.58)		

^a Upfield shifts of the signals for the protons in the assemblies relative to those in free pyridine for complex **7** for assembly **9a**, tetrapyridine **8** for assembly **9b**, for complex **10** for assembly **12a** and tetrapyridine **11** for assembly **12b**. ^b In [D₆]acetone.

The syntheses of the octahedral ruthenium(II) and iron(II) assemblies **12a** and **12b** were accomplished following the previously reported metal-directed synthesis employed to prepare the corresponding metalloporphyrin analogues in Chapter 2 (Scheme 3).^{4a} The addition of [D₆]acetone to a 3:6:1 molar mixture of solid 4,4'-di(4''-pyridyl)-2,2'-bipyridine (dpybpy, **11**),¹⁶ Ru(BSP)(CO) (**4**) and Fe(BF₄)₂·(H₂O)₆ followed by five minutes of heating cleanly afforded assembly **12b**. The octahedral assembly **12a** was

prepared by treating the pre-assembled $[\text{Ru}(\text{dpybpy})_3][\text{PF}_6]_2$ core fragment (dpybpy = 4,4'-di(4''-pyridyl)-2,2'-bipyridine, **10**)¹⁷ with a slight excess of **4**.



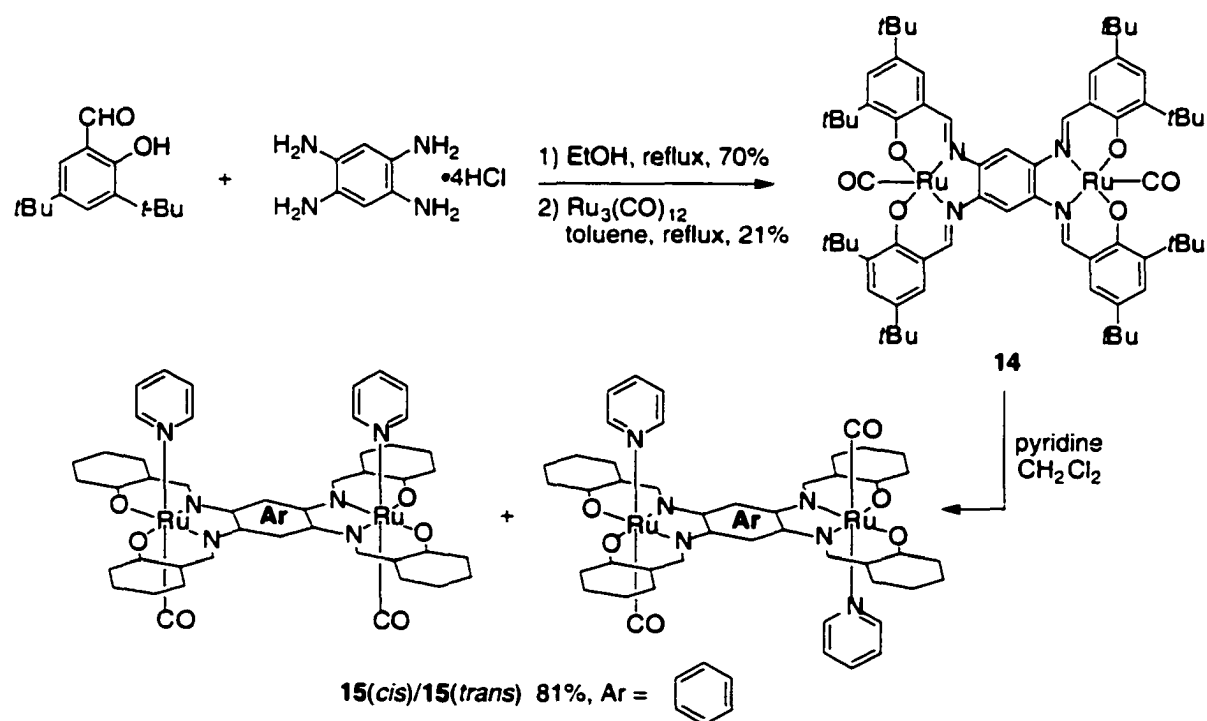
Scheme 3. The salenphens' substituents and double bond representations of **12a** and **12b** have been omitted for clarity.

The ^1H NMR spectrum of **12a** and **12b**, whether generated in situ or isolated, showed the expected upfield shifts for the signals assigned to the protons of the coordinated 4,4'-di(4''-pyridyl)-2,2'-bipyridine fragment (Table 3). The ESI mass spectra of both **12a** and **12b** each show a peak corresponding to the dication ($m/z = 2519$

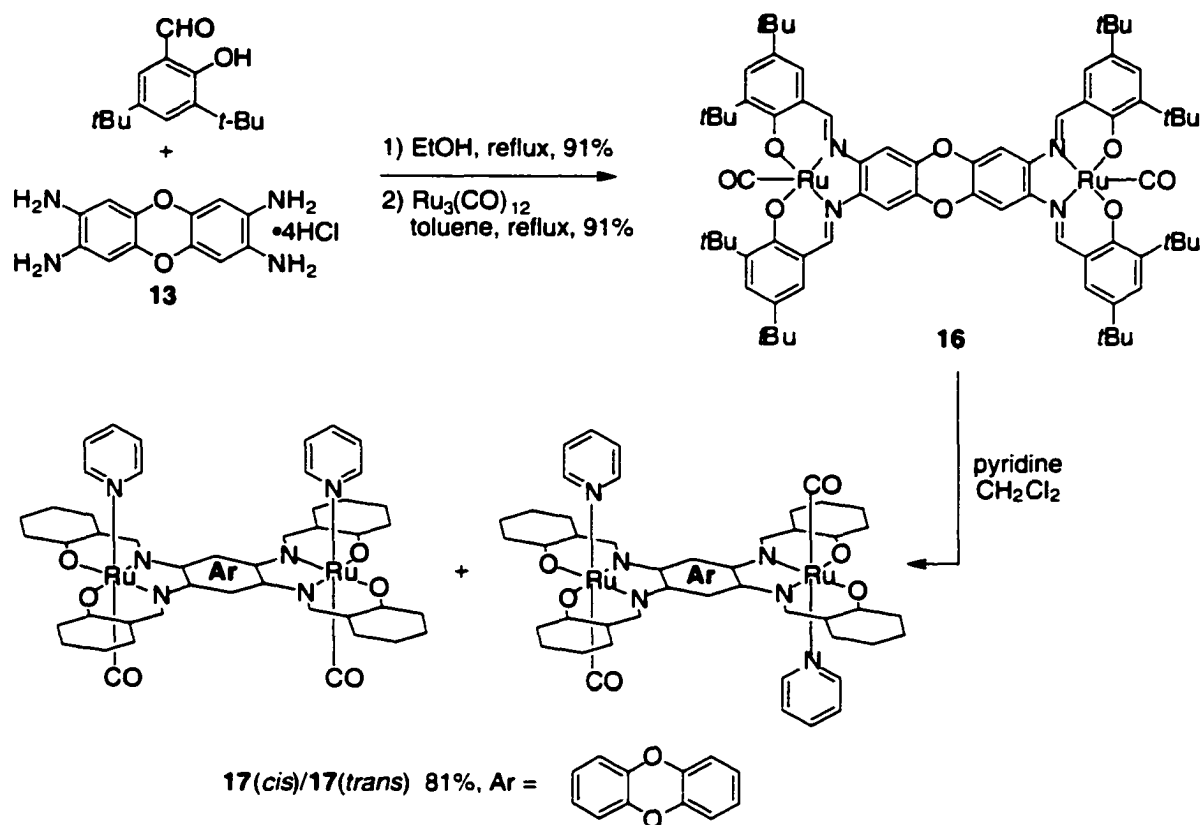
for $[M - 2PF_6]^{2+}$ and 2496 for $[M - 2BF_4]^{2+}$, respectively) as well as peaks for the loss of subsequent metallosalophens. Recall that when pyridine coordinates to $Ru(BSP)(CO)$ (**4**), the ν_{CO} shifted from 1931 cm^{-1} to 1944 cm^{-1} . The IR spectra for **12a** and **12b** obtained in the solid-state exhibit intense bands for ν_{CO} at 1947 and 1946 cm^{-1} , respectively. As expected for the strengthening of the CO bond upon addition of a π -acid.

4.3 – Synthesis of the Bis(salophens) and Bis(metallosalophens)

Illustrative examples that highlight the versatility of the salophen ligand are the bis(metallosalophen) complexes **14–17** (Scheme 4 and Scheme 5).



Scheme 4. The substituents and double bond representations of **15** have been omitted for clarity.



Scheme 5. The substituents and double bond representations of **17** have been omitted for clarity

These metallocalophens offer two accessible axial metal binding sites separated by different intermetal distances based on the size of the tetraamine synthon (7.62 Å for **14** and **15**, and 12.32 Å for **16** and **17**). The corresponding salophen ligands used to prepare these complexes were synthesized by condensing 1,2,4,5-tetraaminobenzene hydrochloride salt for **14** and the unknown 2,3,7,8-tetraaminodibenzo[1,4]dioxin hydrochloride salt **13**¹⁸ for **16** with 3,5-di-*tert*-butylsalicylaldehyde in ethanol at reflux (Scheme 4 and Scheme 5 respectively). Metal insertion was accomplished by heating the resulting salophens with $\text{Ru}_3(\text{CO})_{12}$ in either toluene or diglyme, followed by purification using column chromatography through alumina (activity II-III). Complexes **14** and **16**

were isolated as deep-red air stable solids. The ESI mass spectrum of **14** showed a parent ion peak ($m/z = 1258$) as well as peaks corresponding to the solvated complex ($m/z = 1336$ for $[M + H_2O + CH_3NO_2]^+$, 1318 for $[M + CH_3NO_2]^+$ and 1370 for $[M - CO + H_2O + 2CH_3NO_2]^+$). The ESI mass spectrum of **16** shows a similar trend. The IR spectra for these bis(metallosalophens) obtained in the solid state exhibit intense bands for ν_{CO} at 1950 cm^{-1} for **14**, and at 1943 cm^{-1} for **16**.

The ^1H NMR spectrum of **14** in acetone reveals that the isolated product is a mixture of *cis*- and *trans*-diastereomers based on how the two carbonyl ligands project in space with respect to each other. This is manifested as the appearance of two singlets of equal intensity corresponding to the C–H protons on the central tetraaminobenzene ring fragment of **14**. The production of these stereoisomers is not unexpected as the chelation sites are far enough removed from each other so that they can act independently during the metal-insertion reactions. The diastereomeric mixture is even more apparent in the case of the pyridine adduct **15**, which was formed by treating the hydrated complex **14** with pyridine, followed by filtering the solution through a plug of silica gel to remove trace amounts of unreacted **14**. The ^1H NMR spectrum of **15** shows an analogous pair of singlets corresponding to the C–H hydrogens on central tetraaminobenzene fragment. The signals corresponding to the imine and flanking *tert*-butyl substituents on the bis(salophen) ligand as well as C–H protons on the coordinated pyridine also appear as duplicate signals. The detection of these diastereomers was not limited to ^1H NMR spectroscopy, but were also apparent in the ^{13}C NMR spectrum for **15** which contains duplicate signals for the coordinated pyridine ligand. On the other hand, the symmetrical

nickel(II) analogue of **13** (Figure 14), prepared as a burgundy precipitate by reacting the metal-free salophen ligand with five equivalents of $\text{Ni}(\text{OAc})_2(\text{H}_2\text{O})_4$, showed the expected absence of signal splitting in both the ^1H and ^{13}C NMR spectra.

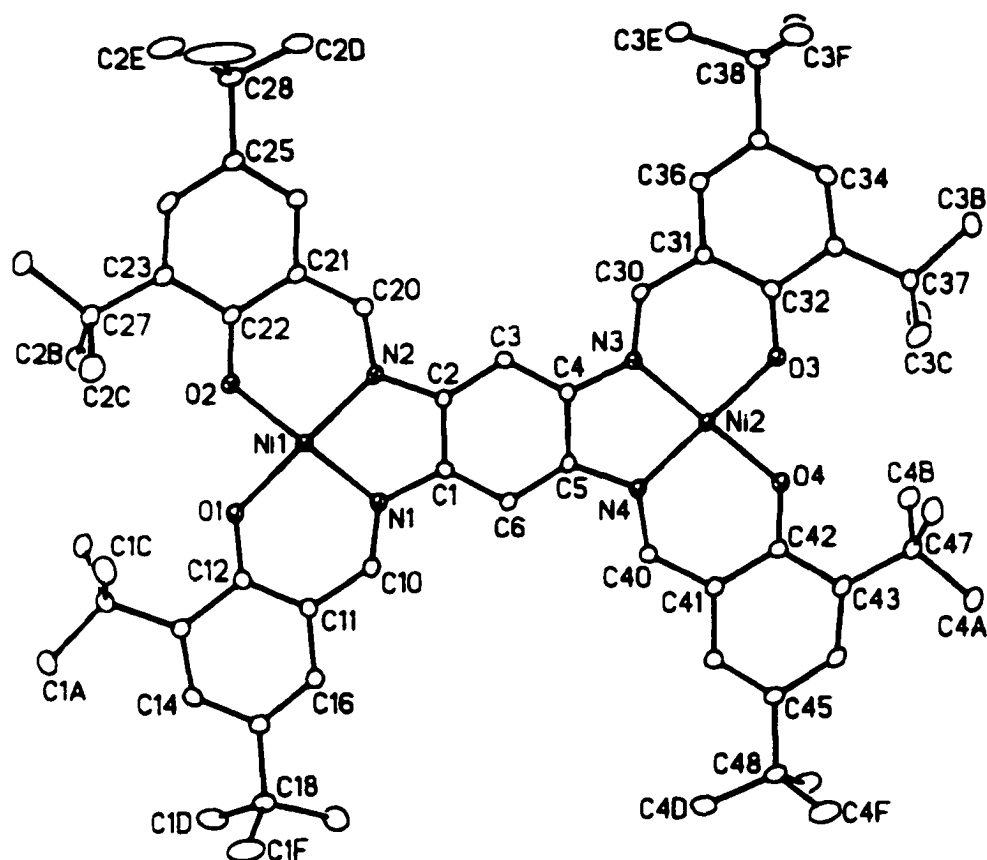


Figure 14. Molecular structures of the nickel(II) analogs of **14** in the crystal. The thermal ellipsoids are drawn at the 20% probability level.

The ^1H NMR spectra of the coordination compounds using the larger bis(metallosalophens) **16** and **17** show an absence of signal splitting for all protons due to the greater separation between the two coordination sites. The ^{13}C NMR spectrum of **16** also lacks any signal splitting, however, the ^{13}C NMR spectrum of **17** exhibits two sets of signals corresponding to the coordinated pyridine ligands. All of the carbons on the

salophen ligand remain unaffected and appear as one set of signals. The symmetrical nickel(II) analogue of **16** (Figure 15) does not result in any multiple peaks in the NMR spectra.

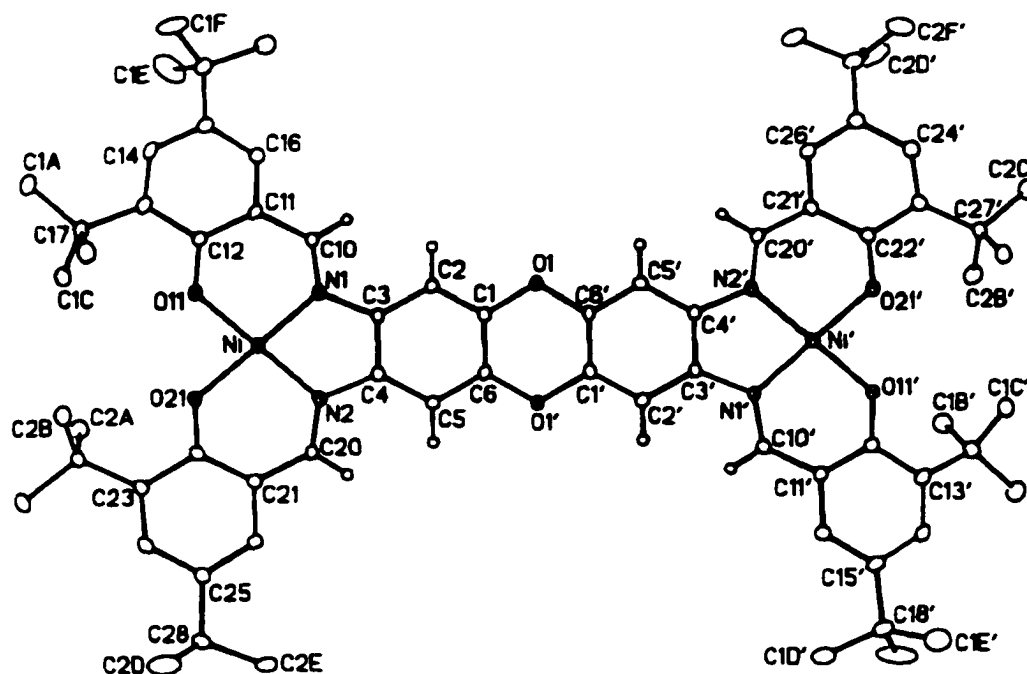


Figure 15. Molecular structures of the nickel(II) analogs of **16** in the crystal. The thermal ellipsoids are drawn at the 20% probability level.

The ESI mass spectrum of **15** is made up of the parent ion peak ($m/z = 1416$) and peaks corresponding to the loss of pyridine ($m/z = 1338$ for $[M - \text{py}]^+$ and 1258 for $[M - 2\text{py}]^+$). The ESI mass spectrum of **17** shows a similar pattern. The IR spectra of the pyridine complexes **15** and **17** in the solid-state show two intense overlapping bands for stretching vibrations of the axial carbon monoxide (1955 cm^{-1} and 1924 cm^{-1} for **15**, 1951 cm^{-1} and 1934 cm^{-1} for **17**). The IR spectra measured in toluene exhibit two completely resolved ν_{CO} at 1944 cm^{-1} and 1924 cm^{-1} for **15** and at 1947 cm^{-1} and 1924 cm^{-1} for **17**. A solvent dependency was also observed for the ν_{CO} of both pyridine complexes, and the IR

spectra of dichloromethane solutions show a single band at 1940 cm^{-1} and 1931 cm^{-1} for **15** and **17**, respectively.

The convenience of incorporating the bis(metallosalophens) into supramolecular chemistry becomes clear when their syntheses are compared to that for the analogous bis(metalloporphyrin) **18a** (Figure 16).

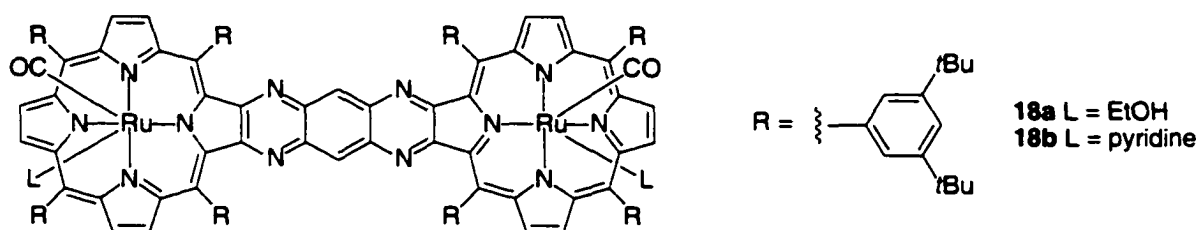


Figure 16.

Although the metal insertion into Crossley's bis(porphyrin)¹⁹ proceeded uneventfully by heating the bis(porphyrin) with an excess of $\text{Ru}_3(\text{CO})_{12}$ in phenol, the preparation of the free-based porphyrin was accomplished in 5 steps and a 50% yield as reported by Burn and coworkers.²⁰ This is a significant drawback when compared to our single-step preparation of the bis(salophen) precursor to **14** and two-step procedure for the precursor of **16**. The bis(metalloporphyrin) **18a** was purified as a brown air stable solid by a combination of column chromatography through alumina (activity II-III) and recrystallization from aqueous ethanol. When an excess of pyridine was added to **18a** in dichloromethane, the more Lewis basic amine immediately displaced the labile ethanol affording the pyridine adduct.

4.4 – UV/Vis Spectroscopic Analysis

Initial photophysical studies reveal that the UV/Vis absorption spectra of the metallosalophen assemblies **6**, **9**, and **12** are essentially the sum of the absorption spectra of the corresponding components, and electronic absorptions are limited to minor shifts ($\Delta\lambda = \pm 2$ nm) (Table 4).

Table 4. Selected UV/Vis absorption data for the pyridyl-coordinated assemblies prepared in this study

Compound	$\lambda_{\max} / \text{nm}$ ($\log \epsilon / \text{M}^{-1}\text{cm}^{-1}$) ^a					
	4	258 (4.48)	306 (4.26)	382 (4.38)	491 (3.91)	541 ^b (3.75)
5	264 (4.68)	310 (4.38)	391 (4.60)	503 (4.02)	555 ^b (3.09)	
6	264 (4.81)	310 (4.56)	391 (4.70)	501 (4.17)	555 ^b (4.00)	
9a	276 (5.01)	312 (4.88)	330 (4.77)	390 (4.74)	493 (4.59)	555 ^b (4.18)
9b	282 (5.02)	291 (5.02)	327 (4.82)	393 (4.75)	508 (4.35)	573 ^b (4.52)
12a	255 (5.34)	311 (5.19)	388 (5.18)	490 (4.77)	555 ^b (4.53)	
12b	285 (5.39)	311 (5.16)	391 (5.21)	506 (4.72)	555 ^b (4.70)	
15^c	313 (4.58)	325 (4.57)	407 (4.62)	492 (4.42)	551 ^b (4.37)	614 ^b (4.35)
17^c	263 (4.75)	304 (4.70)	317 (4.70)	400 (4.80)	520 (4.29)	566 ^b (4.22)

^a Run in deoxygenated CH_2Cl_2 at 10^{-4} to 10^{-5} M.

^b Observed as a shoulder.

^c As a mixture of both *cis*- and *trans*-isomers.

The absorption spectra of dichloromethane solutions of **5**, **15** (as the mixture of *cis*- and *trans*-isomers), and **17** (as the mixture of *cis*- and *trans*-isomers) are characterized by intense ligand-centred (LC) bands with maxima in the 250–400 nm region (Figure 17).^{8,21}

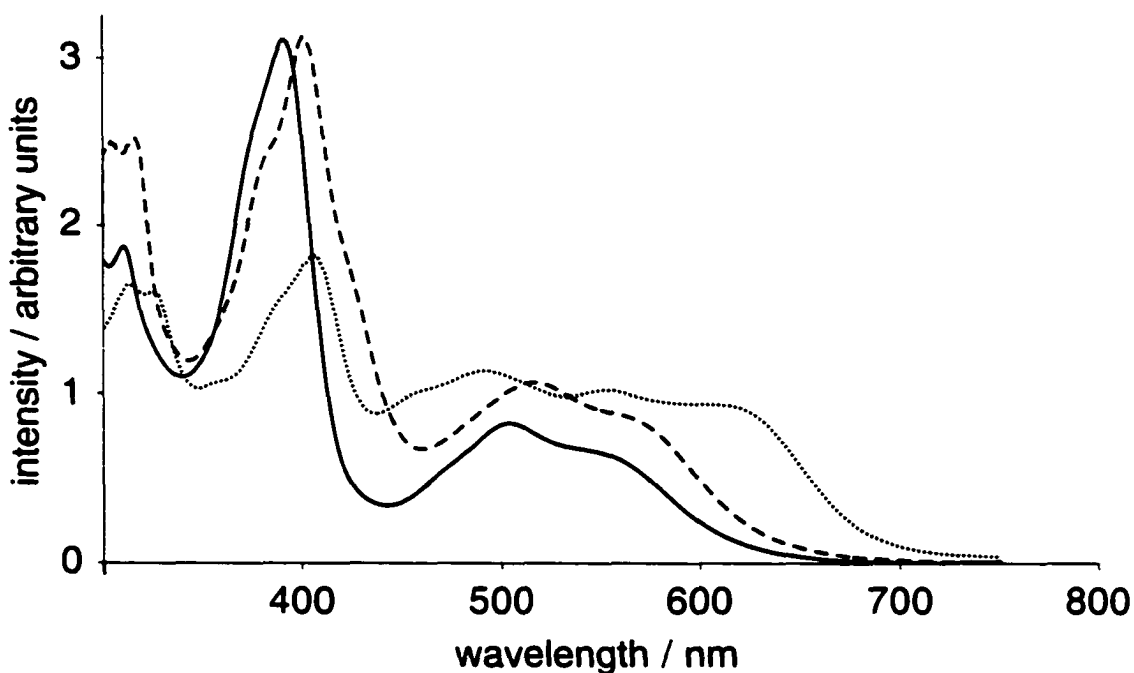


Figure 17. UV/Vis absorption spectra of Ru(BSP)(CO)(py) (**5**) (solid line), [Ru₂(BS2P)(CO)₂(py)₂] (**15**, both isomers) (dotted line) and [Ru₂(BS2DP)(CO)₂(py)₂] (**17**, both isomers) (dashed line) in CH₂Cl₂ at room temperature.

These bands have been designated as π – π^* transitions for the electrons localized on the azomethine group of the Schiff base ligand. The bands at longer wavelengths are most likely due to ligand(π)–metal(d^*) charge transfer, as has been reported for similar complexes.^{8,21a,21c} The similarity of the electronic spectra of complexes **5** and **17** suggests that the central dibenzo[1,4]dioxin fragment laterally separates the metal centers adequately to regulate electronic communication, allowing them to act independently.

This effect, however, does not apply to complex **15**, which exhibits a unique pattern of red-shifted charge transfer bands. This observation is indicative of the fact that **15** is behaving as one extended chromophore and not as two independent metallosalophens.

4.5 – Electrochemistry of the Metallosalophens

The cyclic voltammograms of dichloromethane solutions of complexes **5**, **15** (as the mixture of *cis*- and *trans*-isomers), and **17** (as the mixture of *cis*- and *trans*-isomers) are shown in Figure 18. The voltammograms do not show any reduction waves at negative potentials, but do show two quasi-reversible ($\Delta E = 70\text{--}90$ mV) oxidation waves centred at 0.58 V (assigned as a Ru(II)/Ru(III) process) and 1.29 V (assigned as a Ru(III)/Ru(IV) process) vs. saturated Ag/AgCl (Figure 18).^{21a} For the scan rates used, the cathodic-to-anodic peak current ratio ($i_{pc} : i_{pa}$) is constantly equal to unity for the first oxidation and slightly less than unity for the second oxidation; the quotient of the anodic peak current and the square root of the scan rate ($i_{pa} / \nu^{1/2}$) remains constant. Complex **5** is well-behaved, showing two one-electron oxidations at 0.56(7) and 1.29(4) V. For the bimetallic species **15** and **17**, the first oxidation waves are two-electron processes (actually, twice a one-electron oxidation of each ruthenium(II) centre) and are shifted to slightly more positive potentials (0.60(0) and 0.58(2) V for **15** and **17**, respectively). This indicates that the metal centers do not communicate with each other for the Ru(II)/Ru(III) couple. The second oxidation wave of the bimetallic species are split into two one-electron oxidation waves at 1.27(7)|1.36(8) V for **15** and 1.28(4)|1.33(0) for **17**

indicative of weak interactions between the covalently linked metallosalophens. This metal-to-metal communication is amplified in the case of the smaller complex **15** ($\Delta V = 91$ mV) as compared to the larger complex **17** ($\Delta V = 50$ mV).

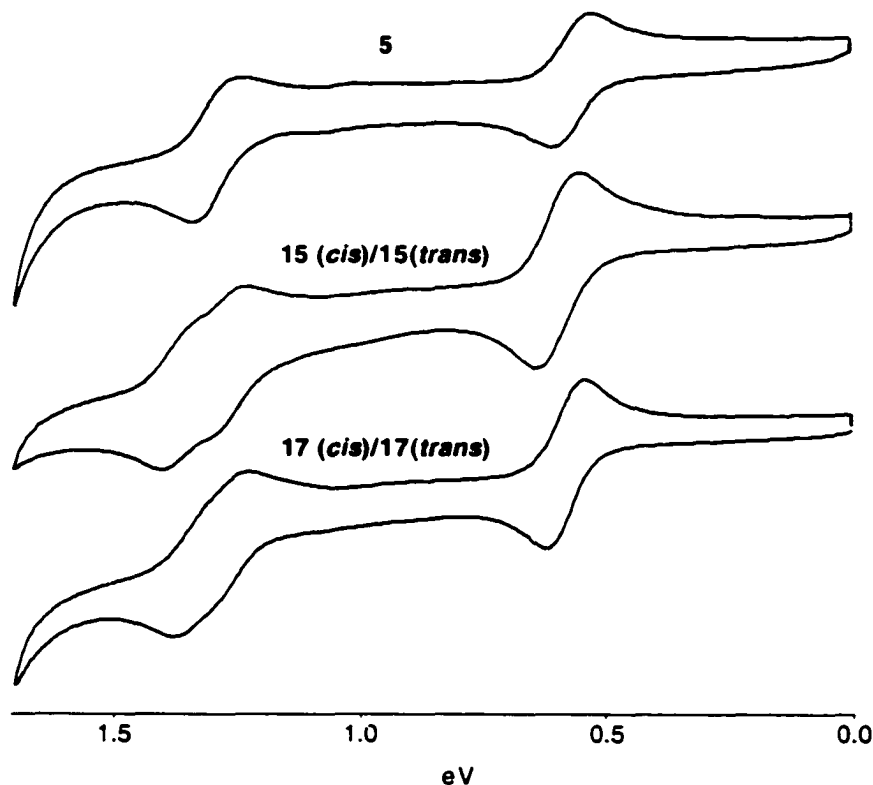


Figure 18. Cyclic voltammograms of (a) Ru(BSP)(CO)(py) (**5**), (b) [Ru₂(BS2P)(CO)₂(py)₂] (**15(cis)** and **15(trans)**) (c) [Ru₂(BS2DP)(CO)₂(py)₂] (**17(cis)** and **17(trans)**) at identical scan rates of 50 mV/s in CH₂Cl₂ with 0.1 M TBAP at room temperature.

4.6 – Self-Assembly Studies of Bimetallic Salophens and Porphyrins

An alternative to the molecular templating approach to construct encapsulating molecules described in Chapter 1 is molecular paneling, an approach that only requires simple mixing of components. The literature examples of Fujita and Raymond mentioned in Chapter 1 serve to illustrate how molecular paneling can be used to construct three

dimensional molecules from singular metals and chelating aromatic ligands that form the walls or panels. The two bimetallic complexes **17** and **18** can be used as flat panels. These complexes provide two axial coordination sites that are laterally separated and can be used to possibly form squares and closed-shelled molecules. This next section of the thesis describes the preliminary self-assembly studies using two different types of two-dimensional linkers that axial coordinate to these bimetallic panels to form molecular squares and closed-shelled molecules (Figure 19).

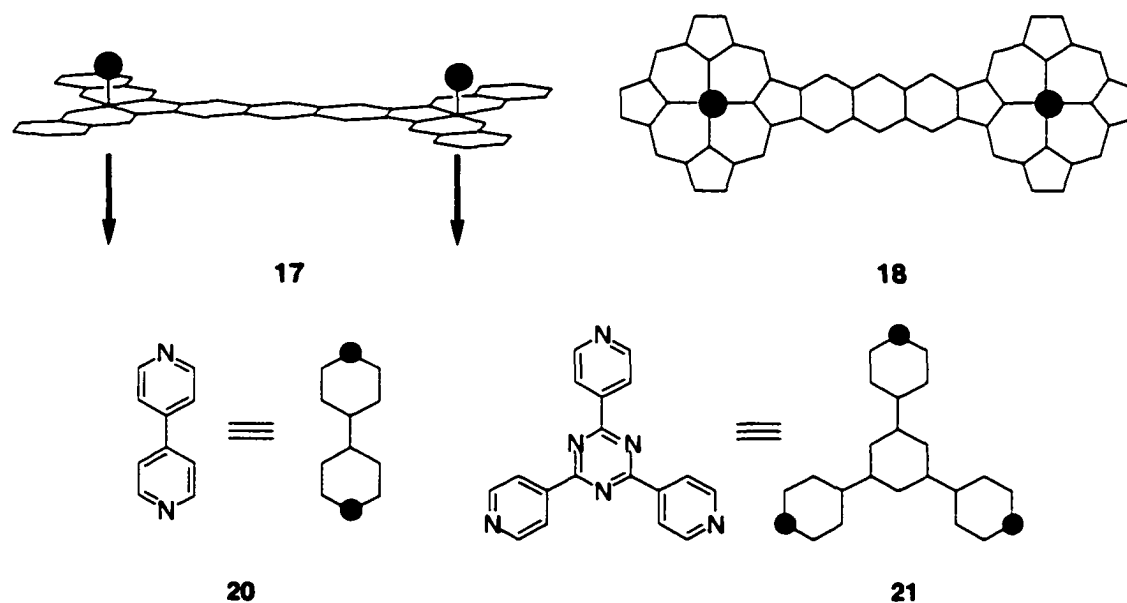
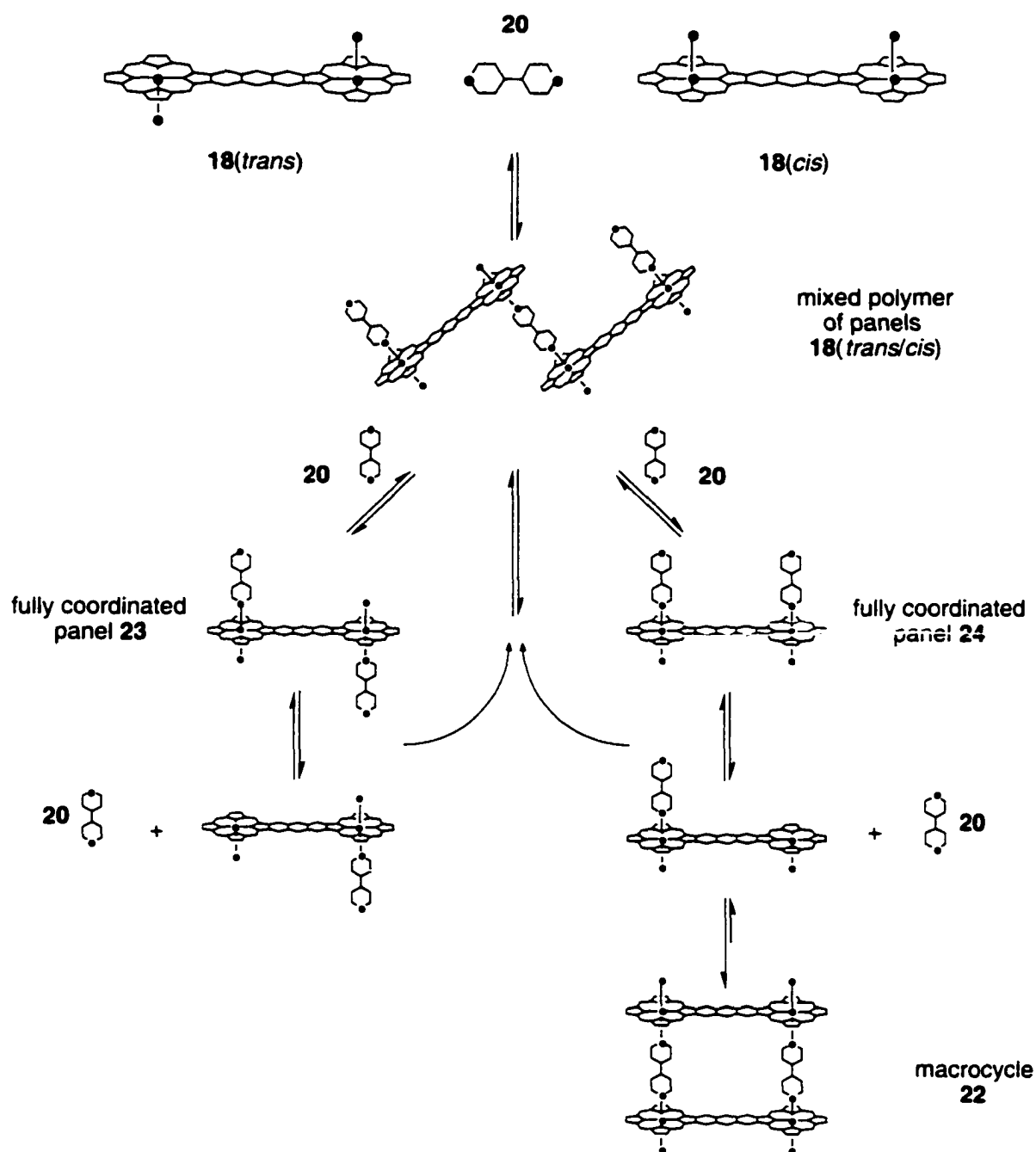


Figure 19. Schematic representations of the required rectangular panels and linkers. The substituents, double bond representations, and atom labels have been omitted for clarity.

4.6.1 – The Construction of Two Dimensional Rectangles

The *cis*- and *trans*- mixture of carbonyl compounds of **18** were not separated but used as is to study the self-assembly synthesis of closed-shelled molecules. Some of the

possible products of a self-assembly reaction using the linear 4,4'-bipyridine **20** linker are shown in Equation 4.



Equation 4. Schematic representation of some of the possible products during the self-assembly reaction using *cis*-/*trans*-**18** and **20**. The substituents, double bond representations, and atom labels have been omitted for clarity.

A series of competitive axially-coordinating reactions involving both components will exist and form the fully coordinated panels, (also mixed polymers of **23** and **24**), the desired macrocycle, and other aggregates that have a 1:1 component stoichiometry of the linker **20** and the panel **18**. As depicted in Equation 4, the fully coordinated panels **23** and **24** should be involved in an exchange process with any non-coordinated 4,4'-bipyridine in solution or with any mono-coordinated 4,4'-bipyridine on a panel. The equilibrium concentrations should be controlled by the amount of 4,4'-bipyridine present in solution. The macrocycle **22** can be formed when two *cis*-carbonyl panels each bearing one linear linker combine. It was postulated that cooperative metal coordination should exist in the macrocycle **22** because of the additive effects of the two associations. It should, therefore, be harder to break two bonds in **22** to reform the fully coordinated panel **24**. In addition to cooperative associations, the direct access of competitive ligands to the coordination sites of **22** should be restricted in the cyclic form, and thus, the macrocycle acts as thermodynamic trap for the *cis*-panel **18**. Another important consideration, is the amount of solvent reorganization that occurs when two of the *cis*-**18** panels combine to form the macrocycle, and if this occurs, then macrocyclization will be favoured due to an increase in the entropy and favour the formation **22**.

To highlight these self-assembly pathways, the ¹H NMR studies of *cis*-/*trans*-**18** and **20** will be shown, primarily because axial coordination to porphyrins produces diagnostic shifts in the ¹H NMR spectra that are easily monitored. Two approaches were used to probe the self-assembly pathway. In the first approach, 4,4'-bipyridine (**20**) was added to a solution containing the mixture of *cis*-/*trans*-**18** in a 1:1 molar ratio. It was

expected that a complicated polymer should form first. The second approach keeps 4,4'-bipyridine in large excess, which should prevent polymer formation in the first step, and produce the two fully coordinated products **23** and **24** as highlighted in Equation 4.

Using the first approach, the addition of one molar equivalent of 4,4'-bipyridine to *cis/trans*-**18** resulted in the formation of broad signals in the ^1H NMR spectrum (Figure 20b).

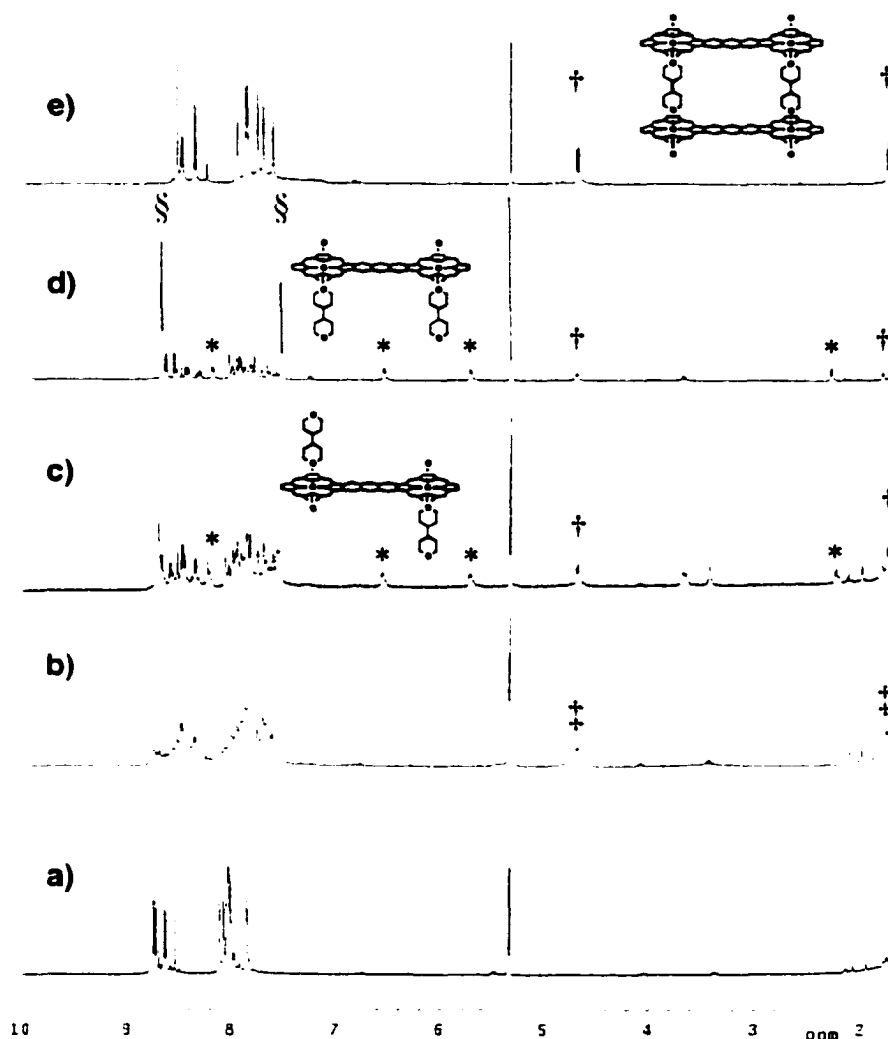
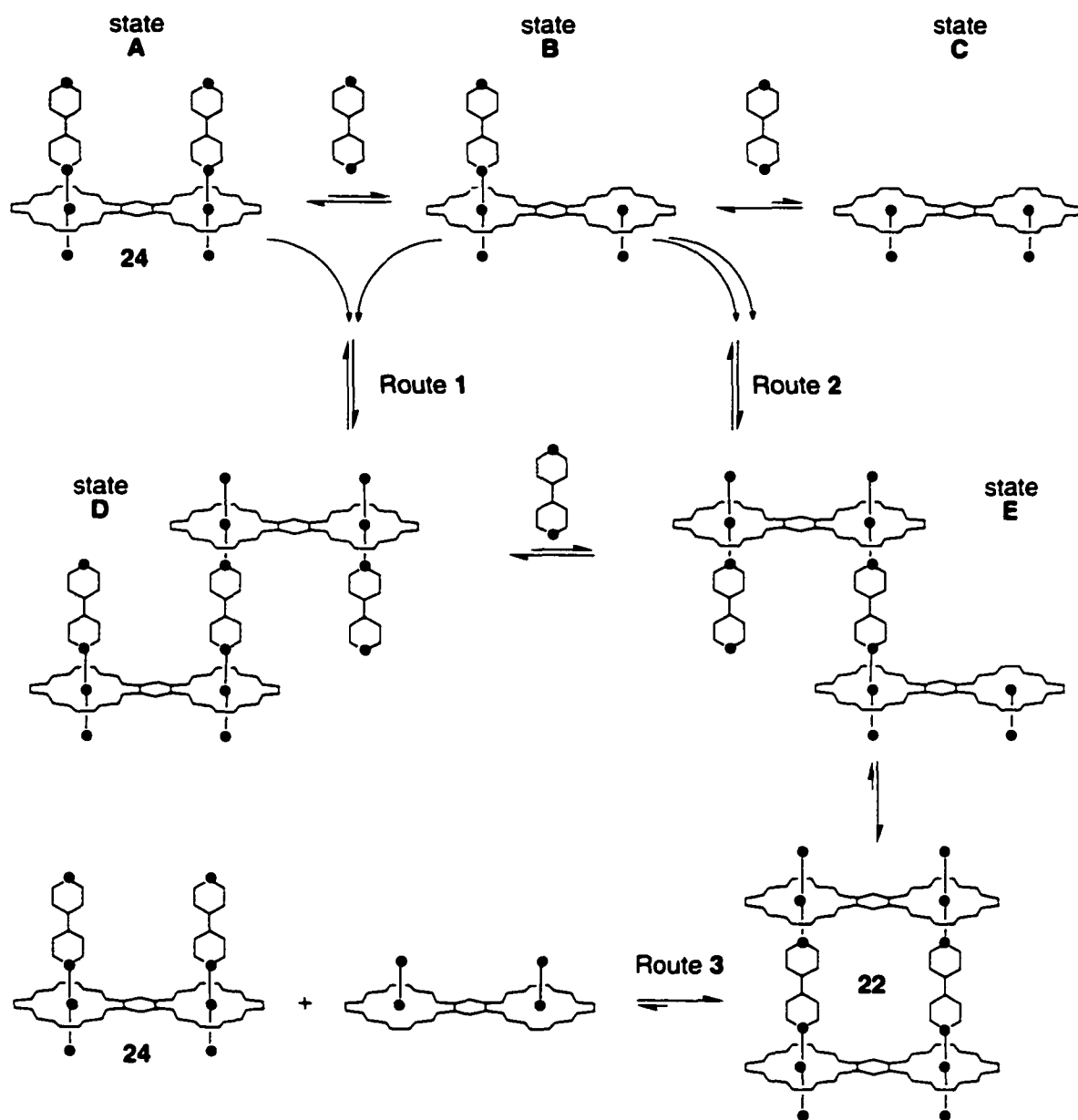


Figure 20. ^1H NMR (500 MHz, CD_2Cl_2) self assembly studies of a) *cis/trans*-**18**, b) *cis/trans*-**18** plus one molar equivalent **20**, c) *cis/trans*-**18** plus excess **20**, d) **20** plus 0.1 molar equivalents of *cis/trans*-**18**, e) the isolated macrocycle. The symbols: '†' refers to signals corresponding to polymer, '*' refers to signals of the biscoordinated panel, '†' refers to signals of the macrocycle, and '§' refers to excess 4,4'-bipyridine.

The two broad signals, which are shifted furthest upfield from the broad porphyrin signals in the aromatic region, correlate well to the formation of a polymeric species made up of both **23** and **24** (signals labeled '‡' in Figure 20b). If a polymer was formed in the first step, then the addition of 4,4'-bipyridine should break the polymer apart and form the fully coordinated panels **23** and **24**. This hypothesis was supported by the appearance of four sharp signals, after the addition of 4,4'-bipyridine, which correlate to the non-cyclic products **23** and **24** (signals labeled '*' in Figure 20c). Also, the signals that remained furthest upfield sharpened in their appearance which suggested that the symmetrical product **22** was formed (signals labeled '†' in Figure 20c). Also revealed, were the additive porphyrin anisotropic ring current effects centered on the two linear linkers **20** when forming the symmetrical macrocycle **22**. These two signals were shifted furthest upfield from the four signals that correspond to the fully coordinated panels of **23** and **24** (signals labeled '*' in Figure 20c). The macrocycle **22** was also formed when *cis-/trans-18* was added to a solution containing excess 4,4'-bipyridine **20** (Figure 20d). In this way, the formation of polymer was prevented during the self-assembly process and the fully ligated porphyrins were formed first. The integration of the area under the peaks labeled '*' and '†' in Figure 20d suggested that the second approach afforded the macrocycle **22** in substantially lower quantities.

By disregarding the competitive effects that the unproductive *trans-18* panel would have on the self-assembly processes, the results obtained from these two approaches can be compiled, combined, and three general routes emerge for the formation of macrocycle **22**. Route (1): from the union of bis-coordinated and mono-coordinated

panels. Route (2): from the union of two mono-coordinated panels. Route (3): from the union of bis-coordinated and non-coordinated panels (Equation 5).



Equation 5. Schematic representation of three possible routes that lead to the formation of macrocycle **22** from *cis*-**18** and **20**. The substituents, double bond representations, and atom labels have been omitted for clarity.

The third would probably be the least common route when the solution was saturated with 4,4'-bipyridine because the number of free coordination sites would be

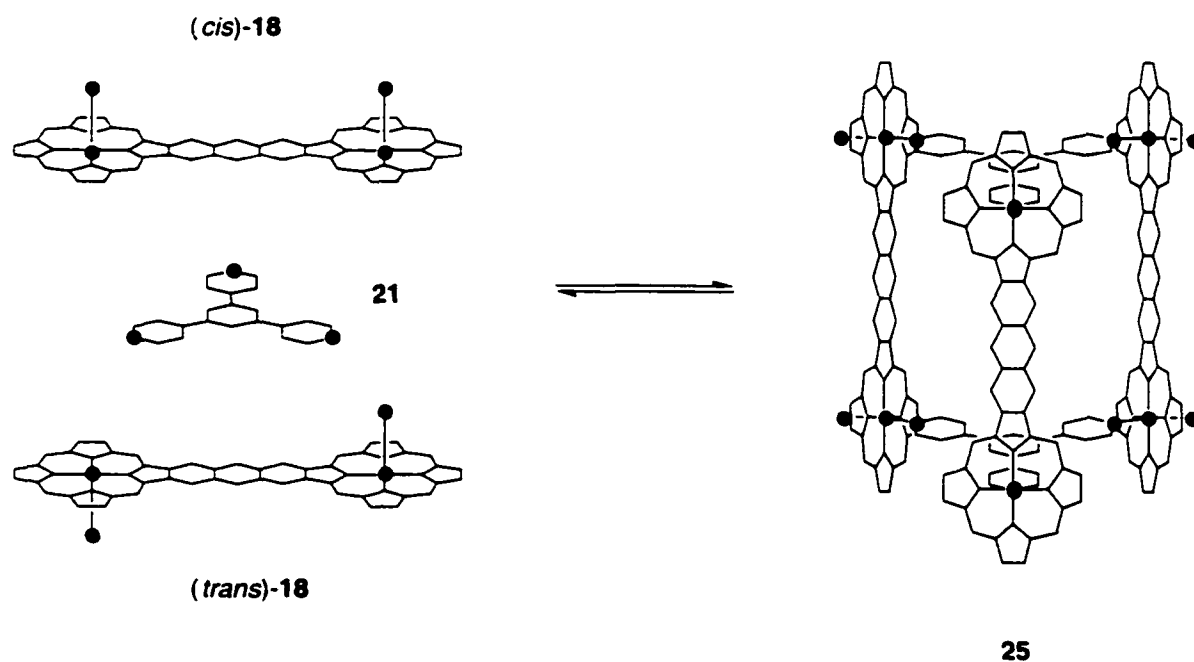
appreciably low, and therefore, the quantity of non-coordinated panels at any given time would be limited. In light of this, Routes 1 and 2 would be more plausible because the concentrations of the important building blocks, namely the bis- and mono-coordinated panels, should exist in the greatest amounts at any given time (states labeled 'A' and 'B'). By following these two routes, the two states labeled 'D' and 'E' in Equation 5 emerge. In order to form the macrocycle **22** from state 'D', the removal of one 4,4'-bipyridine linker is required and this aids in populating the last and most important state labeled 'E'. From state 'E', the rotation of one of the three bonds of the shared 4,4'-bipyridine would result in the formation of macrocycle **22** and this intramolecular reaction should occur rapidly. With regard to the second approach where 4,4'-bipyridine is present in excess, the pathways that populate the important state 'E' will be impeded because the number of free coordination sites will always be very low and hence form **22** in substantially lower yields. The fact that **22** still forms under these conditions should support the existence of cooperative associations, which increases the stability of the macrocycle **22**. In light of these results, the macrocycle **22** should be synthesized by adding a slight excess of 4,4'-bipyridine (1.1 molar equivalents) to a solution containing *cis-/trans-18* and then heated because **22** will be produced in substantially higher yields.

The reaction mixture was purified by filtering the solution through silica gel which effectively removed any unchanged **18** and any bis-coordinated panels (**23** and **24**) as the macrocycle was the only product that elutes with CH₂Cl₂ (Figure 20e). The fact that the product comes off intact lends support to the stability of the metal-coordinated macrocycle.

Preliminary self-assembly studies showed that molecular rectangles were also formed using the binuclear salophen panel **17** with **20** as a linker using the same self-assembly protocol described for **18**. Modeling provided an estimate of the size of the cavities of the porphyrin and salophen rectangles which have dimensions of $15.4 \times 7.0 \text{ \AA}^2$ and $12.5 \times 7.0 \text{ \AA}^2$ respectively.

4.6.2 – The Construction of Three Dimensional Prisms

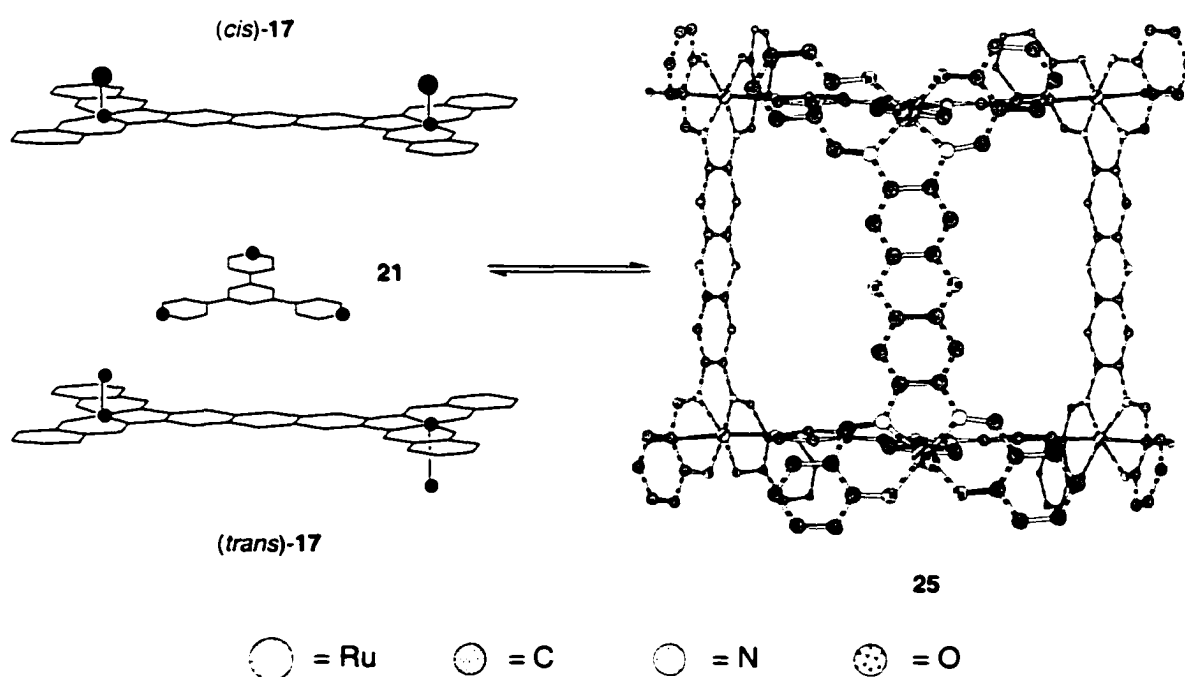
To make closed-shelled molecules using bimetallic panels, two triangular ligands **21** can be used to hold three bis-porphyrin panels **18** together forming a triangular prism (Equation 6).



Equation 6. Schematic of the self-assembly reaction using *cis/trans*-**18** and **21**. The porphyrins' substituents and double bond representations have been omitted for clarity.

Self-assembly reactions using *cis*-/*trans*-**18** panels failed to form the desired prism. Molecular modeling suggested that unfavorable intraligand interactions occur when positioning and holding the rather bulky platform around the small triangular template. The bulky *tert*-butyl substituents on the inner flanking phenyl rings interact with adjacent substituents to destabilize the prism and prevent its formation.

On the other hand, the less sterically demanding *cis*-/*trans*-**17** panel was shown to assemble into the desired triangular prism (Equation 7 and Figure 21). The reaction conditions were slightly different. In this case, a 50/50 mixture of chloroform/methanol was used as the solvent because Lewis basic solvents would increase the ligand exchange rates and assist in breaking up the more complicated polymer.



Equation 7. The salophens' substituents and double bond representations have been omitted for clarity. The molecular model of **25** was obtained by MM2 calculations.

The addition of the three molar equivalents of *cis/trans*-**17** panel to two molar equivalents of **21** in an NMR tube resulted in the formation of a precipitate, most likely a polymer. Broad resonances for all signals present in the spectrum were observed in the ^1H NMR spectrum of this reaction (Figure 21b).

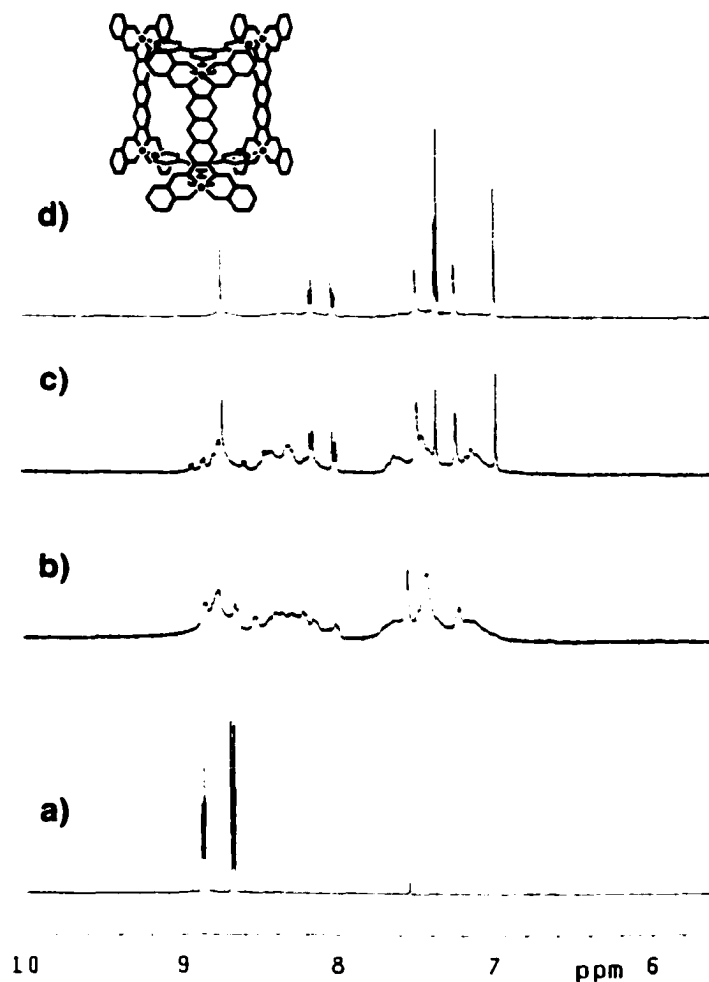


Figure 21. ^1H NMR (500 MHz, CD_2Cl_2) of a) **21**, b) **21** plus 1.5 molar equivalents of *cis/trans*-**17** at room temperature, c) after heating, d) the isolated prism

The reaction mixture was then heated which resulted in the appearance of well ordered signals that were superimposed on the broad signals (Figure 21c). The reaction mixture was purified by filtering and eluting the solution through silica gel with CH_2Cl_2 .

The product that was eluted clearly consists of unique triangles and panels consistent of a D_{3h} -symmetric prism (Figure 21d).

The cavity of the triangular prism can be more clearly viewed by examining its molecular model which shows the water-accessible surfaces (Figure 22). The top and bottom faces cannot be penetrated, but the cavity can be accessed by passage through any of the three apertures $10.2 \times 10.4 \text{ \AA}$ in size. With this in mind and a better understanding of the cavity size, the encapsulation of small organic molecules using this prism is possible and studies of this nature still need to be explored.

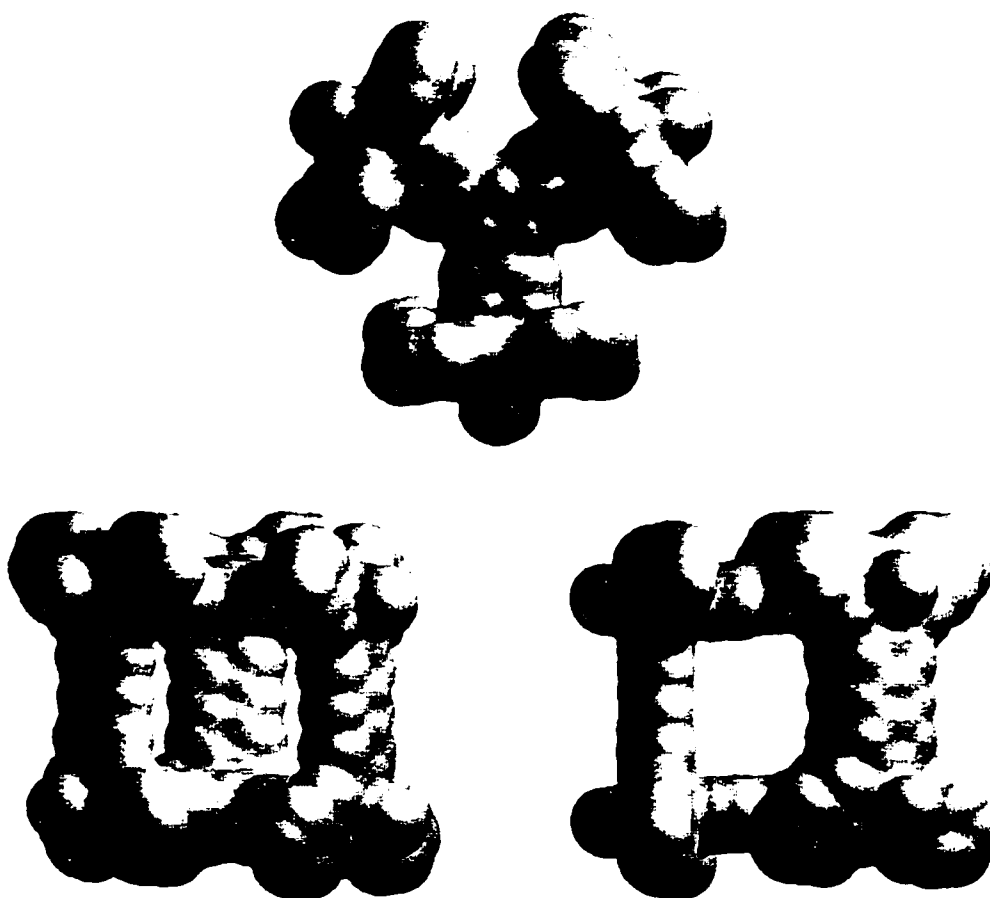
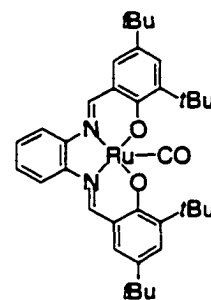


Figure 22. The water accessible surfaces of the prism. The molecular model of **25** was obtained by MM2 calculations.

4.7 – Experimental Section

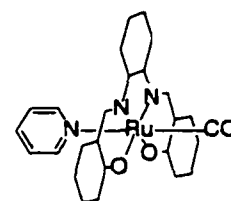
General Remarks: All solvents (Caledon) were distilled prior to use. Solvents used for UV/Vis spectroscopy were deoxygenated by bubbling argon through the solvent. Solvents for NMR spectroscopic analysis (Cambridge Isotope Laboratories) were used as received. All reagents and starting materials were purchased from Aldrich. *N,N'*-bis-(3,5-di-*tert*-butylsalicylidene)-1,2-phenylenediamine (**3**),⁹ [Ru(pytpy)₂][PF₆]₂ (**7**)¹⁴ (pytpy = 4'-(4'''-pyridyl)-2,2':6',2''-terpyridine), 4'-(4'''-pyridyl)-2,2':6',2''-terpyridine (**8**),¹⁵ [Ru(dpybpy)₃][PF₆]₂ (**10**)^{1a,17} (dpybpy = 4,4'-di(4''-pyridyl)-2,2'-bipyridine) and 4,4'-di(4''-pyridyl)-2,2'-bipyridine (**11**)¹⁶ were prepared as described in the literature. ¹H NMR spectroscopic characterizations were performed on a Varian Inova-500 instrument, working at 499.92 or on a Varian Inova-300 instrument, working at 299.96 MHz. Chemical shifts (δ) are reported in parts per million relative to tetramethylsilane using the residual solvent peak as a reference standard. FT-IR measurements were performed using a Nicolet Magna-IR 750 on solid samples equipped with a microscope unless otherwise stated. UV/Vis measurements were performed using a Varian Cary 400 Scan spectrophotometer. Cyclic voltammetry measurements were performed in CH₂Cl₂ using a PINE bipotentiostat, a platinum working electrode, a platinum counter electrode and a Ag/AgCl reference electrode, and tetrabutyl ammonium hexafluorophosphate as the electrolyte. MALDI mass spectra were recorded on an Applied Biosystems Voyager Elite equipped with delayed extraction and an ion mirror (reflectron). All spectra were

generated with the use of a pulsed nitrogen laser (337 nm) and an ion acceleration voltage of 20 kV. The instrument was operated in delayed extraction mode with the reflectron and with a delay time of 200 ns. Dithranol was used as the matrix and was prepared by dissolving 10 mg/mL in toluene. The sample was prepared by dissolving in 1:1 methanol toluene and mixed 1:1 with the matrix solution. A one microlitre drop was applied to the sample target and allowed to dry. Electrospray ionization mass spectra were recorded on a Micromass ZabSpec Hybrid Sector-TOF with positive mode electrospray ionization. The liquid carrier was infused into the electrospray source by means of a Harvard syringe pump at a flow rate of 10 μ L/minute. The sample solution, in the same solvent, was introduced *via* a 1 μ L-loop-injector. Purified nitrogen gas was used as a pneumatic aid and filtered air as the bath gas, heated at *ca.* 80°C. For low resolution, the mass spectra were acquired by magnet scan at a rate of 5 seconds/decade at *ca.* 1000 resolution. For exact mass measurements, the spectra were obtained by voltage scan over a narrow mass range at *ca.* 10000 resolution. Data acquisition and processing was achieved by using the OPUS software package on a Digital Alpha station with VMS operating system.



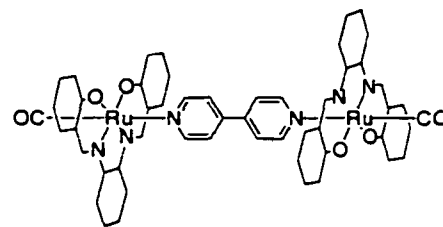
Ru(BSP)(CO) (4): A solution of *N,N'*-bis(3,5-di-*tert*-butylsalicylidene)-1,2-phenylenediamine (**3**) (130 mg, 0.242 mmol) and Ru₃(CO)₁₂ (65.0 mg, 0.102 mmol) in toluene (5 mL) was heated at reflux for 15 h under an argon atmosphere. The reaction mixture was cooled to room temperature, filtered through Celite and concentrated under reduced pressure. The resulting dark red residue was chromatographed through alumina (activity II-III) eluting first with toluene to remove an orange band followed by CH₂Cl₂ to remove a yellow band and then with a mixture of EtOH/CH₂Cl₂ (5:95) to remove a red-pink band. The red-pink band was concentrated to dryness under vacuum affording **4** as a glassy red solid which was recrystallized from aqueous EtOH. Yield: 73 mg (46%).

M.p. >300°C (decomp); ¹H NMR (300 MHz, [D₆]acetone, 22°C): δ = 9.34 (s, 2 H), 8.29 (dd, *J* = 3.3, 9.6 Hz, 2 H), 7.48 (d, *J* = 2.7 Hz, 2 H), 7.40 (d, *J* = 2.7 Hz, 2 H), 7.33 (dd, *J* = 3.3, 9.6 Hz, 2 H), 1.55 (s, 18 H), 1.33 (s, 18 H); ¹³C NMR APT (125.7 MHz, [D₆]acetone, 22°C): δ = 170.6 (C), 157.2 (CH), 146.9 (C), 142.7 (C), 135.2 (C), 131.0 (CH), 130.1 (CH), 126.7 (CH), 121.7 (C), 116.1 (CH), 36.6 (C), 34.5 (C), 31.7 (CH₃), 30.4 (CH₃); HSMS (ESI+): *m/z* = Calcd for M⁺ (C₃₇H₄₆N₂O₃Ru) 668.2252. Found: 668.2251; UV/Vis (CH₂Cl₂): λ_{max} / nm (log ε / M⁻¹cm⁻¹) = 258 (4.48), 306 (4.26), 382 (4.38), 491 (3.91) 541sh (3.75); Selected IR (microscope): ν = 1931 (CO) cm⁻¹.



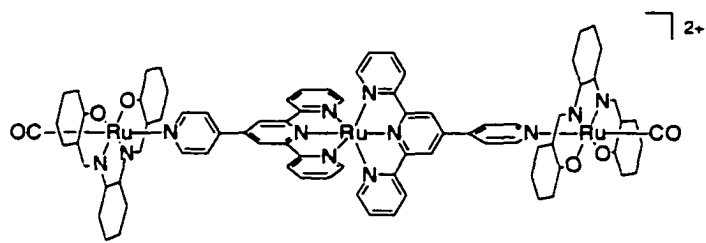
Ru(BSP)(CO)(py) (5): A solution of pyridine (0.25 mL) in CH₂Cl₂ (5 mL) was treated with Ru(BSP)(CO) (**4**) (38.0 mg, 0.055 mmol) and stirred at room temperature for 30 min. Silica gel (1 g) was added and the mixture was evaporated to dryness. The solid residue was applied to a small column of silica gel (1 × 2 cm) and eluted with CH₂Cl₂. The first band was collected and concentrated to dryness affording **5** as a purple solid. Yield: 37 mg (90%).

M.p. >300°C (decomp); ¹H NMR (300 MHz, CD₂Cl₂, 22°C): δ = 8.90 (s, 2 H), 8.12 (m, 2 H), 8.01 (dd, *J* = 3.3, 9.9 Hz, 2 H), 7.59 (m, 1 H), 7.42 (d, *J* = 2.7 Hz, 2 H), 7.32 (dd, *J* = 3.3, 9.6 Hz, 2 H), 7.09 (m, 4 H), 1.56 (s, 18 H), 1.28 (s, 18 H); ¹³C NMR APT (125.7 MHz, CD₂Cl₂, 22°C): δ = 170.0 (C), 155.0 (CH), 149.5 (CH), 145.9 (C), 143.0 (C), 138.0 (CH), 135.1 (C), 130.1 (CH), 130.0 (CH), 126.2 (CH), 124.6 (CH), 120.5 (C), 115.1 (CH), 36.3 (C), 34.1 (C), 31.4 (CH₃), 29.9 (CH₃); HSMS (ESI+): *m/z* = Calcd for M⁺ (C₄₂H₅₁N₃O₃Ru) 747.2974. Found: 747.2965; UV/Vis (CH₂Cl₂): λ_{max} / nm (log ε / M⁻¹cm⁻¹) = 264 (4.68), 310 (4.38), 391 (4.60), 503 (4.02) 555sh (3.09); Selected IR (microscope): ν = 1942 (CO) cm⁻¹.



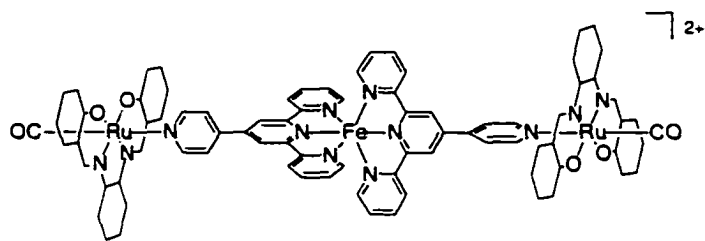
[Ru(BSP)(CO)]₂[4,4'-bipy] (6): A solution of 4,4'-bipyridine (3.9 mg, 0.025 mmol) in CH₂Cl₂ (5 mL) was treated with Ru(BSP)(CO) (4) (35.0 mg, 0.051 mmol) and stirred at room temperature for 30 min. Silca gel (1 g) was added and the mixture was evaporated to dryness. The solid residue was applied to a small column of silica gel (1 × 2 cm) and eluted with CH₂Cl₂. The first band was collected and concentrated to dryness affording **6** as a purple solid. Yield: 34 mg (92%).

M.p. >300°C (decomp); ¹H NMR (300 MHz, CD₂Cl₂, 22°C): δ = 8.91 (s, 4 H), 8.19 (dd, *J* = 1.5, 6.6 Hz, 4 H), 8.02 (dd, *J* = 3.6, 9.9 Hz, 4 H), 7.43 (d, *J* = 2.4 Hz, 4 H), 7.34 (dd, *J* = 3.3, 9.6 Hz, 4 H), 7.16 (dd, *J* = 1.5, 6.6 Hz, 4 H), 7.11 (d, *J* = 2.4 Hz, 4 H), 1.50 (s, 36H), 1.27 (s, 36 H); ¹³C NMR APT (125.7 MHz, CD₂Cl₂, 22°C): δ = 169.9 (C), 155.1 (CH), 150.3 (CH), 146.4 (C), 145.8 (C), 143.0 (C), 135.2 (C), 130.0 (CH), 126.1 (CH), 122.4 (CH), 120.5 (C), 115.1 (CH), 36.2 (C), 34.1 (C), 31.3 (CH₃), 29.9 (CH₃); MS (ESI⁺): *m/z* = 1492 M⁺; UV/Vis (CH₂Cl₂): λ_{max} / nm (log ε / M⁻¹cm⁻¹) = 264 (4.81), 310 (4.56), 391 (4.70), 501 (4.17) 555sh (4.00); Selected IR (microscope): ν = 1938 (CO) cm⁻¹.



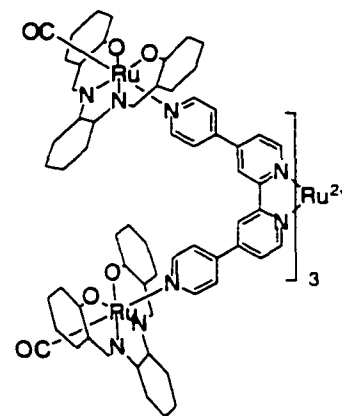
[Ru(BSP)(CO)]₂[Ru(pytpy)₂][PF₆]₂ (9a**):** A solution of [Ru(pytpy)₂][PF₆]₂ (**7**)¹⁴ (2.2 mg, 2.2 μmol) in acetone (5 mL) was treated with Ru(BSP)(CO) (**4**) (3.4 mg, 5.0 μmol) and stirred at room temperature for 30 min. The solvents were evaporated to dryness and the resulting solid was triturated with a mixture of Et₂O/pentane (20:80) and dried under vacuum. Yield: 4.7 mg (91%).

¹H NMR (300 MHz, [D₆]acetone, 22°C): δ = 9.40 (s, 4 H), 9.39 (s, 4 H), 8.91 (d, *J* = 8.1 Hz, 4 H), 8.48 (d, *J* = 6.6 Hz, 4 H), 8.39 (dd, *J* = 3.6, 9.9 Hz, 4 H), 8.17 (d, *J* = 6.6 Hz, 4 H), 8.00 (t, *J* = 7.8 Hz, 4 H), 7.63 (d, *J* = 4.8 Hz, 4 H), 7.50 (d, *J* = 2.4 Hz, 4 H), 7.40 (m, 8 H), 7.21 (t, *J* = 6.0 Hz, 4 H), 1.61 (s, 36 H), 1.32 (s, 36 H); MS (ESI+): *m/z* = 1028 [M – 2PF₆]²⁺; UV/Vis (CH₂Cl₂): λ_{max} / nm (log ε / M⁻¹cm⁻¹) = 276 (5.01), 312 (4.88), 330 (4.77), 390 (4.74) 493 (4.59), 555sh (4.18); Selected IR (microscope): ν = 1933 (CO) cm⁻¹.



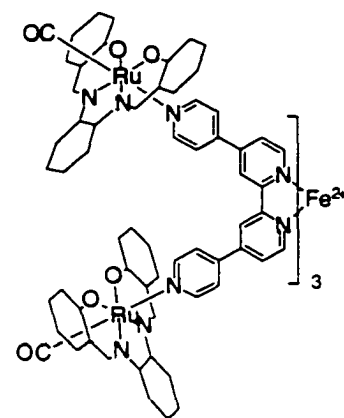
[Ru(BSP)(CO)]₂[Fe(pytpy)₂][BF₄]₂ (9b): A solid mixture of 4'-(4''-pyridyl)-2,2':6',2''-terpyridine (**8**)¹⁵ (3.1 mg, 0.01 mmol), Fe(BF₄)₂•(H₂O)₆ (1.7 mg, 5.0 μmol), and Ru(BSP)(CO) (**4**) (15.0 mg, 0.022 mmol) was dissolved in acetone (5 mL) and stirred at room temperature for 30 min. The solvents were evaporated to dryness and the resulting solid product was triturated in a mixture of Et₂O/pentane (20:80) and dried under vacuum. Yield: 20 mg (92%).

¹H NMR (300 MHz, [D₆]acetone, 22°C): δ = 9.56 (s, 4 H), 9.42 (s, 4 H), 8.86 (d, *J* = 7.8 Hz, 4 H), 8.53 (d, *J* = 6.6 Hz, 4 H), 8.40 (dd, *J* = 3.3, 9.6 Hz, 4 H), 8.27 (d, *J* = 6.6 Hz, 4 H), 7.95 (t, *J* = 7.8 Hz, 4 H), 7.50 (d, *J* = 2.4 Hz, 4 H), 7.40 (m, 12 H), 7.11 (t, *J* = 6.0 Hz, 4 H), 1.63 (s, 36 H), 1.32 (s, 36 H); MS (ESI⁺): *m/z* = 1006 [M – 2BF₄]²⁺; UV/Vis (CH₂Cl₂): λ_{max} / nm (log ε / M⁻¹cm⁻¹) = 282 (5.02), 291 (5.02), 327 (4.82), 393 (4.75) 508 (4.35), 573sh (4.52); Selected IR (microscope): ν = 1934 (CO) cm⁻¹.



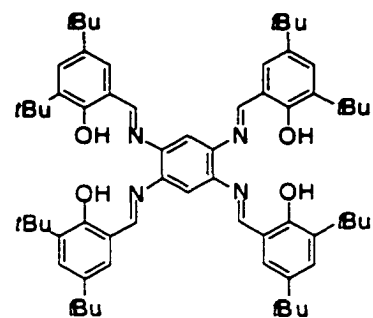
[Ru(BSP)(CO)]₆[Ru(dpybpy)₃][PF₆]₂ (12a): A solution of [Ru(dpybpy)₃][PF₆]₂ (**10**)^{4a.17} (2.0 mg, 1.5 mmol) in acetone (5 mL) was treated with Ru(BSP)(CO) (**4**) (6.4 mg, 9.6 mmol) and stirred at reflux for 30 min. The solvents were evaporated to dryness and the resulting solid product was triturated in a mixture of Et₂O/pentane (20:80) and dried under vacuum. Yield: 6.8 mg (84%).

¹H NMR (500 MHz, [D₆]acetone, 22°C): δ = 9.27 (s, 12 H), 9.04 (s, 6 H), 8.31 (m, 12 H), 8.23 (d, *J* = 6.5 Hz, 12 H), 7.88 (d, *J* = 6.0 Hz, 6 H), 7.58 (d, *J* = 6.5 Hz, 12 H), 7.45 (m, 18 H), 7.38 (dd, *J* = 3.5, 9.5 Hz, 12 H), 7.30 (s, 12 H), 1.55 (s, 108 H), 1.30 (s, 108 H); MS (ESI+): *m/z* = 2519.5 [M - 2PF₆]²⁺; UV/Vis (CH₂Cl₂): λ_{max} / nm (log ε / M⁻¹cm⁻¹) = 255 (5.34), 311 (5.19), 388 (5.18), 490 (4.77) 555sh (4.53); Selected IR (microscope): ν = 1946 (CO) cm⁻¹.



[Ru(BSP)(CO)]₂[Fe(dpybpy)₂][BF₄]₂ (12b): A solid mixture of 4,4'-di(4''-pyridyl)-2,2'-bipyridine (**11**)¹⁶ (1.2 mg, 3.9 μmol), Fe(BF₄)₂•(H₂O)₆ (0.5 mg, 1.5 μmol), and Ru(BSP)(CO) (**4**) (6.5 mg, 9.5 μmol) was dissolved in acetone (5 mL) and stirred at reflux for 30 min. The solvents were evaporated to dryness and the resulting solid product was triturated in a mixture of Et₂O/pentane (20:80) and dried under vacuum. Yield: 7.1 mg (94%).

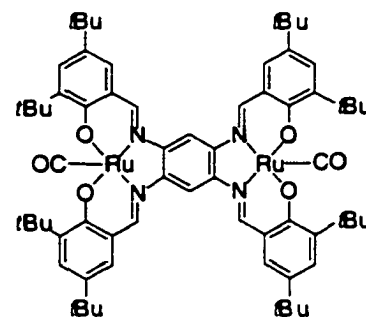
¹H NMR (500 MHz, [D₆]acetone, 22°C): δ = 9.28 (s, 12 H), 9.03 (s, 6 H), 8.32 (m, 12 H), 8.24 (d, *J* = 7.0 Hz, 12 H), 7.59 (d, *J* = 7.0 Hz, 12 H), 7.56 (dd, *J* = 1.5, 6.0 Hz, 6 H), 7.54 (d, *J* = 6.0 Hz, 6 H) 7.45 (m, 12 H), 7.38 (dd, *J* = 3.5, 10.0 Hz, 12 H), 7.31 (d, *J* = 2.5 Hz, 12 H), 1.57 (s, 108 H), 1.31 (s, 108 H); MS (ESI+): *m/z* = 2496.5 [M - 2BF₄]²⁻; UV/Vis (CH₂Cl₂): λ_{max} / nm (log ε / M⁻¹cm⁻¹) = 285 (5.39), 311 (5.16), 391 (5.21), 506 (4.72) 614sh (4.35); Selected IR (microscope): ν = 1946 (CO) cm⁻¹.



***N,N'',N''',N''''*-Tetra-(3,5-di-*tert*-butylsalicylidene)-1,2,4,5-phenylenetetraamine**

(bis(salophen) precursor to 14) (BS2P): 3,5-Di-*tert*-butylsalicylaldehyde (1.00 g, 4.27 mmol) and 1,2,4,5-benzenetetramine tetrahydrochloride (250 mg, 0.880 mmol) were heated in EtOH (5 mL) at reflux for 15 h. The solution was cooled to -10°C and stirred there for 3 h. The yellow-orange precipitate was collected by filtration, washed with EtOH and dried under vacuum. Yield: 610 mg (70%).

M.p. $285\text{--}286^{\circ}\text{C}$; ^1H NMR (360 MHz, CD_2Cl_2 , 27°C): δ = 13.53 (s, 4 H), 8.83 (s, 4 H), 7.49 (d, J = 2.2 Hz, 4 H), 7.32 (d, J = 2.3 Hz, 4 H), 7.25 (s, 4 H), 1.52 (s, 36 H), 1.33 (s, 36 H); ^{13}C NMR APT (125.7 MHz, CDCl_3 , 27°C): δ = 164.7 (CH), 158.7 (C), 141.6 (C), 140.6 (C), 137.3 (C), 128.6 (CH), 127.0 (CH), 118.4 (C), 111.2 (CH), 35.2 (C), 34.1 (C), 31.5 (CH_3), 29.5 (CH_3); MS (ESI $^{+}$): m/z = 1004 [$\text{M} + \text{H}$] $^{+}$; IR (microscope): ν = 2962, 2908, 2870, 1653, 1615, 1607, 1580, 1492, 1463, 1440, 1392, 1362, 1316, 1273, 1250, 1168, 1027, 983, 963, 937, 909, 882, 874, 866, 837, 771, 749, 686, 642 cm^{-1} .

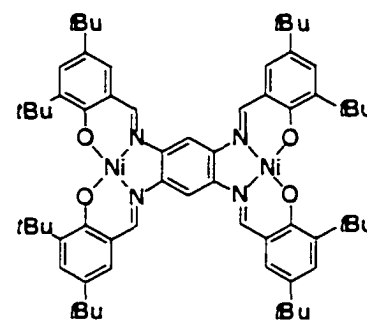


Ru₂[(BS2P)(CO)₂] (14): A solution of **BS2P** (200 mg, 0.20 mmol), Ru₃(CO)₁₂ (102 mg, 0.16 mmol) in toluene (5 mL) was heated at reflux for 40 h under an atmosphere of argon. The reaction mixture was cooled to room temperature, filtered through Celite and concentrated under reduced pressure. The resulting dark red residue was chromatographed through alumina (activity II-III) eluting first with CHCl₃ to remove a red-orange band followed by EtOH/CHCl₃ (5:95) to remove a purple band. The purple band was concentrated to dryness under vacuum affording the product as a glassy purple solid. Yield: 52.0 mg (21%).

¹H NMR (300 MHz, [D₆]acetone, 22°C): δ = 9.41 (s, 4 H), 9.14 (s, 1 H), 9.13 (s, 1 H), 7.51 (d, *J* = 2.7 Hz, 4 H), 7.31 (d, *J* = 2.4 Hz, 4 H), 1.56 (s, 36 H), 1.36 (s, 36 H); ¹³C NMR APT (125.7 MHz, [D₆]acetone, 22°C): δ = 170.9 (C), 156.9 (CH), 144.7 (C), 142.9 (C), 135.5 (C), 130.6 (CH), 130.4 (CH), 121.8 (C), 101.3 (CH), 36.7 (C), 34.5 (C), 30.3 (CH₃), 31.7 (CH₃); MS (ESI⁺): *m/z* = 1258 M⁺; UV/Vis (CH₂Cl₂): λ_{max} / nm (log ε / M⁻¹cm⁻¹) = 320 (4.58), 395 (4.62), 486 (4.47), 539sh (3.75) 568sh (4.42), 579sh (4.41); Selected IR (microscope): ν = 1950 (CO) cm⁻¹.

Ru₂[(BS2P)(CO)₂(py)₂] (15): A solution of pyridine (0.25 mL) in dichloromethane (5 mL) was treated with Ru₂[(BS2P)(CO)₂(H₂O)₂] (14) (35.0 mg, 0.055 mmol) and stirred at room temperature for 30 min. The mixture was evaporated to dryness and applied to a small column of silica gel (1 × 2 cm) and eluted with CH₂Cl₂. The first band was collected and concentrated to dryness affording a dark purple solid. Yield: 32.0 mg (81%).

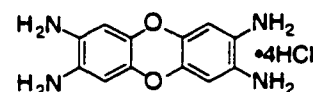
¹H NMR (500 MHz, CD₂Cl₂, 22°C): δ = 9.04 (s, 2 H), 8.52 (s, 1 H), 8.51 (s, 1 H), 8.20 (m., 4 H), 7.64 (m, 2 H), 7.47 (d, *J* = 2.5 Hz, 4 H), 7.28 (d, *J* = 2.5 Hz, 4 H), 7.16 (m, 4 H), 1.56 (s, 18H), 1.55 (s, 18 H), 1.35 (2 singlets, 36 H); ¹³C NMR APT (125.7 MHz, CD₂Cl₂, 22°C): δ = 170.3 (C), 154.3 (CH), 149.6 (CH), 149.5 (CH), 143.5 (C), 143.2 (C), 143.2 (C), 138.2 (C), 135.6 (C), 130.6 (CH), 130.1 (CH), 130.0 (CH), 124.8 (CH), 124.6 (CH), 120.9 (C), 99.7 (CH), 99.6 (CH), 36.35 (C), 34.3 (C), 31.6 (CH₃), 29.9 (CH₃); MS (ESI+): *m/z* = 1416 M⁺; UV/Vis (CH₂Cl₂): λ_{max} / nm (log ε / M⁻¹cm⁻¹) = 313 (4.58), 325 (4.57), 407 (4.62), 492 (4.42) 551sh (4.37), 614sh (4.35); Selected IR (microscope): ν = 1954 (CO) cm⁻¹.



Ni₂(BS2P): A solution of BS2P (100 mg, 0.1 mmol), Ni(OAc)₂(H₂O)₄ (124 mg, 0.5 mmol) in absolute EtOH (5 mL) was heated at reflux for 2 h. The reaction mixture was

cooled to room temperature and the red solid was collected by filtration, washed with cold EtOH and dried under vacuum. Yield: 100 mg (89%).

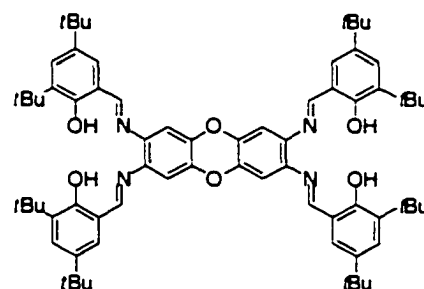
^1H NMR (300 MHz, CD_2Cl_2 , 22°C): δ = 8.33 (s, 4 H), 8.01 (s, 2 H), 7.46 (d, J = 2.7 Hz, 4 H), 7.28 (d, J = 2.4 Hz, 4 H), 1.45 (s, 36 H), 1.36 (s, 36 H); ^{13}C NMR APT (125.7 MHz, CDCl_3 , 22°C): δ = 165.4 (C), 153.5 (CH), 141.5 (C), 140.9 (C), 137.4 (C), 131.2 (CH), 126.5 (CH), 119.7 (C), 98.5 (CH), 35.9 (C), 34.0 (C), 31.2 (CH_3), 29.7 (CH_3); MS (MALDI, no matrix) : m/z = 1116 M^- ; UV/Vis (CH_2Cl_2): λ_{max} / nm ($\log \epsilon$ / $\text{M}^{-1}\text{cm}^{-1}$) = 268 (4.78), 322 (4.45), 374sh (4.46), 394 (4.55), 494 (4.58), 541sh (4.50); IR (microscope): ν = 2957, 2907, 2869, 1703, 1616, 1589, 1546, 1522, 1495, 1462, 1423, 1385, 1359, 1322, 1258, 1177, 1130, 1026, 971, 933, 916, 868, 828, 788, 749, 654, 637 cm^{-1} .



2,3,7,8-Tetraaminodibenzo[1,4]dioxin tetrahydrochloride (13)¹⁸: Tin metal (7.0 g 59.0 mmol) was added in small portions to a suspension of 2,3,7,8-tetranitrodibenzo[1,4]dioxin (1.70 g, 4.72 mmol) in concentrated hydrochloric acid (25 mL). The reaction mixture became extremely exothermic after 30 min. at which point the color of the suspension changes from yellow to creamy-white. The mixture was heated at reflux for 8 h to dissolve any residual solid tin metal. The mixture was filtered leaving a

white solid. The product was washed with concentrated HCl, then with EtOH and finally with Et₂O, and dried under vacuum. Yield: 1.35 g (74%).

¹H NMR (300 MHz, D₂O/CD₃CO₂D, 22°C): δ = 6.63 (s); ¹³C NMR APT (125.7 MHz, D₂O/CD₃CO₂D, 22°C): δ = 140.6 (C), 123.1 (C), 112.4 (CH); MS (ESI+): *m/z* = 244 [M - 4 HCl]⁺.

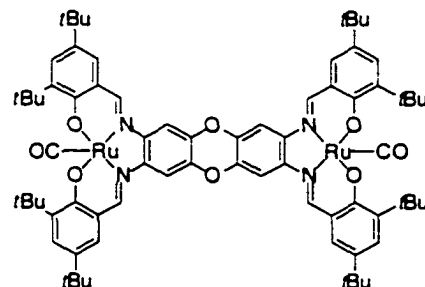


***N,N'',N''',N''''*-Tetra-(3,5-di-*tert*-butylsalicylidene)-2,3,7,8-dibenzo-[1,4]-**

dioxintetraamine (bis(salophen) precursor to 16) (BS2DP): 3,5-Di-*tert*-butylsalicylaldehyde (750 mg, 3.20 mmol) and tetraaminodibenzo[1,4]dioxin tetrahydrochloride (310 mg, 0.795 mmol) were heated in EtOH (18 mL) at reflux for 15 h. The solution was cooled to -10°C and stirred at that temperature for 3 h. The yellow precipitate was collected by filtration, washed with cold EtOH and dried under vacuum. Yield: 802 mg (91%).

M.p. > 350°C; ¹H NMR (500 MHz, [D₈]THF, 22°C): δ = 13.57 (br s, 4 H), 8.85 (s, 4 H), 7.46 (d, *J* = 2.5 Hz, 4 H), 7.37 (d, *J* = 2.5 Hz, 4 H), 7.14 (s, 4 H), 1.45 (s, 36 H), 1.33 (s, 36 H); ¹³C NMR APT (125.7 MHz, [D₈]THF, 22°C): δ = 165.9 (CH), 159.5 (C), 141.6 (C), 141.0 (C), 140.3 (C), 137.6 (C), 128.7 (CH), 128.2 (CH), 119.7 (C), 108.2

(CH), 35.8 (C), 34.8 (C), 31.8 (CH₃), 30.0 (CH₃); MS (ESI⁺): $m/z = 1109 [M + H]^+$; IR (microscope): $\nu = 2957, 2907, 2870, 1615, 1593, 1489, 1440, 1393, 1369, 1307, 1275, 1252, 1229, 1203, 1167, 937, 875, 861, 811, 774, 687 \text{ cm}^{-1}$.



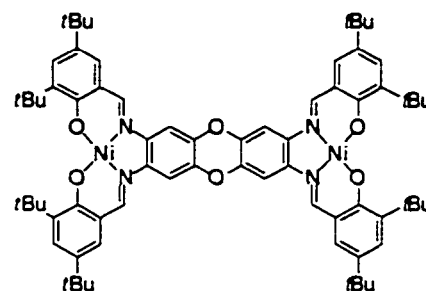
Ru₂[(BS2DP)(CO)₂] (16): A solution of **BS2DP** (250 mg, 0.225 mmol) and Ru₃(CO)₁₂ (220 mg, 0.470 mmol) in diglyme (15 mL) was heated at 135°C for 12 h. The reaction mixture was cooled to room temperature, filtered and concentrated to dryness under reduced pressure. The resulting dark red residue was chromatographed through alumina (activity II-III) eluting first with CHCl₃ to remove a yellow and an orange band followed by EtOH/CHCl₃ (5:95) to remove a red-pink band. The latter was concentrated to dryness under vacuum affording a glassy purple solid. Yield: 277 mg (91%).

¹H NMR (300 MHz, [D₆]acetone, 22°C): $\delta = 9.20$ (s, 4 H), 7.96 (s, 4 H), 7.49 (d, $J = 2.7$ Hz, 4 H), 7.41 (d, $J = 2.4$ Hz, 4 H), 1.55 (s, 36 H), 1.35 (s, 36 H); ¹³C NMR APT (125.7 MHz, [D₆]acetone, 22°C): $\delta = 170.6$ (C), 157.1 (CH), 143.2 (C), 142.7 (C), 140.4 (C), 135.4 (C), 130.9 (CH), 130.2 (CH), 121.8 (C), 103.5 (CH), 36.6 (C), 34.5 (C), 31.7 (CH₃), 30.4 (CH₃); MS (ESI⁺): $m/z = 1363 M^+$; UV/Vis (CH₂Cl₂): $\lambda_{\text{max}} / \text{nm}$ (log $\epsilon /$

$\text{M}^{-1}\text{cm}^{-1}$) = 262 (4.67), 302 (4.59), 313 (4.61), 375sh (4.59), 393 (4.64), 420sh (4.44), 507 (4.30) 550sh (4.19); Selected IR (microscope): $\nu = 1943$ (CO) cm^{-1} .

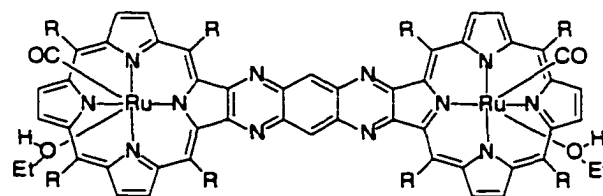
$\text{Ru}_2[(\text{BS2DP})(\text{CO})_2(\text{py})_2]$ (17): A solution of pyridine (0.25 mL) in CH_2Cl_2 (5 mL) was treated with **16** (50 mg, 0.055 mmol) and stirred at room temperature for 30 min. The mixture was evaporated to dryness and applied to a small column of silica gel (1 × 2 cm) and eluted with CH_2Cl_2 . The first band was collected and concentrated to dryness under vacuum affording a dark purple solid. Yield: 51.4 mg (81%).

^1H NMR (300 MHz, CD_2Cl_2 , 22°C): $\delta = 8.72$ (s, 4 H), 8.16 (m., 4 H), 7.63 (t, $J = 2.4$ Hz, 2 H), 7.60 (s, 4 H), 7.43 (d, $J = 2.4$ Hz, 4 H), 7.14 (m, 8 H), 1.54 (s, 36 H), 1.32 (s, 36 H); ^{13}C NMR APT (125.7 MHz, CD_2Cl_2 , 22°C): $\delta = 170.0$ (C), 154.5 (CH), 149.5 (CH), 149.5 (CH), 143.1 (C), 142.1 (C), 139.9 (C), 138.1 (CH), 135.3 (C), 130.2 (CH), 130.0 (CH), 124.7 (CH), 124.6 (CH), 120.5 (C), 102.5 (CH), 36.3 (C), 34.2 (C), 31.4 (CH₃), 29.9 (CH₃); MS (ESI+): $m/z = 1522$ M⁺; UV/Vis (CH_2Cl_2): λ_{max} / nm (log ϵ / $\text{M}^{-1}\text{cm}^{-1}$) = 263 (4.75), 304 (4.70), 317 (4.70), 400 (4.80) 520 (4.29), 566sh (4.22); Selected IR (microscope): $\nu = 1933$ (CO) cm^{-1} .



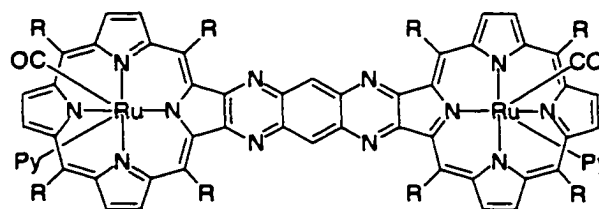
Ni₂(BS2DP): A solution of **BS2DP** (150 mg, 0.135 mmol) and Ni(OAc)₂(H₂O)₄ (168 mg, 0.676 mmol) in diglyme (15 mL) was heated at 140°C for 10 h under an inert atmosphere of argon. The reaction mixture was cooled to room temperature and the red solution was concentrated to dryness. The residue was suspended in hot 95% EtOH (30 mL), filtered while hot and washed with EtOH. The product was then dried under vacuum. Yield: 140 mg (85%).

¹H NMR (300 MHz, [D₈]THF, 22°C): δ = 8.40 (s, 4 H), 7.63 (s, 2 H), 7.41 (d, *J* = 2.7 Hz, 4 H), 7.26 (d, *J* = 2.4 Hz, 4 H), 1.47 (s, 36 H), 1.33 (s, 36 H); ¹³C NMR APT (125.7 MHz, [D₈]THF, 22°C): δ = 165.4 (C), 156.2 (CH), 141.0 (C), 141.0 (C), 140.1 (C), 137.2 (C), 130.9 (CH), 127.8 (CH), 120.9 (C), 103.2 (CH), 36.6 (C), 34.6 (C), 31.6 (CH₃), 30.3 (CH₃); MS (MALDI, no matrix): *m/z* = 1222 M⁺; UV/Vis (CH₂Cl₂): λ_{max} / nm (log ε / M⁻¹cm⁻¹) = 246sh (4.74), 270 (4.88), 304sh (4.61), 313 (4.63), 392 (4.65), 429 (4.63), 505 (4.40); IR (microscope): ν = 2956, 2908, 2869, 1617, 1590, 1526, 1494, 1480, 1464, 1429, 1386, 1358, 1322, 1298, 1258, 1238, 1207, 1175, 1130, 1024, 960, 934, 917, 867, 842, 787, 676, 638 cm⁻¹.



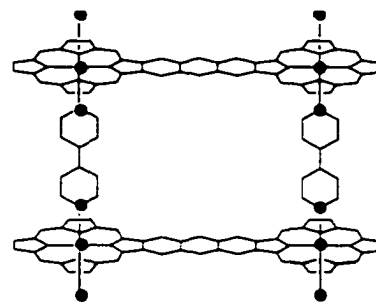
Porphyrin Complex (18a): A solution of Crossely's bis(porphyrin)^{19,20} (225 mg, 0.100 mmol) and $\text{Ru}_3(\text{CO})_{12}$ (215 mg, 0.338 mmol) in phenol (2.0 g) was heated at reflux for 1 h under an atmosphere of argon. The reaction mixture was cooled to room temperature and diluted with EtOH (2 mL) and the crude product was precipitated by adding water. The crude product was collected by filtration and washed with $\text{H}_2\text{O}/\text{EtOH}$ (50:50) to remove the phenol. The dark brown solid was dissolved in toluene and chromatographed through alumina(II-III) eluting first with toluene to remove an orange band followed by CH_2Cl_2 to remove a yellow band and then with a mixture of $\text{EtOH}/\text{CH}_2\text{Cl}_2$ (5:95) to remove a dark brown band. The latter was concentrated to dryness under vacuum and recrystallized from hydrous ethanol to give a brown solid. Yield 168 mg (65%).

^1H NMR (500 MHz, CD_2Cl_2 , 22°C): δ = 8.75 (s, 4 H), 8.72 (d, J = 5.0 Hz, 4 H), 8.63 (d, J = 5.0 Hz, 4 H), 8.53 (s, 2 H), 8.11 (m, 4 H), 8.06 (m, 4 H), 8.02 (m, 8 H), 7.99 (m, 4 H), 7.83 (m, 4 H), 1.56 (m, 144 H), 0.83 (broad, EtOH); ^{13}C NMR (125.7 MHz, CD_2Cl_2 , 22°C): δ = 153.1, 149.4, 149.3, 149.2, 147.0, 144.4, 143.0, 141.6, 141.5, 139.9, 137.1, 132.8, 131.0, 132.43, 129.5, 129.3, 129.2, 129.2, 128.9, 128.8, 125.9, 121.5, 120.3, 120.2, 35.4, 35.3, 32.3, 31.9; MS (ESI+): m/z = 2508 [$\text{M} - 2\text{EtOH}$]⁺; Selected IR (microscope): ν = 1933 (CO) cm^{-1} .



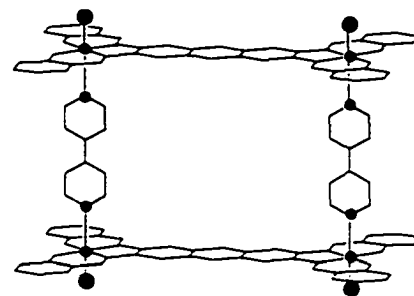
Porphyrin Pyridine Complex (18b): A solution of pyridine (0.25 mL) in dichloromethane (5 mL) was treated with porphyrin complex (18a) (30.0 mg, 0.012 mmol) and stirred at room temperature for 30 min. The mixture was evaporated to dryness and applied to a small column of silica gel (1 × 2 cm) and eluted with CH₂Cl₂. The first band was collected and concentrated to dryness affording a dark brown solid. Yield: 20.0 mg (63%).

¹H NMR (300 MHz, CD₂Cl₂, 22°C): δ = 8.69 (s, 4 H), 8.65 (d, *J* = 4.8, Hz 4 H), 8.57 (d, *J* = 4.8 Hz 4 H), 8.45 (s, 2 H), 8.05 (m, 4 H), 8.03 (m, 4 H), 7.96 (m, 8 H), 7.90 (m, 4 H), 7.81 (m, 4 H), 6.29 (t, *J* = 7.5 Hz, 2 H), 5.46 (t, *J* = 7.5 Hz, 4 H), 2.13 (d, *J* = 5.1 Hz, 4 H), 1.55 (s, 72 H), 1.53 (s, 36 H), 1.52 (s, 36 H); ¹³C NMR (125.7 MHz, CD₂Cl₂, 22°C): δ = 153.4, 149.4, 149.3, 149.3, 149.2, 149.0, 146.4, 144.8, 143.9, 142.6, 141.7, 141.7, 139.8, 136.5, 135.4, 135.4, 132.8, 132.1, 131.4, 130.0, 129.8, 129.5, 129.4, 129.0, 128.7, 128.6, 125.5, 122.6, 121.4, 120.2, 120.1, 35.4, 35.3, 32.3, 31.8; MS (ESI+): *m/z* = 2508 [M – 2py]⁺; Selected IR (microscope): ν = 1933 (CO) cm⁻¹.



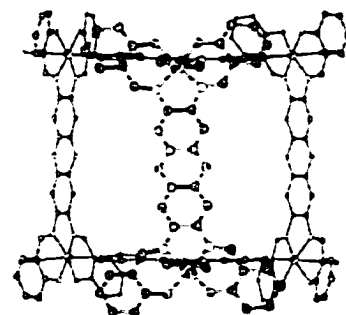
Porphyrin Bipyridine Complex (22): A solution of 4,4'-bipyridine (15.0 mg, 0.096 mmol) in CH_2Cl_2 (10 mL) was treated with porphyrin complex (18a) (55.0 mg, 0.021 mmol) and stirred at room temperature for 15 h. The mixture was evaporated to dryness and filtered through a small two-layered pipette of celite and silica gel (3 cm each) and eluted with CH_2Cl_2 . The first band was collected and concentrated to dryness affording a dark brown solid. Yield: 28.0 mg (50%).

^1H NMR (500 MHz, CD_2Cl_2 , 22°C): δ = 8.54 (s, 8 H), 8.50 (d, $J=4.8$, Hz, 8 H), 8.37 (d, $J=4.8$ Hz, 8 H), 8.24 (s, 8 H), 7.95 (t, $J=2.0$ Hz, 8 H), 7.87 (t, $J=2.0$ Hz, 8 H), 7.86 (t, $J=2.0$ Hz, 8 H), 7.76 (t, $J=2.0$ Hz, 8 H), 7.70 (t, $J=2.0$ Hz, 8 H), 7.61 (t, $J=2.0$ Hz, 8 H), 4.70 (dd, $J=1.5$, 6.0 Hz, 8 H), 1.77 (dd, $J=1.5$, 6.0 Hz, 8 H), 1.48 (s, 72 H), 1.45 (s, 72 H), 1.45 (s, 72 H), 1.40 (s, 72 H); ^{13}C NMR (125.7 MHz, CD_2Cl_2 , 22°C): δ = 183.2, 153.2, 149.4, 149.3, 148.9, 148.8, 146.3, 144.9, 143.7, 142.5, 142.4, 141.5, 141.4, 139.6, 136.2, 132.6, 132.0, 131.3, 130.0, 129.5, 129.2, 128.8, 128.4, 125.4, 121.4, 119.9, 119.8, 35.3, 35.21, 35.19, 32.19, 32.16, 31.9, 31.8; Selected IR (microscope): ν = 1969 (CO) cm^{-1} .



Bis(salophen) Bipyridine Complex : A solution of 4,4'-bipyridine (15.0 mg, 0.096 mmol) in acetone (10 mL) was treated with salen complex (**16**) (50.0 mg, 0.037 mmol) and stirred at room temperature for 15 h. The mixture was evaporated to dryness and filtered through a small two-layered pipette of celite and silica gel (3 cm each) and eluted with CH_2Cl_2 . The first band was collected and concentrated to dryness affording a dark purple solid. Yield: 28.0 mg (50%).

^1H NMR (500 MHz, CD_2Cl_2 , 22°C): δ = 8.63 (br s, 8H), 8.21 (br d, $J=1.5$, 6.5 Hz, 8H), 7.56 (br s, 8H), 7.40 (br d, $J=1.5$ Hz, 8H), 7.26 (dd, $J=1.5$, 6.5 Hz, 8H), 7.06 (br d, $J=1.5$ Hz, 8H), 1.52 (br s, 72H), 1.27 (br s, 72H).



Bis(salophen) Tripyridyltriazine Complex (25): A solution of 2,4,6-tripyridyltriazine (8.9 mg, 0.029 mmol) in 1/1 CHCl_3 -EtOH (10 mL) was treated with salen complex (**16**) (58.5 mg, 0.043 mmol) and stirred at room temperature for 15 h. The mixture was

evaporated to dryness and filtered through a small two-layered pipette of celite and silica gel (3 cm each) and eluted with CH₂Cl₂. The first band was collected and concentrated to dryness affording a dark purple solid. Yield: 30 mg (45%).

¹H NMR (500 MHz, CD₂Cl₂, 22°C): δ = 8.72 (s, 12H), 8.14 (dd, *J*=1.5, 6.5 Hz, 12H), 7.99 (dd, *J*=1.5, 6.5 Hz, 12H), 7.46 (d, *J*=1.5 Hz, 12H), 7.34 (s, 12H), 7.21 (d, *J*=1.5 Hz, 12H), 1.40 (s, 108H), 1.32 (s, 108H).

X-ray Crystallographic Study: The crystallographic data for the complexes Ni₂(BS2P), and Ni₂(BS2DP) are shown in Table 5. Crystals of Ni₂(BS2P) were grown from a mixture acetone/CH₂Cl₂ and crystals of Ni₂(BS2DP) were grown from THF. X-Ray data were collected on a Bruker PLATFORM/SMART 1000 CCD at 193 K using a graphite-monochromated *Mo-K_α* radiation ($\lambda = 0.71073 \text{ \AA}$) by taking ω scans at 0.2° intervals. The structures were solved by direct methods/fragment search using the computer program DIRDIF-96 and refined by full-matrix least-squares with anisotropic displacement parameters for the non-hydrogen atoms using the computer program SHELXL-93.²² Hydrogen atoms were introduced in their idealized positions as indicated by the *sp*² or *sp*³ geometries of their attached carbon atoms.

Table 5. Crystallographic data for the Nickel(II) analogs of 14 and 16

	Ni ₂ (BS2P)	Ni ₂ (BSD2P)
Molecular Formula	C _{70.625} H _{95.25} Cl _{0.625} N ₄ Ni ₂ O _{5.4375}	C ₈₀ H ₁₀₄ N ₄ Ni ₂ O ₈
Molecular Weight	1226.83	1367.09
Crystal size/mm	0.38 × 0.37 × 0.33	0.28 × 0.27 × 0.08
Crystal system	orthorhombic	monoclinic
Space group	<i>Pbcn</i> (No. 60)	<i>P2₁/c</i> (No. 14)
<i>a</i> /Å	27.4494(13)	10.6955(15)
<i>b</i> /Å	21.7996(11)	14.073(2)
<i>c</i> /Å	23.3535(12)	25.424(4)
β /°		95.733
<i>Z</i>	8	2
<i>V</i> /Å ³	13974.4(12)	3807.7(9)
Density/g cm ⁻³	1.166	1.192
μ /mm ⁻¹	0.612	0.550
Data collection 2 θ limit/°	52.82	52.82
Total data collected	88377	16031
Independent reflections	14337	7685
Observed data with $I \geq 2\sigma(I)$	10691	4974
Absorption correction method	SADABS	SADABS
Range of transmission factors	0.8236–0.8007	0.9574–0.8613
Data/restraints/parameters	14337 / 15 ^b / 740	7685 / 0 / 424
Goodness-of-fit on F^2	1.054	0.972
Final R indices [$I \geq 2\sigma(I)$] ^a		
$R_1 = [F_o^2 \geq 2\sigma(F_o^2)]$	0.0667	0.0519
$wR_2 = [F_o^2 \geq -3\sigma(F_o^2)]$	0.2130	0.1291
Largest difference peak and hole	2.350 and -1.647 e Å ⁻³	0.577 and -0.273 e Å ⁻³

^a $R_1 = \sum ||F_o| - |F_c|| / \sum |F_o|$; $wR_2 = \{ \sum [w(F_o^2 - F_c^2)^2] / \sum [w(F_o^2)] \}^{1/2}$.

^b The following distance restraints were applied to the disordered solvent acetone and dichloromethane molecules: $d(O2S-C5S) = d(O3S-C8S) = 1.22$ Å; $d(C4S-C5S) = d(C5S-C6S) = d(C8S-C9S) = 1.54$ Å; $d(O2S...C4S) = d(O2S...C6S) = d(O3S...C9S) = 2.40$ Å; $d(C4S...C6S) = d(C9S...C9S')$ = 2.67 Å; $d(C11S-C7S) = d(C12S-C7S) = d(C13S-C10S) = 1.80$ Å; $d(C11S...C12S) = d(C13S...C13S')$ = 2.95 Å (primed atoms are related to unprimed ones via the crystallographic twofold rotational axis (0, *y*, 1/4)).

4.8 – References

1. (a) T. Imamura, K. Fukushima, *Coord. Chem. Rev.*, **2000**, *198*, 133; (b) M. J. Gunter, N. Bampos, K. D. Johnstone, J. K. M. Sanders, *New J. Chem.*, **2001**, *25*, 166; (c) J. E. Redman, N. Feeder, S. J. Teat, J. K. M. Sanders, *Inorg. Chem.*, **2001**, advanced article; (d) E. Iengo, E. Zangrando, S. Mestroni, G. Fronzoni, M. Stener, E. Alessio, *J. Chem. Soc., Dalton Trans.*, **2001**, 1338; (e) U. Michelsen, C. A. Hunter, *Angew. Chem. Int. Ed.*, **2000**, *39*, 764; (f) R. A. Haycock, A. Yartsev, U. Michelsen, V. Sundström, C. A. Hunter, *Angew. Chem. Int. Ed.*, **2000**, *39*, 3616; (g) Y. Diskin-Posner, S. Dahal, I. Goldberg, *Angew. Chem. Int. Ed.*, **2000**, *39*, 1288; (h) A. Prodi, M. T. Indelli, C. J. Kleverlaan, F. Scandola, E. Alessio, T. Gianferrara, L. G. Mazilli, *Chem. Eur. J.*, **1999**, *5*, 2668.
2. (a) D. Gust, T. A. Moore, A. L. Moore, *Acc. Chem. Res.*, **2001**, *34*, 40; (b) M. Andersson, M. Linke, J.-C. Chambron, J. Davidsson, V. Heitz, J.-P. Sauvage, L. Hammarström, *J. Am. Chem. Soc.*, **2000**, *122*, 3526; (c) L. Flamigni, I. M. Dixon, J.-P. Collin, J.-P. Sauvage, *Chem. Commun.*, **2000**, 2479; (d) R. K. Lammi, A. Ambroise, T. Balasubramanian, R. W. Wagner, D. F. Bocian, D. Holten, J. S. Lindsey, *J. Am. Chem. Soc.*, **2000**, *122*, 7579; (e) S. I. Yang, J. Li, H. S. Cho, D. Kim, D. F. Bocian, D. Holten, J. S. Lindsey, *J. Mater. Chem.*, **2000**, *10*, 283; (f) J. Brettar, J.-P. Gisselbrecht, M. Gross, N. Solladié *Chem. Commun.*, **2001**, advanced article; (g) S. Richeter, C. Jeandon, R. Ruppert, H. J. Callot, *Chem. Commun.*, **2001**, 91; (h) C. M.

- Drain, X. Shi, T. Milic, F. Nifiatis, *Chem. Commun.*, **2001**, 287; (i) S. Yagi, I. Yonekura, M. Awakura, M. Ezoe, T. Takagishi *Chem. Commun.*, **2001**, 557; (j) A. Nakano, T. Yamazaki, Y. Nishimura, I. Yamazaki, A. Osuka, *Chem. Eur. J.*, **2000**, *6*, 3254; (k) N. Aratani, A. Osuka, Y. H. Kim, D. H. Jeong, D. Kim, *Angew. Chem. Int. Ed.*, **2000**, *39*, 1458; (l) K. Kilså, J. Kajanus, A. N. Macpherson, J. Mårtensson, B. Albinsson, *J. Am. Chem. Soc.*, **2001**, *123*, 3069; (m) H. Imahori, K. Tamaki, D. M. Guldi, C. Luo, M. Fujitsuka, O. Ito, Y. Sakata, S. Fukuzumi, *J. Am. Chem. Soc.*, **2001**, *123*, 2607; (n) H. Imahori, H. Norieda, H. Yamada, Y. Nishimura, I. Yamazaki, Y. Sakata, S. Fukuzumi, *J. Am. Chem. Soc.*, **2001**, *123*, 100; (o) K. Ogawa, Y. Kobuke, *Angew. Chem. Int. Ed.*, **2000**, *39*, 4070; (p) F. Fungo, L. A. Otero, L. Sereno, J. J. Silber, E. N. Durantini, *J. Mater. Chem.*, **2000**, *10*, 645; (q) Y. Sakakibara, S. Okutsu, T. Enokida, T. Tani, *Thin Solid Films*, **2000**, *363*, 29.
3. A. W. Herlinger, K. Ramakrishna, *Polyhedron*, **1985**, *4*, 551.
 4. (a) K. Chichak, N. R. Branda, *Chem. Commun.*, **2000**, 1211; (b) K. Chichak, M. C. Walsh, N. R. Branda, *Chem. Commun.*, **2000**, 847; (c) K. Chichak, N. R. Branda, *Chem. Commun.*, **1999**, 523.
 5. F. Calderazzo, C. Floriani, R. Henzi, F. L'Eplattenier, *J. Chem. Soc., A*, **1969**, *2*, 1243.
 6. M. Gerloch and F. E. Mabbs, *J. Chem. Soc., A*, **1967**, 1900.
 7. N. Farrell, M. N. De Oliveira Bastos, A. A. Neves, *Polyhedron*, **1983**, *2*, 1243.
 8. M. M. Taqui Khan, Z. A. Shaikh, *Ind. J. Chem.*, **1992**, *31A*, 191.

9. J. Wöltinger, J.-E. Bäckvall, Á. Zsigmond, *Chem. Eur. J.*, **1999**, *5*, 1460.
10. (a) A. L. Singer, D. A. Atwood, *Inorg. Chim. Acta*, **1998**, *277*, 157; (b) M.-A. Muñoz-Hernández, B. Sannigrahi, and D. A. Atwood, *J. Am. Chem. Soc.*, **1999**, *121*, 6747.
11. (a) R. N. Mukherjee, T. D. P. Stack, R. H. Holm, *J. Am. Chem. Soc.*, **1988**, *110*, 1850; (b) F. M. Ashmawy, A. R. Ujaimi, C. A. McAuliffe, R. V. Parish, and R. G. Pritchard, *Inorg. Chim. Acta.*, **1991**, *187*, 155; (c) A. Elmali, Y. Elerman, I. Svoboda, H. Fuess, K. Griesar, and W. Haase, *Z. Naturforsch., Teil B*, **1993**, *48*, 313.
12. (a) P. Zanello, R. Cini, and A. Cinquantini, *Polyhedron*, **1985**, *4*, 1383; (b) M. M. Taqui Khan, CH. Sreelatha, S. A. Mirza, G. Ramachandraiah, and S. H. R. Abdi, *Inorg. Chim. Acta.*, **1988**, *154*, 103.
13. R.-J. Cheng, S.-H. Lin and H.-M. Mo, *Organometallics*, **1997**, *16*, 2121
14. E. C. Constable, A. M. W. Cargrill Thompson, *J. Chem. Soc., Dalton Trans.*, **1994**, 1409.
15. E. C. Constable, A. M. W. Cargrill Thompson, *J. Chem. Soc., Dalton Trans.*, **1992**, 2947.
16. R. J. Morgan, A. D. Baker, *J. Org. Chem.*, **1990**, *55*, 1986.
17. H. Dürr, U. Thiery, P. P. Infelta, and A. M. Braun, *New J. Chem.*, **1989**, *13*, 575.
18. For the synthesis of the dibenzodioxane fragment, see: (a) R. C. Cambie, S. J. Janssen, P. S. Rutledge, P. D. Woodgate, *J. Organomet. Chem.*, **1991**, *420*, 387; For the nitration of the dibenzodioxane fragment, see: (b) H. Gilman, J. J. Dietrich, *J. Am.*

- Chem. Soc.*, **1958**, *80*, 366; For the reduction of the nitrated compound, see: (c) W. Knobloch, H. Niedrich, *Chem. Ber.*, **1958**, *91*, 2562.
19. M. J. Crossley, P. L. Burn, *J. Chem. Soc., Chem. Commun.*, **1987**, 39.
20. V. Promarak, P. L. Burn, *J. Chem. Soc., Perkin Trans. I*, **2001**, 14.
21. (a) A. M. El-Hendawy, A. H. Alkubaisi, A. El-Ghany El-Kourashy, M. M. Shanab, *Polyhedron*, **1993**, *12*, 2343; (b) M. M. Taqui Khan, Z. A. Shaikh, R. I. Kureshy, A. B. Boricha, *Polyhedron*, **1992**, *11*, 91; (c) M. M. Taqui Khan, D. Srinivas, R. I. Kureshy, N. H. Khan, *Inorg. Chem.*, **1990**, *29*, 2320.
22. G. M. Sheldrick, *Acta Crystallogr.*, **1990**, *A46*, 467.

Chapter 5 – Conclusions

Despite the fact that the templated synthesis of a cubic molecular-scale chamber was not completed, the body of this thesis work clearly illustrates the ease of bringing axial coordinated ruthenium(II) carbonyl porphyrin and salophen complexes around central templates that bear divergent pyridines. The design and synthesis of suitable building blocks, and the exploitation of coordination chemistry and self-assembly synthetic methods provides an attractive approach to construct complex architectures with novel morphologies and interesting supramolecular properties. The distinct advantage that self-assembly synthesis has over its classical counterpart is that the desired assemblies form rapidly and in fewer synthetic steps. The self-assembly approach is also modular because the key components are interchangeable, as illustrated by employing axial coordination to either metalloporphyrins or metallosalophens. Also, the spatial arrangements of the molecular components can be modified and controlled by the central template building block. This synthetic strategy is an alternative method to construct, control, and tailor the position of chromophores around transition metal complexes and provides suitable model systems to study electron and energy transfer processes within supramolecular assemblies.

In this chapter, the important supramolecular properties associated with metalloporphyrins and metallosalophens will be summarized and compared. Then, a description of the important studies that are required to completely characterize the supramolecular photophysical properties of the axially coordinated porphyrin and salophen arrays described in this thesis will be outlined. The chapter closes with a

discussion highlighting the design of a second-generation core template for the synthesis of a porphyrin cube suggesting possible future extensions of this aspect of the thesis work.

5.1 – Metalloporphyrins and Metallosalophens in Supramolecular Chemistry

The direct comparison of the important chemical properties and design features of ruthenium(II) carbonyl porphyrin and salophen complexes is useful to reveal their utility as building blocks in supramolecular chemistry.

1. The rich electrochemical, photophysical, and coordination properties of ruthenium(II) porphyrin carbonyl complexes have been extensively documented and, thus, represent a significant advantage over the lesser known properties of the salophen analogues. (Although, the absence of a full understanding of these properties is certainly the impetus for studying the latter in more detail).
2. Axial coordination to either the ruthenium(II) carbonyl porphyrin or the salophen complexes is monitored due to their characteristic signals in their ^1H NMR spectra. However, the larger shielding effect of the porphyrin produces more diagnostic upfield shifts ($\Delta\delta$ as much as 7.0 ppm) of the axial ligands proton resonances and, thus, represents a significant advantage over the smaller upfield shifts ($\Delta\delta = 0.5$ ppm) provided by the salophen analogue.
3. A less significant but common feature used to verify the success of axial coordination of pyridines to either the ruthenium(II) carbonyl porphyrin or the salophen complexes

are the characteristic shifts produced in their IR vibrational and UV/Vis absorption spectra.

4. The most important feature that determines the utility of using porphyrins and salophens in supramolecular chemistry is the preparation of the building blocks themselves. The synthetic routes to porphyrins provide the macrocycles in low yields. The macrocycles are also tedious to isolate and purify, making the “design-to-realization” of new supramolecular building blocks lengthy. On the other hand, the ease at which salophens can be prepared, isolated, and tailored represents a significant synthetic advantage over their porphyrin analogues, as was demonstrated by the formation of the ruthenium(II) carbonyl bis(metallosalophens). This last argument should spark efforts to further develop this class of supramolecular building blocks.

5.2 – Future Studies

5.2.1 – Characterization of the Supramolecular Properties

The photophysical properties of the axially coordinated metalloporphyrin and metallosalophen arrays remain to be studied and should be studied extensively. The experiments should focus on examining the importance of the spatial orientation of the chromophores on the communication between them in each array. A direct comparison of the properties of the arrays with appropriate control molecules must be made. The controls should be analogous to those used to study the photophysical properties of the linear porphyrin arrays (Chapter 2), more specifically, controls that retain the intrinsic

properties of each isolated building block. For example, the origin of the octahedral arrays' excited state behaviour can be probed by synthesizing the known tris(bipyridine)ruthenium(II) octahedral complexes **1** and **2** which are unable to coordinate to Ru(TTP)(CO) or Ru(OEP)(CO) (Figure 1).¹ By studying these complexes, the existence of intermolecular phosphorescence quenching between non-coordinated chromophores can be evaluated and compared to the fully assembled arrays.

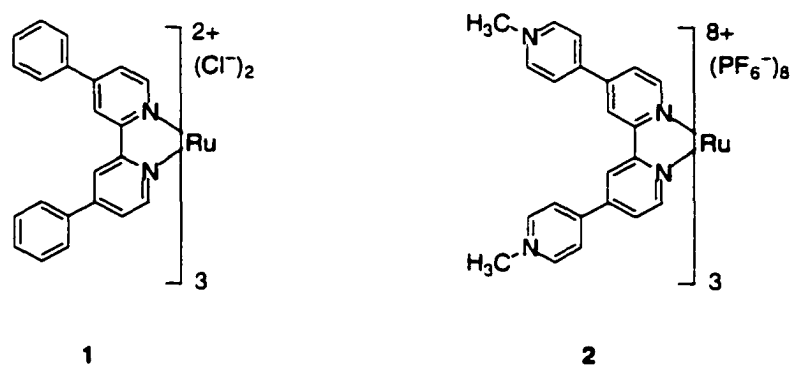


Figure 1.

In order to study the photophysical properties of the tetrahedral array (Chapter 2) an appropriate method to isolate the core complex needs to be found. Once the core complex has been isolated and characterized. A complete comparison can be made between the UV/Vis absorption properties of the array and its constituent parts. The tetraphenylbipyridine analog of the tetrahedral core complex (Structure [Cu(**16**)₂]PF₆ in Chapter 2) can be used as the control to evaluate the importance of intermolecular phosphorescence quenching between non-coordinated chromophores. The same approach can be taken to study the excited state behaviour of the [2]rotaxane, the salophen arrays, and their components. These future studies also should include detailed electrochemical, time-resolved luminescence and absorption spectroscopy to reveal the existence of any electronic communication between the components of the arrays. In light of this, Dr.

Luca Prodi, at the University of Bologna, has expressed his interest in studying the time-resolved luminescence and absorbance properties of the porphyrin arrays. Dr. Piero Zanello, at the University of Sienna, has studied the electrochemical properties of the porphyrin arrays. When these results are compiled with the time-resolved luminescence and absorbance experimental data the true pathway behind any excited state quenching processes of the arrays can be extracted.

Since the excited state properties of the ruthenium(II) carbonyl salophen building blocks are unknown, they need to be studied in order to evaluate the photophysical properties of the salophen arrays. Dr. Luca Prodi, at the University of Bologna, has expressed his interest in studying the time-resolved luminescence and absorbance properties of the metallosalophen monomer and the bimetallic metallosalophen pyridine complexes. Also, the association constant for the coordination of pyridine to the metal is not known and can be measured either by monitoring changes in the UV/Vis spectrum or by performing Isothermal Titration Calorimetry (ITC) experiments.

5.2.2 – The Templated Synthesis of the Porphyrin Cube

The major problem associated with the first-generation template is how the components are organized. To highlight this problem and to provide solutions, molecular models of the first-generation template and two alternative second-generation templates are shown in Figure 2. The organization problem stemmed from how the small bite angles provided by the bipyridine ligand **3** force the pyridines involved in axial coordination to be positioned in a distorted octahedral geometry (**3a** in Figure 2). As is

clear in the molecular model of the porphyrin array **3b**, the first-generation template improperly positions the six porphyrins in space and, thus, makes it difficult to design a substituted porphyrin with appropriate wall-connecting reaction sites to synthesize the cube.

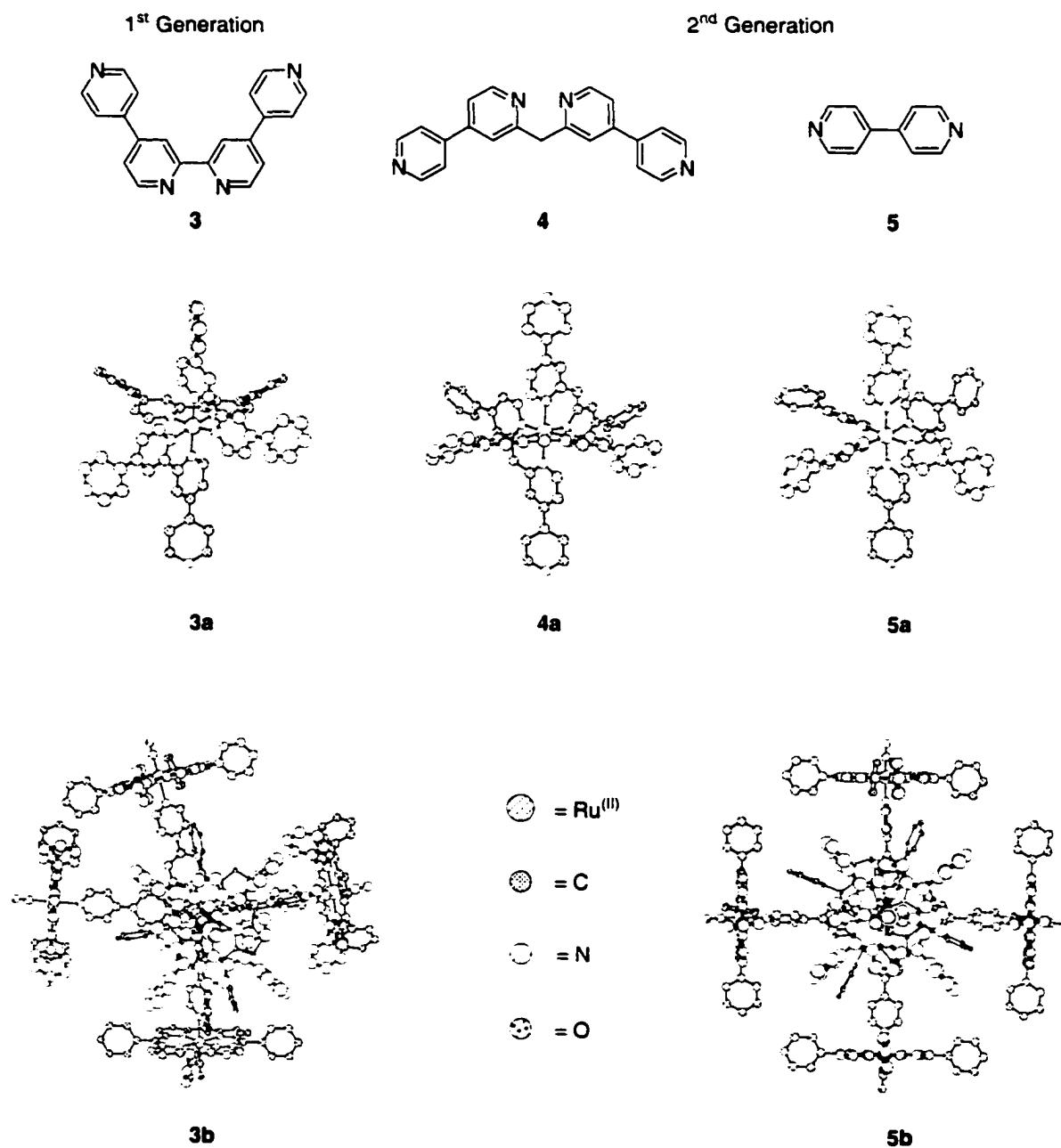


Figure 2.

To solve this problem, a second-generation template should use a ligand that exhibits a larger bite angle. In this way, distortions further away from the central templating metal are minimized. For example, the methylene spacer of ligand **4** positions the divergent pyridines of the octahedral template **4a** in a more appropriate geometry. However, this ligand might be more difficult to synthesize. On the other hand, these distortions can be minimized if 4,4'-bipyridine (**5**) is used as the templating ligand. The octahedral template **5a** that is created using the 4,4'-bipyridine ligand organizes the divergent pyridines and positions the six porphyrins so that they are evenly spaced when forming the octahedral array **5b**. As such, the octahedral array **5b** provides a better model to design an appropriately substituted porphyrin and to find an appropriate wall-connecting reaction to synthesize the porphyrin cube.

5.3 – Future Extensions

5.3.1 – Photoelectrochemical Devices Using Axial Coordination

The axial coordinated arrays described in this thesis illustrate the ease of bringing two, four, and six porphyrins together in a single step and may direct attention towards the advancement of creating tunable nanoscale devices. In order to achieve this, the porphyrin antennae must be within appropriate distances to provide suitable electronic interactions between chromophores. Naturally, having a larger number of antennae units will lead to higher efficiencies in harnessing light energy for electron transfer reactions. The ability to harness the energy and perform electron transfer reactions in the presence

of tunable photo- and redox-active molecules (transition metal complexes) may lead to the successful design of prototypical photoelectrochemical devices.

An example of a known version of such a device is shown in Figure 3. The device is divided into three parts: 1) antennae, 2) a sensitizer, and 3) a semiconductor surface of TiO_2 .

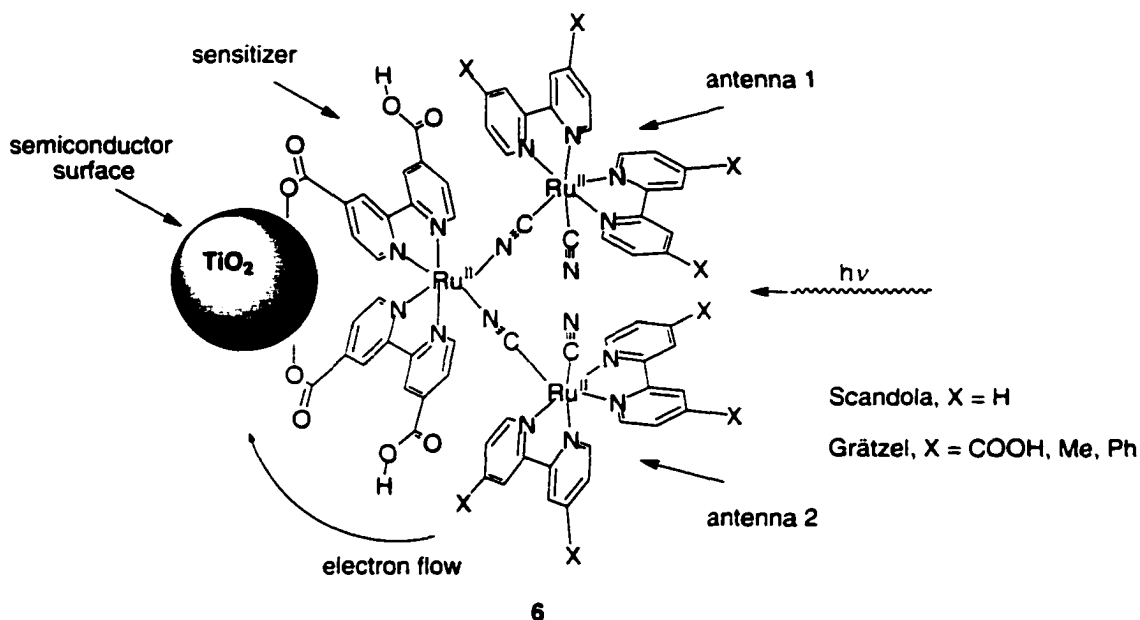


Figure 3. An example of a photoelectrochemical device.

The antennae and sensitizer are covalently linked through bridging cyanides and serve as the light harvesting and the electron injecting components, respectively. The carboxylic acid groups located on the sensitizer are used to adhere the bridged trimeric ruthenium(II) complex onto TiO_2 particles which are immobilized on a conducting glass sheet surface. The properties of device **6** are described by two independent literature reports by Grätzel and Scandola.² The results from each report are the same. Excitation of the external ruthenium(II) complexes results in the injection of an electron into the conduction band of a semiconductor film of TiO_2 which produces a current.

The major problem that these reports attribute to this device is the antenna's efficiency at harvesting the incident light energy. One possible solution to improve the light-harvesting efficacy of device **6** is to incorporate more effective antennae units, porphyrins for example (Figure 4). By following a similar procedure used to prepare the photoelectrochemical device **6**, it should be possible to manufacture the photoelectrochemical device **7** using axial coordination to position four light harvesting antennae onto the scaffold (Figure 4).

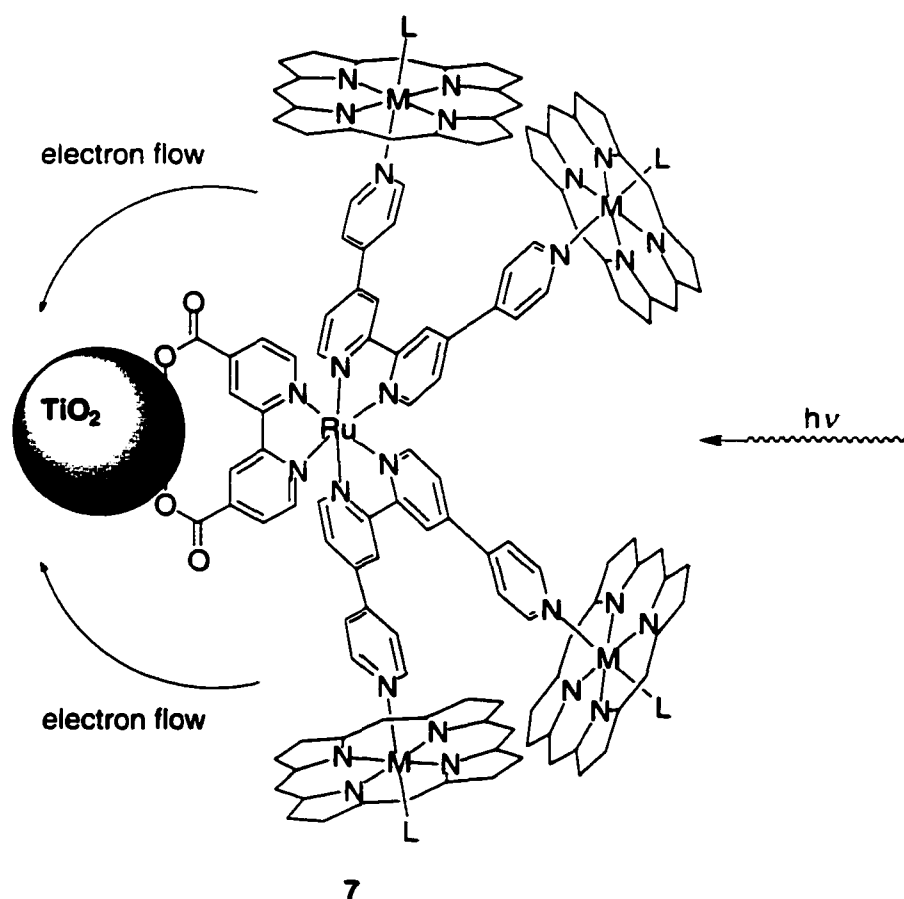


Figure 4. A photoelectrochemical device that uses axial coordination. The porphyrins' double bond representations have been omitted for clarity.

The antennae (porphyrins) can be removed and, thus, provides a means to tune and maintain the device. For example, the surface can be treated with a Lewis basic

solvent, such as pyridine, removing the porphyrins that are located on the TiO_2 surface, and replace them with different porphyrins. Different types of metals that display axial coordination sites can be inserted into the porphyrins to provide a method to readily tune the photo- and electrochemical properties of the proposed photoelectrochemical device 7. A larger photoelectrochemical device 8 can be envisaged which uses 4,4'-bipyridine as spacers instead of the cyano spacers of 6. This design provides a route to introduce eight additional light harvesting antennae (Figure 5).

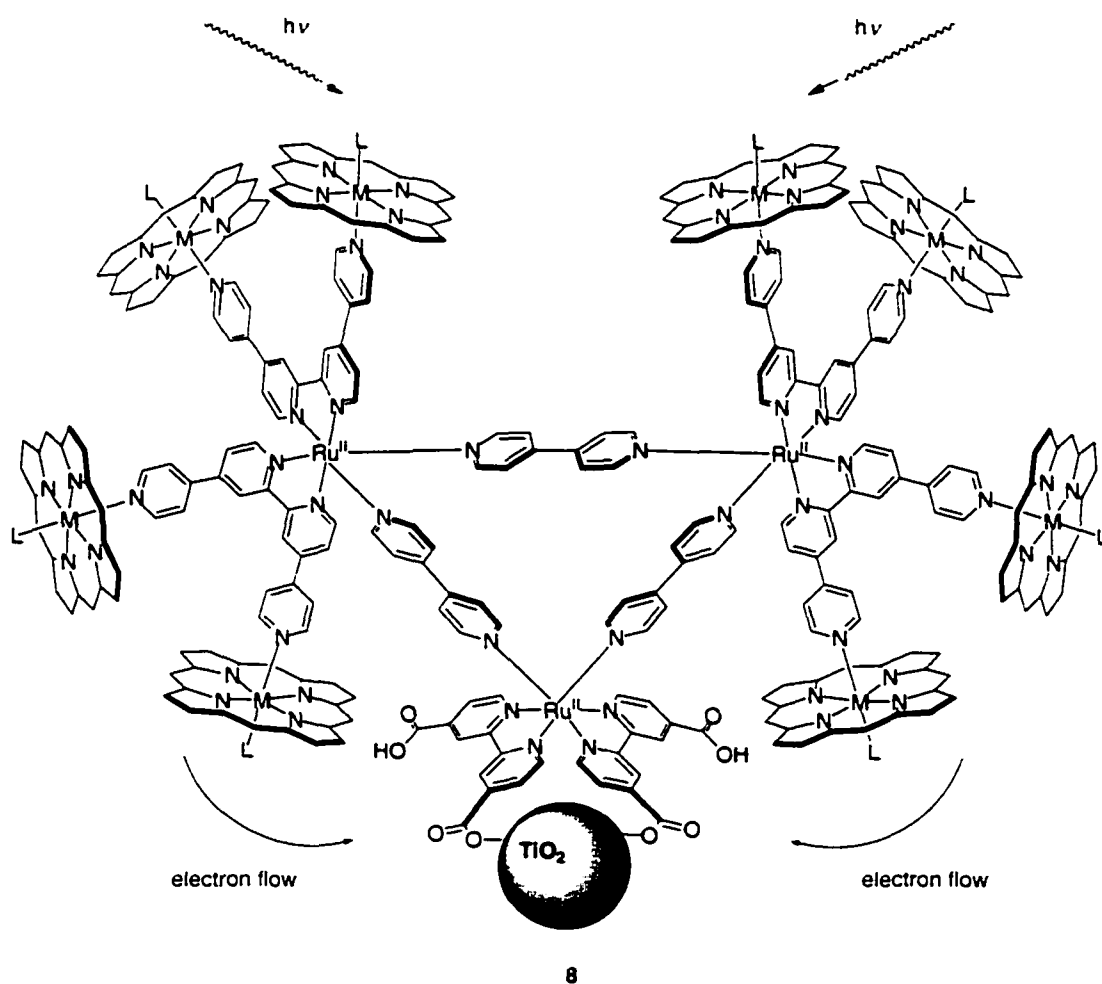


Figure 5. A larger photoelectrochemical device that uses axial coordination. The porphyrins' double bond representations have been omitted for clarity.

5.4 – References

1. (a) M. J. Cook, A. P. Lewis, G. S. G. McAuliffe, V. Skarda, A. J. Thompson, J. L. Glasper, and D. J. Robins, *J. Chem. Soc., Perkin Trans. II*, **1984**, 1293; (b) L. De Cola, F. Barigelletti, and M. J. Cook, *Helv. Chim. Acta*, **1988**, *71*, 733; H. Dürr, U. Thiery, P. P. Infelta, and A. M. Braun, *New J. Chem.*, **1989**, *13*, 575.
2. (a) B. O'Regan and M. Grätzel, *Nature*, **1991**, *353*, 737; (b) M. K. Nazeeruddin, P. Liska, J. Moser, N. Vlachopoulos, and M. Grätzel, *Helv. Chim. Acta*, **1990**, *73*, 1788; (c) R. Amadelli, R. Argazzi, C. A. Bignozzi, and F. Scandola, *J. Am. Chem. Soc.*, **1990**, *112*, 7099.